Elastic - Plastic Interfacial Crack Problems

by

Junhong Li, M.Sc

Thesis submitted to the Faculty of Engineering of
University of Glasgow for
the degree of Doctor of Philosophy

February 1998

Summary

Plane strain asymptotic solutions for the stress fields of a stationary crack in a homogeneous isotropic material under mixed-mode loading have been constructed analytically. Without loss of generality the fields are taken to comprise elastic and plastic sectors. Slip line solutions have been developed for the plastic sectors and semi-infinite elastic wedge solutions for the elastic sectors. The fields, which exhibit full continuity of tractions, have been verified by numerical calculations based on modified boundary layer formulations. For mode I, the loss in constraint depends on the second order term in the Williams expansion (T). A compressive T stress results in the formation of an elastic wedge on the crack flanks and a loss of crack tip constraint. The relation between the loss of constraint and the structure of the asymptotic field has been determined analytically. These fields form the basis of a two parameter, constraint-based characterisation of mode I fields. For mixed mode fields in non-hardening and incompressible conditions, the loss of constraint has been correlated to plastic mode mixity.

The asymptotic crack tip fields of a stationary crack located on the interface between a rigid body and an elastic-plastic matrix subject to mixed mode loading have been investigated under small scale yielding and incompressible deformation. The analysis does not require the assumption that plasticity fully surrounds the crack tip and satisfies continuity of stress, except for an allowable discontinuity in radial stress across the interface. Under negative mode mixities, the maximum hoop stress is located in the matrix and leads to the possibility that the crack may propagate into the matrix rather than along interface. The crack tip fields and hence the fracture toughness for this failure mode can be correlated with the fields and toughness in unconstrained mode I loading.

The plane strain asymptotic stress fields of interface cracks in elastically matched but strength mismatched materials have been examined numerically and analytically under mixed mode loading. Stationary cracks located in the interface, as well as normal to the interface have been studied. A family of

interface crack fields which depend on strength mismatch factor and phase angle have been constructed analytically in association with Prof. T-L Sham. These have been verified by a finite element method using boundary layer formations. For cracks normal to the interface, the crack tip stress field has been investigated by using boundary layer formulations under mode I with different levels of T stress and mixed mode loading. For weak and moderate strain hardening, the loss of constraint due to compressive T stress gives rise a family of fields which differ in a largely hydrostatic manner. This feature of mixed mode fields is similar to that of homogeneous materials. Both T and Mode II component cause a loss of constraint at the crack tip.

All these fields have the same important feature, that they differ in a largely hydrostatic manner on the plane of the maximum principal stress. For stress controlled failure, these fields can be correlated with the homogeneous mode I small scale yielding field allowing constraint based homogeneous mode I failure criterion to be used for bi-material interface cracks as well cracks in homogenous materials under mixed mode loadings.

Acknowledgements

I would like to most gratefully acknowledge my principal supervisor, Prof. J. W. Hancock, for all his supervision, encouragement, patience and particularly for his kindness throughout this work.

I also wish to thank Dr. D. V. Phillips, my second supervisor, for giving me the opportunity to carry out this study. I am grateful for his kindness and his helpful suggestions during the preparation of this manuscript.

I am indebted to Prof T-L. Sham, Raennsellar Polytechnic Institute, New York State, USA, for the discussion regarding the strength mismatched interfacial crack problem.

My friends and colleagues in Glasgow have been a constant source of encouragement, stimulation and company in the last three years. I would like to take this opportunity to thank them all.

Finally, a special thanks must go to my husband, Zhangwu, for his continuing support during last three years.

Declaration

The analytical solutions for strength mismatched interfacial crack problems are the results of co-operation with Prof T-L. Sham. Apart from this, the hypotheses, study design, numerical calculations, interpretation and review of publications were all originated and performed by the author subject to the above acknowledgements.

Contents

List of Figures

List of Tables

Chapter 1 Introduction

Composite materials are important in structural engineering because they can be designed to have a desired combination of mechanical and physical properties. For this reason they are now widely used for aerospace and other applications where high strength and stiffness-to-weight ratios are required. However such composites may have flaws or cracks due to processing, and in particular, defects may occur on weak interfaces. The effect of these defects can be addressed through fracture mechanics. The purpose of fracture mechanics is to ensure the fitness for purpose, and structural integrity, of engineering components which contain defects. The foundations of the subject lie in the energetics of crack advance, paralleled by descriptions of the crack tip field by a suitable characterising parameter. The internationally accepted approaches for homogenous material are through the measurement of a single parameter such as the *J*-integral introduced by Rice (1968a) or two parameters *J* and a constraint parameter *Q/T*. The first parameter, *J*, scales the asymptotic singularity at the crack tip while the second parameter, *Q/T*, indicates the level of stress triaxiality at the crack tip fields and characterises geometric constraint. However, current standards for failure assessment using fracture mechanics were developed for homogenous materials and can not be directly applied to the assessment of fracture behaviour of bi-material.

The present study is mainly concerned with small scale yielding analysis of elastically mismatched and strength mismatched interfacial crack tip fields under mixed mode loading. The primary aim is to find a relation between bi-material crack tip stress fields and homogenous crack tip stress fields. The objective is to develop a method to characterise elastic-plastic crack tip fields and develop a failure criterion for bi-material in terms of the known behaviour of single-phase materials.

In Chapter 2, elasticity, plasticity and slip line fields are briefly reviewed as a necessary background to this study. Chapter 3 introduces the fundamentals of

linear elastic fracture mechanics, elastic plastic fracture mechanics and two parameter fracture mechanics for homogeneous materials. Then the fracture mechanics of bi-material is reviewed in chapter 4 which includes elastic fracture mechanics of a bi-material, the stress fields of a crack on an elastically mismatched interface and the fields on strength mismatched interface under mode I with a T stress.

Chapters 5 and 6 develop analytic solutions for characterising homogenous mode I and mixed mode crack tip stress fields under non-hardening perfectly plastic deformation. Chapter 7 presents a small scale yielding analysis of an elastically mismatched interfacial crack tip under mixed mode loading. The strength mismatched interfacial crack tip stress fields under mixed mode loading are discussed in Chapter 8. Chapter 9 investigates a crack normal to a strength mismatched interface. In Chapters 7, 8, and 9, the crack tip stress fields for both non-hardening and strain hardening response are examined. In several significant cases the maximum principal stress is located in the matrix rather than on the interface. On the plane of the maximum principal stress direction, these fields belong to a similar family to the homogenous mode I fields which are deviatorically similar but differ mainly hydrostatically. The loss of constraint of bi-material fields due to mode II loading have been correlated with homogenous mode I fields. This allows the constraint based homogenous mode I failure loci to be mapped into bi-material data.

Finally, Chapter 10 summarises the work, presents conclusions and suggestions for future work.

Chapter 2 Constitutive relations: Elasticity and plasticity

The constitutive relations of elasticity and plasticity are fundamental to the material behaviour in the present work. This chapter describes these relations. Firstly, the concepts of the stress and strain are introduced and stress strain transformation are reviewed in both compact and expanded forms. The yield criteria are introduced and finally, plane strain slip line theory is presented to describe the stress and strain fields of a plastically deforming region.

2.1 Constitutive relations of elasticity

The constitutive relations for elastic deformation are discussed in a number of standard texts including Timoshenko and Goodier, (1970) and Slater, (1977). It is convenient to use an orthogonal Cartesian co-ordinate system with axes x_i, *(i=1,2,3)* as shown in Figure 2.1. The Cauchy stress tensor is denoted σ_{ij} *(i,j=1,2,3)*. Normal stresses are indicated by repeated subscripts, while shear stresses are indicated by mixed subscripts. Let t and u_i denote time and displacement and ρ the density. The equilibrium equation of motion under body forces F_i can then be written as:

$$\frac{\partial \sigma_{ij}}{\partial x_j} + F_i = \rho \frac{\partial^2 u_i}{\partial t^2} \quad \text{and} \quad \sigma_{ij} = \sigma_{ji} \tag{2.1-1}$$

Under conditions of small deformation, the displacement of particles in a deformed body can be resolved into components u_i parallel to the co-ordinate axes x_i as illustrated in Figure 2.2. The strain-displacement relation is written as:

$$\varepsilon_{ij} = \frac{1}{2}\left(\frac{\partial u_i}{\partial x_j} + \frac{\partial u_j}{\partial x_i} \right) \tag{2.1-2}$$

For an isotropic elastic solid the stress and strain are related by relations such as:

$$\sigma_{ij} = \lambda e_{kk}\delta_{ij} + 2\mu e_{ij} \tag{2.1-3}$$

Here λ and μ are the Lamé constants and δ_{ij} is the Kronecker delta.

$$\begin{aligned} \delta_{ij} &= 1 \quad i = j \\ \delta_{ij} &= 0 \quad i \neq j \end{aligned} \tag{2.1-4}$$

The relationship between stress and strain for a general elastic anisotropic solid is described by Hooke's law:

$$\sigma_{ij} = C_{ijkl}\,\varepsilon_{kl} \tag{2.1-5}$$

where C_{ijkl} are the elastic constants or stiffness. Equation (2.1-5) is written in tensor notation, which is very compact. Written out in the full expanded form, this equation has 81 elastic constants. It is however common practice to use a contracted matrix notation for writing stresses, strains, and elastic constants. C_{mn} is used for C_{ijkl}, σ_m for σ_{ij}, and ε_n for ε_{kl} as indicated in the following procedure:

ij or kl	*11*	*22*	*33*	*23*	*31*	*12*
m or n	*1*	*2*	*3*	*4*	*5*	*6*

Equation (2.1-5) can be then rewritten

$$\sigma_m = C_{mn}\,\varepsilon_n \tag{2.1-6}$$

The energy stored in an elastically strained body depends on the current strain state, and not on the path by which the strain state is reached, which implies the symmetry $C_{mn} = C_{nm}$. (Kelly and Groves, 1970)

Equation (2.1-6) can be written with the stress as the subject of the equation using S_{mn}, the compliance matrix as the inverse of the stiffness matrix C_{mn}.

$$\varepsilon_m = S_{mn}\,\sigma_n \tag{2.1-7}$$

In the expanded form, equation (2.1-6) may be written as

$$\begin{bmatrix}\sigma_1\\ \sigma_2\\ \sigma_3\\ \sigma_4\\ \sigma_5\\ \sigma_6\end{bmatrix} = \begin{bmatrix} C_{11} & C_{12} & C_{13} & C_{14} & C_{15} & C_{16}\\ & C_{22} & C_{23} & C_{24} & C_{25} & C_{26}\\ & & C_{33} & C_{34} & C_{35} & C_{36}\\ & & & C_{44} & C_{45} & C_{46}\\ & & & & C_{55} & C_{56}\\ & & & & & C_{66}\end{bmatrix}\begin{bmatrix}\varepsilon_1\\ \varepsilon_2\\ \varepsilon_3\\ \varepsilon_4\\ \varepsilon_5\\ \varepsilon_6\end{bmatrix} \tag{2.1-8}$$

The matrix is symmetric and in the most general case contains 21 independent elastic constants. The number of independent elastic constants can be further reduced because of the symmetry elements present. For an orthotropic material with the co-ordinate axes parallel to the symmetry axes of the material, many of the stiffnesses are zero, allowing equation (2.1-8) to be written as:

$$\begin{bmatrix}\sigma_1\\ \sigma_2\\ \sigma_3\\ \sigma_4\\ \sigma_5\\ \sigma_6\end{bmatrix} = \begin{bmatrix} C_{11} & C_{12} & C_{13} & 0 & 0 & 0\\ & C_{22} & C_{23} & 0 & 0 & 0\\ & & C_{33} & 0 & 0 & 0\\ & & & C_{44} & 0 & 0\\ & & & & C_{55} & 0\\ & & & & & C_{66}\end{bmatrix}\begin{bmatrix}\varepsilon_1\\ \varepsilon_2\\ \varepsilon_3\\ \varepsilon_4\\ \varepsilon_5\\ \varepsilon_6\end{bmatrix} \tag{2.1-9}$$

For isotropic materials in which elastic properties are independent of direction, only two of the elastic constants are independent, allowing equation (2.1-9) to be further reduced.

$$\begin{bmatrix}\sigma_1\\ \sigma_2\\ \sigma_3\\ \sigma_4\\ \sigma_5\\ \sigma_6\end{bmatrix} = \begin{bmatrix} C_{11} & C_{12} & C_{12} & 0 & 0 & 0 \\ & C_{11} & C_{12} & 0 & 0 & 0 \\ & & C_{11} & 0 & 0 & 0 \\ & & & \frac{C_{11}-C_{12}}{2} & 0 & 0 \\ & & & & \frac{C_{11}-C_{12}}{2} & 0 \\ & & & & & \frac{C_{11}-C_{12}}{2} \end{bmatrix} \begin{bmatrix}\varepsilon_1\\ \varepsilon_2\\ \varepsilon_3\\ \varepsilon_4\\ \varepsilon_5\\ \varepsilon_6\end{bmatrix} \qquad (2.1\text{-}10)$$

This equation can also be written in terms of the compliance matrix for isotropic materials.

$$\begin{bmatrix}\varepsilon_1\\ \varepsilon_2\\ \varepsilon_3\\ \varepsilon_4\\ \varepsilon_5\\ \varepsilon_6\end{bmatrix} = \begin{bmatrix} S_{11} & S_{12} & S_{12} & 0 & 0 & 0 \\ & S_{11} & S_{12} & 0 & 0 & 0 \\ & & S_{11} & 0 & 0 & 0 \\ & & & \frac{S_{11}-S_{12}}{2} & 0 & 0 \\ & & & & \frac{S_{11}-S_{12}}{2} & 0 \\ & & & & & \frac{S_{11}-S_{12}}{2} \end{bmatrix} \begin{bmatrix}\sigma_1\\ \sigma_2\\ \sigma_3\\ \sigma_4\\ \sigma_5\\ \sigma_6\end{bmatrix} \qquad (2.1\text{-}11)$$

For an isotropic material these compliances can easily be expressed in terms of Youngs' modulus, E, Poissons' ratio ν and the shear modulus G (Chawla, 1987):

$$E = \frac{1}{S_{11}} \qquad \upsilon = -\frac{S_{12}}{S_{11}} \qquad G = -\frac{1}{2}(S_{11} - S_{12}) \qquad (2.1\text{-}12)$$

For incompressible deformation, Poisson's ratio is equal to 0.5 and the compliances are related to the stiffness by:

$$S_{11} = \frac{C_{11} + C_{22}}{(C_{11} - C_{22})(C_{11} + 2C_{22})}$$

$$S_{12} = \frac{C_{12}}{(C_{11} - C_{22})(C_{11} + 2C_{22})} \qquad (2.1\text{-}13)$$

2.2 Plasticity

When a material is loaded beyond its elastic limit, the deformation is not entirely recoverable and the body does not regain its original shape on unloading. This non-recoverable or irreversible deformation is defined as plastic deformation (Hill,1950). The material is said to have yielded. In uniaxial tension, the stress at which the plastic deformation starts is called the yield strength, σ_0. Two yield criteria are commonly used to define the limit of elastic behaviour under general stress states: the Tresca yield criterion and the von Mises criterion. Tresca (1864) predicted that yielding would occur if the maximum shear stress, τ_{max}, exceeded the yield stress in shear, k. If σ_1, σ_2 and σ_3 are the principal stresses and $\sigma_1 > \sigma_2 > \sigma_3$, $\tau_{max} = (\sigma_1 - \sigma_3)/2$. The Mises yield criterion (1913) can be conveniently written in terms of deviatoric stresses S_{ij} which are defined as:

$$S_{ij} = \sigma_{ij} - \delta_{ij}\sigma_{kk}/3 \qquad (2.2\text{-}1)$$

The Mises yield criterion is then:

$$S_{ij}S_{ij}/2 = k^2 \qquad (2.2\text{-}2)$$

Where k is the yield stress in pure shear. Writing the yield criterion out in full leads to

$$\left[(\sigma_x-\sigma_y)^2+(\sigma_y-\sigma_z)^2+(\sigma_z-\sigma_x)^2\right]/6+\left(\sigma_{yz}^2+\sigma_{zx}^2+\sigma_{xy}^2\right)=k^2 \qquad (2.2\text{-}3)$$

In terms of the principal stresses, (σ_1, σ_2, σ_3)

$$(\sigma_1-\sigma_2)^2+(\sigma_2-\sigma_3)^2+(\sigma_3-\sigma_1)^2=2\sigma_o^2 \qquad (2.2\text{-}4)$$

where σ_o is the uniaxial yield stress. Under incompressibility and plane strain conditions, the Mises yield criterion is reduced to

$$(\sigma_{11}-\sigma_{22})^2+4\sigma_{12}^2=4k^2 \qquad (2.2\text{-}5)$$

Within a plastically deforming region, the stress state in plane strain and non-hardening conditions may be represented by a point P in the Mohr stress circle diagram shown in Figure 2.3b. The corresponding physical plane is illustrated in Figure 2.3a. Two mutually orthogonal planes are represented by the points (1) and (2) on which the shear stresses attain the maximum possible values of $\pm k$ respectively while the normal stress has the values of hydrostatic stress of $\sigma_m=(\sigma_x+\sigma_y)/v$. These planes are the planes of maximum shear strain but are directions of zero extension or contraction rate. The stress components on any other plane can be expressed in terms of the hydrostatic stress, $\sigma_m=\sigma_{kk}/3$, and the yield shear stress, k,

$$\sigma_x = \sigma_m - k\sin 2\phi$$

$$\sigma_y = \sigma_m + k\sin 2\phi$$

$$\pm\sigma_{xy} = \pm k\cos 2\phi \qquad (2.2\text{-}6)$$

here ϕ is the angle through which the plane PY must rotate anti-clockwise to coincide with the first shear line.

2.3 Plane strain slip line theory

The maximum principal stresses (σ_1, σ_2, σ_3) in the plastically deforming field can be expressed as

$$\sigma_1 = \sigma_m + k \quad \sigma_2 = \sigma_m \quad \text{and} \quad \sigma_3 = \sigma_m - k \tag{2.3-1}$$

The direction of the maximum principal stress is oriented 90^0 from the minimum principal stress while the intermediate principal stress is normal to the direction of maximum and minimum principal stresses. The maximum shear stress (k) acts on surfaces which make angles of $\pm\pi/4$ with the principal directions (Slater,1977). The directions of these surfaces are usually designated the alpha, α, and beta, β, directions. The α direction or first shear direction is 45^0 clockwise from the first principal direction and β direction or second shear direction is therefore 90^0 anti-clockwise from the first shear direction. The maximum principal stress thus lies in the first and third quadrants of the α, β, curvilinear co-ordinate system. There are two orthogonal families of curves whose directions at every point coincide with those of the direction of maximum shear stress in the plastic region. These families of curves are known as slip lines called α lines and β lines. The maximum shear stress, k, is constant throughout the plastic region and can be related to the uniaxial tensile yield stress, σ_o, by the Mises yield criterion, $k = \sigma_o/\sqrt{3}$.

2.3.1 Hencky stress equations

The equilibrium equations can be expressed in terms of the independent quantities $p = -\sigma_m = -\sigma_{ii}/3$, k and ϕ following Hencky (1923):

$$\frac{\partial p}{\partial l_1} + 2k\frac{\partial \phi}{\partial l_1} = 0$$

$$\frac{\partial p}{\partial l_2} - 2k\frac{\partial \phi}{\partial l_2} = 0 \qquad (2.3\text{-}2)$$

These equations are applicable to all points along the slip lines. Integration produces the relationships:

$p+2k\phi = C_1$ *along an* α *line.*

$p-2k\phi = C_2$ *along a* β *line* (2.3-3)

The constants C_1 and C_2 vary from one slip line to another. If p and ϕ are prescribed for a boundary condition then the hydrostatic pressure everywhere in the slip line field can be determined along constant α and β lines.

Two common slip line fields are shown in Figure 2.4. In Figure 2.4a, the slip line field consists of two orthogonal families of straight lines. The angle ϕ is constant because the slip lines are straight. As a result of the Hencky equilibrium equations, the hydrostatic stress, σ_m, is constant and the stress components are also constant. This slip line field thus represents a constant stress state.

The slip line field shown in Figure 2.4b comprises a set of radial straight lines emanating from a point O, say α lines, and a family of concentric circular arcs, say β lines. Since ϕ is constant along an α line, the hydrostatic stress, p, must be constant. However ϕ varies linearly along a β line and the hydrostatic stress must also varies linearly along a β line because $\ell = R\phi$ where ℓ and R are the length and radius of a concentric circular arcs respectively. Thus, the hydrostatic stress is constant in the radial direction and varies linearly with angle measured from the x axis. This type of slip line field is known as a centred fan.

2.3.2 Geiringer velocity equations

If the displacements or velocities are prescribed at a point P in a plastically deforming region, the Hencky equations are not sufficient to obtain a solution and velocity compatibility equations derived by Geiringer (1930) must be considered. Let the displacement components of displacement along the α and β slip lines be u and v respectively. Then the displacement components u_x and u_y in the PX and PY direction shown in Figure 2.5 are:

$$u_x = u\cos\phi - v\sin\phi \qquad (2.3\text{-}4a)$$

$$u_y = u\sin\phi + v\cos\phi \qquad (2.3\text{-}4b)$$

Differentiating equations (2.3-4a and 2.3-4b) with respect to x and y produces:

$$\frac{\partial u_x}{\partial x} = \left(\frac{\partial u}{\partial x} - v\frac{\partial \phi}{\partial x}\right)\cos\phi - \left(\frac{\partial v}{\partial x} + u\frac{\partial \phi}{\partial x}\right)\sin\phi \qquad (2.3\text{-}5a)$$

$$\frac{\partial u_y}{\partial y} = \left(\frac{\partial v}{\partial y} + u\frac{\partial \phi}{\partial y}\right)\cos\phi + \left(\frac{\partial u}{\partial y} - v\frac{\partial \phi}{\partial y}\right)\sin\phi \qquad (2.3\text{-}5b)$$

When $\phi = 0$, PX and PY coincide with the tangents to the α and β slip lines. Since no extension or contraction can occur along the slip lines, $u=v=0$ and equation 2.3-5 can be reduced to:

$$\left[\frac{\partial u_x}{\partial x}\right]_{\phi=0} = \frac{\partial u}{\partial x} - v\frac{\partial \phi}{\partial x} = 0 \qquad (2.3\text{-}6a)$$

$$\left[\frac{\partial u_y}{\partial y}\right]_{\phi=0} = \frac{\partial v}{\partial x} + u\frac{\partial \phi}{\partial y} = 0 \qquad (2.3\text{-}6b)$$

This leads to

$du - vd\phi = 0$ *along an* α *line* (2.3-7a)

$dv + ud\phi = 0$ *along a* β *line* (2.3-7b)

When the stress boundary conditions are insufficient to obtain a unique slip line field then the Hencky equations must be solved simultaneously with the Geiringer velocity equations using both the stress boundary conditions and the velocity boundary conditions.

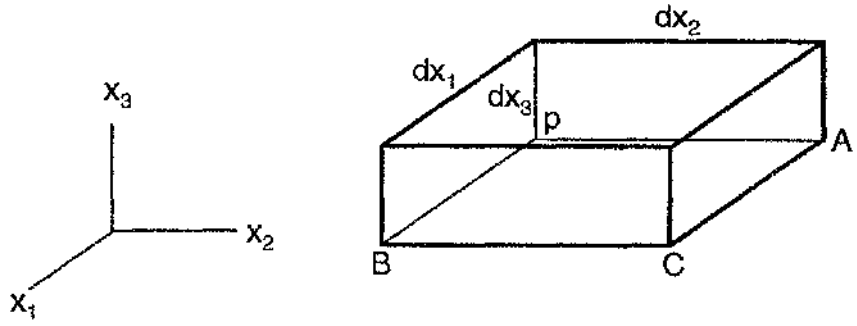

Figure 2.1 Cartesian co-ordinate system.

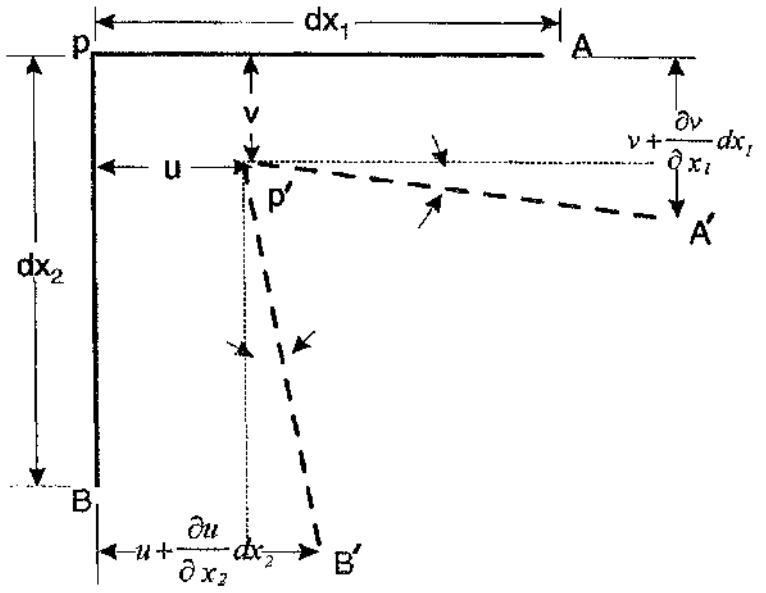

Figure 2.2 Illustration of normal and shear deformation.

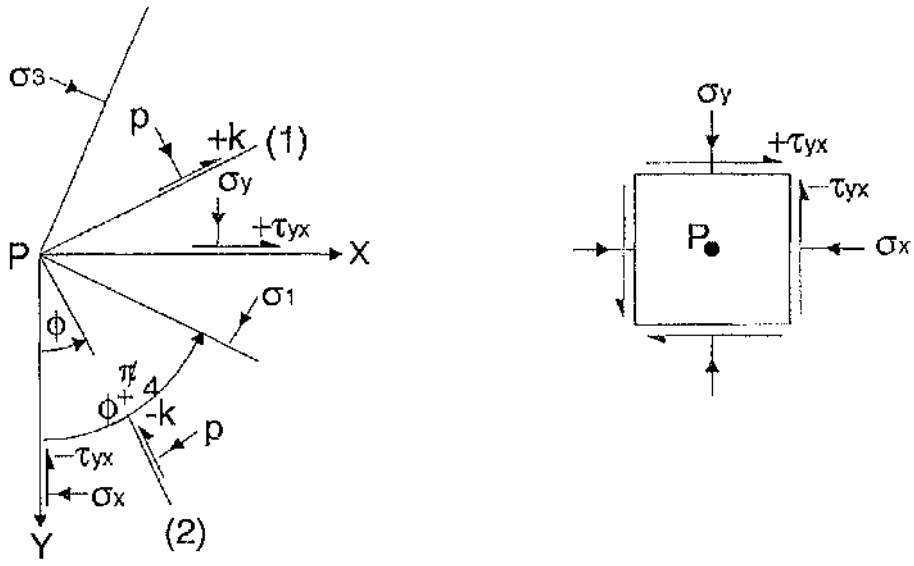

(a)

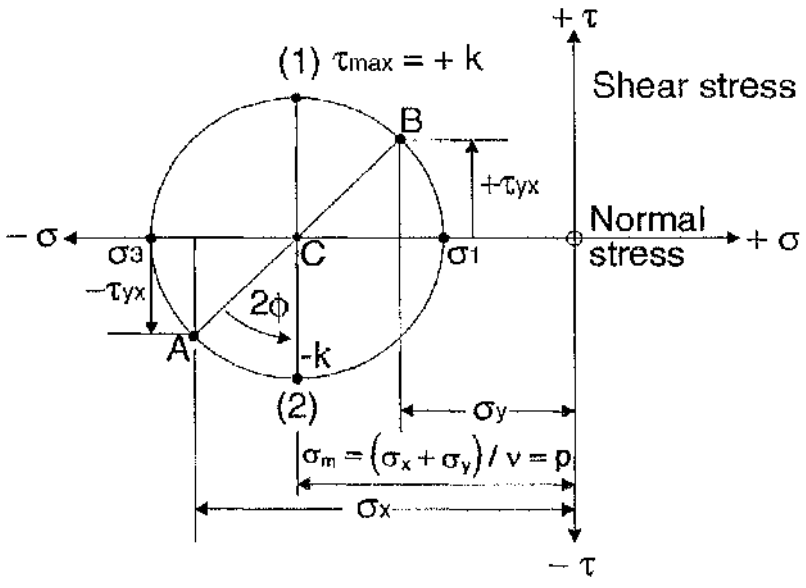

(b)

Figure 2.3 Mohr stress circles in a plastically deforming region.

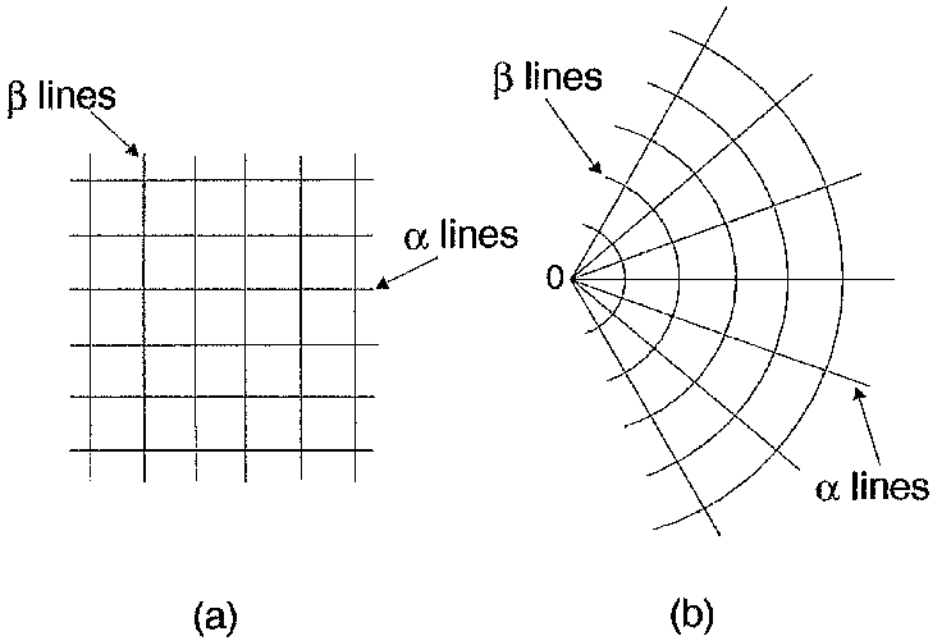

Figure 2.4 Two common slip line fields.

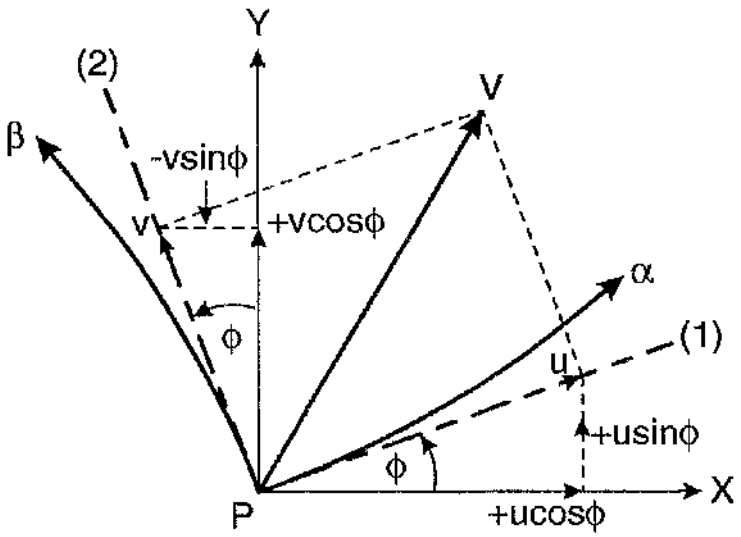

Figure 2.5 Component velocities of a particle in the x and y directions and α and β directions at a point within a plastically deforming region.

Chapter 3 Fracture mechanics

The failure of engineering structures containing cracks or defects may occur at very low stress levels due to the stress concentration at the crack tip. Fracture mechanics quantifies the critical combination of the flaw size, the fracture toughness and the applied stress, and hence ensures the integrity and safety of these structures.

This chapter introduces single and two parameter fracture mechanics. The first two sections overview linear elastic fracture mechanics and elastic-plastic fracture mechanics, including the *J* integral. In the third section, two parameter fracture mechanics is reviewed. The effect of the second term in Williams expansion, *T*-stress and *J*-*Q* theory are described under elastic-plastic conditions.

3.1 Single parameter fracture mechanics

3.1.1 Linear elastic fracture mechanics

In a cracked body the asymptotic stress field for a crack tip in a homogeneous isotropic elastic solid under tension or shear can be described by the Williams (1957) expansion using cylindrical co-ordinates (r,θ) centred at the crack tip as shown in Figure 3.1. The crack lies on the plane $\theta = \pm\pi$.

$$\sigma_{ij} = A_{ij}(\theta) r^{-\frac{1}{2}} + B_{ij}(\theta) + C_{ij}(\theta) r^{\frac{1}{2}} + \ldots \qquad (3.1\text{-}1)$$

In this expression, the first term is singular, the second term is finite whereas the remaining high order terms are zero at the crack tip. This allows the dominant elastic singularity to be expressed in term of the stress intensity factor *K*.

$$\sigma_{ij} = \frac{K}{\sqrt{2\pi r}} f_{ij}(\theta) \qquad (3.1\text{-}2)$$

The stress intensity factor K depends on the level and mode of loading and geometry of the body while the angular function $f_{ij}(\theta)$ depends on the mode of loading only. Three failure modes are illustrated in Figure 3.2. Mode I is defined as an opening mode where the crack surfaces move directly apart with the crack plane being a plane of symmetry. Mode II is an in-plane sliding mode, in which the crack surfaces slide over one another in a direction perpendicular to the leading edge of the crack and anti-symmetry is maintained across the crack plane. Mode III is a out-of-plane tearing mode, where the crack surfaces move relative to one another and parallel to the leading edge of the crack. In most structural applications mode I is generally the most important. The stress intensity factor introduced by Irwin (1957) for a mode I crack is defined as:

$$K_I = \lim_{r \to 0} \sigma_{ij} \sqrt{2\pi r} \qquad (\theta=0) \qquad (3.1\text{-}3)$$

K_I is thus proportional to the remotely applied load and the square root of a characteristic dimension such as crack length. It can be envisaged as characterising the magnitude of the crack tip singularity. A critical value of the stress intensity factor K_{Ic} is used as a measure of fracture toughness under plane strain and small scale yielding conditions. Methods for determining K_{Ic} are given in both British and American standards (B.S. 7448, 1991b, ASTM E399-83, 1983).

3.1.2 The Griffith criterion

Griffith (1920) introduced the concept that the work required to extend a crack is a balance between the released strain energy and the surface energy. The strain energy, Ω^{strain}, is a function of the applied stress and crack length. For a central crack of length $2a$ in an infinite plate of thickness, t, subject to a remote tensile stress the strain energy is:

$$\Omega^{strain} = \frac{\pi \sigma^2 a^2 t}{E'} \qquad (3.1\text{-}4)$$

The term E' is defined to equal Young's modulus, E, for plane stress and $E' = E/(1-\nu^2)$ for plane strain conditions. The surface energy, $\Omega^{surface}$, of the cracked surfaces is:

$$\Omega^{surface} = 4at\gamma_s \qquad (3.1\text{-}5)$$

where γ_s is the surface energy per unit area. The work required to extend a crack is equal to the increase in the potential energy of the elastic body (Π) which has the form:

$$\Pi - \Pi_o = 4at\gamma_s - \frac{\pi \sigma^2 a^2 t}{E'} \qquad (3.1\text{-}6)$$

Π and Π_o are the potential energy of a body with and without a crack. The critical condition is determined by differentiating the potential energy (Π) with respect to the crack length and setting the differential equal to zero

$$\frac{\partial \Pi}{\partial a} = 4t\gamma_s - \frac{2\pi \sigma^2 at}{E'} = 0 \qquad (3.1\text{-}7)$$

This leads to the well known Griffith criterion which defines the fracture conditions as:

$$\sigma_f = \sqrt{\frac{2\gamma_s E'}{\pi a}} \qquad (3.1\text{-}8)$$

The strain energy per unit thickness for extending a crack at distance *da*:

$$G = \left(\frac{d\,\Omega_{I=I}^{strain}}{2da} \right) = \frac{\pi \sigma^2 a}{E'} \qquad (3.1\text{-}9)$$

The critical stress intensity factor K_I for a Griffith crack can then be written as

$$K_{Ic} = \sigma_f \sqrt{\pi a} \qquad (3.1\text{-}10)$$

The critical value of the strain energy released rate G_c can thus be expressed in terms of K_{Ic} ;

$$G_c = \frac{K_{Ic}^2}{E'} \qquad (3.1\text{-}11)$$

3.1.3 The application of elastic fracture mechanics

The application of linear elastic fracture mechanics is subject to severe size limitations intended to ensure that plasticity is restricted to a local perturbation of the elastic field. When the material fails in a macroscopically elastic manner the critical value of the stress intensity factor, K_{Ic}, is a measure of fracture toughness. ASTM (E 399-83, 1983) and British Standard (BS-7448, 1991b) gave the standard test methods for determining the fracture toughness K_{Ic} experimentally. A standard text geometry is the deeply cracked bend bar shown in Figure 3.3 which has a crack length, *a*, a thickness, *B* and ligament length *W-a*. To obtain valid LEFM results, every dimension is required to be large

compared to the radius of the plastic zone. In plane strain conditions, the requirements given by ASTM (E339-83,1983) are:

$$a \geq 2.5\left(\frac{K_{Ic}}{\sigma_o}\right)^2$$

$$B \geq 2.5\left(\frac{K_{Ic}}{\sigma_o}\right)^2$$

$$(W-a) \geq 2.5\left(\frac{K_{Ic}}{\sigma_o}\right)^2 \qquad (3.1\text{-}12)$$

σ_o is the uniaxial yield stress. The value of K_{Ic} is calculated from a critical applied load, P_{cr}^{app}. The standards give the requirements for the determination of P_{cr}^{app}, while the corresponding critical stress intensity factor K_{Ic} can be calculated from the expression:

$$K_{Ic} = \frac{P_{cr}^{app}}{B\sqrt{W}} f(a/W) \qquad (3.1\text{-}13)$$

where $f(a/W)$ is a dimensionless function of *a/W*.

3.1.4 Crack tip plasticity

The crack tip stress concentration causes the material at the tip to yield locally. The maximum radius of the crack tip plastic zone can be estimated by combining either the Tresca or the von Mises yield criterion with crack tip stress equations (Broek, 1991). In plane stress, the radius of the Tresca plastic zone is

$$r^p = \frac{K^2}{2\pi\sigma_o^2}\left[\cos\frac{\theta}{2}\left(1+\sin\frac{\theta}{2}\right)\right]^2 \qquad (3.1\text{-}14)$$

and in plane strain condition, it is the larger of:

$$r^p = \frac{K^2}{2\pi\sigma_o^2}\cos^2\frac{\theta}{2}\left[1-2\nu+\sin\frac{\theta}{2}\right]^2 \quad \text{and} \quad r^p = \frac{K^2}{2\pi\sigma_o^2}\cos^2\frac{\theta}{2} \tag{3.1-15}$$

where ν is Poisson's ratio. The maximum radius of von Mises plastic zone in plane stress condition can be written as:

$$r^p = \frac{K^2}{2\pi\sigma_o^2}\left[1+\frac{3}{2}\sin^2\frac{\theta}{2}+\cos\theta\right] \tag{3.1-16}$$

For plane strain condition, it is:

$$r^p = \frac{K^2}{4\pi\sigma_o^2}\left[\frac{3}{2}\sin^2\frac{\theta}{2}+(1-2\nu)^2(1+\cos\theta)\right] \tag{3.1-17}$$

Figure 3.4 shows the plastic zone shapes determined using the Tresca and von Mises yield criteria.

Interest is now focused on an elastic perfectly plastic material under plane strain mode I deformation. Within the framework of small deformation theory, the stresses close to the crack tip can be derived from an Airy stress function $F(r,\theta)$.

$$\sigma_{rr} = \frac{\partial F}{r\partial r}+\frac{\partial^2 F}{r^2\partial\theta^2} \tag{3.1-18a}$$

$$\sigma_{\theta\theta} = \frac{\partial^2 F}{\partial r^2} \tag{3.1-18b}$$

$$\sigma_{r\theta} = -\frac{\partial}{\partial r}\left(\frac{\partial F}{r\partial\theta}\right) \tag{3.1-18c}$$

The assumption that the crack tip stresses are finite at crack tip leads to the condition (Rice, 1968)

$$F(r,\theta) = r^2 f(\theta) \qquad \text{as } r \to 0 \qquad (3.1\text{-}19)$$

This allows the stress at the crack tip to be written as

$$\sigma_{rr} = 2f(\theta) + \frac{\partial^2 f(\theta)}{\partial \theta^2} \qquad (3.1\text{-}20a)$$

$$\sigma_{\theta\theta} = 2f(\theta) \qquad (3.1\text{-}20b)$$

$$\sigma_{r\theta} = -\frac{\partial f(\theta)}{\partial \theta} \qquad (3.1\text{-}20c)$$

Substituting (3.1-20) into the Mises yield criterion gives

$$f(\theta) = \pm 2k\theta + C_1 \qquad (3.1\text{-}21a)$$

and

$$f(\theta) = (k/2)\cos 2(\theta + \theta_o) + C_2 \qquad (3.1\text{-}21b)$$

where C_1, C_2 and θ_o are constants of integration. From (3.1-19~21) it follows that only the following two types of stress fields can appear in the plastic zone near the crack tip:

$$\sigma_{rr} = \sigma_{\theta\theta} = \sigma_{zz} = \sigma_m = \pm 2k\theta + C_1 \qquad (3.1\text{-}22a)$$

$$\sigma_{r\theta} = \mp k \qquad (3.1\text{-}22b)$$

and

$$\sigma_{rr} = -k\cos 2(\theta + \theta_o) + 2C_2 \qquad (3.1\text{-}23a)$$

$$\sigma_{\theta\theta} = k\cos 2(\theta + \theta_o) + 2C_2 \quad (3.1\text{-}23b)$$

$$\sigma_{zz} = \sigma_m = 2C_2 \quad (3.1\text{-}23c)$$

$$\sigma_{r\theta} = k\sin 2(\theta + \theta_o) \quad (3.1\text{-}23d)$$

The Prandtl field shown in Figure 3.5 is an important crack tip stress field in which the yield criterion is satisfied at all angles. The complete crack tip stress field is assembled from constant stress and centred fan sections in such a way that continuity of hoop and shear stresses and the boundary conditions are met (Rice, 1982). The field may be solved by starting with the boundary condition on the traction free flanks ($\theta=\pm\pi$, $\sigma_{r\theta} = \sigma_{\theta\theta} = 0$) and following the slip lines into the constant stress sector ahead of the crack. The stress field in the constant stress sector on the crack flank is:

$$\sigma_{\theta\theta} = k(1 - \cos 2\theta) \quad (3.1\text{-}24a)$$

$$\sigma_{rr} = k(1 + \cos 2\theta) \quad (3.1\text{-}24b)$$

$$\sigma_{r\theta} = k\sin 2\theta \quad (3.1\text{-}24c)$$

$$\sigma_{zz} = \sigma_m = k \quad (3.1\text{-}24d)$$

The straight lines in this region imply a homogeneous stress state. Following a slip line into the centred fan gives the stress distribution in this sector:

$$\sigma_{\theta\theta} = \sigma_{rr} = \sigma_{zz} = \sigma_m = k\left(1 + \frac{3\pi}{2} - 2\theta\right) \quad (3.1\text{-}25a)$$

$$\sigma_{r\theta} = k \quad (3.1\text{-}25b)$$

The mean stress in this sector varies linearly with angle. The change in the mean stress is associated with rotation of the slip lines through the Hencky equilibrium equations (Hill, 1950). Finally the stress field in the constant sector ahead of the crack is:

$$\sigma_{\theta\theta} = k(\pi + 1 + \cos 2\theta) \quad (3.1\text{-}26a)$$

$$\sigma_{rr} = k(\pi + 1 - \cos 2\theta) \qquad (3.1\text{-}26b)$$

$$\sigma_{r\theta} = k \sin 2\theta \qquad (3.1\text{-}26c)$$

$$\sigma_{zz} = \sigma_m = k(\pi + 1) \qquad (3.1\text{-}26d)$$

The Prandtl fields is significant in the sense that it has been widely identified with the development of local plasticity at the crack tip under constrained yielding conditions, and appears as a example of the crack tip fields identified by Hutchinson (1968) and Rice and Rosengren (1968) for non-hardening plasticity.

3.1.5 Elastic-plastic fracture mechanics

The severe restrictions on the use of linear elastic fracture mechanics can be relaxed by non-linear elastic-plastic fracture mechanics. Hutchinson (1968), Rice and Rosengren (1968) independently argued that the stress and strain field in a non-linear material for a mode I deformation can be expressed as an asymptotic series:

$$\sigma_{ij} = A_{ij} r^s \tilde{\sigma}_{ij}^{(1)}(\theta,n) + B_{ij} r^t \tilde{\sigma}_{ij}^{(2)}(\theta,n) + C_{ij} r^u \tilde{\sigma}_{ij}^{(3)}(\theta,n) + \ldots \quad s < t < u \qquad (3.1\text{-}27)$$

The strength of the singularity is determined by the exponents of the radial distance *r*. For non-linear elasticity, *s* is equal to *1/(n+1)*. A_{ij}, B_{ij}, C_{ij} ... are dimensionless amplitudes of each term and $\tilde{\sigma}_{ij}^{(i)}(\theta,n)$ are angular functions which depend on the strain hardening exponent *n* in a Ramberg-Osgood stress-strain relation:

$$\frac{\varepsilon}{\varepsilon_0} = \frac{\sigma}{\sigma_0} + \alpha\left(\frac{\sigma}{\sigma_0}\right)^n \qquad (3.1\text{-}28)$$

where ε_0, σ_0, and α are material properties. The leading term in (3.1-27) is identified as the HRR field:

$$\sigma_{ij} = \sigma_o \left[\frac{J}{\varepsilon_o \sigma_o \alpha I_n r} \right]^{\frac{1}{n+1}} \tilde{\sigma}_{ij}^{(1)}(\theta, n) \qquad (3.1\text{-}29)$$

Shih (1983) has tabulated the functions of $\tilde{\sigma}_{ij}(\theta, n)$ in terms of their arguments as shown graphically in Figure 3.6 for n=3 and 13. I_n is an integration constant which is a function of the strain hardening exponent n shown in Figure 3.7. The HRR fields are essentially small geometry change solutions where the crack tip is assumed to remain sharp. The strength of the singular field is characterised by the J integral introduced by Rice (1968). J integral is a line integral describing the amount of released energy during crack extension, and is directly related to the crack tip opening displacement. Rice expressed the path independent integral in the form:

$$J = \int_{\Gamma} W d x_2 - P \frac{\partial u}{\partial x_1} ds \qquad (3.1\text{-}30)$$

Γ is the length of the path surrounding the crack tip as shown in Figure 3.8. The first term in the expression is the strain energy density or work of deformation per unit volume, which is defined by:

$$W = \int_0^{\varepsilon} \sigma_{ij} d \varepsilon_{ij}, \qquad i,j = 1,2,3 \qquad (3.1\text{-}31)$$

The second term in (3.1-30) is the work done by the external forces, in which P is the traction vector applied to the body bounded by Γ, u is the displacement vector. The level of deformation is characterised by J, which is related to the crack opening displacement δ by a relation given by Rice (1968b) for a non-hardening material under plane strain conditions.

$$J = 2\left(1+\frac{\pi}{2}\right)k\delta \qquad (3.1\text{-}32)$$

The role of J in non-linear field is analogous to the manner in which K is used to characterise the strength of the elastic singularity. J is used to characterise the strength of the elastic-plastic singularity in constrained elastic-plastic crack tip fields. By making contact with both linear and non-linear material response it provides the most general single parameter characterisation of crack tip deformation. Equation (3.1-32) enables the crack displacements within the plastic zone to be related to the outer elastic field, where the plane strain small-scale yielding relation establishes the relationship between J and K.

$$K^2 = \frac{EJ}{\left(1-\nu^2\right)} \qquad (3.1\text{-}33)$$

Fracture criteria based on J assume that the crack tip stresses can be uniquely described by the *HRR* fields as characterised by the J-integral. McMeeking and Parks (1979) demonstrated that fields characterised by J are identical to those observed in small scale yielding when a single parameter characterisation based on J is valid.

3.1.6 Limits for one parameter characterization

In 1971, McClintock noted that in the absence of strain hardening, single parameter characterisation is limited by the lack of uniqueness of the fully plastic flow field. For example, centre cracked panels are incapable of maintaining full constraint under fully plastic conditions, and the maximum principal stress within plastic zone is approximately 61% less than that in the HRR (Prandtl) field. Figure 3.9 Shows the slip line field for a centre cracked panel. Shallow edge cracked bars exhibit unconstrained flow fields while fully constrained Prandtl field is only developed in deeply cracked bend bars. The slip line fields for both shallow and deep double edge cracked bars are shown in Figure 3.10 (Ewing,

1968, and Green, 1953). In full plasticity shallow edge cracked bars lose crack-tip constraint.

In 1981, Shih and German proposed a J-dominance criterion which required that the stress field is within 10% of the HRR field at a distance $r\sigma_o / J$=2 ahead of the tip. Since the difference between the HRR field and the small scale yielding field is in general less than 5% (Du and Hancock 1991), Karstensen (1996) used the small scale yielding field as a reference field and found that shallow edge cracked bars exhibit a compressive *T* stress and lose *J* dominance at low levels of deformation. As an example, for shallow single edge cracked bars (shown in Figure 3.3) in bending, single parameter characterisation seems to be lost for a very low level of deformation characterised by $c\sigma_o / J$ as illustrated in table 3.1 and Figure 3.11 where c is the width of the ligament (W-a). At *a/W=0.1* and *n=13* the breakdown of a *J*-characterisation occurs at $c\sigma_o / J$=3200, the limit calculated in terms of the crack length extend the singular parameter characterisation to $a\sigma_o / J = 360$. Deeply edge cracked bars retain J-dominance line until $c\sigma_o / J$=20, independent of *a/W* ratio and hardening rate, indicating that the crack length is the controlling dimension rather than the ligament.

3.2 Two parameter fracture mechanics

3.2.1 T-stress

Larsson and Carlsson (1973) demonstrated that the second term in the Williams expansion has a significant effect on the shape and size of the plastic zone which develops at the crack tip. Rice (1974) denoted the second non-singular term as the *T*-stress which is independent of the radial distance and corresponds to a uniaxial stress parallel to the crack.

$$\begin{bmatrix} \sigma_{11} & \sigma_{12} \\ \sigma_{21} & \sigma_{22} \end{bmatrix} = \frac{K}{\sqrt{2\pi r}} \begin{bmatrix} f_{11}(\theta) & f_{12}(\theta) \\ f_{21}(\theta) & f_{22}(\theta) \end{bmatrix} + \begin{bmatrix} T & 0 \\ 0 & 0 \end{bmatrix} \qquad (3.2\text{-}1)$$

where f_{ij} are universal functions of the angular co-ordinate θ.

$$f_{11} = \cos\left(\frac{\theta}{2}\right)\left[1 - \sin\left(\frac{\theta}{2}\right)\sin\left(\frac{3\theta}{2}\right)\right]$$

$$f_{22} = \cos\left(\frac{\theta}{2}\right)\left[1 + \sin\left(\frac{\theta}{2}\right)\sin\left(\frac{3\theta}{2}\right)\right]$$

$$f_{12} = f_{21} = \cos\left(\frac{\theta}{2}\right)\sin\left(\frac{\theta}{2}\right)$$

The value of the T stress depends on the geometry and the applied load. A range of analytical and numerical techniques have been used to calculate T, but the simplest method is to examine the stress field on the crack flanks. The leading term in the Williams expression is zero for $\theta=\pi$ because $f_{ij}(\pi)=0$, and the T-stress is consequently identical to σ_{11}:

$$T = \lim_{r \to 0} \sigma_{11(\theta=\pi)} \qquad (3.2\text{-}2)$$

It should be mentioned that the use of numerical methods in conjunction with a singular stress field requires a highly refined mesh if accurate results are to be obtained. Most refined methods have been discussed by Kfouri (1986).

The T-stress is sometimes expressed in terms of a bi-axiality parameter β following Leevers and Radon (1983) which has been tabulated for a wide range of geometries $T = \beta K / \sqrt{\pi a}$. Table 3.2 and 3.3 show the value of K_I and β for a range of *a/W* ratios of single edge cracked bars under tension and bending following (Sham, 1991). Data for centre cracked panels (Nekkal, 1991) and double edge cracked panels (Leevers and Radon, 1983) are given in Table 3.4.

3.2.2 Modified boundary layer formulations

Fracture processes occur in a physically small region close to the crack tip where plastic deformation occurs due to the stress and strain concentration. In order to investigate the nature of elastic-plastic crack tip fields, it is desirable to avoid modelling a complete engineering structure. This problem was resolved by Rice and Tracey (1973) who introduced the concept of a boundary layer formulation for analysing crack tip plasticity in small scale yielding. The circular region close to a crack tip shown in Figure 3.12 can be regarded as a substructure of a whole body in which the local boundary conditions are based on the first term or the first two terms of the Williams expansion. The small scale yielding condition is satisfied by restricting plasticity to a very small proportion of the surrounding elastic region. Because boundary layer formulation analysis isolates the non-linear area, it reduces computational time and removes geometry effects while allowing mixed mode calculations.

Figure 3.13 shows a typical focused finite element mesh for modelling crack tip plasticity. The loading applied on the elastic boundary corresponds to mode I (K_I) plus T stress term giving rise to displacements u_i^K and u_i^T

$$u_1 = u_1^K + u_1^T = \left(\frac{r}{2\pi}\right)^{\frac{1}{2}} \frac{K}{2G} \cos\frac{\theta}{2}\left[\eta - 1 + 2\sin^2\left(\frac{\theta}{2}\right)\right] + \frac{1+\eta}{8G} rT\cos\theta$$

$$u_2 = u_2^K + u_2^T = \left(\frac{r}{2\pi}\right)^{\frac{1}{2}} \frac{K}{2G} \sin\frac{\theta}{2}\left[\eta - 1 + 2\cos^2\left(\frac{\theta}{2}\right)\right] + \frac{\eta-3}{8G} rT\sin\theta \qquad (3.2\text{-}3)$$

where η=3-4ν in plane strain conditions, ν is Poisson's ratio and G the shear modulus. K is established by far field conditions.

The two parameter approach has been developed by Bilby et al. (1986) and more recently by Betegón and Hancock (1991), Al-Ani and Hancock (1991) and O'Dowd and Shih (1991). The T-stress affects not only the shape of crack tip

plastic zone but also the stresses within plastic zone. Detailed investigations of the non-hardening problem have been presented by Du and Hancock (1991) using finite element analysis methods based on modified boundary layer formulations. As *T* is proportional to the applied load, the *T=0* field is significant in the sense that it is the field which applies at very small load levels and is thus the small scale yielding field. Du and Hancock (1991) found that compressive *T* stresses both enlarge the maximum radius of the plastic zone and cause the plastic lobes to swing forward. In contrast, tensile stresses cause the plastic zone to decrease in size and to rotate backwards. The change of plastic zone shape due to the *T*-stress is illustrated in Figure 3.14. Plasticity only encompasses the tip for closely defined conditions in which T is positive (tensile). When T is negative (compressive) plasticity does not surround the tip and an elastic sector appears on the crack flank giving rise to an incomplete Prandtl field. Figure 3.15 shows the slip line field representation of the mode I crack tip stress fields with different level of T stress. Of particular significance is the observation that compressive T stress causes a loss of crack tip constraint ahead of the crack. Parallel experimental work has demonstrated that this leads to enhanced level of toughness for both cleavage given by Betegón, 1990, Betegón and Hancock, 1991, Kirk, Koppenhoefer and Shih in 1993 (see Figure 3.16) and ductile tearing given by Hancock, Reuter and Parks, 1993.

3.2.3 J-Q theory

The higher order terms in the non-linear asymptotic expansion of the mode I crack tip field shown in equation (3.1-27) have been investigated recently. Li and Wang (1986) and Sharma and Avaras (1991) have examined the first two terms in this series, Following their work Yang and co-workers (1993a, b) and Xia, Wang and Shih (1993) have sough three and four terms expansions. But a major simplification was proposed by O'Dowd and Shih (1991a,b) who introduced a widely accepted notation in which the amplitude of the second term in the expansion is denoted Q.

$$\frac{\sigma_{ij}}{\sigma_o} = \left[\frac{J}{\varepsilon_o \sigma_o \alpha I_n r}\right]^{\frac{1}{n+1}} \tilde{\sigma}_{ij}(\theta, n) + Q\left(\frac{\frac{r}{J}}{\sigma_o}\right)^t \tilde{\sigma}_{ij}(\theta, n) + \textit{higher order terms} \qquad (3.2\text{-}4)$$

On this basis Q may be defined as

$$Q = \lim_{r \to 0} \frac{\sigma_{ij} - \sigma_{HRR}}{\left(\frac{\frac{r}{J}}{\sigma_o}\right)^t \tilde{\sigma}_{ij}(\theta, n)} \left(\frac{1}{\sigma_o}\right) \qquad (3.2\text{-}5)$$

It is argued that the exponent t can be approximated to zero, leading to a distance independent second order term. For non-hardening plasticity Du and Hancock (1991) found that the difference between $\sigma_{\theta\theta}$ in the HRR field and the small scale yielding (T=0) field is about 2% directly ahead of the crack. This allows the reference field to be defined as small scale yielding (T=0) field or the HRR field

$$\sigma_{ij} = \sigma_{ij}^{T=0} + Q\sigma_o \delta_{ij} \qquad (3.2\text{-}6)$$

where δ_{ij} is the Kronecker delta. The Q parameter can be inferred by subtracting the stress field for the *T=0* reference state from stress field of interest:

$$Q = \frac{\sigma_{yy} - \sigma_{yy}^{T=0}}{\sigma_o} \qquad \text{at } \theta=0 \quad \text{and} \quad \frac{r\sigma_o}{J} = 2 \qquad (3.2\text{-}7)$$

In small scale yielding, *T* and *Q* are uniquely related. Betegón and Hancock (1991) have given a relation based on numerical calculations for *n=13*:

$$Q = 0.64\left(\frac{T}{\sigma_o}\right) - 0.4\left(\frac{T}{\sigma_o}\right)^2 \qquad \frac{T}{\sigma_o} \leq 0 \qquad (3.2\text{-}8)$$

Both Q and T can be used as a measure of the loss of constraint in small scale yielding.

3.2.4 J-Q toughness locus

Fracture mechanics attempts to ensure structural integrity by applying toughness measurements obtained from laboratory specimens to real defects. Classical single-parameter fracture mechanics assumes that fracture toughness is a material constant and geometry independent. Nevertheless, crack tip deformation and fracture toughness are geometry independent only within a limited range of loading and geometric conditions, which ensure fully constrained fields. The restrictive nature of these size and geometric requirements is a major limitation on the applications of plane strain elastic-plastic fracture mechanics. It is necessary to characterise fracture toughness as a function of constraint for allowing the application of fracture mechanics to a wider and less restrictive range of configurations.

$$J_c = J_c(Q) \quad \text{or} \quad J_c = J_c(T) \qquad (3.2\text{-}9)$$

Thus fracture toughness is no longer viewed as a single value; rather, it is a curve that defines a critical locus of J and Q or T values. This relationship has been discussed by Betegón and Hancock (1991), Hancock, Reuter and Parks (1993), Sumpter and Forbes (1992) and Sumpter and Hancock (1994). They examined the critical value of J for geometries with different levels of constraint (T or Q), and found that shallow edge cracked bars and centre cracked panels with the most negative T values are tougher than deeply cracked specimen with positive T values. Figure 3.17 is an example of a J-T fracture locus determined by Sumpter (1993) from three point bend tests and centre cracked tensile tests. Figure 3.18 shows the same data but re-plotted as J - Q fracture locus (Sumpter

and Hancock, 1994). Although there is some scatter, the trend in these figures are clear. The critical J values increases as Q or T become more negative. Fracture toughness tends to increase as constraint decreases.

Single parameter fracture mechanics theory assumes that toughness values obtained from laboratory specimens can be transferred to structural applications. J-Q theory implies that the laboratory specimen must match the constraint of the fracture; i.e., the two geometry must have the same Q or T at failure in order for the respective J_c values to be equal. Figure 3.19 illustrates the application of the J-Q approach to structures. The applied J versus Q curve for the configuration of interest is obtained from finite element analysis. It is plotted with the J-Q toughness locus which is a range of possible J_c values for the structure incorporating the scatter in toughness data. Failure is predicted when the driving force curve passes through the toughness locus.

3.2.5 Crack tip stress fields under mixed mode loading

Under mixed mode loading, comprising combinations of mode I loading and mode I in plane strain conditions, the elastic crack tip stress field in a homogeneous material can be written as:

$$\begin{Bmatrix}\sigma_{xx}\\ \sigma_{yy}\\ \sigma_{xy}\end{Bmatrix}=\frac{K_I}{\sqrt{2\pi r}}\begin{Bmatrix}\cos(\theta/2)\left[1-\sin(\theta/2)\sin(3\theta/2)\right]\\ \cos(\theta/2)\left[1+\sin(\theta/2)\sin(3\theta/2)\right]\\ \sin(\theta/2)\cos(\theta/2)\cos(3\theta/2)\end{Bmatrix}+\frac{K_{II}}{\sqrt{2\pi r}}\begin{Bmatrix}-\sin(\theta/2)\left[2+\cos(\theta/2)\cos(3\theta/2)\right]\\ \sin(\theta/2)\cos(\theta/2)\cos(3\theta/2)\\ \cos(\theta/2)\left[1-\sin(\theta/2)\sin(3\theta/2)\right]\end{Bmatrix}$$

$$\begin{Bmatrix}\sigma_{rr}\\ \sigma_{\theta\theta}\\ \sigma_{r\theta}\end{Bmatrix}=\frac{K_I}{\sqrt{2\pi r}}\begin{Bmatrix}\cos(\theta/2)\left[1+\sin^2(\theta/2)\right]\\ \cos^3(\theta/2)\\ \sin(\theta/2)\cos^2(\theta/2)\end{Bmatrix}+\frac{K_{II}}{\sqrt{2\pi r}}\begin{Bmatrix}\sin(\theta/2)\left[1-3\sin^2(\theta/2)\right]\\ -3\sin(\theta/2)\cos^2(\theta/2)\\ \cos(\theta/2)\left[1-3\sin^2(\theta/2)\right]\end{Bmatrix}$$

$$\sigma_{zz}=\nu\left(\sigma_{xx}+\sigma_{yy}\right)=\nu\left(\sigma_{rr}+\sigma_{\theta\theta}\right)$$

$$\sigma_{xz}=\sigma_{yz}=\sigma_{rz}=\sigma_{\theta z}=0 \qquad (3.2\text{-}10)$$

The nature of the remote elastic field can be defined by an elastic mixity parameter introduced by Shih (1974) for homogeneous material.

$$M_{el} = \frac{2}{\pi} tan^{-1}\left(\frac{K_I}{K_{II}}\right) = \frac{2}{\pi} tan^{-1}\left\{\lim_{r\to 0}\left[\frac{\sigma_{\theta\theta}(r,0)}{\sigma_{r\theta}(r,0)}\right]\right\} \qquad (3.2\text{-}11)$$

The elastic mixity defines both the ratio of tension to shear in the remote elastic field and also directly ahead of the crack in the fully elastic case. However when crack tip plasticity occurs, the ratio of tension to shear directly ahead of the crack is defined by a plastic mixity factor M_p (Shih, 1974).

$$M_p = \frac{2}{\pi} tan^{-1}\left\{\lim_{r\to 0}\left[\frac{\sigma_{\theta\theta}(r,0)}{\sigma_{r\theta}(r,0)}\right]\right\} \qquad (3.2\text{-}12)$$

In general the remote elastic and plastic mixities are not identical. For small scale yielding, the elastic mixity provides a measure of the relative strength of the shear and direct stresses in the outer elastic field, while the plastic mixity gives the relative contribution of the local shear to tension in the plastic zone at the tip. The relation of near field plastic mode mixity versus far-field elastic mode mixity given by Shih (1974) under small scale yielding and plane strain conditions is shown in Figure 3. 20.

For non hardening plasticity, Shih (1974) sought mixed mode slip line fields in which plasticity was assumed fully surround crack tip. Since the equilibrium equations demand that the hoop and shear stresses are continuous, but allow a jump in the radial stress, a stress discontinuity was postulated along a radial line emanating from the crack tip. Figure 3.21 illustrates the discontinuity occurs at an angle α from the crack flank. The angle α increases with the Mode II component until it equals $\pi/4$. At this mixity a centred fan develops and giving

rise to continuous stress fields. In pure Mode II the angular span of the fan is 8.2° recovering a field originally discussed by Hutchison (1968b).

Hancock and co-workers (1997) presented a set of mixed mode slip line fields under small scale yielding using boundary layer formulation shown in Figure 3.22, without the assumption that plasticity fully surrounds crack tip. In comparison with those given by Shih (1974), the fundamental difference is that the fields do not exhibit stress discontinuities and feature an elastic sector on one crack flank except pure mode II loading. The mode I field is the incomplete Prandtl field. With increasing levels of mixity the constant stress diamond ahead of the crack rotates. The maximum principal stress and the maximum hydrostatic stress occur across a radial plane through the centre of the constant stress diamond. This angle is of particular interest in terms of stress controlled brittle fracture, as it is frequently argued that such failure occurs at the orientation at which the propagating crack extends locally in mode I. In the case of non-hardening plasticity the stress at this angle was matched with the stress in an unconstrained mode I field. For non-hardening plasticity, the fields within $\pm\pi/4$ of the direction of maximum hoop stress can only differ by a hydrostatic term. However Hancock, Nekkal and Karstensen (1997) have shown that for moderately hardening materials the fields also differ hydrostatically but are deviatorically similar. On this basis the constraint of mode I fields parameterised by Q or T can be correlated with the constraint of mixed mode fields parameterised by elastic mixity as shown in Figure 3.23.

3.2.6 Limitation of two parameter characterization

The limitations of two parameter characterisation have been described by Karstensen (1996) by comparing full field solutions with modified boundary layer solutions at the same level of *T*-stress. The *T*-stress in full field solutions was defined from a biaxiality parameter, β, and the stress intensity factor, *K*:

$$T = \frac{\beta K}{\sqrt{a\pi}} \qquad (3.2\text{-}13)$$

The values of β and K are given in Table 3.2~4. T is proportional to the remote load level. The modified boundary layer formulation solutions were obtained by applying the displacement loading associated with *T and K* on the outer-boundary of the mesh. Two parameter characterisation was considered to be valid as long as the stresses were within 10% of the stress field defined by the modified boundary layer formulation at the same value of T. This reference stress is denoted as σ_{MBLF}. Figures 3.24~26 show the stress at distance $r\sigma_o/J=2$ non-dimensionalised by σ_{MBLF} as a function of the level of deformation $c\sigma_o/J$ for single edge cracked bend bars, single edge cracked tension bars and centre cracked bars respectively. The results for each geometry are shown for four different hardening rates. Perfect agreement between MBLFs and full geometry solutions corresponds to $\sigma_{\theta\theta}/\sigma_{MBLF}=1$.

Tables 3.5 gives the critical values of $c\sigma_o/J$ for the three types of geometry: edge cracked bend bars, edge cracked tention bars and centre cracked panels. Comparing this table with Table 3.1 demonstrates that two parameter J-T characterisation extends the limits beyond one parameter characterisation for shallow edge cracked bars and centre cracked panels because these geometries exhibit loss of constraint due to negative T stress. Deeply cracked bars ($a/W \geq 0.35$ in bending and $a/W \geq 0.55$ in tension) are within the limits of single parameter characterisation until $c\sigma_o/J>25$.

The limits of J-Q characterisation for shallow cracked bars in bending and tension have been discussed by Shih and O'Dowd (1992). Because Q varies with distance at high deformation levels for the edge cracked bars, they suggested a criterion by limiting the Q gradient term Q':

$$Q' = \frac{dQ}{d\frac{r\sigma_o}{J}} \qquad (3.2\text{-}14)$$

In practice Shih and O'Dowd (1992) have used the mean gradient of Q over the interval $1 \leq r\sigma_0/J \leq 5$ from the crack tip.

$$Q' = \frac{Q\left(\frac{r\sigma_0}{J} = 5\right) - Q\left(\frac{r\sigma_0}{J} = 1\right)}{4} \qquad (3.2\text{-}15)$$

This leads to $|Q'| \leq 0.03$ as the limit for *J-Q* characterisation. *J-Q* characterisation is thus valid as long as the distance dependency of the stress field compared to the reference field is small.

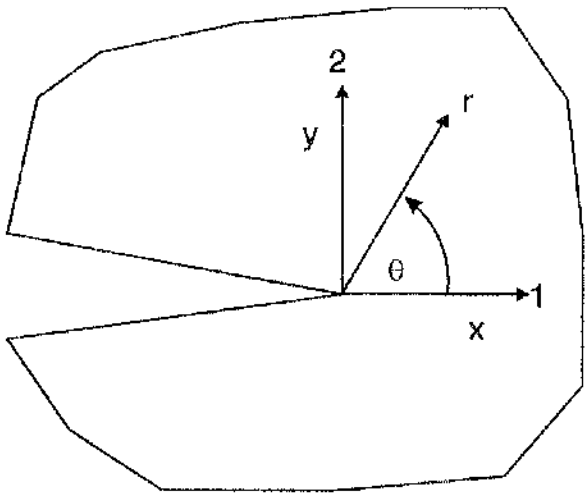

Figure 3.1 Definition of coordinate system for a stationary crack.

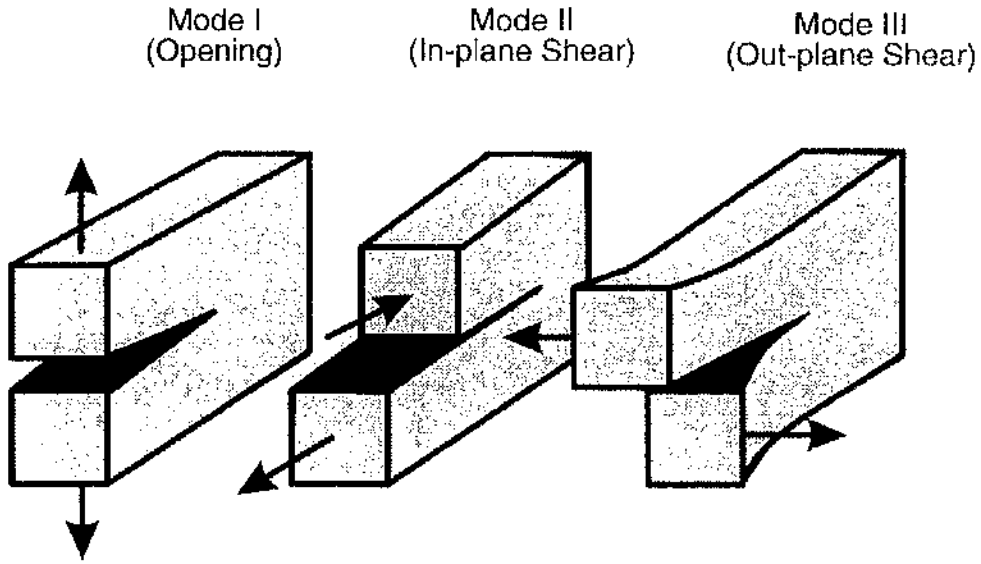

Figure 3.2 Three types of mode applied at a crack tip.

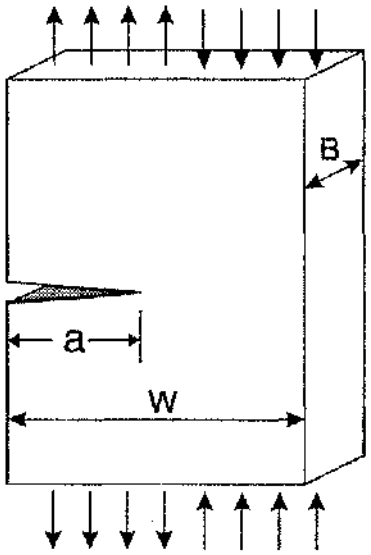

Figure 3.3 Illustration of a bend bar.

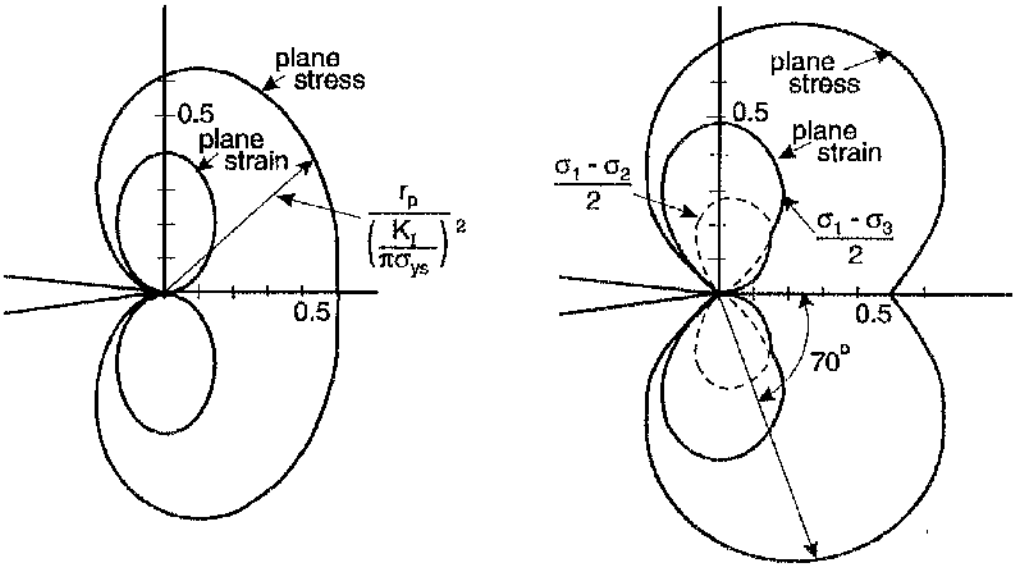

Figure 3.4 Plastic zone shapes according to Von Mises (a) and Tresca (b) yield criteria, Broek, 1991.

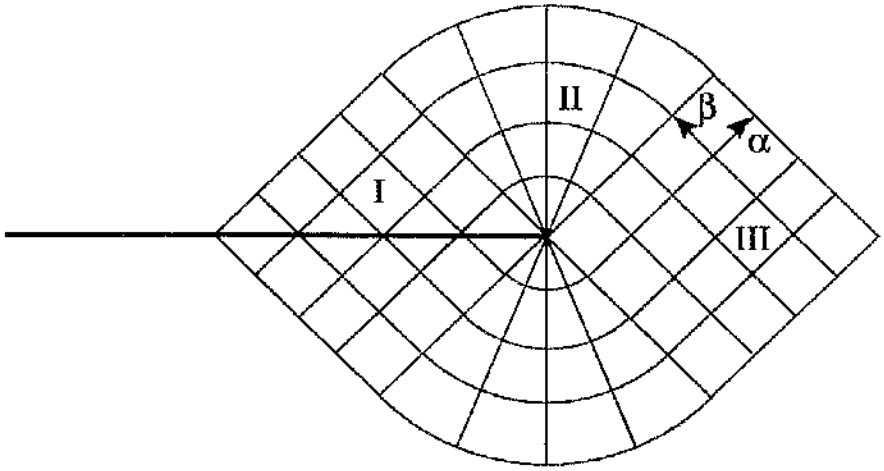

Figure 3.5. Prandtl field.

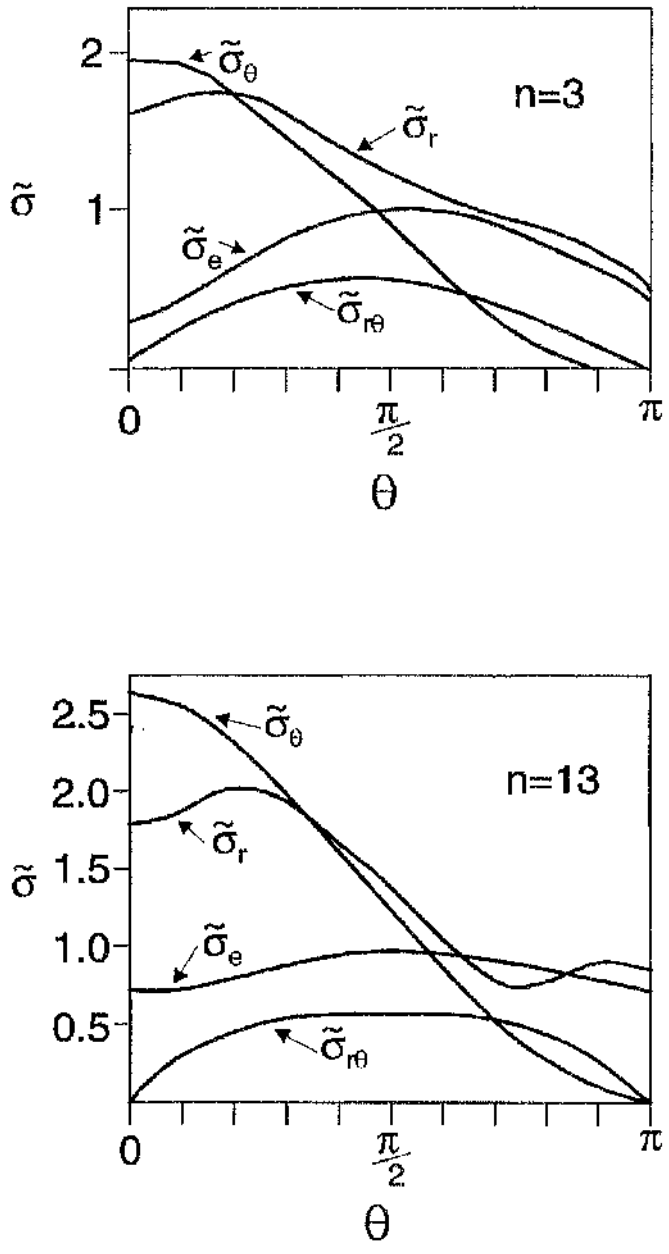

Figure 3.6 Angular variation of stresses at a crack tip in HRR fields in plane strain conditions, Shih, 1983.

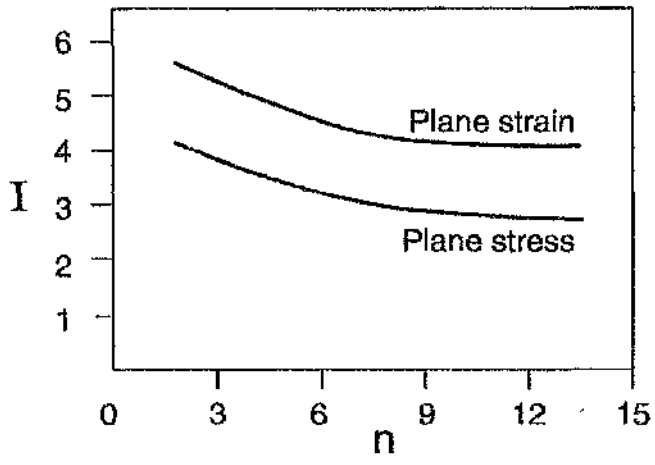

Figure 3.7 Value of I as function of strain hardening rate *n*, Shih, 1983.

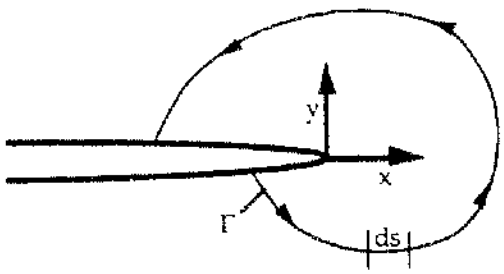

Figure 3.8 Arbitrary contour around the tip of a crack.

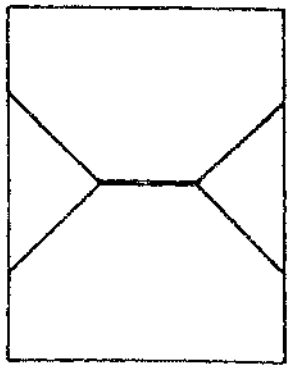

Figure 3.9 Slip line field for a centre cracked panel, McClintock, 1971.

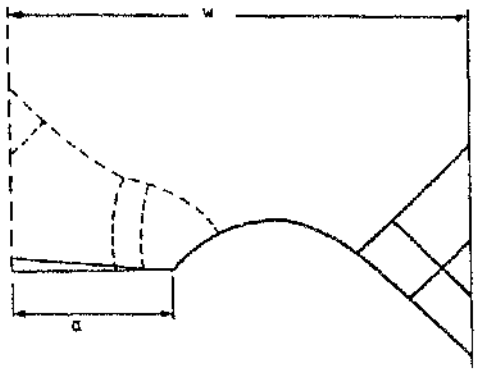

Figure 3.10 Slip line fields for both shallow and deep double edge cracked bars, Ewing, 1968, and Green, 1953.

a/W	$n=3$	$n=6$	$n=13$	$n=\infty$
	$\frac{c\sigma_0}{J} \geq$	$\frac{c\sigma_0}{J} \geq$	$\frac{c\sigma_0}{J} \geq$	$\frac{c\sigma_0}{J} \geq$
0.1	160	1600	≈ 3200	≈ 5000
0.2	60	100	500	1200
0.3	40	40	40	50
0.4	20	20	20	30
0.5	20	20	20	30
0.6	20	20	20	30
0.7	20	20	20	30
0.8	20	20	20	30
0.9	20	20	20	30

(i) Single edge cracked bend bars.

a/W	$n=3$	$n=6$	$n=13$	$n=\infty$
	$\frac{c\sigma_0}{J} \geq$	$\frac{c\sigma_0}{J} \geq$	$\frac{c\sigma_0}{J} \geq$	$\frac{c\sigma_0}{J} \geq$
0.1	280	≈ 3000	≈ 5000	≈ 5000
0.2	60	1000	2000	3500
0.3	40	500	1000	1000
0.4	25	120	300	450
0.5	20	45	60	100
0.6	20	20	20	25
0.7	20	20	20	25
0.8	20	20	20	25
0.9	20	20	20	25

(ii) Single edge cracked tension bars.

a/W	$n=3$	$n=6$	$n=13$	$n=\infty$
	$\frac{c\sigma_0}{J} \geq$	$\frac{c\sigma_0}{J} \geq$	$\frac{c\sigma_0}{J} \geq$	$\frac{c\sigma_0}{J} \geq$
0.1	3000	≈ 5000	≈ 5000	≈ 5000
0.2	1200	4800	≈ 5000	≈ 5000
0.3	800	3200	4600	≈ 5000
0.4	550	2000	2800	≈ 5000
0.5	400	1300	1800	≈ 5000
0.6	350	950	1600	4000
0.7	280	800	1200	2800
0.8	250	750	1100	2000
0.9	250	600	900	1800

(iii) Centred cracked panels.

Table 3.1 Limits for one parameter characterisation of single edge cracked bend bars, Karstensen,1996.

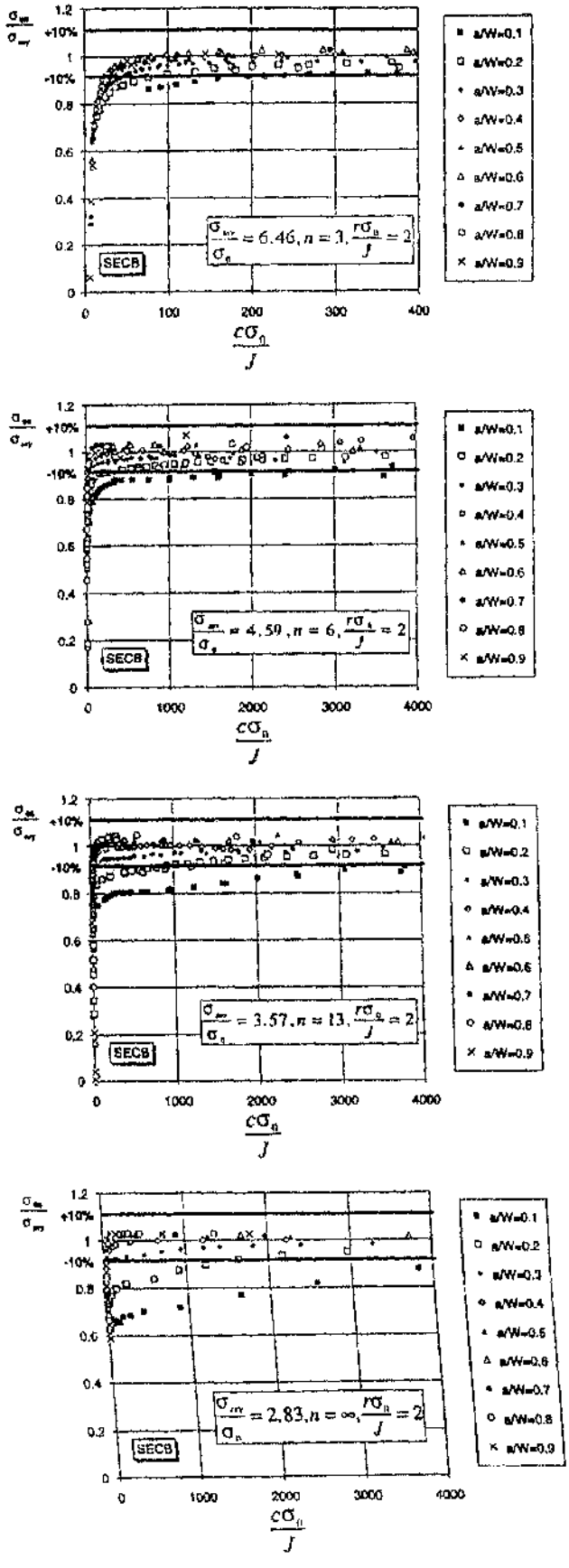

Figure 3.11 The stresses directly ahead of a crack in edge cracked bend bars normalised by the small scale yielding field, Karstensen,1996.

a/W	$\frac{K}{\sigma\sqrt{\pi a}}$	$\beta = \frac{T\sqrt{\pi a}}{K}$
0.1	0.11877E1	-0.46436E0
0.2	0.13650E1	-0.43362E0
0.3	0.16570E1	-0.37070E0
0.4	0.21083E1	-0.27762E0
0.5	0.28210E1	-0.15293E0
0.6	0.40254E1	0.69027E-2
0.7	0.63457E1	0.21010E0
0.8	0.11926E2	0.50105E0
0.9	0.34485E2	0.10306E1

Table 3.2 Values of K_I and β for single notched bars in tension, Sham,1991.

	Pure Bending		Three Point Bending	
a/W	$\frac{K}{\sigma\sqrt{\pi a}}$	$\beta = \frac{T\sqrt{\pi a}}{K}$	$\frac{K}{\sigma\sqrt{\pi a}}$	$\beta = \frac{T\sqrt{\pi a}}{K}$
0.1	0.10458E1	-0.36263E0	0.10234E1	-0.36062E0
0.2	0.10534E1	-0.22852E0	0.10272E1	-0.23295E0
0.3	0.11220E1	-0.73444E-1	0.10937E1	-0.90071E-1
0.4	0.12586E1	0.92115E-1	0.12290E1	0.60928E0
0.5	0.14951E1	0.26160E0	0.14647E1	0.21685E0
0.6	0.19100E1	0.43325E0	0.18787E1	0.37921E0
0.7	0.27210E1	0.61041E0	0.26880E1	0.55311E0
0.8	0.46642E1	0.83862E0	0.46270E1	0.78585E0
0.9	0.12406E2	0.12675E1	0.12358E2	0.12273E1

Table 3.3 Values of K_I and β for single notched bars in bending and three point bending, Sham,1991.

	Centre Cracked Panels		Double Edge Cracked Bars	
a/W	$\frac{K}{\sigma\sqrt{\pi a}}$	$\beta = \frac{T\sqrt{\pi a}}{K}$	$\frac{K}{\sigma\sqrt{\pi a}}$	$\beta = \frac{T\sqrt{\pi a}}{K}$
0.1	0.1006E1	-0.1017E1	0.12130E1	-0.436E0
0.2	0.1025E1	-0.1034E1	0.12123E1	-0.445E0
0.3	0.1058E1	-0.1051E1	0.12175E1	-0.458E0
0.4	0.1109E1	-0.1068E01	0.12322E1	-0.463E0
0.5	0.1187E1	-0.1085E1	0.12659E1	-0.471E0
0.6	0.1303E1	-0.1102E1	0.13342E1	-0.441E0
0.7	0.1488E1	-0.1261E1	0.14588E1	-0.411E0
0.8	0.1816E1	-0.1460E1	0.16671E1	-0.330E0
0.9	0.2312E1	-0.1930E1	0.19927E1	-0.196E0

Table 3.4 Values of K_I and β for centre cracked panels and double edge cracked bars, Nekkal, 1991 and Leevers and Radon, 1983.

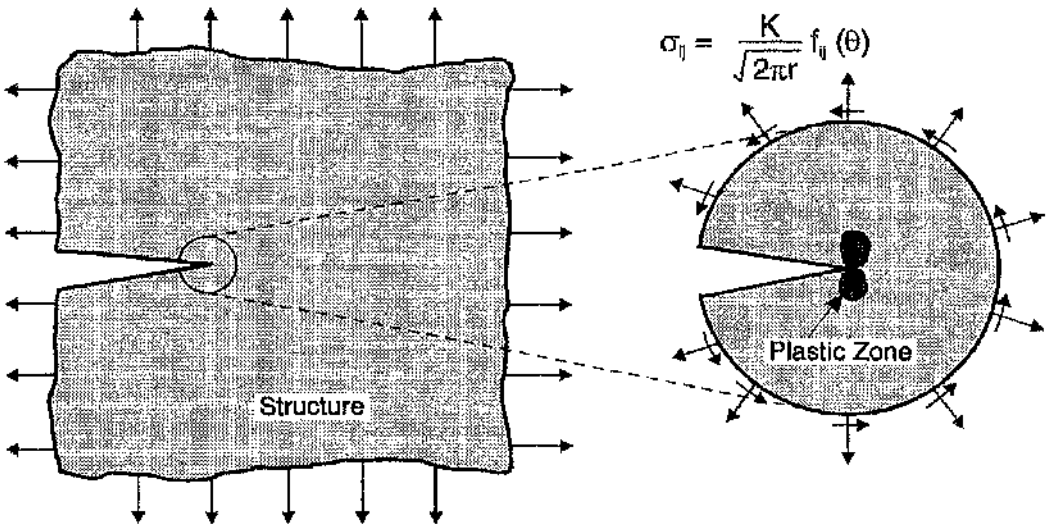

Figure 3.12 Schematic boundary layer formulations.

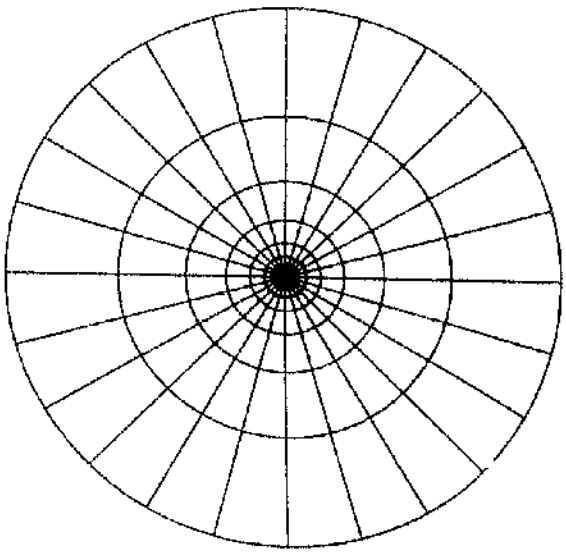

Figure 3.13 Focused mesh.

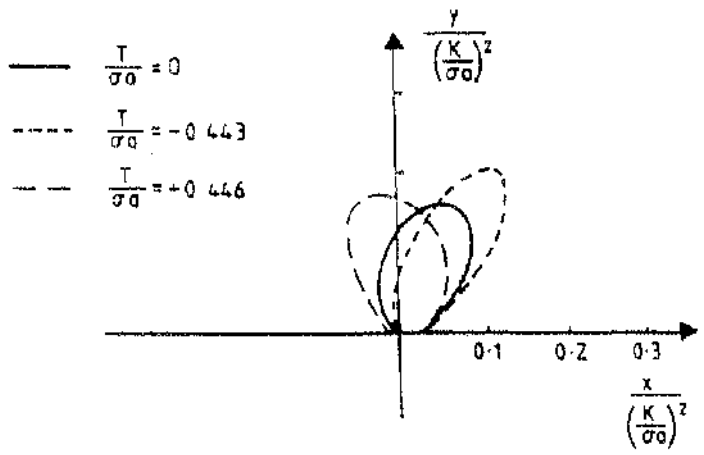

Figure 3.14 The effect of the T-stress on the non-dimensionalized plastic zone shape ., Du and Hancock, 1991.

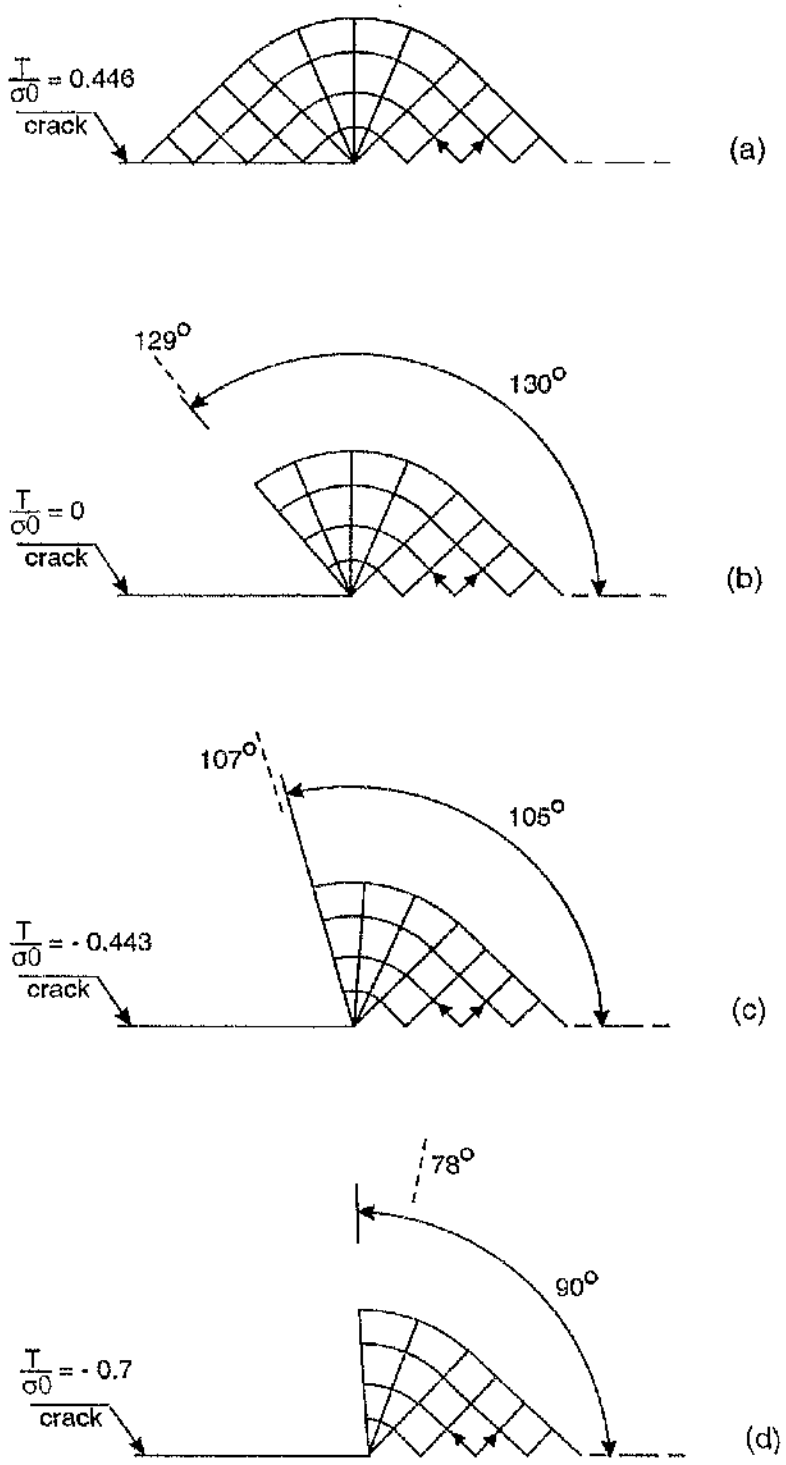

Figure 3.15 Effect of T stress on mode I slip line fields, following Du and Hancock, 1991.

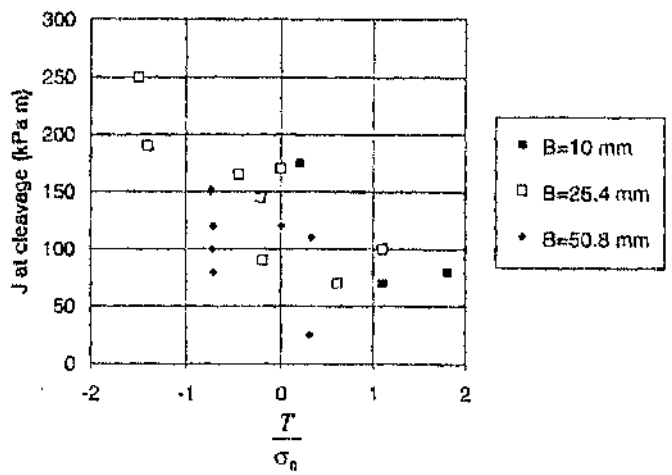

Figure 3.16 Fracture toughness versus T/σ_o for ASTM A515 Grade 70 steels at 20° C from edge cracked bend bars for three thicknesses, Kirk et al., 1993.

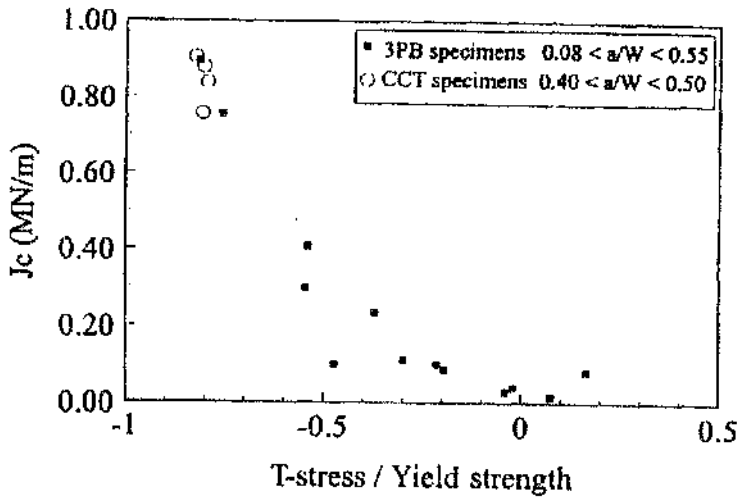

Figure 3.17 *J-T* locus for 3PB and CCT specimens, high strength weld steel at -30^0 C, Sumpter, 1993.

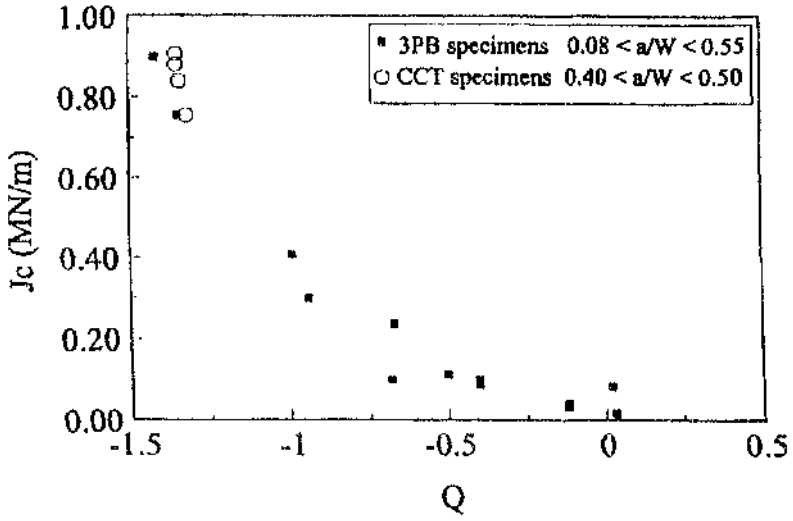

Figure 3.18 *J-Q* locus for 3PB and CCT specimens, high strength weld steel at -30^0 C, Sumpter and Hancock, 1994.

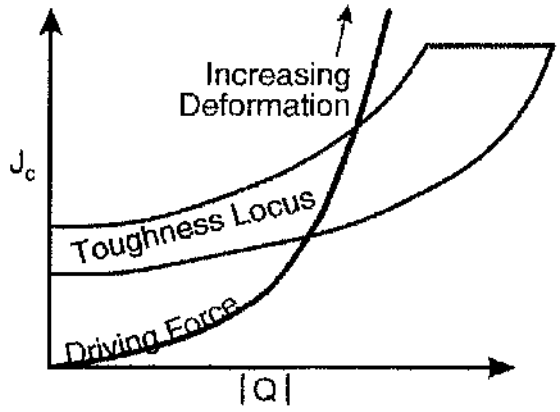

Figure 3.19 Application of a J-Q toughness locus.

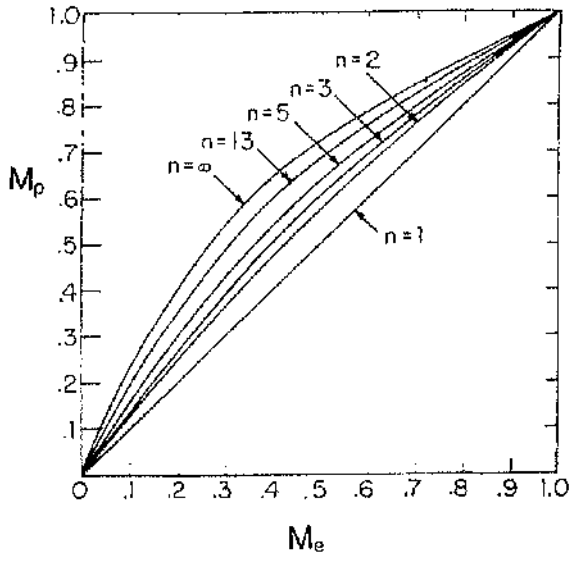

Figure 3.20 Near-field mixity M_p versus far-field mixity M_e for small-scale yielding in plane strain, Shih, 1974.

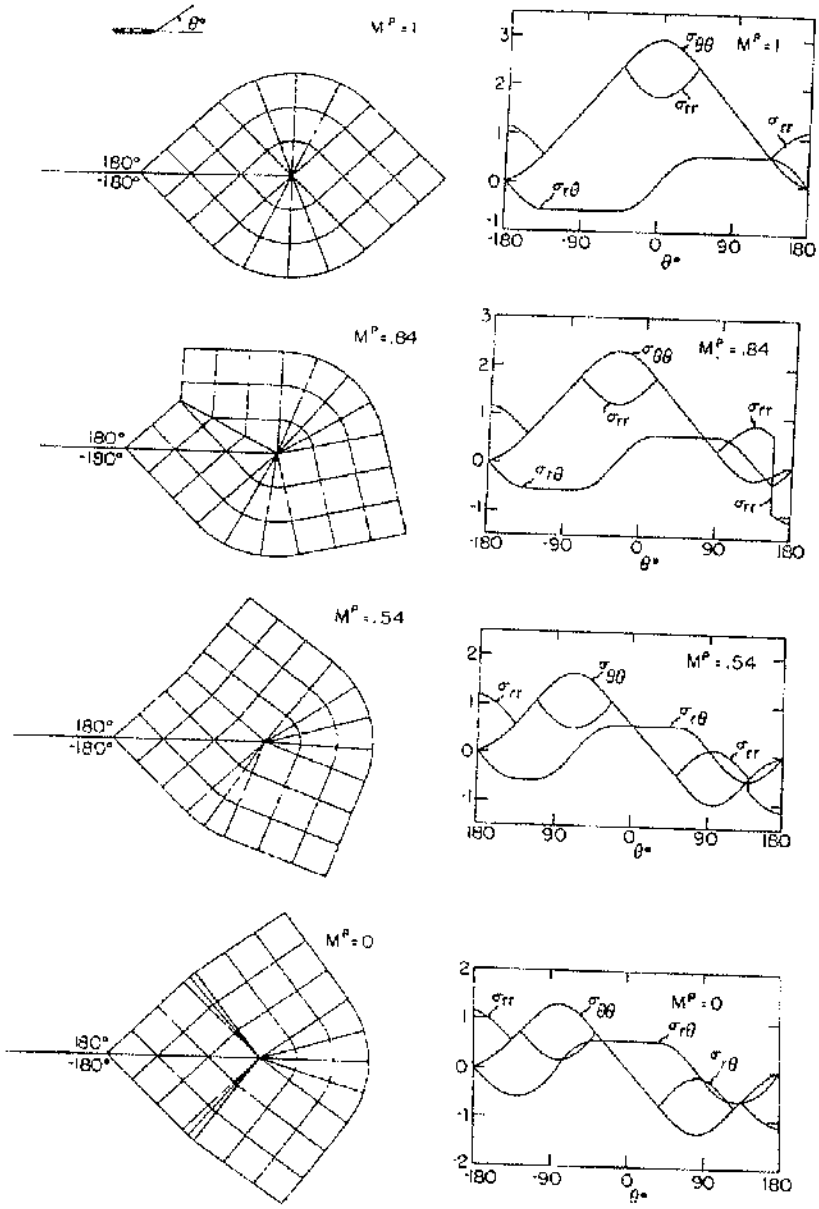

Figure 3.21 Slip line fields and stress distributions at the tip of a crack in a perfectly plastic material for plane strain, Shih, 1974.

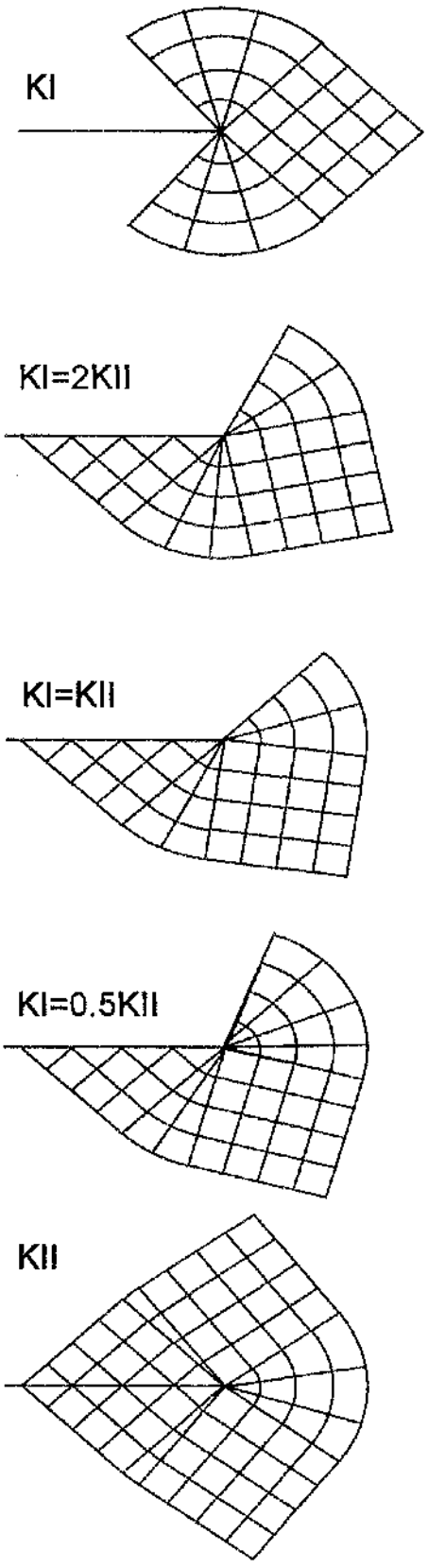

Figure 3.22 Slip line fields under mixed mode loading in homogeneous material, following Hancock, al,et., 1997.

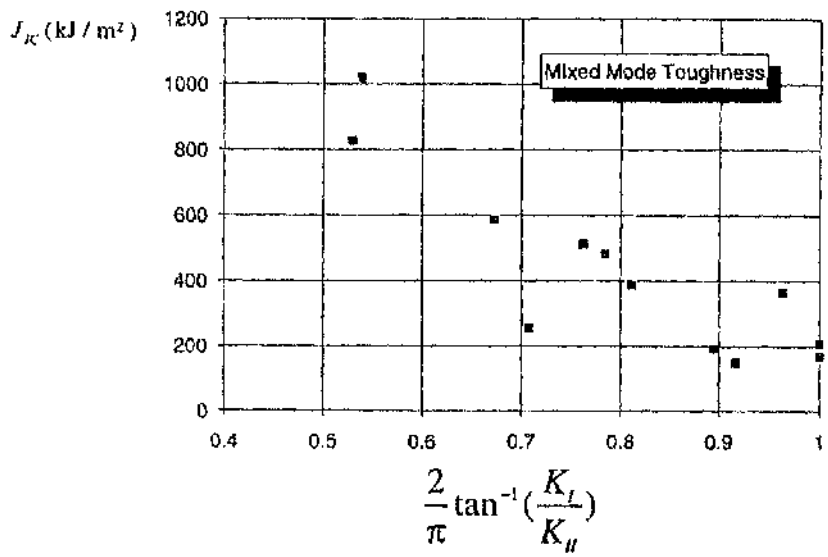

Figure 3.23 Correlation of constraint and elastic mixity, Hancock, Nekkal and Karstensen, 1997.

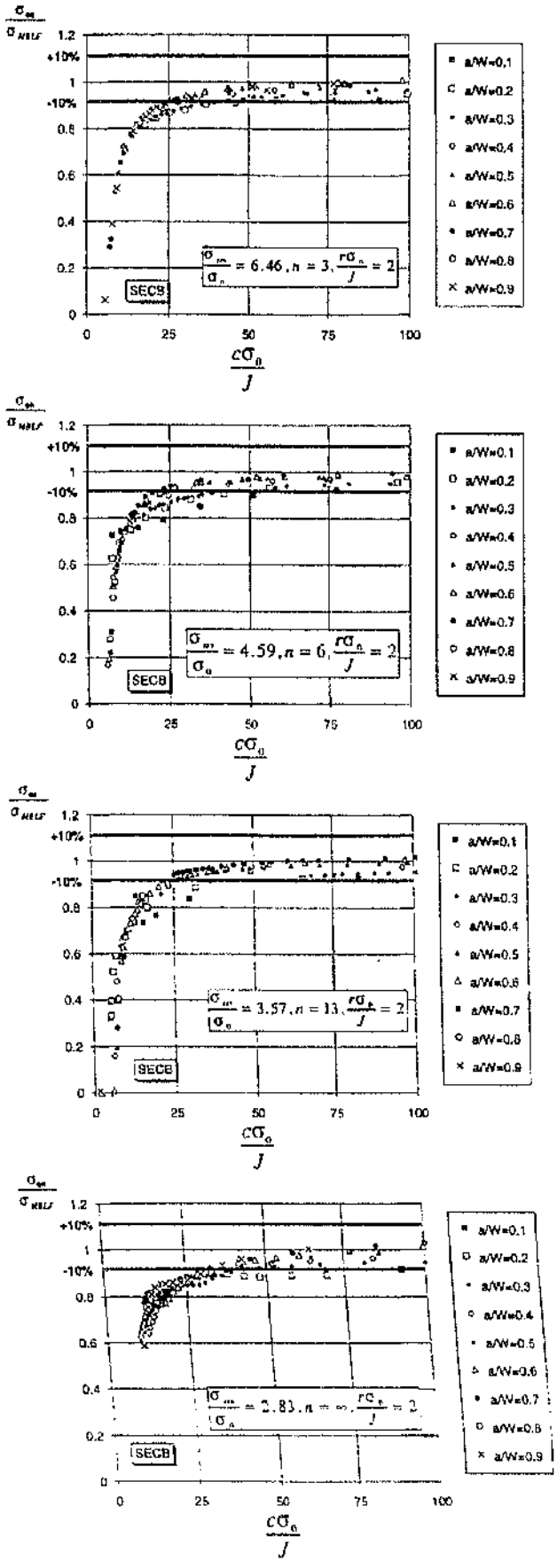

Figure 3.24 The stress directly ahead of crack in an edge cracked bend bars for Limits of J-T characterisation, Karstensen,1996.

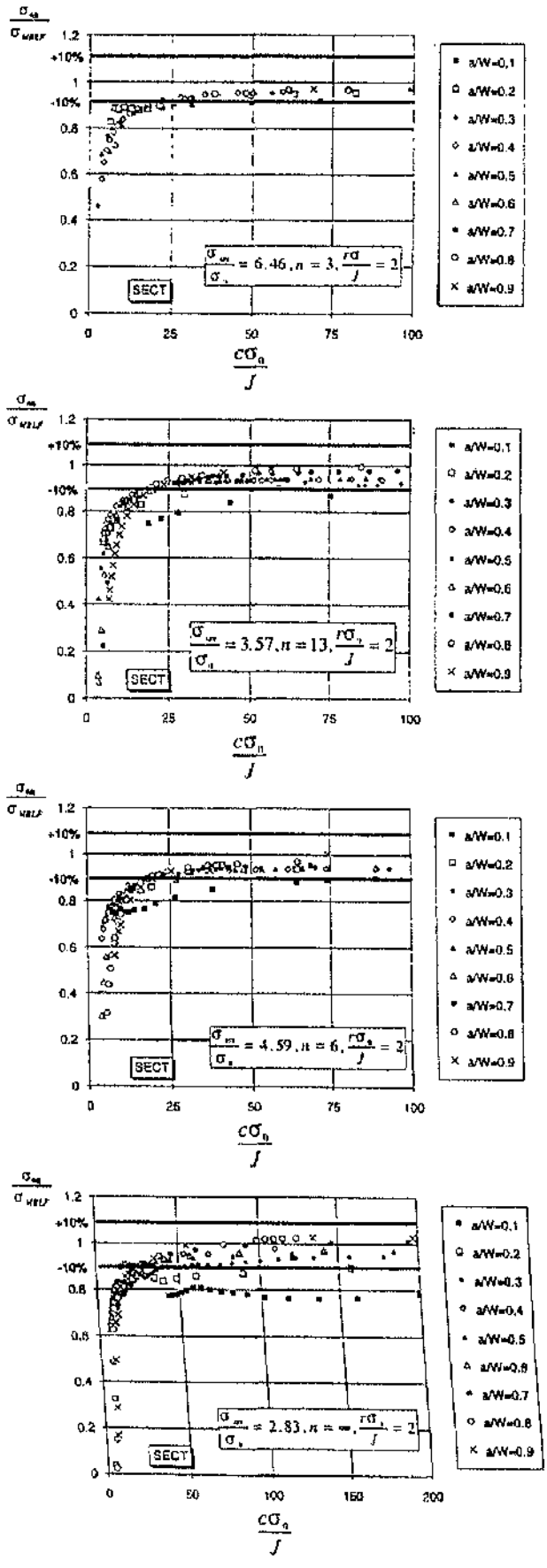

Figure 3.25 The stress directly ahead of crack in an edge cracked tension bars for Limits of J-T characterisation, Karstensen,1996.

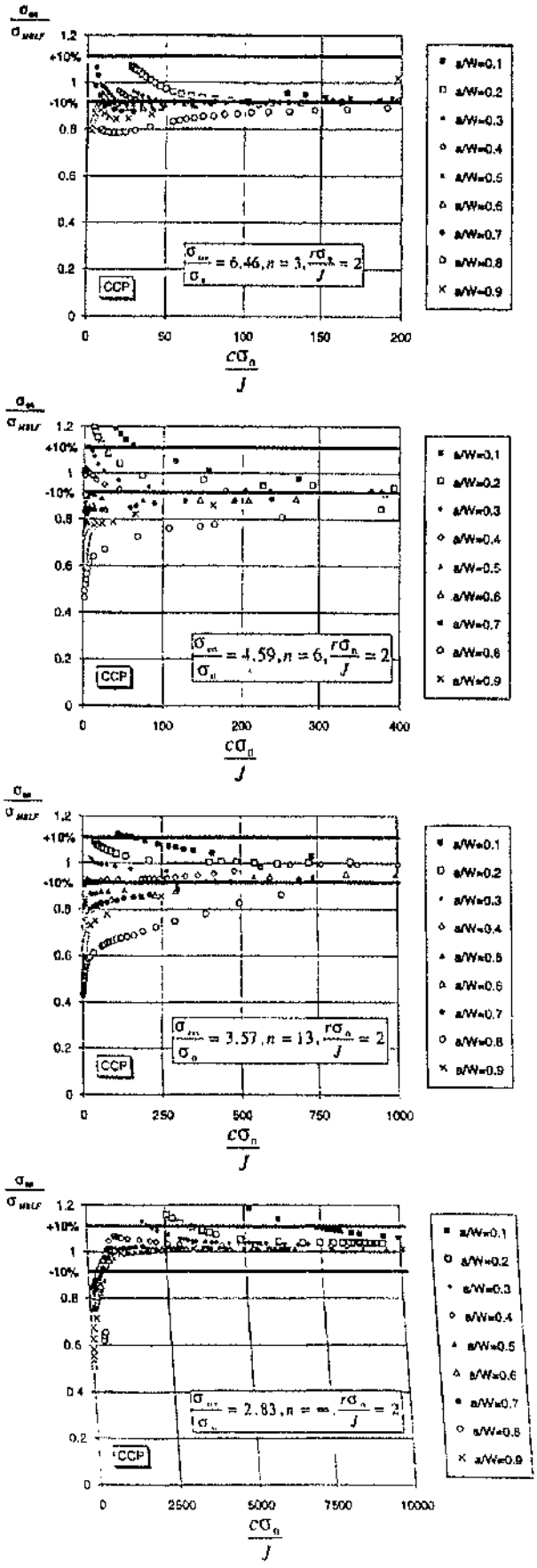

Figure 3.26 The stress directly ahead of crack in a centred cracked panel for Limits of J-T characterisation, Karstensen,1996.

a/W	$n=3$	$n=6$	$n=13$	$n=\infty$
	$\frac{c\sigma_0}{J} \geq$	$\frac{c\sigma_0}{J} \geq$	$\frac{c\sigma_0}{J} \geq$	$\frac{c\sigma_0}{J} \geq$
0.1	35	50	65	30
0.2	35	40	40	30
0.3	35	40	30	30
0.4	20	20	20	30
0.5	20	20	20	30
0.6	20	20	20	30
0.7	20	20	20	30
0.8	20	20	20	30
0.9	20	20	20	30

(i) Single edge cracked bend bars.

a/W	$n=3$	$n=6$	$n=13$	$n=\infty$
	$\frac{c\sigma_0}{J} \geq$	$\frac{c\sigma_0}{J} \geq$	$\frac{c\sigma_0}{J} \geq$	$\frac{c\sigma_0}{J} \geq$
0.1	30	100	180	1000
0.2	20	25	120	160
0.3	20	20	20	50
0.4	20	20	20	25
0.5	20	20	20	25
0.6	20	20	20	25
0.7	20	20	20	25
0.8	20	20	20	25
0.9	20	20	20	25

(ii)Single edge cracked tension bars.

a/W	$n=3$	$n=6$	$n=13$	$n=\infty$
	$\frac{c\sigma_0}{J} \geq$	$\frac{c\sigma_0}{J} \geq$	$\frac{c\sigma_0}{J} \geq$	$\frac{c\sigma_0}{J} \geq$
0.1	-	75	200	≈ 5000
0.2	-	25	50	3200
0.3	-	-	-	2000
0.4	-	-	-	280
0.5	-	-	300	420
0.6	-	260	350	500
0.7	80	280	400	400
0.8	80	250	400	450
0.9	80	300	500	450

(iii) Centred cracked panels.

Table 3.5 Limits of J-T characterisation for single edge cracked bend bars, Karstensen,1996.

Chapter 4 Fracture mechanics of bi-materials

The performance of composite materials is often determined by the response of bi-material interfaces, so that failure of the interfaces by crack propagation is particularly important. Characterisation of interfacial crack tip fields is required for the assessment of the integrity of mechanical structures as well as for the transferability of laboratory test results to structural components. This chapter reviews progress in modelling stationary interfacial cracks.

4.1 Elastic fracture mechanics of interface cracks

As usual Cartesian axes (x, y) centred at the crack tip are employed. Two elastically mismatched solids joined along the x-axis, with a crack lying on the -x axis are illustrated in Figure 4.1. Material 1, above the interface, and material 2, below the interface, have Young's modulus E_i and Poisson's ratio ν_i (i=1,2). Two distinct elastic interfacial crack-tip idealisations can be identified: a traction-free crack tip model introduced by Williams (1959), and a frictionless closed crack-tip model discussed by Comninou (1977).

4.1.1 Traction-free crack tip model

Williams (1959) postulated a stress function, ϕ which satisfies traction free boundary conditions on the crack flanks.

$$\phi(r,\theta) = r^{\lambda+1}\left[A\sin(\lambda+1)\theta + B\cos(\lambda+1)\theta + C\sin(\lambda-1)\theta + D\cos(\lambda-1)\theta\right]$$
$$= r^{\lambda+1}F(\theta) \qquad (4.1\text{-}1)$$

where *A, B, C and D* are constants, and θ is identified in Figure 4.1. The relations between stress, displacements and the stress function are given in standard texts including Timoshenko and Goodier (1970):

$$\sigma_{rr} = \frac{1}{r^2}\frac{\partial^2\phi}{\partial\theta^2} + \frac{1}{r}\frac{\partial\phi}{\partial r} = r^{\lambda-1}\left[F''(\theta) + (\lambda+1)F(\theta)\right] \qquad (4.1\text{-}2a)$$

$$\sigma_{\theta\theta} = \frac{\partial^2 \phi}{\partial r^2} = r^{\lambda-1}\left[\lambda(\lambda+1)F(\theta)\right] \quad (4.1\text{-}2b)$$

$$\sigma_{r\theta} = \frac{-1}{r}\frac{\partial^2 \phi}{\partial r \partial \theta} + \frac{1}{r^2}\frac{\partial \phi}{\partial \theta} = r^{\lambda-1}\left[-\lambda F'(\theta)\right] \quad (4.1\text{-}2c)$$

$$u_\theta = \frac{1}{2G} r^\lambda \left\{-F'(\theta) - 4(1-\zeta)\left[C\cos(\lambda-1)\theta - D\sin(\lambda-1)\theta\right]\right\} \quad (4.1\text{-}3a)$$

$$u_r = \frac{1}{2G} r^\lambda \left\{-(\lambda+1)F(\theta) + 4(1-\zeta)\left[C\sin(\lambda-1)\theta + D\cos(\lambda-1)\theta\right]\right\} \quad (4.1\text{-}3b)$$

where the primes denote derivatives with respect to θ. G is the shear modulus, and $\zeta=\nu/(1+\nu)$.

Quantities in regions 1 and 2 have the appropriate subscript, F_1, F_2, λ_1, λ_2, ζ_1, ζ_2, ν_1, ν_2, etc, respectively. If the crack faces are traction free, $\sigma_{\theta\theta}^{\ 1}(\pi) = \sigma_{\theta\theta}^{\ 2}(-\pi) = \sigma_{r\theta}^{\ 1}(\pi) = \sigma_{r\theta}^{\ 2}(-\pi) = 0$, which implies the conditions:

$$F_1(\pi)=F_2(-\pi)=F'_1(\pi)=F'_2(-\pi)=0 \quad (4.1\text{-}4\sim7)$$

Furthermore the hoop and shear stresses and displacements must be continuous across the interface (θ=0).

$$\sigma_{\theta\theta}^{\ 1}(0) = \sigma_{\theta\theta}^{\ 2}(0),\ \sigma_{r\theta}^{\ 1}(0) = \sigma_{r\theta}^{\ 2}(0)$$
$$u_\theta^{\ 1}(0) = u_\theta^{\ 2}(0),\quad u_r^{\ 1}(0) = u_r^{\ 2}(0)$$

In order to make these four boundary conditions independent of radial distance r, λ_1 must be equal to λ_2. These conditions lead to:

$$F_1(0)=F_2(0) \quad (4.1\text{-}8)$$
$$F'_1(0)=F'_2(0) \quad (4.1\text{-}9)$$

$$\frac{1}{2G_1}\left[-F'_1(0) - 4C_1(1-\zeta_1)\right] = \frac{1}{2G_2}\left[-F'_2(0) - 4C_2(1-\zeta_2)\right] \quad (4.1\text{-}10)$$

$$\frac{1}{2G_1}\left[-(\lambda+1)F_1(0)-4D_1(1-\zeta_1)\right]=\frac{1}{2G_2}\left[-(\lambda+1)F_2(0)+4D_2(1-\zeta_2)\right] \quad (4.1\text{-}11)$$

Substitution of $F_1(\theta)$ and $F_2(\theta)$ in (4.1-4~11), leads to the eight homogeneous linear equations with eight unknowns A_1,, A_2, ... D_1,, D_2. By letting the determinant of the eight equations be zero, Williams (1959) gives:

$$\cos^2\lambda\pi+\left[\frac{2\Gamma(1-\zeta_2)-2(1-\zeta_1)-(\Gamma-1)}{2\Gamma(1-\zeta_2)+2(1-\zeta_1)}\right]^2=0 \quad (4.1\text{-}12)$$

where $\Gamma=G_1/G_2$. There are an infinite number of λ values that satisfy the boundary conditions. The dominant complex eigenvalue is $\lambda=\frac{1}{2}+i\varepsilon$ $\left(i=\sqrt{-1}\right)$, which contains a real component (1/2), producing the usual square-root dependence on r seen in homogeneous solutions, and an imaginary component ($i\varepsilon$) (Zywicz and Parks, 1992). The bi-material constant, ε, depends on the elastic mismatch of the two materials which is characterised by two Dundur's parameters α and β:

$$\alpha=\frac{\Gamma(k_2+1)-(k_1+1)}{\Gamma(k_2+1)+(k_1+1)} \quad (4.1\text{-}13)$$

$$\beta=\frac{\Gamma(k_2-1)-(k_1-1)}{\Gamma(k_2+1)+(k_1+1)} \quad (4.1\text{-}14)$$

where $k_i=3-4\nu_i$ for plane strain (i=1,2) and $k_i=(3-\nu_i)/(1+\nu_i)$ for plane stress. The Dundurs parameter α measures the mismatch in the plane tensile modulus whereas β characterises the mismatch in the in-plane bulk modulus and varies from -½ to ½. Under plane strain conditions, β vanishes for: identical materials; two incompressible materials; or one incompressible and one rigid material (Comninou, 1990). The relation between the bi-material constant, ε, and elastic mismatch parameter, β, was given by Rice (1988):

$$\varepsilon = \frac{1}{2\pi} ln \frac{1-\beta}{1+\beta} \tag{4.1-15}$$

For compressible bi-materials, $\varepsilon \neq 0$, interpenetration arises mathematically in a small crack tip zone (England, 1965). This physically inadmissible mathematical crack-face interpenetrating is interpreted as crack face contact which "occurs" whenever $\Re\{\Delta u(r)\} \leq 0$, $\theta = \pi$ (Rice, 1988).

4.1.2 Frictionless closed crack-tip model

The physical anomaly associated with the traction free crack flanks motivated Comninou (1977) to develop a frictionless closed crack-tip model shown in Figure 4.2. Directly ahead of the crack tip only the shear tractions are singular, exhibiting the square-root type of singularity, regardless of the nature of the applied loads. The compressive tractions in the contact zone behind the crack tip have a square-root singularity. A stress intensity factor K_I can be defined and related to the mode II stress intensity factor K_{II} following Comninou, 1990:

$$K_I = \pm \beta K_{II} \tag{4.1-16}$$

where the + sign applies when the bond is to the left of the crack tip, and the - sign when the bond is to the right of the crack tip. Since K_I is always negative due to the nature of compression, it follows that K_{II} has opposite signs at the two tips of a finite crack. Figure 4.3 shows asymptotic of a closed crack tip (Comninou, 1990).

4.1.3 Complex stress intensity factor

The dominant asymptotic traction free interfacial crack tip stress field has been given by Rice and Sih (1965) in terms of a complex stress intensity factor K

$$\sigma_{yy}(r, \theta = 0) + i\,\sigma_{xy}(r, \theta = 0) \equiv \frac{K r^{ic}}{\sqrt{2\pi r}} \tag{4.1-17}$$

where $K=K_I+i\,K_{II}$ and $i=\sqrt{-1}$. Following this work, Hutchinson et al. (1987) proposed a modification in which the complex stress intensity factor was expressed in the form:

$$K=(k_I+i\,k_{II})\sqrt{\pi}\,\cosh\pi\varepsilon \qquad (4.1\text{-}18)$$

The term $\sqrt{\pi}$ arises in converting the lower case k of that period to the more modern definition of the stress intensity factor. The introduction of $\cosh\pi\varepsilon$ makes the magnitude of the traction vector analogous to the homogeneous case.

$$\sqrt{\left(\sigma_{yy}^2+\sigma_{xy}^2\right)}=|K|/\sqrt{2\pi r} \qquad (4.1\text{-}19)$$

The corresponding asymptotic crack-face displacement $\Delta u(r)$ can be written in terms of the complex stress intensity factor K:

$$\Delta u(r)\equiv u(r,\theta=\pi)-u(r,\theta=-\pi)=\frac{2(C_1+C_2)K\,r^{i\varepsilon}\sqrt{r}}{\sqrt{2\pi}(1+i2\varepsilon)\cosh(\pi\varepsilon)} \qquad (4.1\text{-}20)$$

where $u(r,\theta)\equiv u_y(r,\theta)+i\,u_x(r,\theta)$ and $C_j=(1-\nu_j)/G_j$ $(j=1,2)$ are elastic compliances. Equation (4.1-18) reduces to $K=K_I+iK_{II}$ for a homogeneous solid where $C_1=C_2$ and $\varepsilon=0$.

The complex intensity factor K thus uniquely characterises the crack tip field in the same way that a conventional stress intensity factor defines the field of a homogeneous material. Even though non-linearities cause the actual field to differ locally from Williams stress and deformation distributions, the field approaches the standard Williams elastic singularity of a strength characterised by a complex intensity factor K at large radius r. The complex intensity factor, K, therefore provides the boundary conditions determine the onset of crack growth in small scale yielding.

4.1.4 Cracks lying between an elastic matrix and a rigid substrate

In most composite materials the reinforcement is much stiffer than matrix, such as a metal matrix reinforced by ceramic fibres. In these cases, the reinforcement may be modelled as a rigid body (material 2) and matrix (material 1) as an elastic-plastic material. Figure 4.4 illustrates a stationary crack located between a rigid body in the lower half space and an elastic-plastic matrix in the upper region. To avoid the oscillatory asymptotic analysis of the elastic fields at the tip of a open interface crack, interest is currently focused on incompressible elastic deformation. When the matrix is an elastic incompressible continuum, the normal and shear traction singularities can be de-coupled and measured by the standard definition of the intensity factors K_I and K_{II} at the crack tip (Sharma and Aravas, 1993). In a opening crack model, the leading order stress fields in Cartesian co-ordinates system were found to be (Rice and Sih 1965):

$$\begin{Bmatrix}\sigma_{xx}(x,y)\\ \sigma_{yy}(x,y)\\ \sigma_{xy}(x,y)\end{Bmatrix}=\frac{1}{4\sqrt{2\pi r}}\left(K_I\begin{Bmatrix}3\cos\frac{\theta}{2}+\cos\frac{5\theta}{2}\\ 5\cos\frac{\theta}{2}-\cos\frac{5\theta}{2}\\ -\sin\frac{\theta}{2}+\sin\frac{5\theta}{2}\end{Bmatrix}+K_{II}\begin{Bmatrix}-7\sin\frac{\theta}{2}-\sin\frac{5\theta}{2}\\ -\sin\frac{\theta}{2}+\sin\frac{5\theta}{2}\\ 3\cos\frac{\theta}{2}+\cos\frac{5\theta}{2}\end{Bmatrix}\right) \tag{4.1-21}$$

while in polar co-ordinates system, the dominant stress fields were given by Fang and Bassani (1995):

$$\begin{Bmatrix}\sigma_{r\theta}(r,\theta)\\ \sigma_{rr}(r,\theta)\\ \sigma_{\theta\theta}(r,\theta)\end{Bmatrix}=\frac{1}{4\sqrt{2\pi r}}\left(K_I\begin{Bmatrix}\sin\frac{\theta}{2}+\sin\frac{3\theta}{2}\\ 5\cos\frac{\theta}{2}-\cos\frac{3\theta}{2}\\ 3\cos\frac{\theta}{2}+\cos\frac{3\theta}{2}\end{Bmatrix}+K_{II}\begin{Bmatrix}\cos\frac{\theta}{2}+3\cos\frac{3\theta}{2}\\ -5\sin\frac{\theta}{2}+3\sin\frac{3\theta}{2}\\ -3\sin\frac{\theta}{2}-3\sin\frac{3\theta}{2}\end{Bmatrix}\right) \tag{4.1-22}$$

The corresponding dominant asymptotic displacement field is:

$$\begin{Bmatrix} u_r(r,\theta) \\ u_\theta(r,\theta) \end{Bmatrix} = \frac{1}{4G}\sqrt{\frac{r}{2\pi}}\left\{ K_I \begin{bmatrix} \cos\frac{\theta}{2} - \cos\frac{3\theta}{2} \\ 3\sin\frac{\theta}{2} - \sin\frac{3\theta}{2} \end{bmatrix} + K_{II} \begin{bmatrix} -\sin\frac{\theta}{2} + 3\sin\frac{3\theta}{2} \\ -3\cos\frac{\theta}{2} + 3\cos\frac{3\theta}{2} \end{bmatrix} \right\} \quad (4.1\text{-}23)$$

where G is the shear modulus of the matrix. K_I and K_{II} are the stress intensity factors corresponding to mode I and mode II established by far field conditions such as the applied loading and the geometry of the cracked body. In this open crack model, K_I >0. A remote positive shear in the Cartesian axes shown in Figure 4.1 corresponds to K_{II} >0 while negative shear to K_{II} <0.

In the closed face model, the incompressibility assumption can be relaxed. There is only one independent eigenfunction and the leading order solution for frictionless contact at an interfacial crack tip in Cartesian co-ordinates was given by Comminou (1977) and Sharma and Aravas (1993):

$$\begin{Bmatrix} \sigma_{xx} \\ \sigma_{yy} \\ \sigma_{xy} \end{Bmatrix} = -\frac{K_{II}^c}{\sqrt{2\pi r}} \frac{1}{2(k+1)} \begin{Bmatrix} (2k+5)\sin\frac{\theta}{2} + \sin\frac{5\theta}{2} \\ (2k-3)\sin\frac{\theta}{2} + \sin\frac{5\theta}{2} \\ (2k+1)\cos\frac{\theta}{2} + \cos\frac{5\theta}{2} \end{Bmatrix} \quad (4.1\text{-}24)$$

where k = 3 - 4ν for plane strain problems and K_{II}^c is the stress singularity for the frictionless contact. Since the normal tractions are not singular, the mode I strength intensity factor K_I disappears.

The dominant stress fields have also been given in polar co-ordinates by Comninou (1977):

$$\begin{Bmatrix} \sigma_{rr} \\ \sigma_{\theta\theta} \\ \sigma_{r\theta} \end{Bmatrix} = -\frac{K_{II}^c}{4\sqrt{2r}} \begin{Bmatrix} 5(1+\beta)\sin\frac{\theta}{2} - (3-\beta)\sin\frac{3\theta}{2} \\ 3(1+\beta)\sin\frac{\theta}{2} + (3-\beta)\sin\frac{3\theta}{2} \\ (1+\beta)\cos\frac{\theta}{2} + (3-\beta)\cos\frac{3\theta}{2} \end{Bmatrix} \quad (4.1\text{-}25)$$

When the lower region is assumed to be rigid, the Dundurs bi-material constant (β) becomes:

$$\beta = \frac{1-k}{1+k} \tag{4.1-26}$$

The corresponding dominant asymptotic displacement field is:

$$\begin{Bmatrix} u_r(r,\theta) \\ u_\theta(r,\theta) \end{Bmatrix} = -\frac{K_{II}^e\sqrt{2r}}{8G} \begin{Bmatrix} (2k-1)(1+\beta)\sin\frac{\theta}{2} - (3-\beta)\sin\frac{3\theta}{2} \\ (2k+1)(1+\beta)\cos\frac{\theta}{2} - (3-\beta)\cos\frac{3\theta}{2} \end{Bmatrix} \tag{4.1-27}$$

To ensure compressive traction in the contact zone ($\sigma_{\theta\theta} < 0$ when $\theta=\pi$) loading is restricted to $K_{II}^e > 0$ for $\beta>0$ and $K_{II}^e < 0$ for $\beta<0$. However when $\beta=0$ and $\theta=\pi$, $\sigma_{\theta\theta}$ is zero for any value of K_{II}^e. Since the shear stress is the only singular stress component directly ahead of the crack tip as $r\to 0$, the asymptotic solution is mode-II-like.

4.2 Elastic-plastic fracture mechanics of elastically mismatched interface cracks

Interfacial cracks with elastic mismatch have recently received considerable attention because of a variety of applications involving heterogeneous metal combinations. Based on the dominant singularity term determined by Williams (1959), elastically mismatched interfacial crack-tip fields under small scale yielding conditions have been investigated by Shih and co-workers (1988, 1991) and Zywicz and Parks (1989, 1992).

4.2.1 Mixed mode loading

The crack tip stress fields are characterised in terms of a complex stress intensity factor, K, and a near tip phase parameter which is defined by (Zywicz and Parks, 1989)

$$\zeta_0 = \angle K + \varepsilon \ln(r^p) \tag{4.2-1}$$

where $\angle K = atan\ (K_{II}/K_I)$ and r^p represents the maximum radius of a crack tip plastic zone,

$$r^p = \frac{K\,\ddot{K}}{\sigma^2{}_{ys}\pi \cosh^2(\pi\varepsilon)} \tag{4.2-2}$$

σ_{ys} is the yield stress. The near tip phase parameter (ζ_0) depends on β, that is to say, on the elastic constants of the two materials, and accounts for the coupling between $\angle K$ and r_p. Zywicz and Parks noted that near tip fields vary appreciably with the phase parameter. When $-30^0 < \zeta_0 < 0$, interfacial triaxialities reach 3.29, a condition extremely conducive for ductile void nucleation, growth and coalescence, while the fields for $\zeta_0 < -50^0$ contain extremely large interfacial shear strains. As ζ_0 is increased in the range $\zeta_0 > 0$, normal tractions across the interface decrease and the crack face elastic zone extends as shown in Figure 4.5 (Zywicz and Parks, 1992). Correspondingly, the accompanying shear traction increases up to its maximum value of k. Thus interfacial failure governed by maximum shear traction criteria appear more favourable at large positive and most negative ζ_0 values. The largest shear strains reside in centred fans close to the crack face-elastic-constant-state-fan border but slowly reorient toward the interface as $\zeta_0 \rightarrow 90^0$. Under these loading conditions, crack advance by shear localisation appears more favourable at angles slightly inclined from the interface, in the maximum shear strain direction, than along the interface.

Zywicz and Parks (1992) analysed the elastic sectors at the crack tip which behave as semi-infinite plane strain elastic wedges loaded by constant surface tractions. The stress field within the elastic sectors can thus be obtained from the general wedge solution (Timoshenko and Goodier, 1970). Complete

independent analytic solutions were not possible as the boundary conditions were provided by numerical solutions.

However in some cases such as the case described by Li and Hancock (1997), elastic sectors appear between an interfacial crack flank and a centred fan sector under mixed mode loading, and following independent analytical solutions may be established. This will be discussed in chapters 5, 6, and 7.

4.2.2 Effect of T stress

Kim and co-workers (1996) found that the Dundurs parameter, α, also plays an important role in elastically mismatched interfacial crack tip constant due to the linear dependence of the non-singular stress T on α. The magnitude of the non-singular stresses for both materials T_i are given in terms of α:

$$T_1=(1+\alpha)T \quad ; \quad T_2=(1-\alpha)T \tag{4.2-3}$$

T denotes the magnitude of the T stress for elastically homogeneous materials, such that the first two terms of the Williams expansion for material 1 are:

$$\sigma_{kl}(r,\theta) = \frac{|K|}{\sqrt{2\pi r}\cosh(\pi\varepsilon)}\tilde{\sigma}_{kl} + T_1\delta_{1k}\delta_{1l} \tag{4.2-4}$$

The corresponding displacement fields are represented by:

$$u_x = \frac{|K|\sqrt{r}}{\sqrt{2\pi}\cosh(\pi\varepsilon)G_1}\tilde{u}_x + \frac{(k_1+1)}{8G_1}T_1 r\cos\theta \tag{4.2-5a}$$

$$u_y = \frac{|K|\sqrt{r}}{\sqrt{2\pi}\cosh(\pi\varepsilon)G_1}\tilde{u}_y + \frac{(k_1-3)}{8G_1}T_1 r\sin\theta \tag{4.2-5b}$$

For material 2, the stress components are:

$$\sigma_{kl}(r,\theta) = \frac{|K|}{\sqrt{2\pi r}\cosh(\pi\varepsilon)}\tilde{\sigma}_{kl} + T_2\delta_{1k}\delta_{1l} \tag{4.2-6}$$

The corresponding displacement fields are:

$$u_x = \frac{|K|\sqrt{r}}{2\sqrt{2\pi}\cosh(\pi\varepsilon)G_2}\tilde{u}_x + \frac{(k_2+1)}{8G_2}T_2 r\cos\theta \qquad (4.2\text{-}7a)$$

$$u_y = \frac{|K|\sqrt{r}}{2\sqrt{2\pi}\cosh(\pi\varepsilon)G_2}\tilde{u}_y + \frac{(k_2-3)}{8G_2}T_2 r\sin\theta \qquad (4.2\text{-}7b)$$

where $\tilde{\sigma}_{kl}$, $\tilde{u}_x$ and $\tilde{u}_y$ are function of phase angle and material properties (Kim and co-workers, 1996). For, α=β=0, the displacement field reduces to that of a homogeneous materials. The effect of the T-stress on the crack tip constraint for elastically dissimilar bi-material as:

$$\left(\frac{\sigma_m}{\sigma_o}\right)_{\theta=0} = 3.20 + 0.56(1+\alpha)\tau - 1.97\left[(1+\alpha)\tau\right]^2 \qquad (4.2\text{-}8a)$$

$$\left(\frac{\sigma_{00}}{\sigma_o}\right)_{\theta=0} = 3.20 + 0.29(1+\alpha)\tau - 1.60\left[(1+\alpha)\tau\right]^2 \qquad (4.2\text{-}8b)$$

where τ=T/σ_o. It is noteworthy that for identical geometries and loadings, different bi-material specimens (having different value of α) can have very different interfacial crack tip constraints.

4.2.3. Cracks lying between an elastic-plastic matrix and a rigid substrate

For a crack lying between elastic-plastic matrix and a rigid substrate, investigations for the interfacial crack tip stress field can be carried out within the framework of plane strain slip line theory. The fields can be expressed in terms of a plastic mode mixity by noting that the plastic mixity defines the ratio of hoop to shear stress directly ahead of the crack. This can be determined by following the slip lines from a crack flank to the region directly ahead of crack within the plastic zone. Based on the assumption that plasticity entirely surrounds the crack tip, Quanxin Guo and Keer (1990) presented a one-parameter family of asymptotic near tip stress fields for the traction free interfacial cracks lying

between elastic plastic material and a rigid substrate, for a limited range of plastic mixities.

$$M_p = \frac{2}{\pi} tan^{-1}\left[4\theta_1 - 1 - \frac{5\pi}{2}\right] \qquad -0.7638 \le M_p \le 0.3302 \qquad (4.2\text{-}9)$$

Figure 4.6 shows examples of the postulated slip line fields, in which θ_1 is also identified.

Fang and Bassani (1996) have also presented an one-parameter family of asymptotic near tip stress fields which extends the range of plastic mixity.

$$M_p = \frac{2}{\pi} tan^{-1}\left[-\sqrt{2}(cos\,\alpha - sin\,\alpha) - 1 + 2\alpha\right] \quad 0.3302 \le M_p \le 0.8897 \qquad (4.2\text{-}10)$$

The corresponding slip line fields and definition of α are shown in Figure 4.7. The reason that perfect plasticity solutions with M_p approaching ±1 do not exist is evident by examining the boundary conditions prescribed at θ=0. For a rigid substrate, the interface at θ=0 must be a stress characteristic with $\sigma_{r\theta} = \pm k$. Thus the plastic mode mixity evaluated with non-zero shear stresses at θ=0 cannot give M_p=±1. A pure mode I slip-line field, therefore, is not possible to occur directly ahead of the interfacial crack.

4.3 Elastic-plastic fracture mechanics of strength-mismatched interface cracks

In many civil and marine structures, welded steel joints are places of crack initiation due to inherent metallurgical or geometrical defects. The elastic properties of the welding metal and the baseplate are nearly the same but there is often a strong yield strength-mismatch due to differences in alloy content, manufacturing and welding. The problem of an interface crack between elastically matched but yield strength mismatched materials is thus of fundamental and practical significance. When a crack lies along the interface of strength mismatched weldments, there is a significant gradient in plastic

deformation resistance and the crack tip stress and deformation fields (Ganti and Parks, 1997). The features of these fields differ both qualitatively and quantitatively from the homogeneous fields reviewed in chapter 3. Ganti and Parks (1997) developed an idealised model of strength mismatched interface crack subjected to far-field mode I loading under small scale yielding conditions. The symmetry of the crack tip fields that exists for homogeneous materials is lost with strength mismatch. For non-hardening deformation, the angular span of the centred fan increases on the soft side while it decreases on the hard side. At a given remote loading level, strain is focused into the soft side of the mismatch while decreasing the peak plastic strain on the hard side. Hence the stress and deformation intensities locally experienced by material points differs from those in homogeneous specimens of either material. The triaxial constraint increases almost linearly with strength mismatch which is defined as the ratio of yield strength of the hard and soft materials, $y = \sigma_o^H / \sigma_o^S \geq 1$, and reaches a saturation level at y=1.421. Ganti and Parks presented families of slip line fields which depend on the level of mismatch, as well as on overall deformation (J) and triaxial constraint (Q/T). These fields have then been used in conjunction with local fracture criteria to establish models for the toughness of strength-mismatched interface cracks.

The effect of T on the shape of plastic zone at a strength-mismatched interface crack tip has been investigated by Kim and co-workers (1996). The dependence of the plastic zone shape for bi-materials ($y=\infty$) on T-stress is similar to that for the homogeneous material ($y=1$). Figure 4.8 compares the slip line fields under mode I loading with different level of T stress for $y=1$ and $y=\infty$. The angular spans of the centred fan for a bi-material in all loading modes are bigger than that for a homogeneous material. This leads to the observation that the hydrostatic stress at the interface for a bi-material is much higher than in homogeneous materials because the hydrostatic stress, σ_m, changes only in the centred fan sector. The hoop and mean stress directly ahead of crack increase only slightly for a positive T stress, but decrease substantially for a negative T. Kim et.al (1996) adapted Du and Hancock's (1991) idea and proposed a relation for bi-materials $y=\infty$ under mode I loading and negative T-stress

$$\left(\frac{\sigma_m}{\sigma_o}\right)_{\theta=0} = 3.20 + 0.56\tau - 1.97\tau^2 \qquad (4.3\text{-}1)$$

$$\left(\frac{\sigma_{\theta\theta}}{\sigma_o}\right)_{\theta=0} = 3.20 + 0.29\tau - 1.60\tau^2 \qquad (4.3\text{-}2)$$

where $\tau = T/\sigma_o$. Zhang and co-workers (1997) also investigated the near tip stress field of a plastically dissimilar bi-material interface with effect of *T* stress, and established that for a given material mismatch, the *T* stress shifts the near tip stress level of the interface crack up and down without significantly affecting the material mismatch constraint parameter, *y*, and suggested that the effect of *T* stress and material mismatch on the crack tip can be separated allowing a *J*-*Q*-*y* formulation to characterise the near tip stress field.

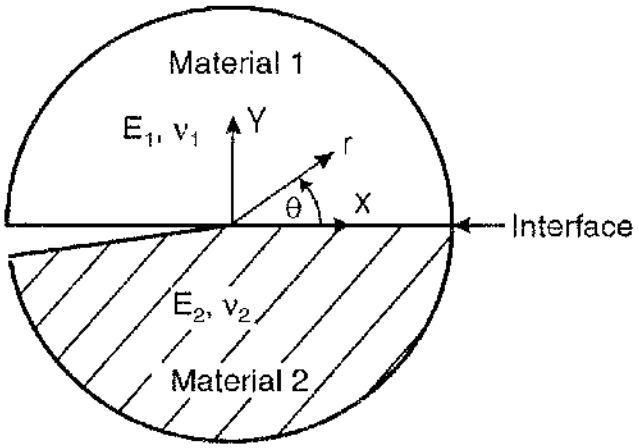

Figure 4.1 Illustration of an elastic mismatched interfacial crack.

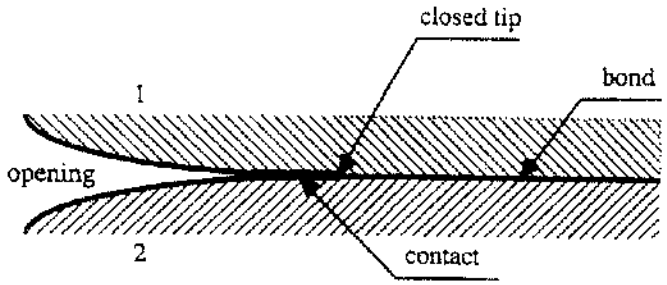

Figure 4.2 Contact zone model, Comninou, 1990.

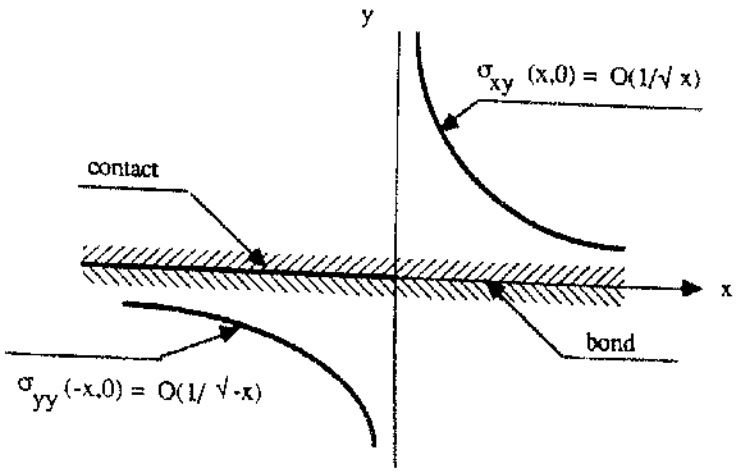

Figure 4.3 Asymptotics of the closed crack tip, Comninou, 1990.

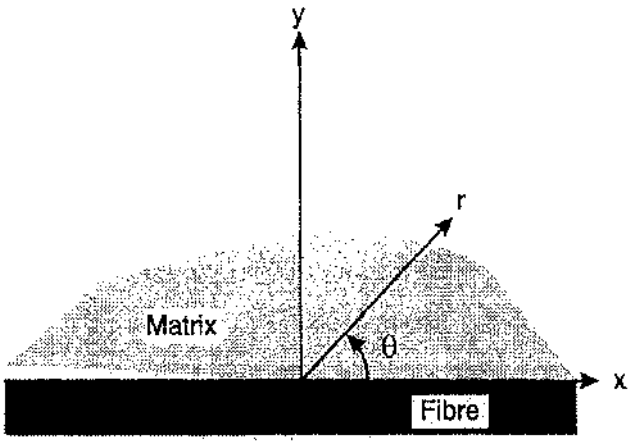

Figure 4.4 Schematic of the crack tip region.

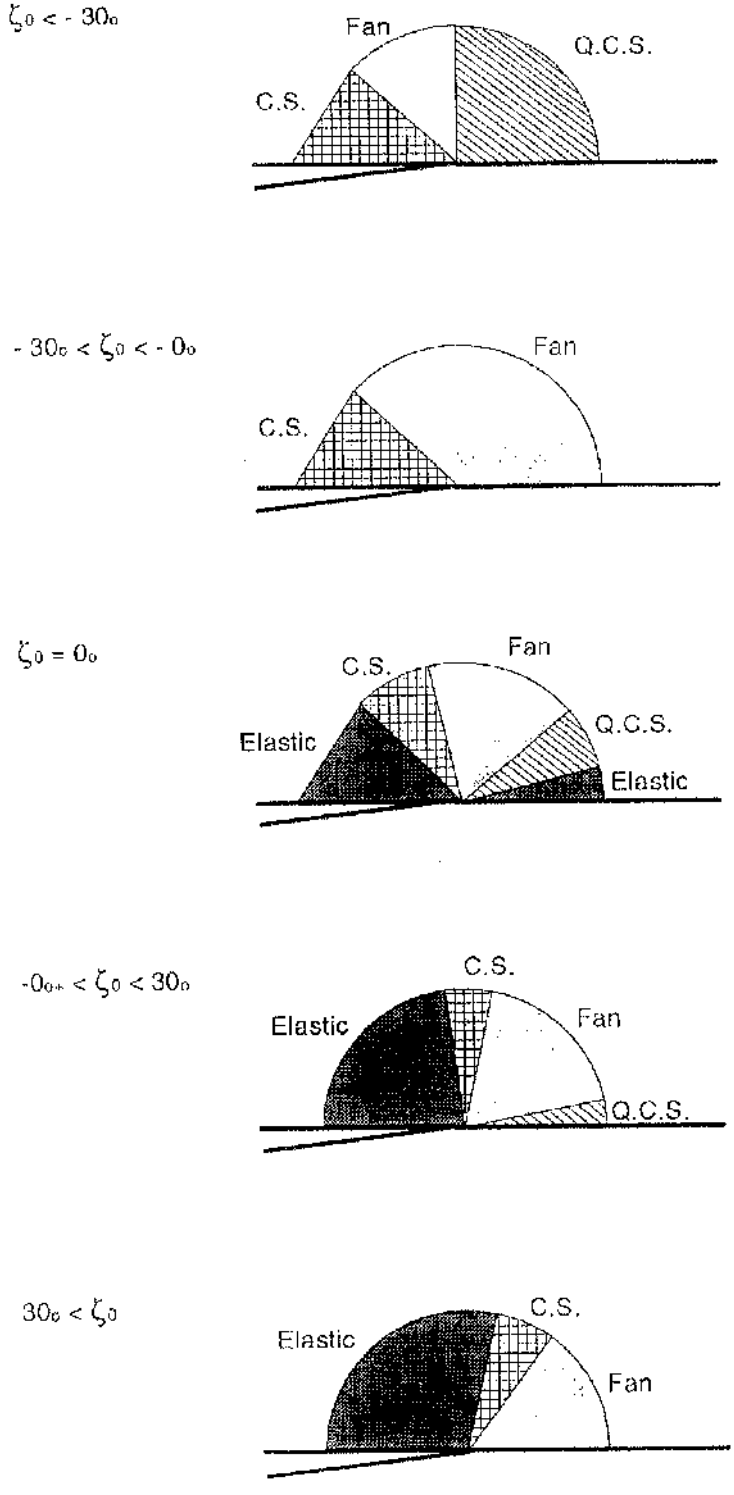

Figure 4.5 Schematic variation of near tip slip line fields. Q.C.S. refers to Quasi-constant sector and its behaviour closely resembles conventional constant-state regions except that the characteristic slip lines have small but finite curvature and produce the stress distribution depending weakly on r. Zywicz and Parks, 1992.

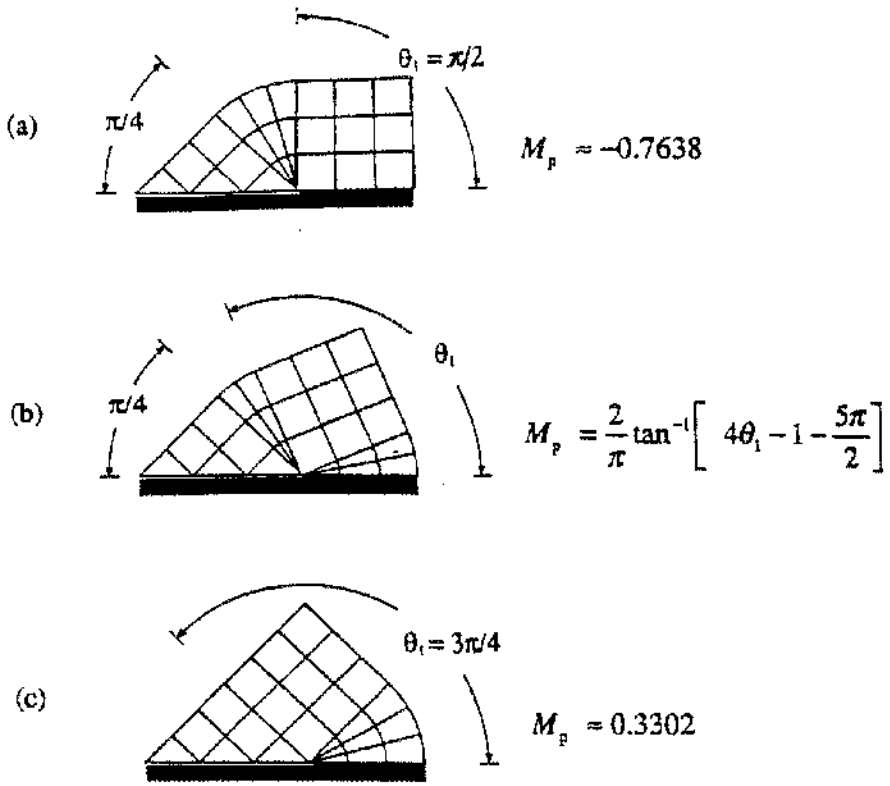

Figure 4.6 One parameter family of asymptotic near tip stress fields, Quanxin Guo and Keer (1990).

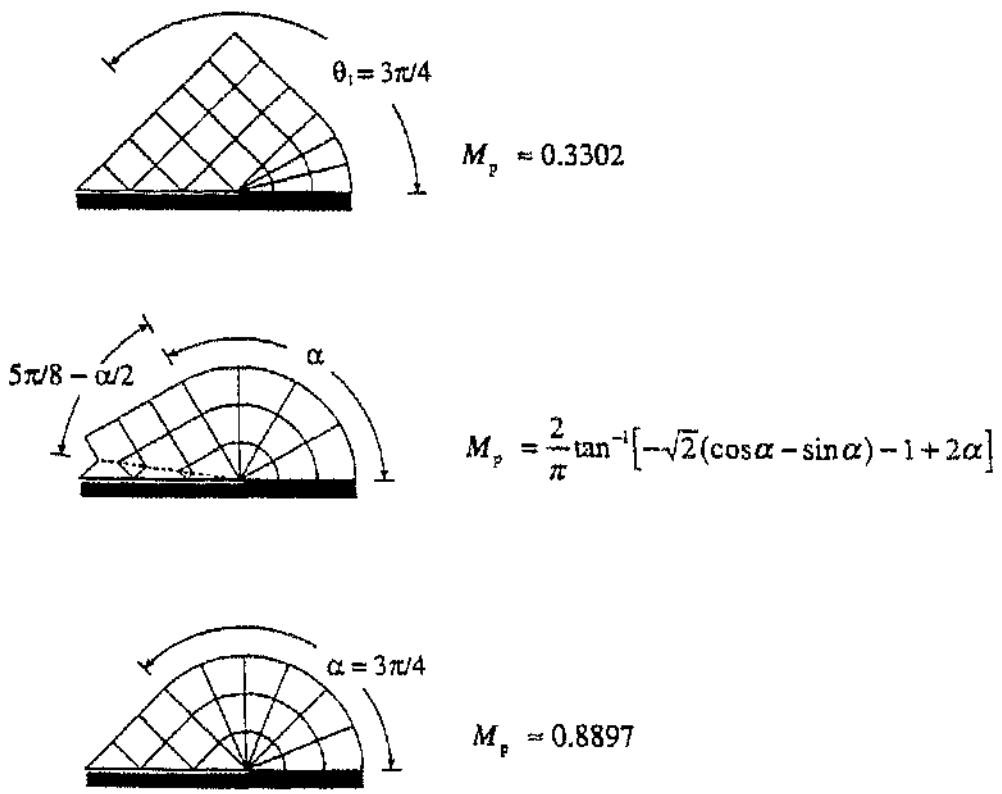

Figure 4.7 One parameter family of asymptotic near tip stress fields, Fang and Bassani (1996a).

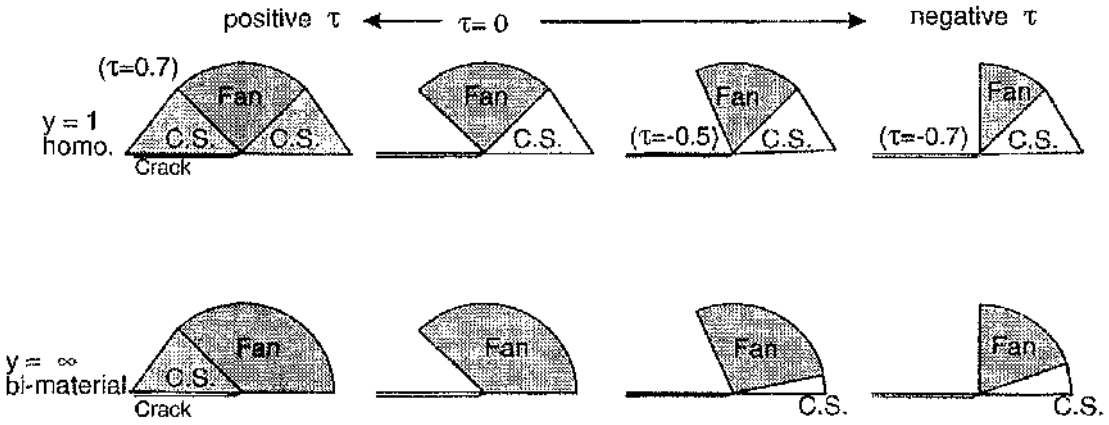

Figure 4.8 Comparion of the effects of the T stress on the homogenous crack tip stress fields and strength mismatched crack tip stress fields, Kim and co-workers, 1996.

Chapter 5 Analytic solutions for mode I crack tip stress fields in a homogeneous elastic-perfectly plastic material

5.1. Introduction

In contained yielding, local crack tip plasticity is completely contained within an outer elastic field. The level of constraint within the plastic zone depends on the nature of the non-singular terms in the outer elastic field. Detailed investigations of the asymptotic field of a mode I crack in a homogeneous solid have been presented by Du and Hancock (1991) using finite element analysis methods based on modified boundary layer formulations. Of particular significance is the observation that compressive T stress causes a loss of crack tip constraint ahead of the crack. Parallel experimental work has demonstrated that this leads to enhanced level of toughness for both cleavage and ductile tearing, Betegón and Hancock, 1991; Hancock, Reuter and Parks, 1993 and Kirk, Koppenhoefer and Shih, 1993.

In this chapter analytical solutions for incompressible deformation under mode I with zero and compressive T-stress are constructed. Without loss of generality these fields are taken to comprise elastic and plastic sectors. The stresses within the elastic sectors are obtained by reference to solutions for a semi-infinite elastic wedge, while the plastic sectors are discussed in terms of plane strain slip line fields. To verify the analytic solutions, numerical solutions were obtained using modified boundary layer formulations.

5.2. Analytical solutions

5.2.1 Stress distribution in elastic sectors

Initially, consider the deformation field within an elastic sector. It is convenient to use polar co-ordinate systems: θ is measured anticlockwise from a plane directly ahead of the crack and right handed rule is used for stresses. The angular span of the elastic wedge is denoted φ as illustrated schematically in Figure 5.1. The

assumption that crack tip stress in elastic and plastic sectors are bounded (Rice, 1974) gives:

$$r\frac{\partial \sigma_{ij}}{\partial r} \to 0 \qquad \text{as } r \to 0 \tag{5-1}$$

This allows the equilibrium equations (Timoshenko and Goodier, 1970),

$$\frac{\partial \sigma_{rr}}{\partial r} + \frac{1}{r}\frac{\partial \sigma_{r\theta}}{\partial \theta} + \frac{\sigma_{rr} - \sigma_{\theta\theta}}{r} = 0$$
$$\frac{1}{r}\frac{\partial \sigma_{\theta\theta}}{\partial \theta} + \frac{\partial \sigma_{r\theta}}{\partial r} + \frac{2\sigma_{r\theta}}{r} = 0 \tag{5-2}$$

to be reduced to:

$$\frac{\partial \sigma_{r\theta}}{\partial \theta} + \sigma_{rr} - \sigma_{\theta\theta} = 0 \tag{5-3a}$$

$$\frac{\partial \sigma_{\theta\theta}}{\partial \theta} + 2\sigma_{r\theta} = 0 \tag{5-3b}$$

The equilibrium equations must be satisfied along with the compatibility conditions in plane strain.

$$\left(\frac{\partial^2}{\partial r^2} + \frac{1}{r}\frac{\partial}{\partial r} + \frac{1}{r^2}\frac{\partial^2}{\partial \theta^2}\right)(\sigma_{rr} + \sigma_{\theta\theta}) = 0 \tag{5-4}$$

The bounded nature of crack tip stresses reduces the compatibility equation to:

$$\frac{\partial^2(\sigma_{rr} + \sigma_{\theta\theta})}{\partial^2 \theta} = 0 \tag{5-5}$$

This equation has a solution in the form:

$$\sigma_{rr} + \sigma_{\theta\theta} = A\theta + B \tag{5-6}$$

Here A and B are constants. Differentiating with respect to θ and combining with equation (5-3b) gives:

$$\frac{\partial \sigma_{rr}}{\partial \theta} - 2\sigma_{r\theta} = A \tag{5-7}$$

Further differentiating this equation with respect to θ and combining with (5-3a) and (5-6) gives

$$\frac{\partial^2 \sigma_{rr}}{2\partial^2 \theta} + 2\sigma_{rr} = A\theta + B \tag{5-8}$$

The solution of this equation is of the form:

$$\sigma_{rr} = C\sin 2\theta + D\cos 2\theta + \frac{A\theta + B}{2} \tag{5-9}$$

Where C and D are constants. The hoop and shear stress can thus be written:

$$\sigma_{\theta\theta} = -C\sin 2\theta - D\cos 2\theta + \frac{A\theta + B}{2} \tag{5-10}$$

$$\sigma_{r\theta} = C\cos 2\theta - D\sin 2\theta + L \tag{5-11}$$

In the present chapter all elastic sectors lie on the crack flanks. The constants A, B and L can therefore be expressed in terms of C and D by using the boundary conditions on the traction free flank, $\theta = \pm\pi$, $\sigma_{r\theta} = \sigma_{\theta\theta} = 0$ and the yield criterion:

$$L = -C,\ A = 4C,\quad B = 2D - 2C\pi \tag{5-12}$$

The stress field within an elastic sector can thus be simplified to:

$$\sigma_{\theta\theta} = C(2\theta - 2\pi - \sin 2\theta) + D(1 - \cos 2\theta) \quad (5\text{-}13a)$$

$$\sigma_{rr} = C(2\theta - 2\pi + \sin 2\theta) + D(1 + \cos 2\theta) \quad (5\text{-}13b)$$

$$\sigma_{r\theta} = C(\cos 2\theta - 1) - D\sin 2\theta \quad (5\text{-}13c)$$

The coefficients C and D can be determined by applying the elastic-plastic boundary conditions $\sigma_{\theta\theta}=H$ and $\sigma_{r\theta}=K$ at $\theta=\pi-\varphi$.

$$C = \frac{H\sin 2\varphi - K(1 - \cos 2\varphi)}{2(1 - \cos 2\varphi - \varphi \sin 2\varphi)} \quad (5\text{-}14a)$$

$$D = \frac{H(1 - \cos 2\varphi) + K(\sin 2\varphi - 2\varphi)}{2(1 - \cos 2\varphi - \varphi \sin 2\varphi)} \quad (5\text{-}14b)$$

5.2.2 *Plastic sectors*

It is now appropriate to consider the form of the deformation within plastic sections at the crack tip. The stresses within the plastic sectors can be conveniently represented by slip line fields as the incompressibility associated with plastic deformation justifies the slip line approach. In the Prandtl field (Figure 3.5), the yield criterion is satisfied at all angles and the crack tip stress distribution can be determined by starting with the boundary condition on the traction free flank ($\theta=\pm\pi$, $\sigma_{r\theta}=\sigma_{\theta\theta}=0$) and moving into the constant stress sector ahead of the crack using the Hencky equations of equilibrum (Hill, 1950). However, for the fields in which plasticity does not fully surround the tip, slip lines can only start or terminate at an elastic and plastic boundary. The stresses in the plastic sectors can, therefore, be expressed in terms of the hoop and shear stresses (H and K) on the elastic-plastic boundary. For the particular case of an elastic sector adjoining a centred fan, the value of K is equal to the yield stress in pure shear k. Thus the analytic solution within a centred fan can be written:

$$\sigma_{\theta\theta} = \sigma_{rr} = \sigma_{zz} = \sigma_m = 2k(\pi - \varphi - \theta) + H \quad (5\text{-}15a)$$

$$\sigma_{r\theta} = k \quad (5\text{-}15b)$$

Within a constant stress sector,

$$\sigma_{\theta\theta} = k\left(\cos 2\theta - 2\varphi + \frac{3}{2}\pi\right) + H \qquad (5\text{-}16a)$$

$$\sigma_{rr} = k\left(-\cos 2\theta - 2\varphi + \frac{3}{2}\pi\right) + H \qquad (5\text{-}16b)$$

$$\sigma_{r\theta} = k \sin 2\theta \qquad (5\text{-}16c)$$

$$\sigma_{zz} = \sigma_m = k\left(\frac{3}{2}\pi - 2\varphi\right) + H \qquad (5\text{-}16d)$$

5.2.3 Assembly of the sectors

The complete asymptotic crack tip field is now determined by assembling the elastic and plastic sectors such that hoop stresses and shear stresses, as well as the hoop displacements are continuous functions of θ. However the equilibrium equations permit a jump in the radial stress. The jump in radial stress can be determined from the allowable two roots of the plane strain yield criterion σ_{rr}^{+} and σ_{rr}^{-} (Shih, 1974).

$$\sigma_{rr}^{+} = \sigma_{\theta\theta} + 2\sqrt{k^2 - \sigma_{r\theta}^2} \qquad (5\text{-}17a)$$

$$\sigma_{rr}^{-} = \sigma_{\theta\theta} - 2\sqrt{k^2 - \sigma_{r\theta}^2} \qquad (5\text{-}17b)$$

The allowable stress discontinuity is therefore:

$$\left(\sigma_{rr}^{+} - \sigma_{rr}^{-}\right) = 4\sqrt{k^2 - \sigma_{r\theta}^2} \qquad (5\text{-}18)$$

For the particular case of a centred fan adjoining an elastic sector, $\sigma_{r\theta} = k$ and there can thus be no jump radial stress, and full continuity of all the stress components is required. Compatibility conditions are satisfied across the boundary as both hoop and radial strains are zero for incompressible deformation in the two types of sector. In this case, the hoop and shear stresses

(*H* and *K*) can be obtained by noting that $\sigma_{r\theta} = k$ and $\sigma_{\theta\theta} = \sigma_{rr}$ on the elastic-centred fan boundary from equations (5-13a) and (5-13b):

$$H = \left| \frac{2\varphi k \cos 2\varphi - k \sin 2\varphi}{1 - \cos 2\varphi} \right| \qquad (5\text{-}19a)$$

$$K = k \qquad (5\text{-}19b)$$

The sectors can now be conveniently assembled by initially selecting a value for the angular span of the elastic wedge, φ. Equations (5-19a~b) define the constants *H* and *K*, which can be used in equations (5-14a~b) to define *C* and *D*. The stresses in the elastic sector are then given by equations (5-13a~c). The stresses in the centred fan are given by equations (5-15a~b), and the constant stress sector by (5-16a~d). These solutions are valid in the range $\pi/4 \geq \varphi \geq 3\pi/4$, outside this range, the yield criterion is violated in any postulated elastic sector.

5.3 Crack tip stress fields in terms of a constraint parameter Q

It is useful to be able to determine the field by assembling the sectors for a given value of the constraint parameter Q, (O'Dowd and Shih, 1991).

$$\sigma_m = \sigma_m^{SSY} + \sqrt{3}kQ \qquad (5\text{-}20)$$

where the superscript SSY denotes the small scale yielding *(T=0)* field. If plasticity surrounds the crack tip, the HRR field describes the nature of the dominant singularity and is the only possible non-trivial field which exhibits full continuity of tractions around the tip. It is therefore an important limiting case of a family of fields which arise when the higher order terms are insignificant. The hoop stress directly ahead of the crack in small scale yielding is $2.83\sigma_o$ while the corresponding HRR value is $2.97\sigma_o$. The small difference allows the small scale yielding field to be approximated by the HRR field:

$$\sigma_m = \sigma_m^{HRR} + \sqrt{3}kQ \qquad (5\text{-}21)$$

The value of Q depends on the elastic wedge angle, and can be determined by combining equations (5-16), (5-19) and (5-21):

$$Q = \left(\frac{\pi}{2} - 1 - \frac{2\varphi - \sin 2\varphi}{1 - \cos 2\varphi} \right) / \sqrt{3} \qquad (5\text{-}22)$$

The complete stress field is then determined for the appropriate elastic wedge angle as already described. Figure 5.2 shows the variation of Q with the elastic wedge angle, φ, in the range $45° \leq \varphi < 135°$. When $\varphi = 45°$, the stress distribution around the crack tip is identical to the fully constrained (HRR) field.

5.4. Finite element solutions

To verify the analytic solutions, a finite element method has been used to obtain numerical solutions. Calculations have been performed in mode I loading with two levels of the T stress, $T=0$ and $T/\sigma_o = -0.443$. The Cartesian displacements, u_i, corresponding to the first two terms of the Williams expression are:

$$u_1 = u_1^K + u_1^T = \left(\frac{r}{2\pi} \right)^{\frac{1}{2}} \frac{K}{2G} \cos\frac{\theta}{2} \left[\eta - 1 + 2\sin^2\left(\frac{\theta}{2}\right) \right] + \frac{1+\eta}{8G} rT\cos\theta \qquad (5\text{-}23a)$$

$$u_2 = u_2^K + u_2^T = \left(\frac{r}{2\pi} \right)^{\frac{1}{2}} \frac{K}{2G} \sin\frac{\theta}{2} \left[\eta + 1 - 2\cos^2\left(\frac{\theta}{2}\right) \right] + \frac{\eta - 3}{8G} rT\sin\theta \qquad (5\text{-}23b)$$

where $\eta = 3\text{-}4\nu$ and G is the shear modulus. K and T are loading parameters established by the far field conditions.

The crack-tip field has been modelled by using the highly focused mesh shown in Figure 3.13. Symmetry allowed the mode I problem to be represented by a symmetric half. The mesh is based on of 24 rings of 24 isoparametric second-order hybrid elements concentric with the crack tip. The crack tip thus consists of 49 initially coincident, but independent nodes. Displacement boundary conditions corresponding to equations (5-23) were applied to the outer

circumference of the mesh corresponding to the nodal displacements associated with mode I and a compressive or zero *T* stress.

The finite element code Abaqus, (1995), was employed to perform all the calculation while Matlab (1995) was used for post processing. The crack tip stress fields with a non-hardening incompressible response were determined by extrapolating the stresses to the tip along radial lines such that the tip was approached asymptotically from different angles. Figures 5.3~4 show the angular variation of the Mises and mean stress. These numerical solutions were interpreted as the slip line fields shown in Figure 5.5. Firstly, the angular span of the elastic sectors was determined from the angular range over which the yield criterion was not satisfied. Secondly the span of the centred fan was determined from the angular range over which the mean stress varied linearly with angle within a plastic sector. Finally the constant stress sector was identified from the region in which the mean stress does not change with angle. The angular variation of each stress component and the Mises stress under mode I with $T=0$ and $-0.443\sigma_o$ are shown in Figure 5.6. These are compared with the analytical solutions and it is clear that there is full agreement between the analytical solutions given by lines and the numerical solutions given as data points.

5.5. Conclusions

Analytic solutions for Mode I fields have been constructed by using slip line solutions for plastic sectors and semi-infinite elastic wedge solutions for elastic sectors for incompressible plane strain deformation. The fields, which exhibit full continuity of tractions, have been verified by numerical calculations based on modified boundary layer formulations. Unlike the HRR fields, these fields do not exhibit plasticity at all angles around the crack tip. The difference between these fields and the HRR fields can be attributed to the effect of higher order terms, which are significant even in small scale yielding ($T=0$). In mode I , the HRR field is identified as the complete Prandtl field, while in small scale yielding the Prandtl field is incomplete.

The loss in constraint depends on the level of the compressive T stress which results in an elastic wedge on the crack flanks. The angular span of the elastic wedge increases as T becomes more negative and corresponds to loss of constraint directly ahead of the crack tip. For a given value of the constraint parameter Q, the span of elastic sector can be determined and the elastic and plastic sectors assembled around the crack tip to give the full analytic solutions. These fields form the basis of a two parameter, constraint based characterisation of mode I fields.

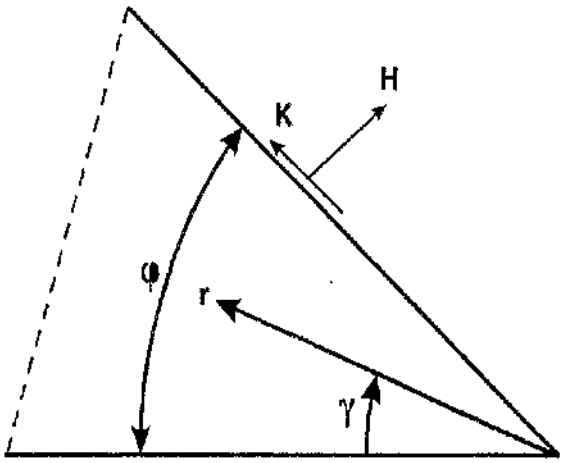

Figure 5.1 Illustration of elastic wedge.

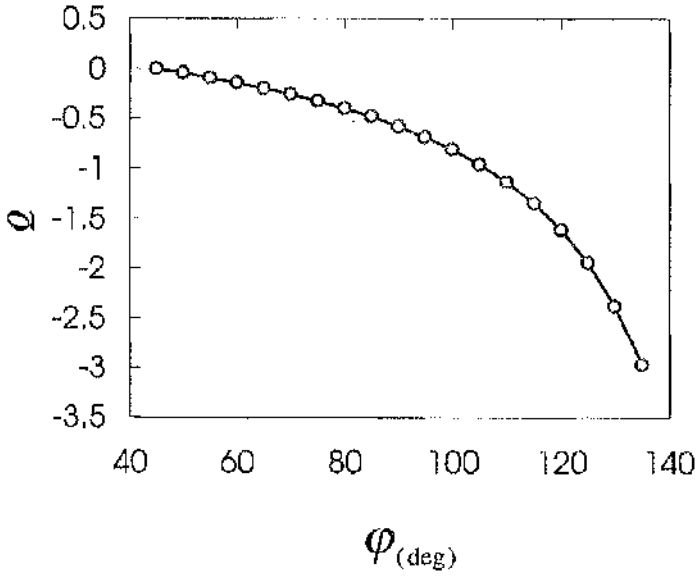

Figure 5.2 Variation of a constraint parameter Q with elastic wedge angle, φ for mode I cracks.

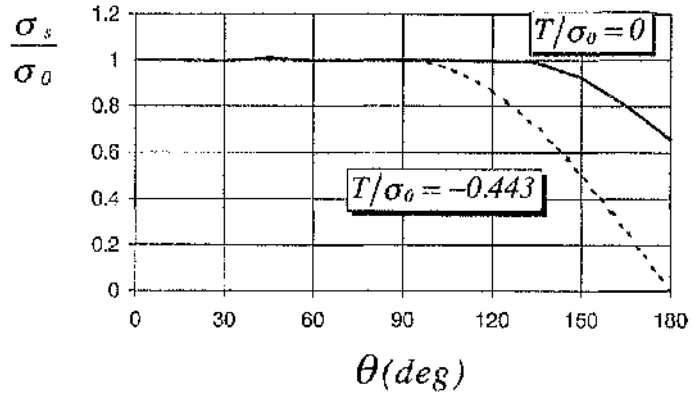

Figure 5.3 Angular variation of Mises stress under mode I with two levels of T stress.

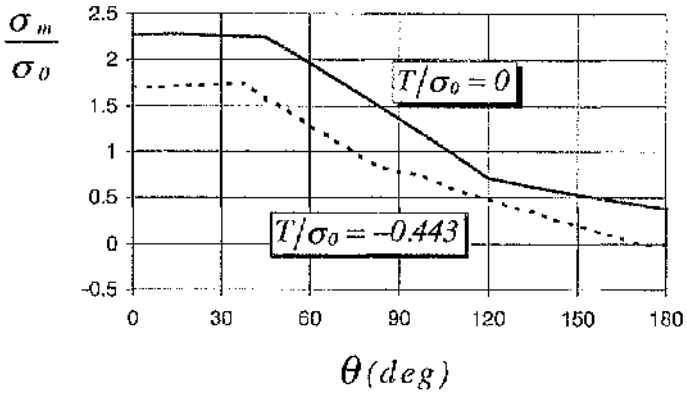

Figure 5.4 Angular variation of mean stress under mode I with two levels of T stress.

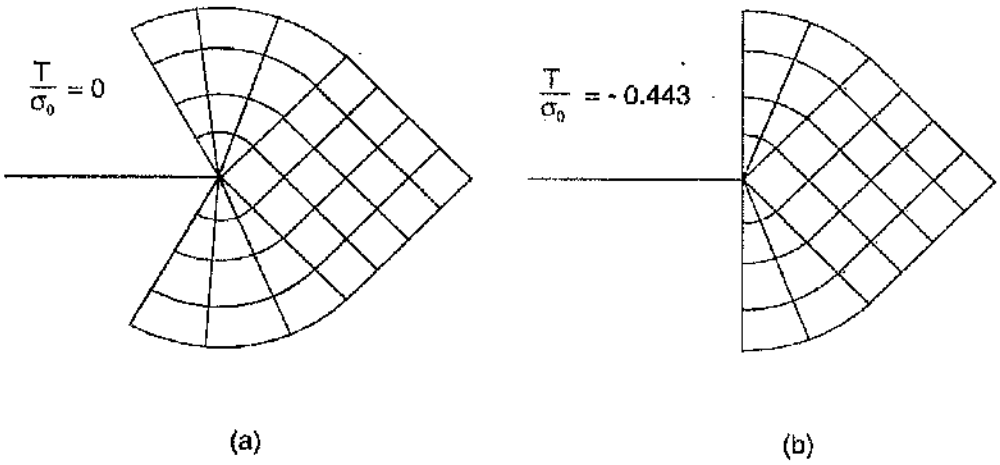

Figure 5.5. Mode I slip line fields.

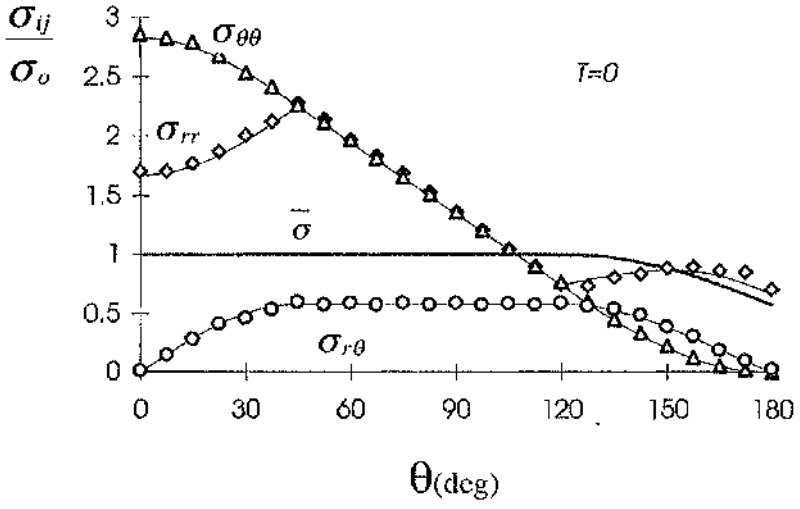

(a)

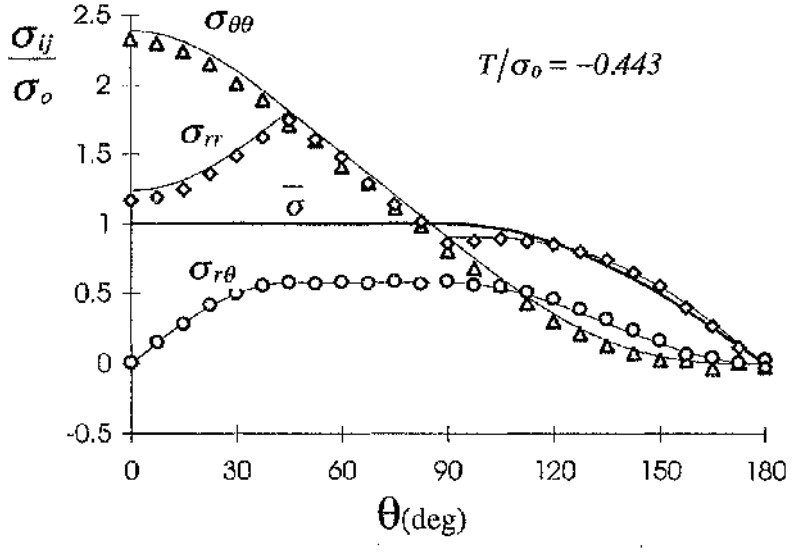

(b)

Figure 5.6. Stress distribution around the crack tip under mode I with two levels c stresses. Marks denote the numerical solutions and lines the analytical solutions.

Chapter 6 Homogeneous crack tip stress fields under mixed mode loading

6.1 Introduction

Plane strain mixed mode I/II fields have been constructed by Shih (1974), on the assumption that plasticity entirely surrounds the crack tip. With the exception of the near mode II fields, the fields require a discontinuity in radial stress in a sector trailing the crack front. In contrast Hancock, Nekkal and Karstensen (1997) have numerically determined fields which differ from those constructed by Shih (1974) in that plasticity does not fully surround the crack tip. With the exception of the fields close to mode II, an elastic wedge appeared on the crack flanks. Following Hancock et al (1997), this chapter will construct the numerical and analytical solutions for the plane strain mixed mode I/II fields with incompressible elastic deformation.

6.2 Numerical solutions

Plane strain small scale yielding calculations have been performed under the five levels of elastic mixity given in Table 6.1. The corresponding boundary conditions have been applied to a full boundary layer formulation mesh shown in Figure 3.13, as the mixed mode problem can not be simplified by symmetry. The mesh, element type and material properties are given in chapter 5. Displacements u_1, u_2, corresponding to stress intensity factors K_I and K_{II} have been applied on the outer boundary of the mesh.

$$u_1 = u_1^{KI} + u_1^{KII} = \left(\frac{r}{2\pi}\right)^{\frac{1}{2}} \frac{1}{2G}\left\{K_I \cos\frac{\theta}{2}\left[\eta - 1 + 2\sin^2\left(\frac{\theta}{2}\right)\right] + K_{II}\sin\frac{\theta}{2}\left[\eta + 1 + 2\cos^2\left(\frac{\theta}{2}\right)\right]\right\}$$

$$u_2 = u_2^{KI} + u_2^{KII} = \left(\frac{r}{2\pi}\right)^{\frac{1}{2}} \frac{1}{2G}\left\{K_I \sin\frac{\theta}{2}\left[\eta + 1 - 2\cos^2\left(\frac{\theta}{2}\right)\right] - K_{II}\cos\frac{\theta}{2}\left[\eta - 1 - 2\sin^2\left(\frac{\theta}{2}\right)\right]\right\}$$

(6-1)

The stress fields at the crack tip were determined by extrapolating the stress to the tip along radial lines such that the tip was approached asymptotically from different angles. Figures 6.1 and 6.2 show the angular variation of the hydrostatic and the Mises stresses under each level of mode mixity. These numerical solutions have been interpreted as slip line fields shown in Figure 6.3 in the way discussed in Chapter 5. These slip line fields are closely similar to those determined by Hancock, Nekkal and Karstensen (1997) for compressible elastic deformation. They can be understood by imagining that the constant stress sector ahead of the crack in mode I loading rotates as the mixed mode loading is applied and the elastic wedge on one crack flank expands.

Table 6.1. Mode mixity for a range of mixed mode problems

	M_{el}	M_p
K_I	1.00	1.00
$K_I = 2K_{II}$	0.71	0.81
$K_I = K_{II}$	0.50	0.69
$K_I = 0.5K_{II}$	0.30	0.50
K_{II}	0.0	0.0

6.3 Analytical solutions of mixed mode crack tip stress fields

Under general mixed mode loadings, the crack tip slip line fields lose the symmetry of pure mode I or mode II loading. The stresses both above and below the line of the crack can be solved starting from the traction free crack flanks. In the lower part, two possible conditions can be identified. In the first, the fully plastic part of the crack comprises a constant stress triangle, a centred fan and part of a constant stress diamond, as illustrated in Figure. 6.4a. In this case, the field is defined by the span of the centred fan, α.

Using the notation of Figure 6.4a the stresses in the constant triangle are,

σ_{rr}=-k(cos2θ+1)

$\sigma_{\theta\theta}$= k(cos2θ+1)

$\sigma_{r\theta}$ =ksin2θ $\quad 180^0 \leq \theta \leq 225^0$ (6-2)

In the centred fan:

$\sigma_{rr} = \sigma_{00} = -2k\theta + k(5\pi/2-1)$

$\sigma_{r\theta} = k$ $\quad 225^0 \leq \theta \leq 225^0+\alpha,\ \alpha \geq 45^0$ (6-3)

In the diamond,

σ_{rr}= k [-cos2(θ - α) - (1+2α)]

$\sigma_{\theta\theta}$= k [cos2(θ - α) - (1+2α)]

$\sigma_{r\theta}$ =ksin2(θ - α) $\quad 225^0+\alpha \leq \theta \leq 360^0,\ \alpha \geq 45^0$

(6-4)

Alternatively for lower values of mixity there may be two centred fans as illustrated in Figure. 6.4b. For complete plasticity in the lower half, the total span of the two fans must be $\pi/4$. Following the slip line to the centred fan directly ahead of the crack, the stress distribution is:

$\sigma_{rr} = \sigma_{\theta\theta} = 2k\theta - k(4\alpha+1+7\pi/2)$

$\sigma_{r\theta} = k$ $\quad 315^0+\alpha \leq \theta \leq 360^0,\ \alpha \leq 45^0$ (6-5)

In the upper half space the field comprises an elastic sector, a centred fan and part of diamond, or a centred fan and an elastic sector. The analytic solutions in the upper half can therefore be obtained in the similar way as for a mode I field. All the sectors can be assembled to give full continuity of tractions (see chapter 5). The analytic solutions for the four levels of mode mixity (except pure mode I case) are shown in Figure 6.5 where they are compared with the finite element solutions and agree perfectly.

6.4 Crack tip stress fields in terms of plastic mode mixity

Under mixed mode loading, comprising combinations of mode I and mode II, the elastic and plastic mixities are in general not identical as shown in Table 6.1. The slip line fields can be also expressed in terms of the plastic mixity by noting that the plastic mixity defines the ratio of hoop to shear stress directly ahead of the crack. This can be determined by following the slip lines from a crack flank to the region directly ahead of the crack within the plastic region. In the lower half space when mode I dominates:

$$M_p = \frac{2}{\pi} tan^{-1}\left(\frac{\cos 2\alpha - 1 - 2\alpha}{-\sin 2\alpha}\right) \qquad \alpha \geq \pi/4 \tag{6-8}$$

and when mode II dominates:

$$M_p = -\frac{2}{\pi} tan^{-1}\left(\frac{\pi}{2} - 4\alpha - 1\right) \qquad \alpha \leq \pi/4 \tag{6-9}$$

In the upper half space in configuration 6.4a, the field is fixed by the span of the elastic sector (φ) and the part span of the diamond in the top side (δ) where $\delta=\alpha-\pi/4$. Thus φ and δ can be expressed in terms of the plastic mixity.

$$M_p = \frac{2}{\pi} tan^{-1}\left\{\frac{\left[\sin 2\delta + 2(\pi - \delta)\right](1 - \cos 2\varphi) - 2\varphi + \sin 2\varphi}{\cos 2\delta(1 - \cos 2\varphi)}\right\} \tag{6.10}$$

For low mixities, such as configuration 6.4b, the field consists of elastic sector and a centred fan ahead of the crack. This geometry is fixed by the span of the elastic sector (φ). The hoop and shear stress directly ahead of the crack can be determined from equation (5-15). Thus the fields in terms of the plastic mixity for low mixities are :

$$M_p = \frac{2}{\pi} tan^{-1}\left(2\pi - \frac{2\varphi - sin\,2\varphi}{1 - cos\,2\varphi}\right) \tag{6-11}$$

6.5 Conclusions

In plane strain mixed mode I/II fields the constant stress sector ahead the mode I *(T=0)* crack rotates with increasing mode II component, and loses constraint. Mixed mode fields except close to mode II, consist of distortions of the mode I field in which the angular span of the crack flank elastic wedge increases with decreasing mixity. Unlike the fields discussed by (Shih 1974), these fields exhibit full continuity of tractions around the crack tip. Close to mode II plasticity surrounds the crack tip, contact is established with the mixed mode HRR fields discussed by Shih (1974) and finally the mode II field originally discussed by Hutchinson (1968b) is recovered. Although analytic solutions for these fields have been assembled, it has not proved the possibility to establish an analytic relation between the inner elastic-plastic field and the outer elastic field, although this relationship has been established computationally.

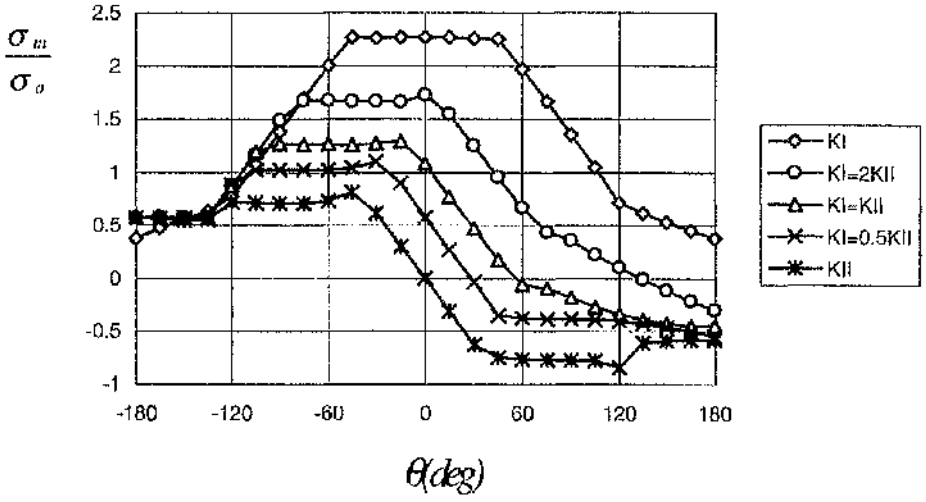

Figure 6.1 Angular variation of mean stress under mixed mode loading.

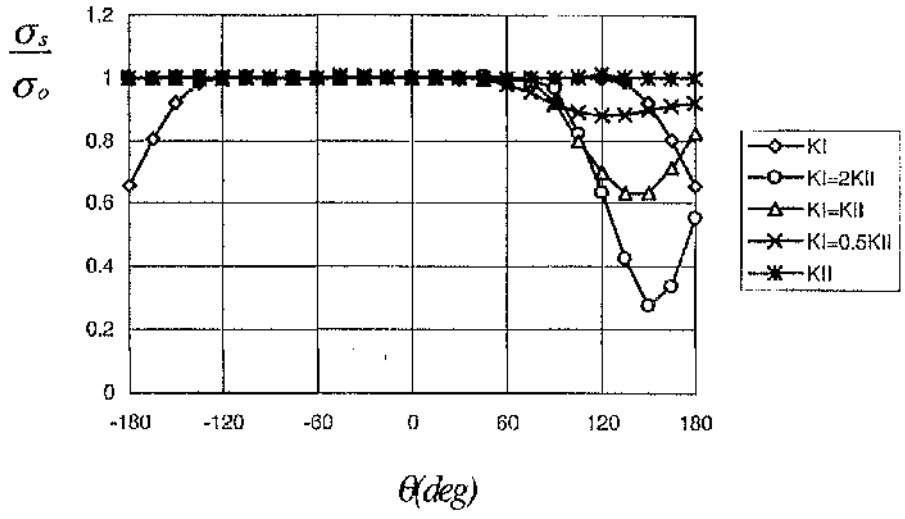

Figure 6.2 Angular variation of Mises stress under mixed mode loading.

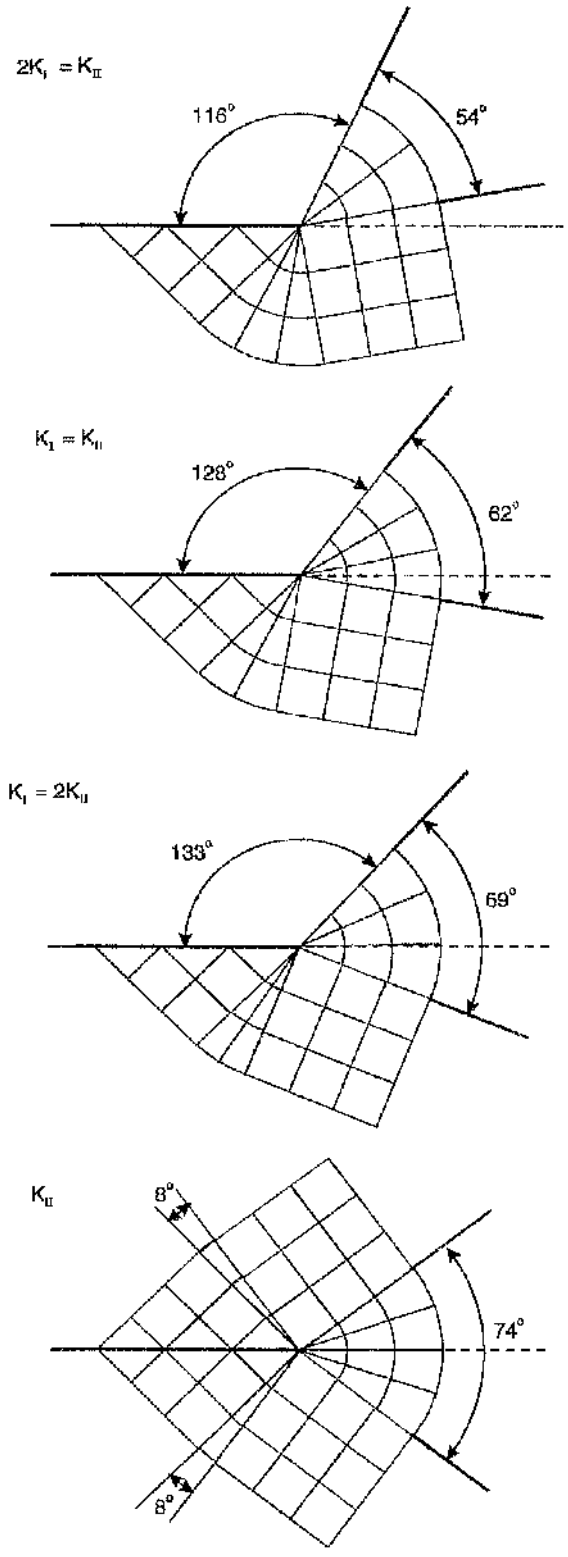

Figure 6.3 Slip line fields under mixed mode loading for a homogeneous material, ν=0.49.

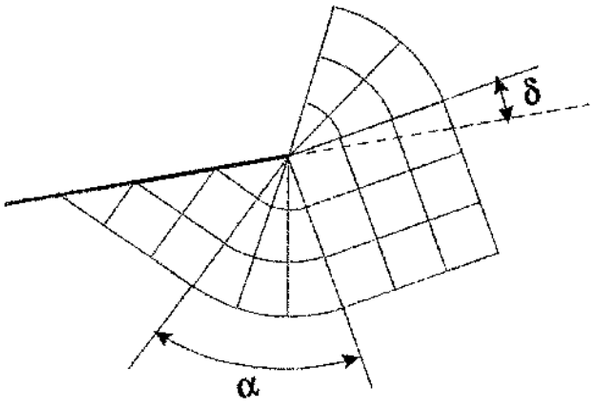

(a)

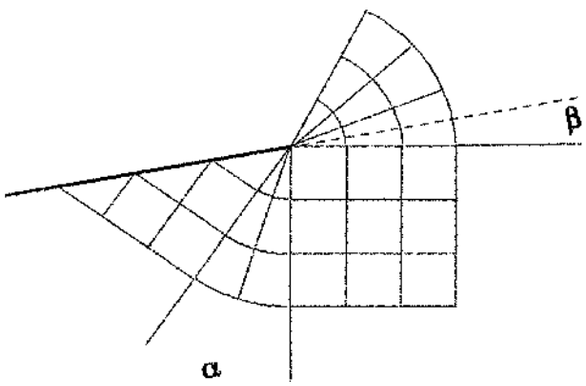

(b)

Figure 6.4 Illustration of mixed mode slip line fields.

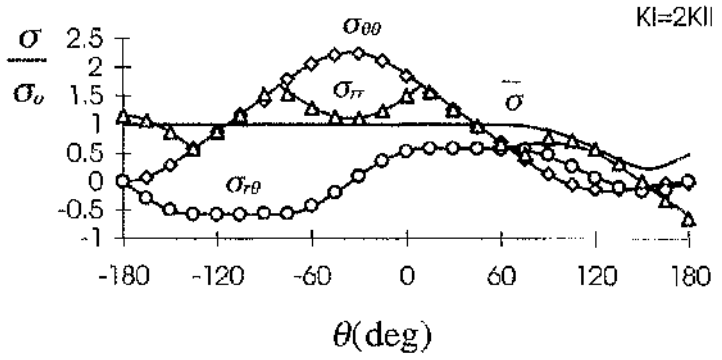

(a)

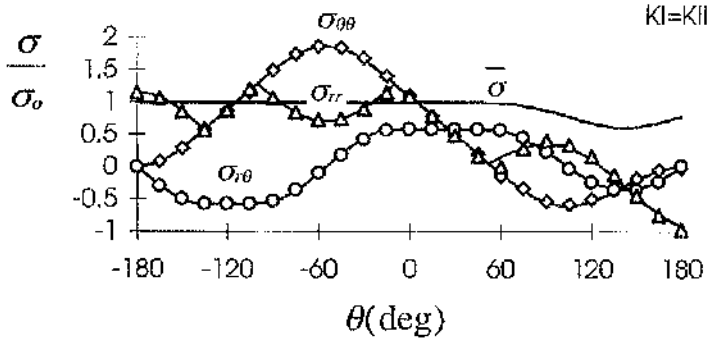

(b)

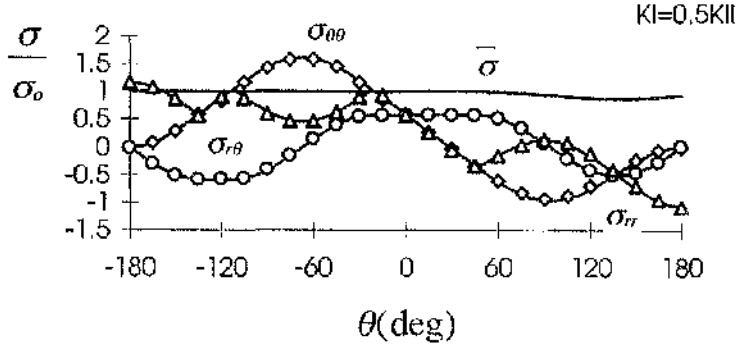

(c)

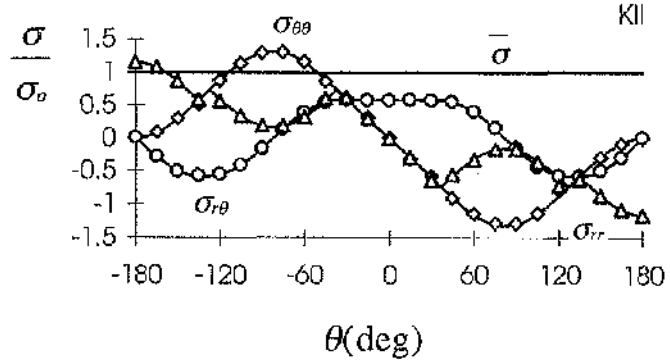

(d)

Figure 6.5 Angular variation of stresses at a homogeneous crack tip under mixed mode loading. Data points refer to the numerical solutions and lines to the analytical solutions.

Chapter 7 Small scale yielding analysis of an interfacial crack on a rigid substrate

7.1 Introduction

The performance of composites is often determined by the integrity of bi-material interfaces. Interface failure by crack propagation is thus particularly important. Recently, attention has focused on the analysis of an interfacial crack lying between an elastic-plastic material and a rigid substrate. On the assumption that plasticity entirely surrounds the crack tip, Quanxin Guo and Keer (1990) and Fang and Bassani (1996) have presented two types of asymptotic near tip stress fields for different ranges of plastic mixity and non-hardening plasticity. It is significant to note that some of these fields feature a discontinuity in radial stress in the constant stress sector.

This chapter addresses the same problem but relaxes the assumption that plasticity fully surrounds the crack tip. Attention is focused on a stationary crack located on the interface between a rigid body in a lower half space and an elastic-plastic matrix in an upper half-space as illustrated schematically in Figure 7.1. As usual in-plane Cartesian co-ordinates x_1 and cylindrical co-ordinates (r,θ) centred at the crack tip are employed. The crack lies on the $-x_1$ axes $(\theta=\pm\pi)$. The matrix is either elastic-perfectly plastic or power law hardening with an incompressible elastic response. Small scale yielding of the upper half space close to the crack tip is examined in plane strain conditions using boundary layer formulations under combinations of mode I and mode II loading. Numerical solutions have been compared with the analytic solutions developed in chapter 5. The relation between the plastic mixity and the configuration of elastic and plastic sections at the tip has been established analytically for non-hardening deformation. The intention is to investigate the hypothesis that mixed mode fields belong to a family of fields which are deviatorically similar but differ mainly

hydrostatically at the angle of maximum hoop stress. In this context, the effect of mode mixity on the interfacial crack tip stress fields has been investigated for strain hardening materials (n=6 and 13). The mixed mode fields have been related to unconstrained mode I J-Q/T fields. Mode I constraint based failure loci have then been used to infer mixed mode failure for stress controlled propagation of interface cracks into the matrix.

7.2 Numerical model

A crack lying on the interface between an elastic-plastic matrix and a rigid substrate (shown in Figure 7.1) is taken to have a perfectly-bonded interface leading to continuity of tractions and displacements between the two media. The rigid substrate assumption simplifies the problem, and is often justified if the two material systems have significantly different yield stresses and elastic moduli. The deformable medium in the upper region is loaded under plane strain conditions and occupies the region $0 \le \theta \le \pi$. The crack face is taken to be open and, therefore, traction free. Consequently, the boundary conditions satisfied by the asymptotic field are:

$$u_r(r,0) = u_\theta(r,0) = 0$$
$$\sigma_{r\theta}(r,\pi) = \sigma_{\theta\theta}(r,\pi) = 0 \qquad (7\text{-}1)$$

Crack tip deformation has been modelled by using the highly focused mesh shown in Figure 7.2. The mesh and the element type are described in detail in Chapter 5. Nodal displacements corresponding mixed mode loading listed in table 7.1 were applied to the outer boundary of the mesh. The nodal displacements on the radial line, θ=0, were completely restrained to model the interface with a rigid substrate.

Table 7.1. Elastic mode mixity for a range of mixed mode problems.

	M_{el}
K_I	1.00
$K_I = \pm 2K_{II}$	±0.71
$K_I = \pm K_{II}$	±0.50
$K_I = \pm 0.5K_{II}$	±0.30
$\pm K_{II}$	0.00

In accord with the procedure described by Tracey (1976), plasticity was only permitted to extend to one hundredth of the radius of the outer boundary of the mesh, corresponding to small-scale yielding conditions. In the calculations the lower rigid region was not explicitly modelled, while the upper region had a ratio of Young's modulus to uniaxial tensile yield stress of 1000 and a Poisson's ratio of 0.49 to give an almost incompressible response.

7.3 Non-hardening materials

For an interfacial crack lying between a rigid substrate and an elastic-plastic deformable material, the symmetry of homogeneous deformation field is lost, and the fields depend on the sense of the applied shear stresses. As an example, consider a crack in a homogeneous material under an arbitrary mixed mode loading, K_I and K_{II}, for which $K_I > 0$ and $K_{II} > 0$. The solution for the problem in which $K_I > 0$ and $K_{II} < 0$ can be obtained by inverting the field about the crack plane. For this reason it is not necessary to present solutions to homogeneous mixed mode problems for $K_I > 0$ and $K_{II} < 0$. However, for interfacial crack problems, these problems are distinct and must be solved

separately. In this chapter, positive shear is defined such that the elastic-plastic deformable material shears towards the interface ($K_{II} > 0$) while negative shear that the elastic-plastic deformable material shears towards the crack flanks ($K_{II} < 0$).

7.3.1 Positive mixities

The size and shape of the plastic zones developed at the interfacial crack tip under positive mode mixities are illustrated in Figure 7.3-(a) for a non-hardening material. Mode II loading enlarges the maximum radius of the plastic zone and causes the plastic lobes to swing ahead of the crack. Figure 7.4 shows the displaced models in an exaggerated form under five levels of mixity.

In order to describe the crack tip stress field, the hydrostatic and Mises stresses have been extrapolated to the tip along radial lines at 15-degree intervals, ignoring data within a radial distance of $2J/\sigma_o$. Figure 7.5 illustrates the angular variation of the hydrostatic stress non-dimensionalised by the uniaxial yield stress, σ_0, under the five levels of mode mixity shown in Table 7.1. These mixities correspond to an opening tensile K_I component and a positive K_{II} component. As the contribution from the remote positive shear increases, the near tip hydrostatic stresses changes from tensile to being slightly compressive in the limit, $M_{el}= 0$. The maximum tensile and hydrostatic stresses occur directly ahead of the interfacial crack, suggesting that stress controlled failure will occur along the interface. The angular extent of yield at the tip under each level of elastic mixity is shown in Figure 7.6. Ahead of the crack, plasticity limits the Mises stress to the yield stress, σ_0, for all mixities. It is, however, significant to note that the near tip material does not yield all angles around the tip.

The slip line fields constructed from Figures 7.5~6 are shown in Figure 7.7. The elastic sector has been identified by the angular range over which the yield criterion is not satisfied. The angular span of the centred fan is determined from the range in which the hydrostatic stress varies linearly with angle within a

plastically deforming region. The constant stress sector is identified as the angular range in which the mean stress does not change with the angle within a plastic region. The complete fields are assembled in such a way that the continuity of hoop and shear stresses and the boundary conditions are met. The slip line fields for the first four levels of mixity thus comprise a centred fan ahead of the crack and an elastic sector extending to the crack flank. The angular span of the centred fan decreases and swings ahead of the crack as the contribution from mode II increases.

For stress controlled brittle fracture, the crack extends in the maximum principal stress direction (Erdogan and Sih (1963), Williams and Ewing (1972) and Budden (1987). For the first four levels of mode mixity, the maximum principal stress occurs on the interface directly ahead of the crack. This stress can be used to establish local failure criteria. Figure 7.8 shows the radial variation of the maximum principal stress directly ahead of the crack and at 30° degrees to the crack plane under five levels of mode mixity. It may be noted that all the stress profiles are very weakly dependent on radius, r. Since the deviatoric stress for incompressible deformation under plane strain and non-hardening conditions is necessarily equal to the yield stress in pure shear, k, within the plastic zone, these stress profiles can only differ by a hydrostatic term. As expected, the stress level directly ahead of the crack is higher than that at 30° degrees under all mixities.

To verify the numerical solutions, corresponding analytic solutions have been developed in chapter 5. Figure 7.9 shows the angular variation of each of the stress components under the first four levels of positive mixity. The numerical solutions, given by data points, match the analytic solutions, given by lines, perfectly.

7.3.2 Negative mixities

When a remote tensile mode I ($K_I > 0$) field and negative shear stresses ($K_{II} < 0$) are applied, the form of crack tip field is fundamentally different from that under positive shear stresses. To understand the difference, calculations under the levels of mixity shown in table 7.1 have been performed. Figure 7.10 illustrates angular variation of the hydrostatic stress. Because the hydrostatic stress decreases as the contribution from mode II increases, the role of mode II is to decrease the constraint at the crack tip. The angular variation of the Mises stress is shown in Figure 7.11 which indicates that the yield criterion is not satisfied in front of the crack tip under near mode I loading. Plasticity, however, develops all angles around the crack tip as the negative shear stress starts to dominate the mixity.

The slip line fields under four levels of negative mode mixity were determined from Figures 7.10~11 in the way described in section 7.3.1. The fields are illustrated in Figure 7.12. When Mode I dominates the mode mixity, an elastic sector emerges in front of the crack tip. But at K_I=-K_{II}, the yield criterion is satisfied at all angles around the crack tip. This then permits only two types of sectors: a constant stress sector and a centred fan. The slip line fields shown in 7.12(b, c, and d) are therefore simple distortions of the mode II field corresponding to a rotation of the main constant stress sector which swings ahead of the crack tip as the contribution from negative mode II decreases. The plane of the maximum principal stress is oriented diagonally through the centre of the constant stress diamond. This plane is located in the matrix and rotates towards the crack flank as the contribution from mode II increases. This implies that failure may occur in the matrix rather than along the interface, if the interface is strongly bonded. Figure 7.13 shows the hoop and deviatoric stresses on the planes of maximum principal stresses for the last three mode mixities given in Table 7.1. The deviatoric stress for non-hardening incompressible deformation within the plastic zone is necessarily equal to the yield stress in pure shear and the fields are thus only hydrostatically different.

For stress controlled fracture, this feature is very important and will be highlighted in section 7.3.4.

7.3.3. Families of near tip stress fields

For positive mixities, the crack tip stress fields comprise an elastic sector and a centred fan except in the pure mode II case. The hoop and shear stress directly ahead of the crack can be obtained by combining equations (5-15) and (5-19)

$$\sigma_{00(\theta=0)} = \frac{\sin 2\varphi - 2\pi\cos 2\varphi + 2(\pi-\varphi)}{(1-\cos 2\varphi)} k \qquad (7\text{-}2)$$

$$\sigma_{r\theta} = k \qquad 45° < \varphi < 135°. \qquad (7\text{-}3)$$

Where φ is the span of elastic sector as shown in Figure 5.1. The plastic mixity can thus be expressed as

$$M_p = \frac{2}{\pi}\tan^{-1}\left(\frac{\sin 2\varphi - 2\pi\cos 2\varphi + 2(\pi-\varphi)}{(1-\cos 2\varphi)}\right) \qquad 45° < \varphi < 135°. \qquad (7\text{-}4)$$

The critical elastic wedge angle, φ or the span of the centred fan β ($\beta=\pi-\varphi$) shown in Figure 7.14 is only functions of the plastic mode mixity, M_p. This analytic solution therefore gives a continuous family of crack tip fields for a range of loading between pure mode I and positive shear with some tension, ($0.8897 \geq M_p \geq 0.3302$). Outside these bounds, the yield criterion is violated in any postulated elastic sector. Figure 7.15 shows variation of the plastic mode mixity M_p at the tip with the angular span of the centred fan β. This relation is also compared with that given by Fang and Bassani (1996) where plasticity is assumed to fully surround the interfacial crack tip with a stress discontinuity in σ_{rr}. The present solutions merge with Fang's solutions for $\beta = 45°$ and $135°$.

For negative mode mixities, the angular span of the centred fan ahead of the crack tip shown in Figure 7.16 is denoted δ. This angle depends on the mixity level and increases with the contribution from negative mode II (see Figure 7.12). The stresses in the constant stress diamond and the centred fan directly ahead of crack can be derived from the boundary condition on the traction free crack flank. Using a cylindrical co-ordinates (r, θ) centred at the crack tip, the stress fields within a constant stress diamond can then be written as:

$$\sigma_{\theta\theta} = k\left(\frac{\pi}{2} + 1 + \sin(2\theta - 2\delta) - 2\delta\right) \qquad (7\text{-}5a)$$

$$\sigma_{rr} = k\left(\frac{\pi}{2} + 1 - \sin(2\theta - 2\delta) - 2\delta\right) \qquad (7\text{-}5b)$$

$$\sigma_{r\theta} = k(\cos(2\theta - 2\delta)) \qquad (7\text{-}5c)$$

$$\sigma_{zz} = \sigma_m = k\left(\frac{\pi}{2} + 1 - 2\delta\right) \qquad (7\text{-}5d)$$

In the centred fan directly ahead of crack, the field becomes:

$$\sigma_{\theta\theta} = \sigma_{rr} = \sigma_{zz} = \sigma_m = k\left(2\theta + \frac{\pi}{2} + 1 - 4\delta\right) \qquad (7\text{-}6a)$$

$$\sigma_{r\theta} = k \qquad (7\text{-}6b)$$

The relation between the angle, δ, and plastic mode mixity, M_p, can be written as

$$\delta = \frac{2 + \pi + 2\tan\left(\frac{\pi M_p}{2}\right)}{8} \qquad 0 \le \delta \le 45° \qquad (7\text{-}7)$$

This gives another family of fields in the range $-0.764 \le M_p \le 0.330$. The difference between the two one parameter family of crack stress fields and those presented by Quanxin Guo and Keer (1990) and Fang and Bassani (1996)

derives from the fact that the present analysis was not limited by the assumption that plasticity fully surrounds the crack tip.

7.3.4 Crack tip stress fields unified by constraint

In the case of non hardening plasticity, the stress fields within the plastic zone only differ by a hydrostatic term. The family of fields under negative mode mixities is therefore deviatorically similar but hydrostatically different, allowing parameterisation by a constraint parameter, such as Q.

Equations (5-20) and (5-21) allow the hydrostatic stress in the constant stress diamond to be written in terms of the fully constrained Prandtl field.

$$\sigma_m = (\pi + 1)k + Q\sigma_o \qquad (7\text{-}8)$$

Constraint characterisation of mode I and mixed mode crack tip fields for homogeneous materials has been investigated by Hancock and co-workers (1997). Figure 3.22 shows the slip line fields for a range of mixed mode problems. The direction of crack propagation has been identified with the plane of maximum hoop stress (Erdogan and Sih (1963), Williams and Ewing (1972) and Budden (1987) which occurs at an inclined angle, such that the propagating crack grows locally in Mode I. In interfacial crack problems, the mixed mode fields dominated by shear ($K_{II} \geq K_I$) exhibit a centred fan ahead of the crack. Directly ahead of the crack (θ=0) the displacements (u, v) must be zero as the slip lines are lines of zero extension rate. There are also the boundary conditions required on a rigid interface. The result is that the homogeneous mixed mode fields can be mapped onto the corresponding rigid interface problem. If the homogenous crack tip stress field is divided into two parts along the crack as illustrated in Figure 7.17, the top part is identical to the corresponding rigid interfacial crack tip stress field under mode I with positive shear while the bottom part to the corresponding rigid interfacial crack tip stress

field under mode I with negative shear. This produces a connection between the constraint of homogeneous mixed mode fields and the constraint of interfacial crack problem under mixed mode loading. The failure criteria based on *J*-Q locus for homogeneous material can therefore be used for bi-material provided the interfacial crack propagates into matrix under mainly negative shear loading.

Using the homogenous HRR field as the reference state, the stress fields can be expressed in terms of the constraint parameter Q for the constant stress diamond:

$$\sigma_{\theta\theta} = k\left(\pi + 1 + \cos 2\theta + \sqrt{3}Q\right) \quad (7\text{-}9a)$$

$$\sigma_{rr} = k\left(\pi + 1 - \cos(2\theta) + \sqrt{3}Q\right) \quad (7\text{-}9b)$$

$$\sigma_{zz} = \sigma_m = k\left(\pi + 1 + \sqrt{3}Q\right) \quad (7\text{-}9c)$$

$$\sigma_{r\theta} = k\sin(\sqrt{3}Q + 2\theta) \quad (7\text{-}9d)$$

In the centred fan directly ahead of crack, the field becomes:

$$\sigma_{\theta\theta} = \sigma_{rr} = \sigma_{zz} = \sigma_m = k\left(2\theta + \frac{3\pi}{2} + 1 + 2\sqrt{3}Q\right) \quad (7\text{-}10a)$$

$$\sigma_{r\theta} = k \quad (7\text{-}10b)$$

Q can be obtained by equating (7-9c) and 7-5d):

$$Q = -\frac{\pi + 4\delta}{2\sqrt{3}} \qquad 0 \le \delta \le 45^{\circ} \quad (7\text{-}11)$$

Where δ is a function of plastic mode mixity, M_p, shown in equation (7-7). Figure 7.18 shows the variation of constraint, Q, with negative plastic mixity, M_p. For any given value of plastic mixity in the range of $-0.7566 \le M_p \le 0.3302$ or constraint parameter in the range $-1.0774 \le Q \le -0.5774$, the interfacial crack tip

field under mainly mode II loading is defined. Mixed mode loading can therefore be regarded as a mechanism leading to loss of in-plane constraint. The loss of constraint, Q, and the plastic mode mixity, M_p, can be correlated in equations (7-7) and (7-11) for non hardening deformation. It may be noted that the angular variation of M_p (equations (6-9) and (7-7)) and the definition of Q for the homogenous material and the bi-material are the same. Consequently, if the material have weak or moderate strain hardening response, it is possible to map the constraint based Mode I failure loci into plastic mixity for interfacial crack problems provided the interface is strongly bonded and the crack propagates locally in Mode I into the matrix.

7.4. Power-law hardening materials

The deformation fields of power-law hardening materials necessarily interpolate between linear elastic materials and those which exhibit a non-hardening response. This leads naturally to the concept that structural materials with low and moderate hardening rates develop deformation fields which share many non-hardening features. The present section develops this theme in the context of elastic-plastic fracture mechanics. Kinematically similar fields which differ only through a hydrostatic stress term have been identified for non-hardening materials. To investigate the possibility of a constraint based characterisation, these crack tip stress fields are re-examined with strain hardening. Numerical calculations were performed under the five levels of elastic mode mixity given in table 7.1 with strain hardening exponents, n=13 and 6. In uniaxial tension the material has an isotropic elastic response for stresses less than the uniaxial yield stress, σ_0. Yield is determined by the von Mises yield criterion and plastic deformation occurs following an associated flow rule. In Abaqus (1994), the yield surface is defined by giving the value of the uniaxial yield stress as a function of the equivalent plastic strain in the form:

$$\varepsilon = \sigma / E \quad , \qquad \sigma \leq \sigma_o$$

$$\frac{\varepsilon}{\varepsilon_o} = \left(\frac{\sigma}{\sigma_o}\right)^n \quad , \qquad \sigma \geq \sigma_o$$

$$\varepsilon = \varepsilon_p + \varepsilon_o \qquad (7\text{-}12)$$

where ε_p is plastic strain component, σ_o and ε_o*(=0.001)* are the uniaxial stress and strain at initial yield, while *n* is the hardening exponent. Figure 7.19 shows the stress-strain relation for both hardening and non-hardening materials.

The size and shape of plastic zones at the crack tip for the hardening materials are shown in Figures 7.3b~c. The plastic zones for both hardening and non-hardening materials have similar shapes when the applied elastic mixities are the same and plastic zone radius increases with the contribution from mode II. As the hardening exponent (n) decreases, the size of the plastic zone decreases and tends to develop in the crack wake.

To understand the role of mixity, the radial variation of the maximum principal stress and the corresponding deviatoric stress for *n=13* and *n=6* have been examined on the plane of maximum principal stress for both positive and negative mode mixities. For positive mode mixity, the maximum principal stresses occur directly on the interface ahead of the crack. Figures 7.20~21 show the radial variation of the maximum principal stress (σ_1) and the corresponding deviatoric stress (σ_s) at these planes under five levels of positive mode mixity for strain hardening exponents n=13 and n=6. These stresses are non-dimensionalised with respect to the uniaxial yield stress, σ_o, while the radial distance from the crack tip is non-dimensionalised by $\frac{K_I^2 + K_{II}^2}{2E\sigma_o}$. It may be noted that the stress profiles for all mixities vary weakly with radial distance and hardening exponent at distances greater than $r/\frac{K_I^2 + K_{II}^2}{2E\sigma_o}$ = 2, which is the

approximate distance over which crack tip blunting and finite geometry changes affects the fields. Comparing Figures 7.20 and 7.21, it is clear that the effects of mixity on the deviatoric stress is weak, especially for the weakly hardening material (n=13). The stresses close to the crack tip can therefore be regarded as a family of fields, which are deviatorically similar but differ mainly hydrostatically.

For negative mode mixities (*n=6* and *13*), the plane of maximum principal stress is close to the orientation for the corresponding non-hardening material. The plane rotates clockwise as the mode II component increases. Figures 7.22~23 illustrate the radial variation of the maximum principal stress (σ_1) and the corresponding deviatoric stress (σ_s) for the two hardening rates. As with the field which develops under positive mode mixities, the crack tip stresses differ mainly by a hydrostatic term for both strong and weak hardening materials. On this basis the constraint of mode I fields parameterised by Q can be correlated with the constraint of mixed mode fields parameterised by elastic mixity, as shown in Figure 7.24 which is compared with homogenous case given by Hancock and co-workers, 1997 for *n=13*. The fracture resistance of these configurations can thus be unified by a single constraint based fracture toughness locus.

7.5 Stress distribution in the rigid substrate

The stress distribution within the rigid substrate in the lower half of an interfacial crack can be solved by using a solution for a semi-infinite elastic body in plane strain loaded by constant shear and pressure as shown in Figure 7.25, (Nadai, 1963). The crack face occupies negative -x axis and the interface positive x axis. The boundary conditions on the plane *y=0*, α=0, $\sigma_t = \tau_{rt} = 0$ and $\alpha=\pi$, σ_t=*p*=constant in Figure 7.25(a) and $\tau_{rt}=\tau$ in Figure 7.25(b). By superposing the two distributions, the stress components can be written as

$$\sigma_x = \frac{p}{2\pi}(2\alpha + sin\,2\alpha) - \frac{\tau}{\pi}(2\,lnr + sin^2\alpha)$$

$$\sigma_y = \frac{p}{2\pi}(2\alpha - sin\,2\alpha) + \frac{\tau}{\pi}sin^2\alpha$$

$$\sigma_{xy} = -\frac{p}{2\pi}(1-\cos 2\alpha) - \frac{\tau}{\pi}(\alpha + \sin\alpha\cos\alpha) \qquad (7\text{-}13)$$

On the interface, $\alpha=\pi$, there is a continuity in hoop and shear stresses but discontinuity in radial stress which is weakly singular due to the logarithmic dependence on the radius, r.

7.6 Conclusions

Mixed mode solutions have been developed for elastic/plastic incompressible material and allow the characterisation of the crack tip fields of an interfacial crack under small scale yielding conditions. In contrast with the analyses of Fang and Bassani (1996), the current analysis does not require the assumption that plasticity fully surrounds the crack tip and satisfies continuity of stress components except across the interface. For a non-hardening material, this leads to incomplete crack tip plasticity: an elastic wedge emerges on the crack flanks under positive mode mixities except those near mode II and directly ahead of crack under mainly mode I with negative shear. The span of the centred fan under positive mode mixities decreases with the increased contribution from applied mode II loading but the maximum principal stress directions all occur on the interface directly ahead of crack. The analytical solutions agree well with numerical solutions.

Under negative mode mixities, the maximum hoop stresses are located within the matrix and the orientation of the relative plane swings to the flank of the crack as the contribution from mode II increases. This leads to the possibility of crack propagating into matrix rather than along the interface under negative mode mixities except those close to mode I. For hardening materials the stress fields can be regarded as a family of fields which are deviatorically similar but

differ mainly hydrostatically for weakly hardening material under positive mode mixities but for both strong and weak hardening materials under negative mode mixities. The fracture resistance of these configurations can thus be unified by a single constraint based fracture toughness locus.

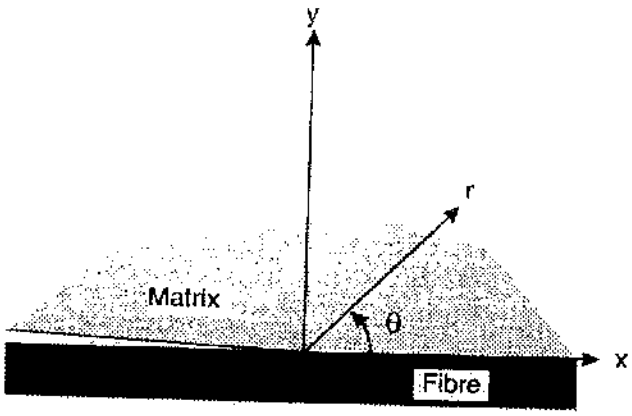

Figure 7.1 Schematic of the crack tip region.

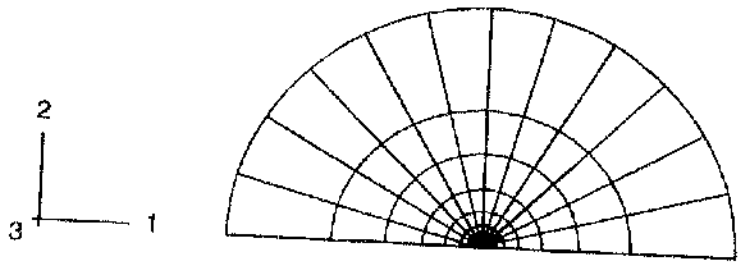

Figure 7.2 Focused mesh.

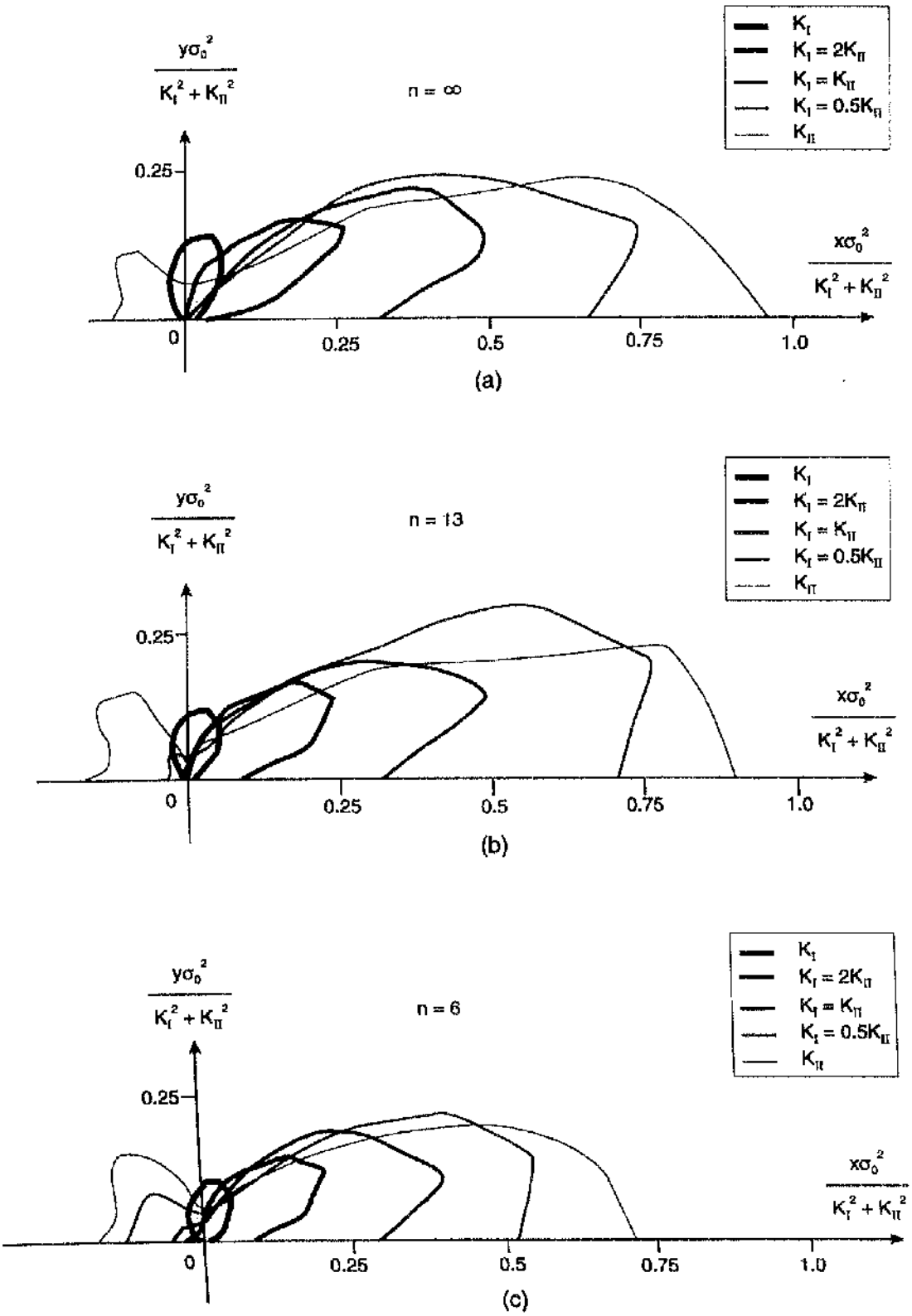

Figure 7.3 Plastic zones for the family of mixed mode problems.

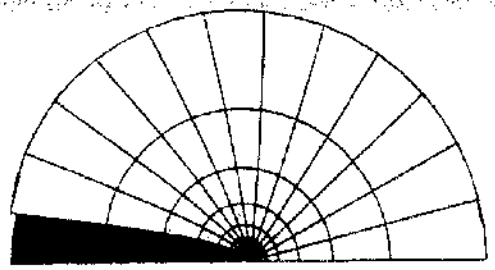

$K_I = 2K_{II}$

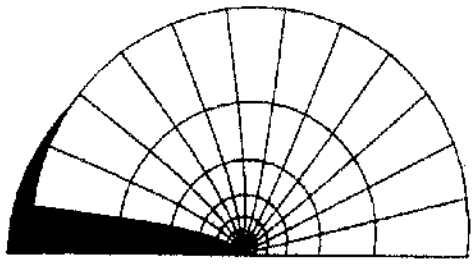

$K_I = K_{II}$

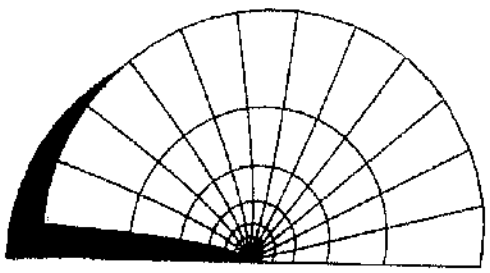

$K_I = 0.5K_{II}$

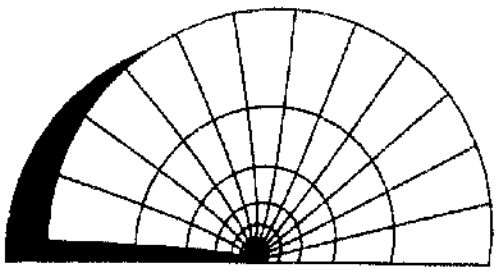

K_{II}

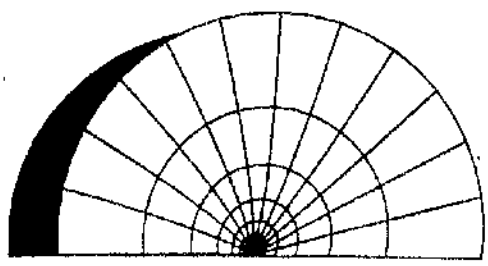

Figure 7.4 Displaced models for mixed mode problems.

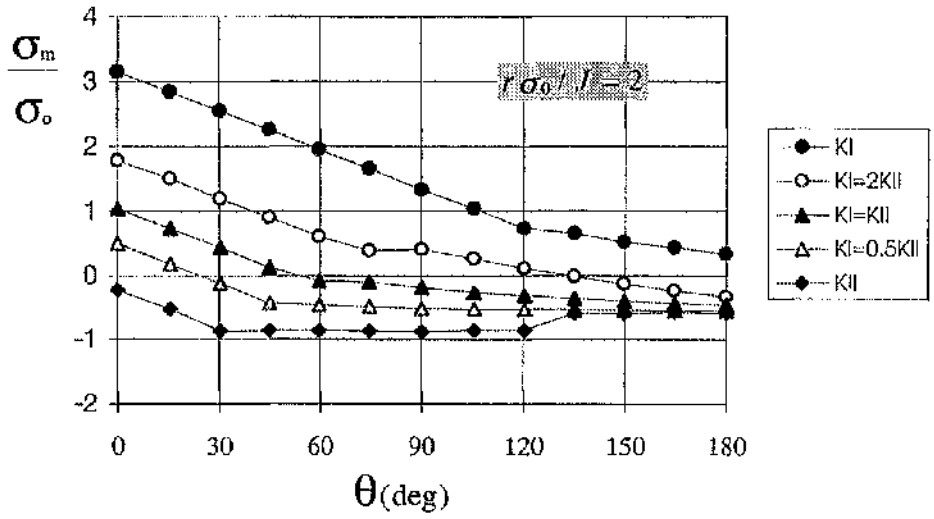

Figure.7.5 Angular variation of mean stress non-dimensionalised by the yield stress for a range of applied elastic mode mixities, non-hardening material.

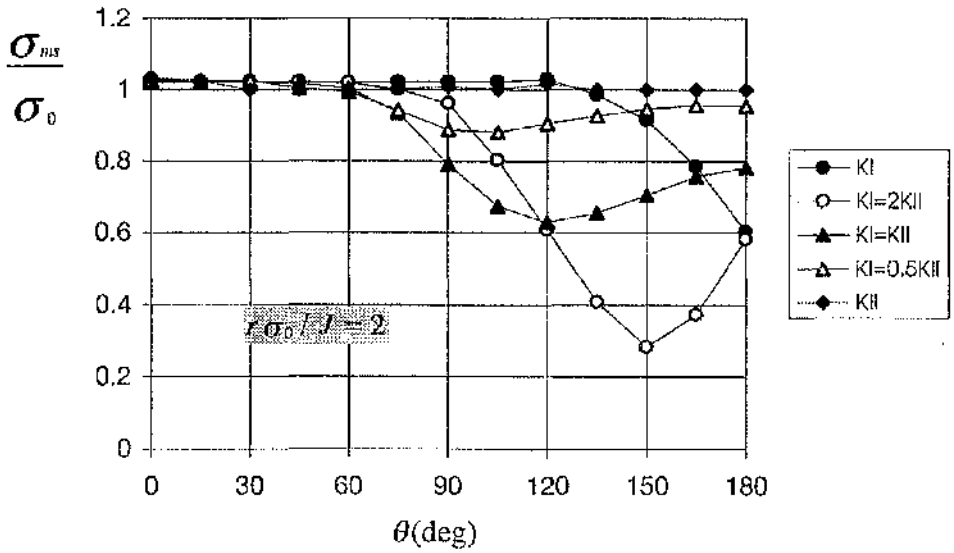

Figure 7.6 Angular variation of the Mises stress non-dimensionalised by the yield stress for a range of applied elastic mode mixities, non-hardening material.

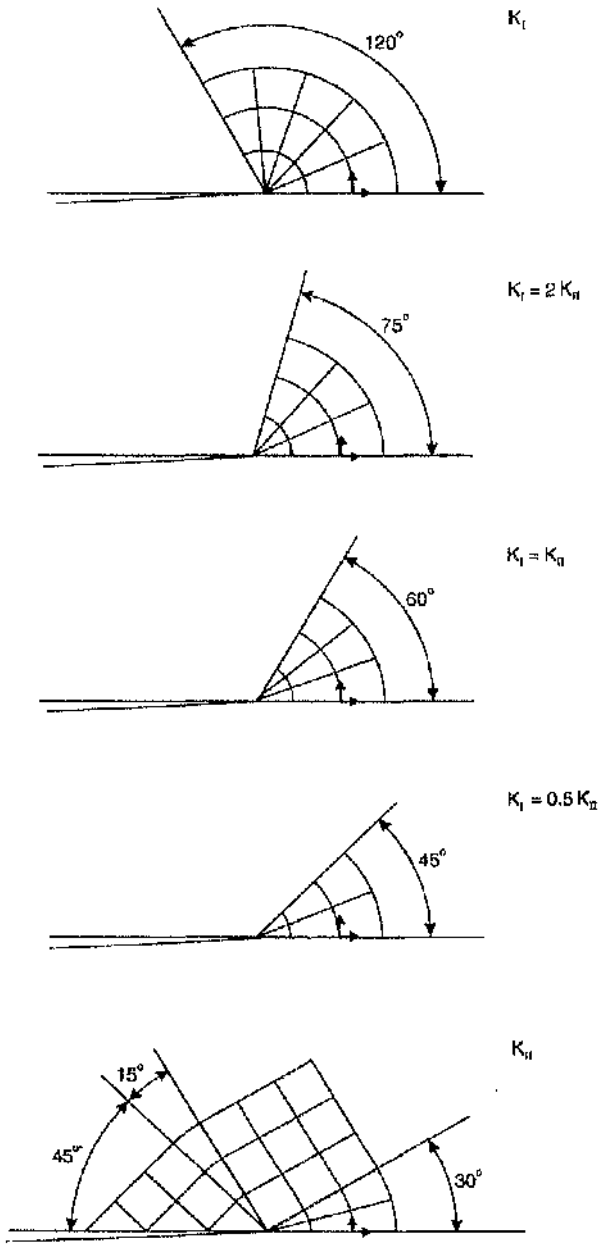

Figure 7.7 Slip line fields under five levels of positive mode mixity.

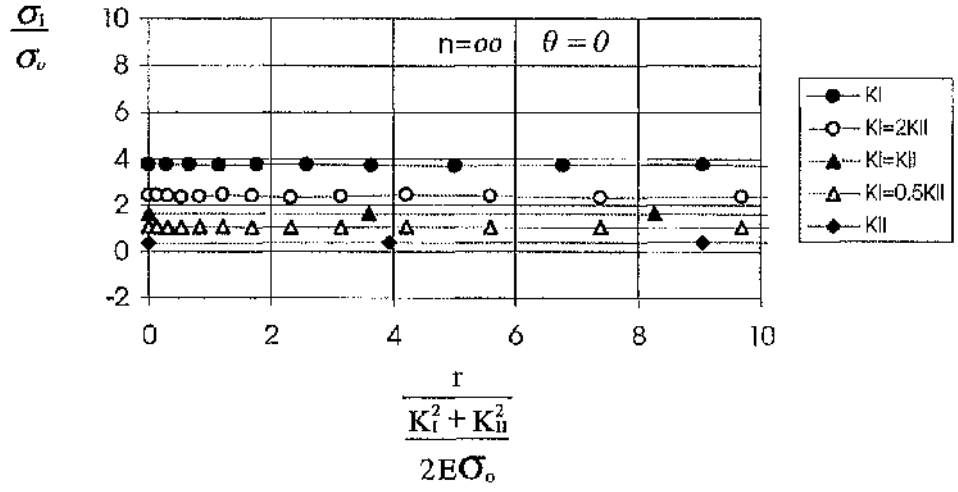

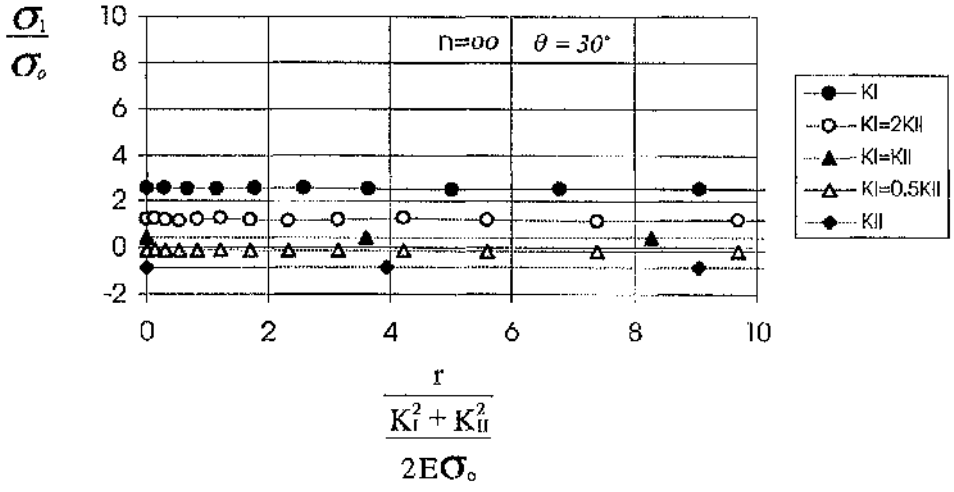

Figure 7.8 Radial variation of maximum principal stresses directly ahead of crack and at 30 degrees.

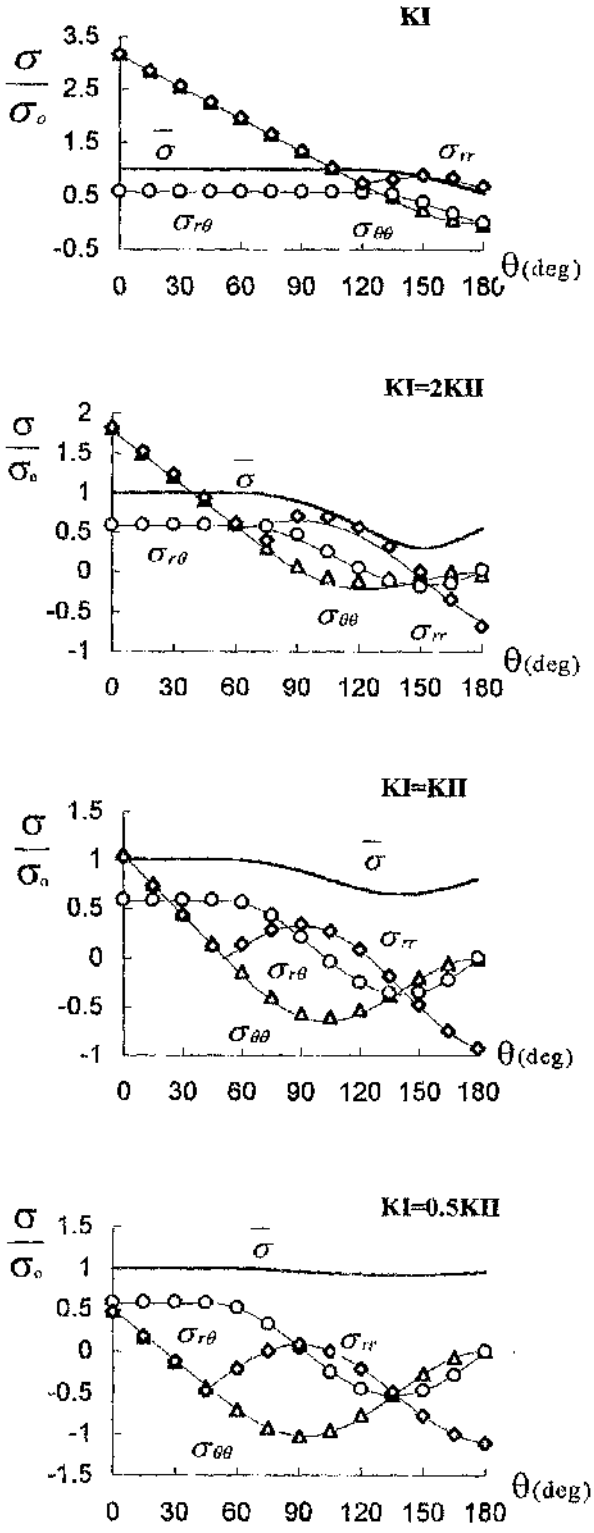

Figure 7.9 Stress distribution at an interfacial crack tip. Data points refer to the finite element solutions and lines to the analytical solutions.

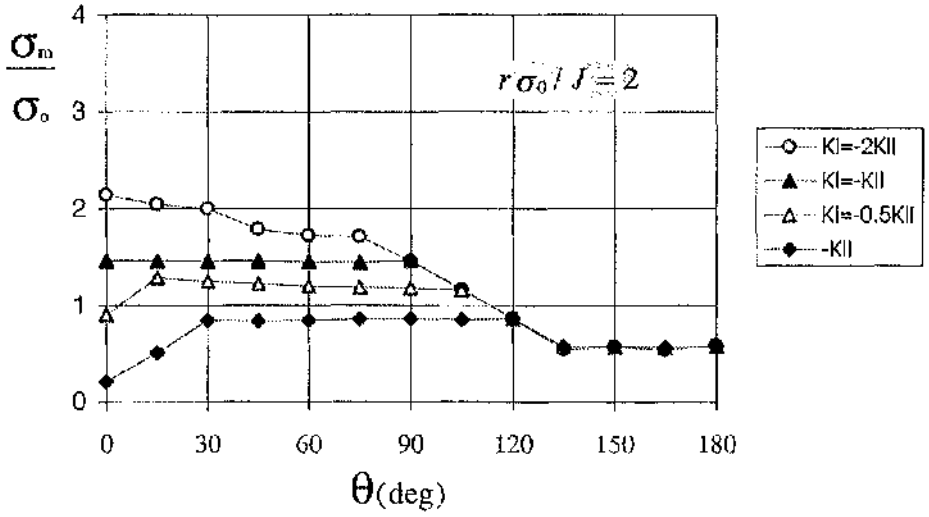

Figure 7.10 Angular variation of mean stress non-dimensionalised by the yield stress for a range of applied negative mode mixities, non-hardening material.

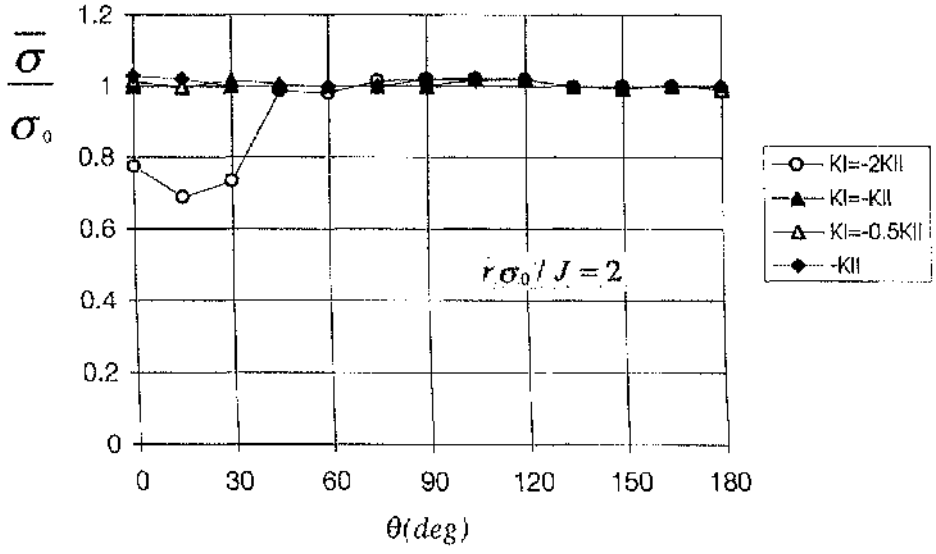

Figure 7.11 Angular variation of Mises stress non-dimensionalised by the yield stress for a range of applied negative mode mixities, non-hardening material.

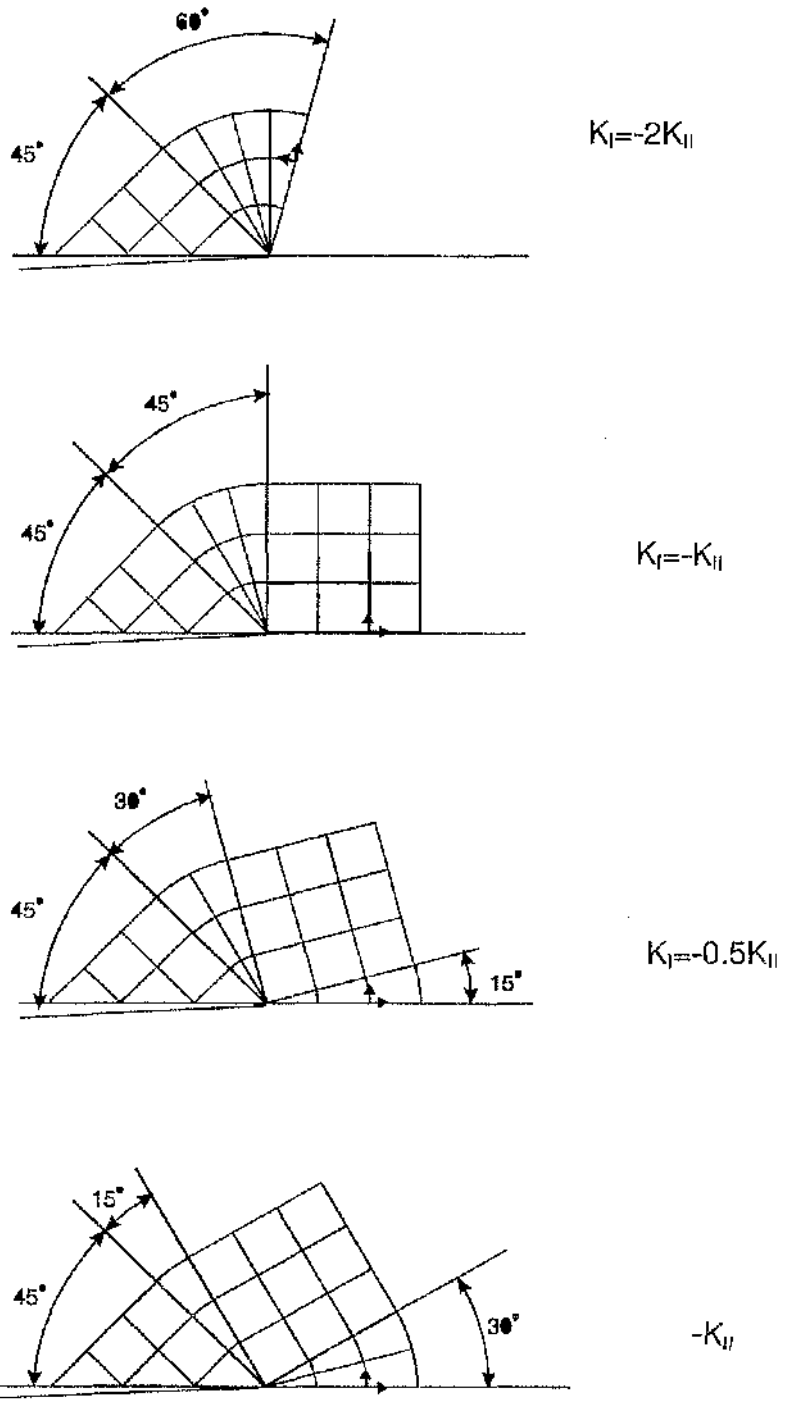

Figure 7.12 Slip line fields under negative mode mixities.

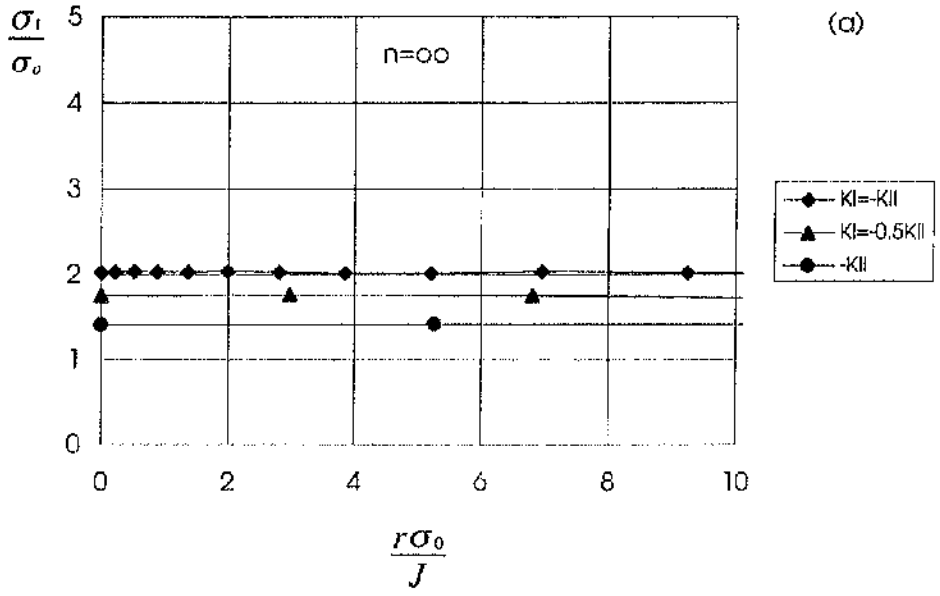

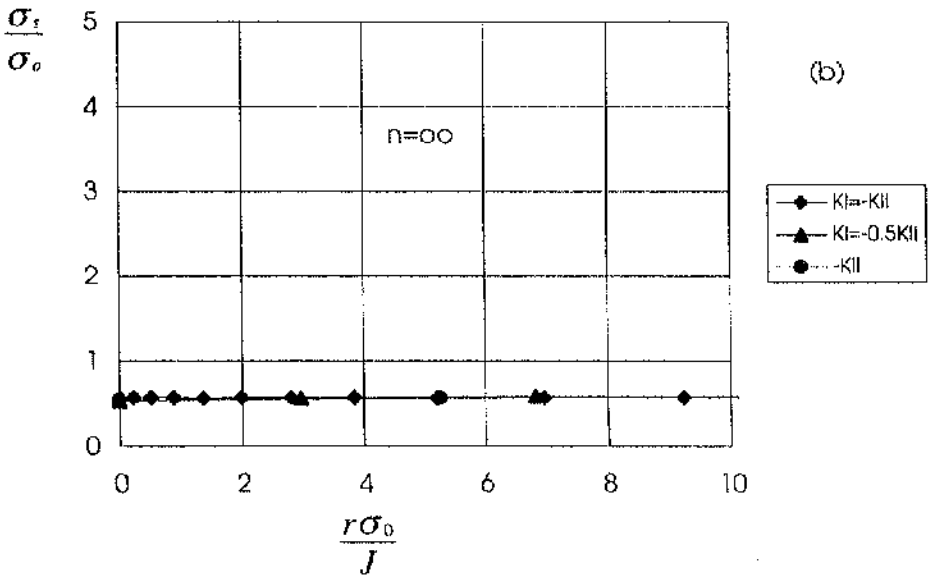

Figure 7.13 Radial variation of maximum principal stress (a) and maximum divatoric (b) stress under three levels of negative mode mixity.

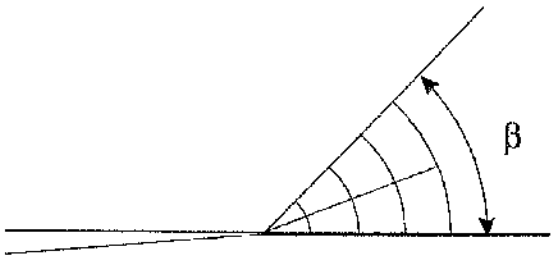

Figure 7.14 Illustration of angle β.

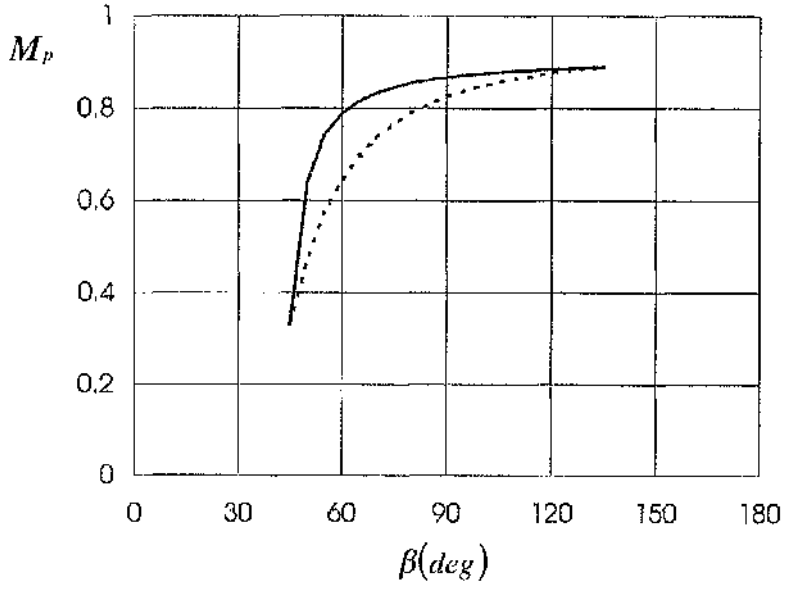

Figure 7.15 Variation of plastic mode mixity with the span of centered fan unde continuous variation of positive mode mixitie $\pi / 4 < \beta < 3\pi / 4$
Solid line refers to the solution from Li and Hancock, 1997 and
Dashed line from Fang and Bassani, 1995.

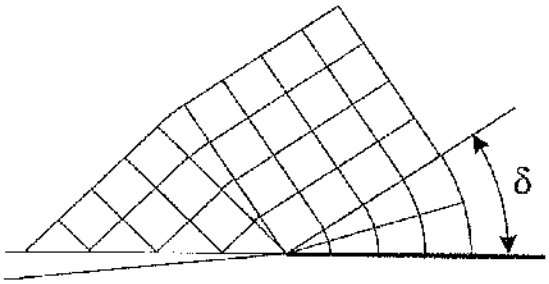

Figure 7.16 Illustration of angle δ.

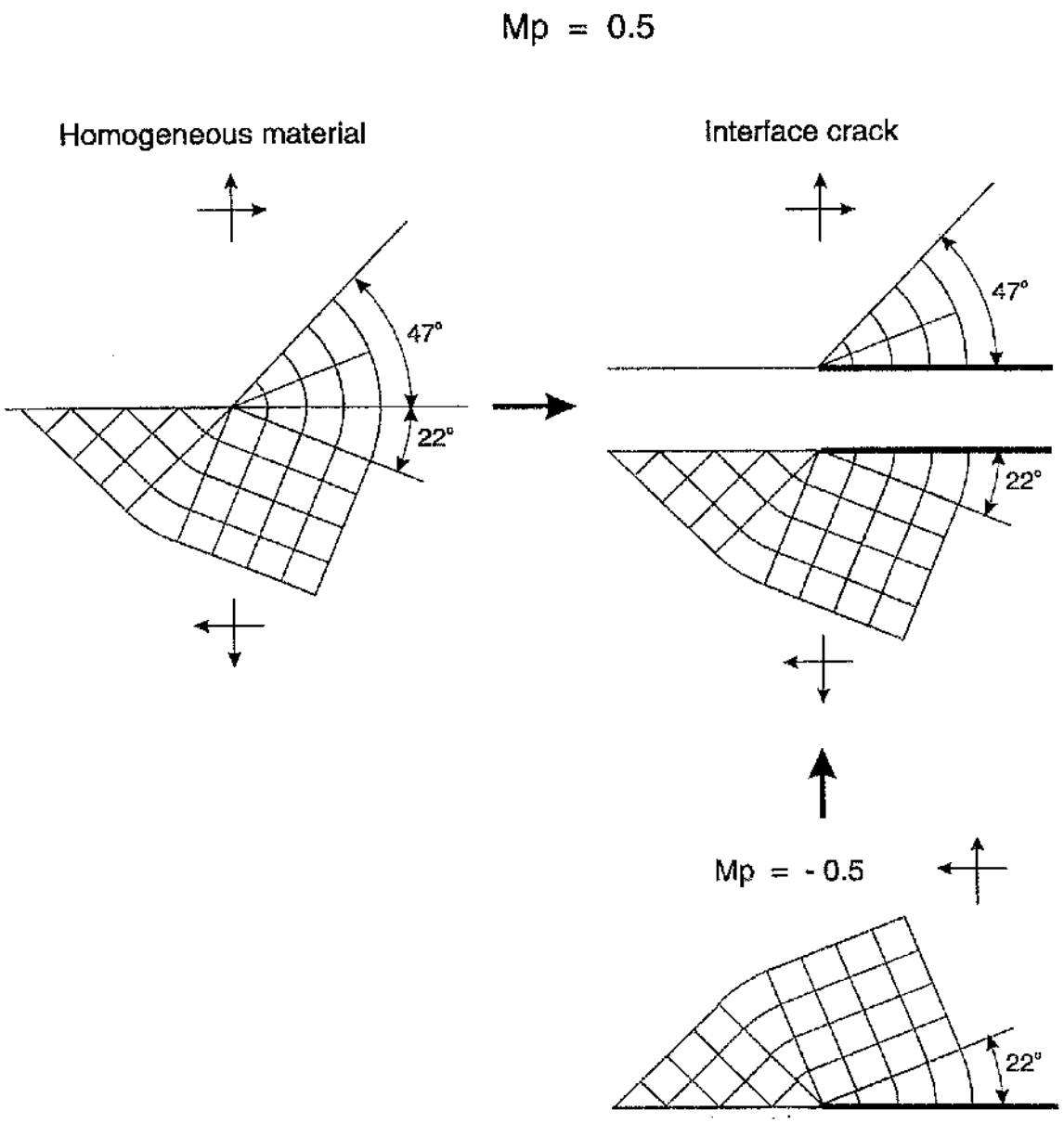

Figure 7.17 Illustration of the relation between homogenous crack tip slip line fields and rigid interfacial crack tip slip line fields.

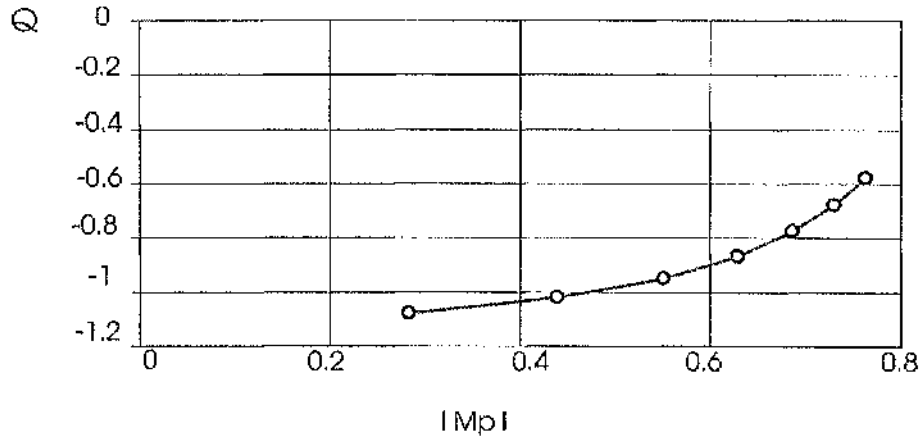

Figure 7.18. Variation of the constant parameter, Q, with negative plastic mode mixity, Mp, for interfacial crack problem.

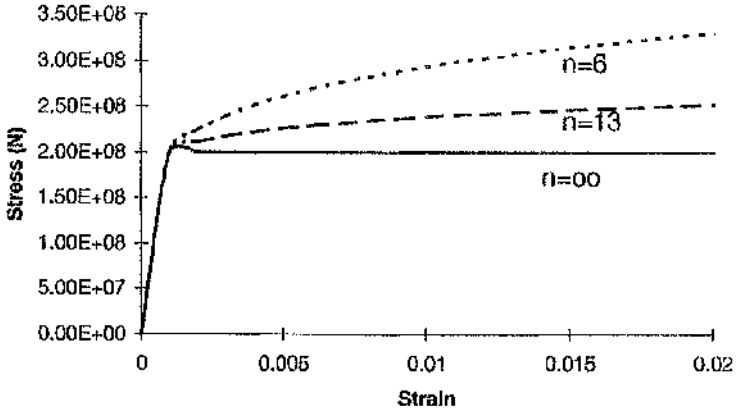

Figure 7.19 Stress-strain relations for both non-hardening and hardening materials.

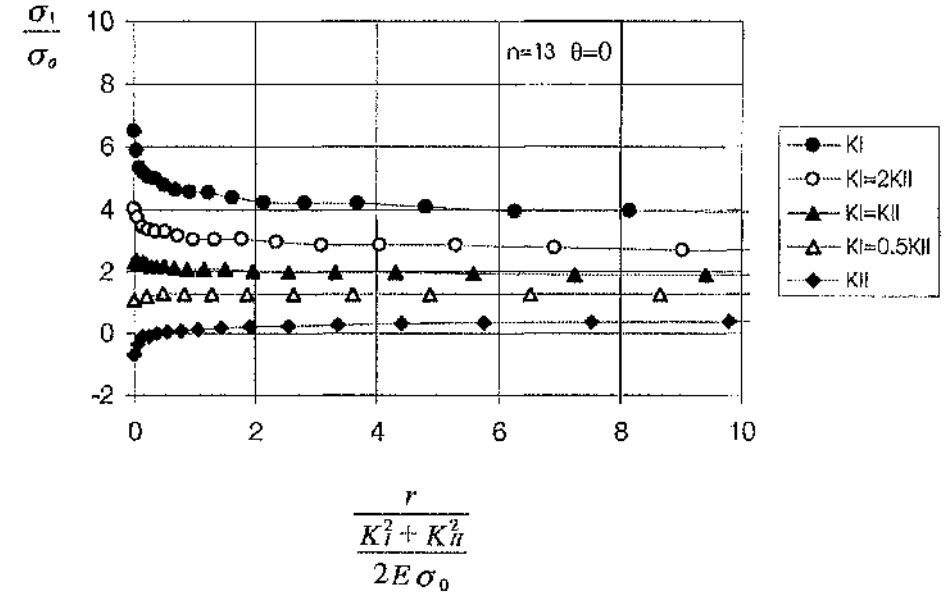

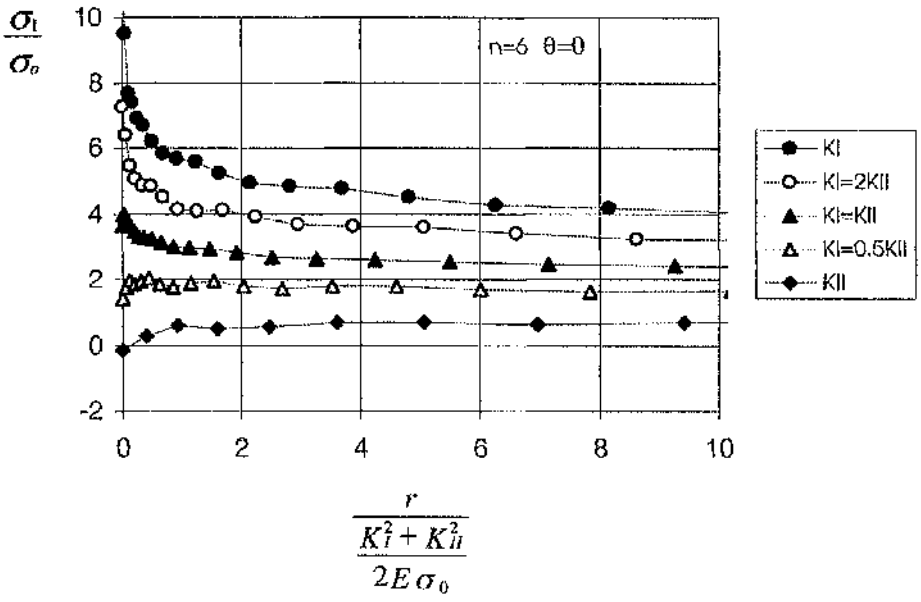

Figure 7.20 Radial variation of the maximum principal stress non-dimensionalised by the uniaxial yield stress under a range of elastic mode mixities.

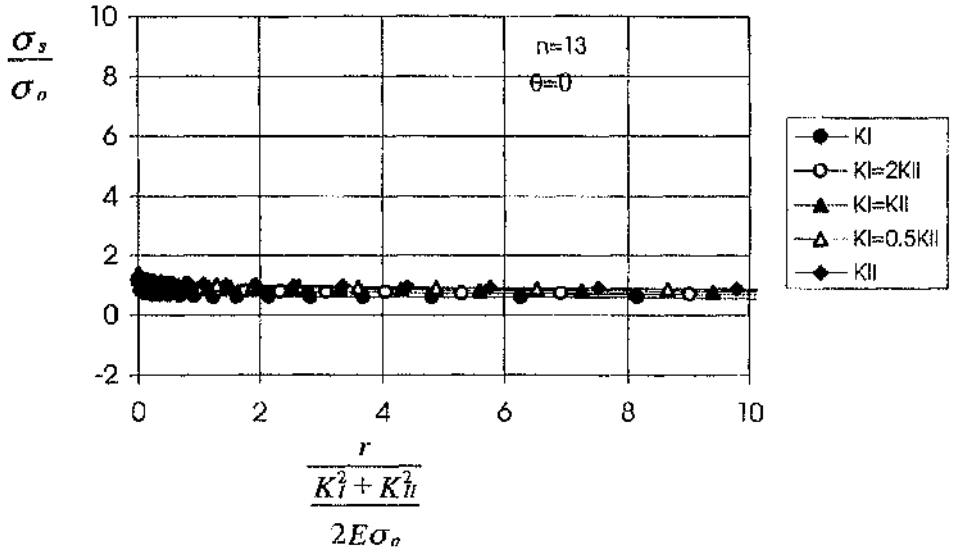

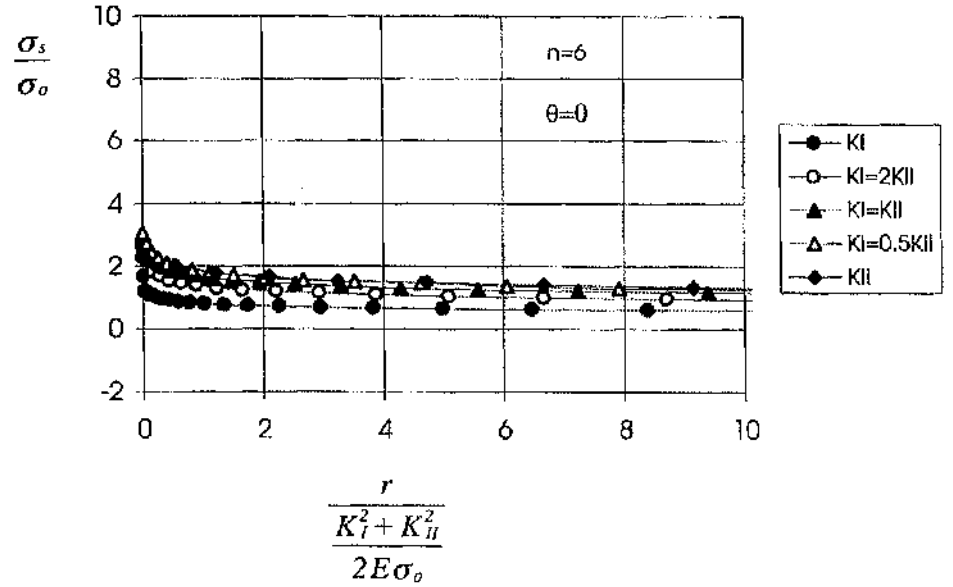

Figure 7.21 Radial variation of the maximum deviatoric stress under a range of mode mixities.

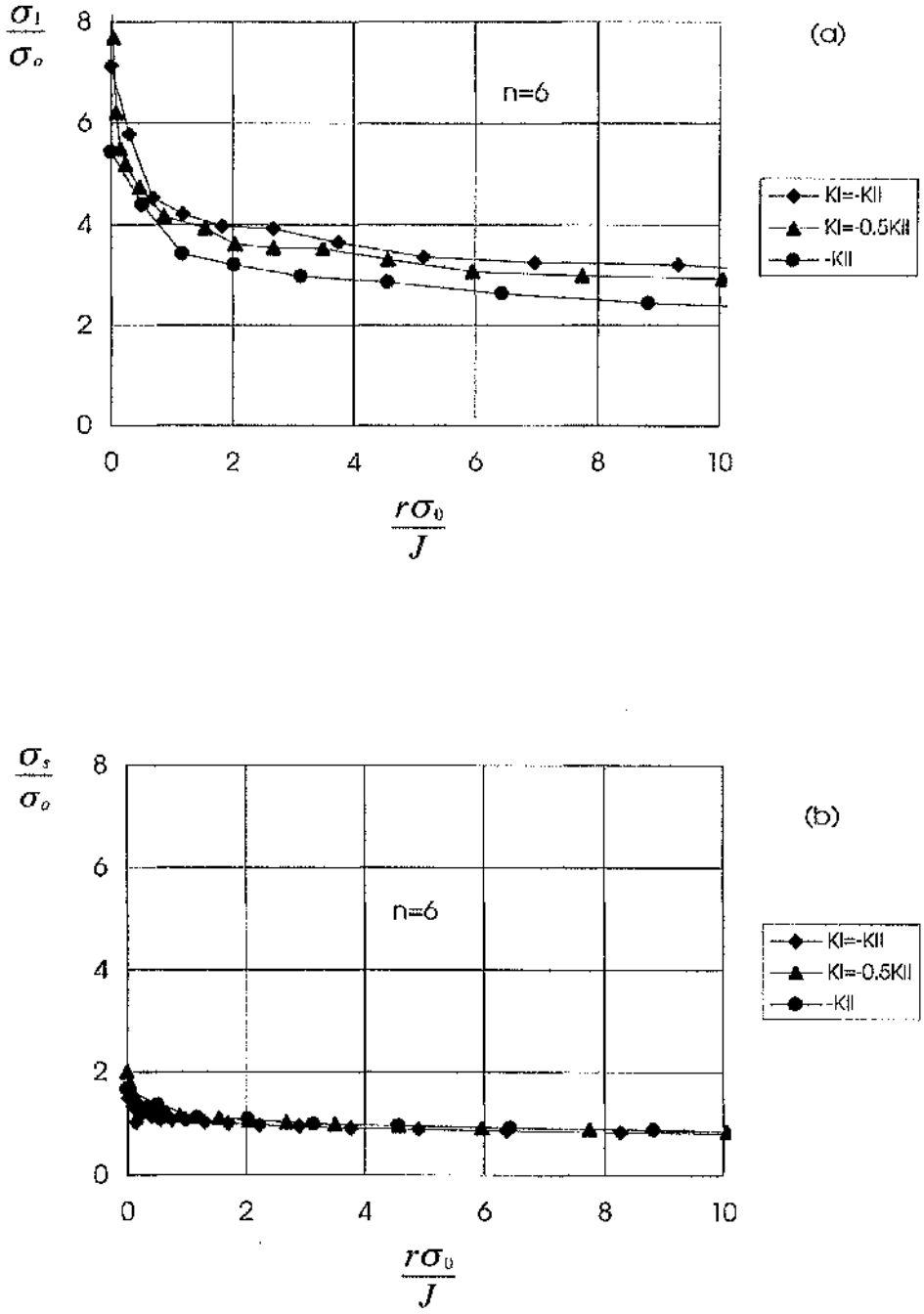

Figure 7.22 Radial variation of maximum principal stress (a) and maximum devatoric stress (b) under three levels of mode mixity.

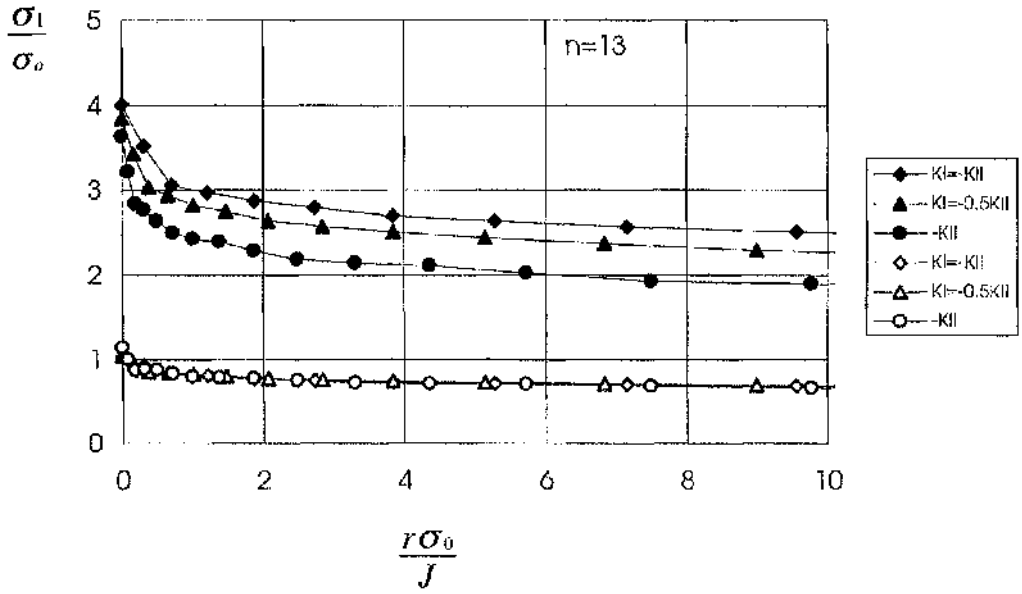

Figure 7.23 Radial variation of maximum principal stress (solid data points) and maximum divatoric stress (open data points) under three levels of mode mixity.

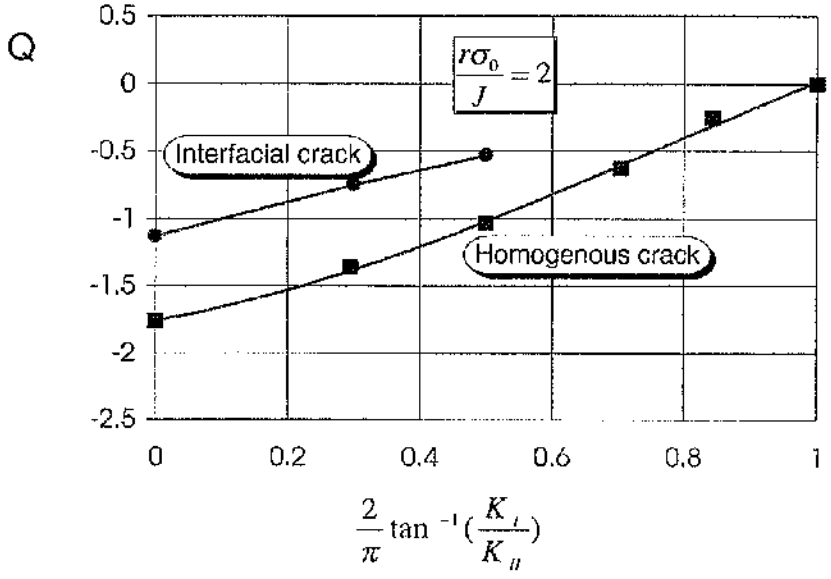

Figure 7.24 Relation of the constraint parameter and remote elastic mode mixity, n=13.

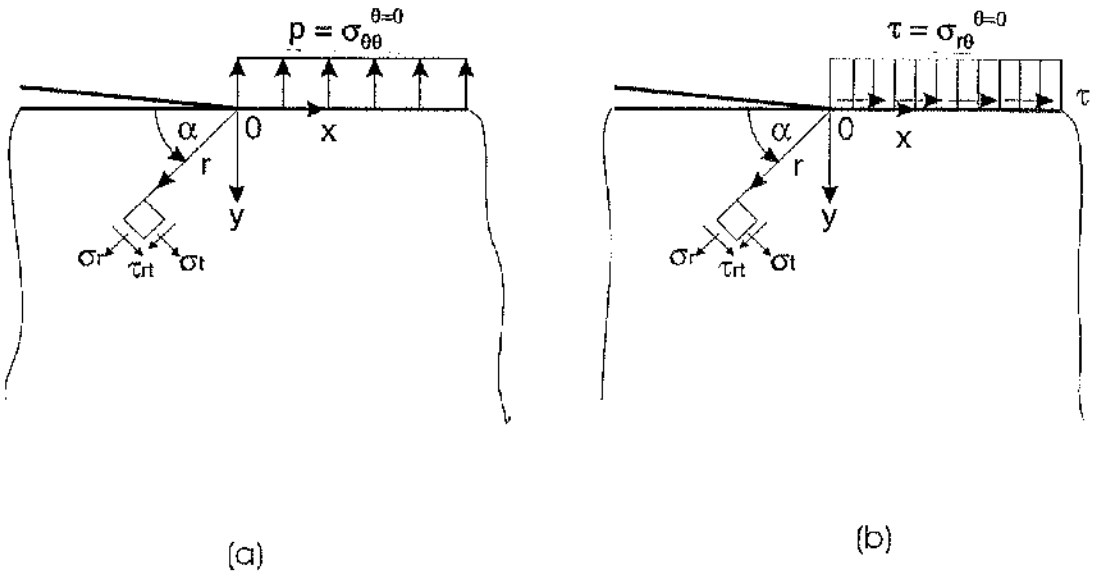

(a) (b)

Figure 7.25 Illustration of co-ordinate system of a semi-infinite elastic body.

Chapter 8 Strength mismatched interfacial crack tip stress fields under mixed mode loading

8.1 Introduction

A crack lying on the interface between a weld metal and the heat-affected-zone in a weldment may have critical effect on the strength of the structure (Thaulow et al., 1994; Minami et al., 1994). Such defects can be modelled as an interfacial crack between two materials that have identical elastic constants but different yield strengths. Strength mismatched interfacial crack tip stress fields under mode I and combined *K-T* stress loading have been investigated by Ganti and Parks (1997), Kim and co-workers, (1996) and Zhang and co-workers (1997) by using modified boundary layer formulations.

This chapter attempts to develop fields for the more general case of remote mixed mode loading. Plane strain slip line fields with matched elastic properties but mismatched yield strengths have been constructed by using a combination of numerical and analytical methods. The numerical solutions are obtained by using modified boundary layer formulations under small scale yielding conditions. In the corresponding analytical method, the local field is characterised by a yield strength mismatch, y, and a phase angle which quantifies the ratio of tension to shear on the interface at the crack tip. The fields are identified starting from an observation Rice (1982), that the asymptotic crack tip field of non-hardening solids can only be combinations of elastic sectors, centred fans and constant stress sectors. Continuity of tractions between the sectors plus the traction free conditions on the flanks determine the family of asymptotic fields. The analytical and numerical solutions are found to agree perfectly.

8.2 Numerical solutions for a non-hardening solid

Figure 8.1 illustrates a crack lying on an interface between two strength mismatched materials which are taken to have identical elastic properties. In-plane Cartesian co-ordinates (x_1, x_2) and polar co-ordinates (r, θ) are employed. Both co-ordinate systems are centred at the crack tip. The crack flanks occupy the negative x_1-axis while the positive x_1-axis coincides with the material

interface. The strength mismatch is defined as the ratio of yield strength of material 2 in the lower half space to that of material 1 in the upper half space, $y = \sigma_0^2 / \sigma_0^1$. Changes in strength mismatch factor were affected by keeping the yield stress of material 1 constant but changing the yield stress of material 2. The elastic response is assumed to be isotropic and incompressible. Thus together with plastic incompressibility, the body is fully incompressible. In uniaxial tension the material response is assumed to be elastic up to the yield stress (σ_0^1 or σ_0^2) after which it is perfectly plastic.

Numerical calculations were carried out by using boundary layer formulations in which the crack tip field was modelled by using the highly focused mesh discussed in chapter 5 (see Figure 3.13). The maximum radius of the plastic zone at a crack tip was limited to less than one hundredth of outer radius of the mesh. Displacement fields corresponding to the *KI* and *KII* stress intensity factors for a homogenous material (equation 6.1) were imposed on the outer boundary of the mesh. Calculations were performed with incompressible deformation for strength mismatch factors of *1.25* and *1.5* under the five levels of elastic mixity shown in Table 6.1

To understand the effect of elastic mixity and strength mismatch on the interfacial crack tip stress field, the angular variation of the Mises and mean stresses under the 5 levels of mode mixity are shown in Figures 8.2~5 for *y=1.25* and *1.5*. Since the error between the computed *J* and the applied *J* at the boundary is less than 5% (Zhang, et.al. 1997), the computed *J* was used in the present calculations. The jumps in Mises and mean stress at interface in both plots are caused by the discontinuity of radial stress across the interface. Under pure mode II loading, plasticity fully surrounds the crack tip in both materials. Figure 8.6 shows the crack tip sector assembly for a homogeneous body under remote pure Mode II loading (Hutchinson, 1968). It may be noted that a centred fan lies directly ahead of the crack tip and extends symmetrically across the crack line. If a centred fan was postulated ahead of the crack tip for an interface crack with mismatched yield strengths, the shear stress, $\sigma_{r\theta}$, would undergo a jump due to the mismatched yield strengths across $\theta=0$. This is not possible as

it violates the traction continuity condition required by the equilibrium equations. However, the crack tip sectors for an interface crack with a relatively small yield strength mismatch should not deviate substantially from those in a homogeneous body. Guided by these considerations, it is postulated that there exists an additional constant stress sector bordering the interface and lying in the part of the body that has higher yield strength. This will enable continuity of hoop and shear stresses but allow a jump in radial stress across the interface.

The slip line fields, shown in Figures 8.7~8, were obtained by noting that the mean stress does not change with angle in constant stress sector but varies linearly in any centred fan sector in the plastic region. The angular span of the sectors agree with analytic solutions to within the accuracy of the numerical interpolations. The angular span of the elastic sector was identified as the region in which the yield criterion was not satisfied. The crack tip stress field in material 1 comprises an elastic sector and a centred fan except in the pure mode I and II cases. The angular span of the centred fan decreases with mode II component. This implies that the plastic deformation in soft material decreases with contribution from mode II loading. In the hard material, an elastic sector appears directly ahead the crack tip under loading close to mode I. When mode II dominates the mode mixity, plasticity in the hard material develops to the interface and a constant stress sector appears ahead of the crack. Plasticity fully surrounds the tip in both hard and soft materials, but is necessarily asymmetric with respect to the interface. When y=1.5, the mode I field is not the same as the limiting case given by Ganti and Parks (1997) for y=1.421. Comparing Figure 8.7 and Figure 8.8, it may be noted that the mixed mode fields for the two strength mismatch factors are very similar.

In order to protect the weld metal from high deformation, the weld metal in welding processes is usually harder than the parent plate. However the maximum principal stress appears in hard material and its magnitude decreases with mode II component but increases with the strength mismatch. For stress controlled fracture, this implies that the interfacial crack may propagate into weld metal under mixed mode loading and high strength mismatch may lead to high constraint at the crack tip and hence low toughness. This prediction agrees with

the observation that the toughness of the Heat Affected Zone decreases with increasing weld metal strength (Kocak, 1988).

8.3 Analytic solutions for a non-hardening solid

To verify the numerical solutions, analytical solutions have been developed by Sham, Li and Hancock (1998). The strength mismatched crack tip stress fields can be assumed to consist of combination of centred fan, constant stress sectors and elastic sectors. This family of crack tip stress fields is parameterised by a local parameter, phase angle ϕ, and strength mismatch factor, y, in the following manner.

Let t be the traction on the interface at the crack tip. The traction t is defined to be a complex quantity with real and imaginary components which correspond to the hoop and shear stresses.

$$t = \sigma_{\theta\theta} + i\,\sigma_{r\theta} \tag{8-1}$$

where i is the imaginary unit. The complex traction can also be represented in terms of a magnitude $|t|$ and a phase angle ϕ.

$$t = |t|(\cos\phi + i\sin\phi) \tag{8-2}$$

Thus

$$\frac{\sigma_{\theta\theta}}{|t|} = \cos\phi \qquad \frac{\sigma_{r\theta}}{|t|} = \sin\phi \tag{8-3}$$

The normalised crack tip tractions on the interface can be expressed graphically in the phase-plane as shown in Figure 8.9. This diagram can be used to identify the regions of positive and negative interface traction components. Equation (8-3) allows the crack tip interface traction components to be related through the phase angle ϕ.

$$\sin\phi\,\sigma_{\theta\theta} = \cos\phi\,\sigma_{r\theta} \tag{8-4}$$

The crack tip stress fields for phase angles in the range $-90° \le \phi \le 90°$ have been determined explicitly. Crack tip stress fields for any phase angles outside this range can be obtained by transformation rules presented in Appendix 3.

For the case of mixed mode loading of a crack in a homogeneous body, a local plastic mixity factor, M_p, is customarily employed to parameterise the mixed mode crack tip stress fields (Shih, 1974; Li and Hancock, 1997). However, for strength mismatched interface cracks, it is important to use the phase angle, ϕ, instead of the local plastic mixity factor, M_p, as it allows a distinction to be drawn between the case of $\sigma_{\theta\theta} = a,\ \sigma_{r\theta} = -b$ from $\sigma_{\theta\theta} = -a,\ \sigma_{r\theta} = b$ where a and b are arbitrary constants.

For convenience, the crack tip sectors to be employed in the assembling the asymptotic fields are categorised in the following way.

(i) Type I Constant Stress (CS-I) Sector:

$$\sigma_{11} = 2k, \quad \sigma_{22} = \sigma_{12} = 0, \quad \sigma_{33} = k \tag{8-5}$$

(ii) Type II Constant Stress (CS-II) Sector:

$$\sigma_{11} = -2k, \quad \sigma_{22} = \sigma_{12} = 0, \quad \sigma_{33} = -k \tag{8-6}$$

(iii) General Constant Stress (CS) Sector:

$$\sigma_{11} = A_1, \quad \sigma_{22} = A_2, \quad \sigma_{12} = A_3, \quad \sigma_{33} = \tfrac{1}{2}(A_1 + A_2) \tag{8-7}$$

(iv) Type I Centred Fan (CF-I) Sector:

$$\sigma_{rr} = \sigma_{\theta\theta} = \sigma_{33} = -2k\theta + constant, \quad \sigma_{r\theta} = k \tag{8-8}$$

(v) Type II Centred Fan (CF-II) Sector:

$$\sigma_{rr} = \sigma_{\theta\theta} = \sigma_{33} = 2k\theta + constant\,, \quad \sigma_{r\theta} = -k \tag{8-9}$$

(vi) Elastic Sector

$$\sigma_{rr} = E_1 \sin 2\theta + E_2 \cos 2\theta + (E_3\theta + E_4)/2 \tag{8-10a}$$

$$\sigma_{\theta\theta} = -E_1 \sin 2\theta - E_2 \cos 2\theta + (E_3\theta + E_4)/2 \tag{8-10b}$$

$$\sigma_{r\theta} = E_1 \cos 2\theta - E_2 \sin 2\theta - E_3/4 \tag{8-10c}$$

$$\sigma_{33} = (E_3\theta + E_4)/2 \tag{8-10d}$$

These sectors will be assembled in a manner that is consistent with continuity of tractions, $\sigma_{\theta\theta}$ and $\sigma_{r\theta}$ across the sector boundaries and the material interface. Traction free boundary conditions on crack faces must also be enforced when necessary. It is noted that both CS-I and CS-II sectors satisfy traction free boundary conditions on the upper and lower crack faces. If an elastic sector is contiguous with a plastic sector within the same material region, the yield condition is enforced on both the elastic and plastic sides of the sector boundary. However, when an elastic sector adjoins a plastic sector along the material interface, the elastic stress state is not required to satisfy the yield condition on the elastic side of the material interface. For general constant stress sectors, the yield condition has to be enforced on the constant stress fields. As the crack tip stress fields are parameterised by the phase angle ϕ, $\sigma_{\theta\theta}$, and $\sigma_{r\theta}$ on the material interface can be related by equation (8-4) and this defines an additional condition.

In assembling the asymptotic crack tip sectors only traction continuity conditions, but not the full stress continuity conditions, are enforced at sector boundaries within the same material. However, the requirement that the elastic stress state satisfies the yield criterion at the elastic-plastic boundary within *the same material region* is identical to the requirement that the Mises stress is continuous across such a sector boundary. Since the Mises stress is necessarily continuous across elastic-plastic sector boundaries that are within the same material region,

this additional requirement at the elastic/plastic sector boundary leads to the conclusion that the yield function is continuous everywhere within the same material region. For the plane strain form of the Mises yield criterion $f=(\sigma_{00}-\sigma_{rr})^2+4\sigma_{r\theta}^2-4k^2$, continuity of f, σ_{00}, and $\sigma_{r\theta}$ implies that σ_{rr} is continuous. Thus, it may be concluded that all stress components are continuous within the same material region for the one-parameter family of crack tip stress fields. Of course, these crack tip stress fields have discontinuities in σ_{rr} across the material interface, but these are consistent with the traction continuity requirement.

There are 7 configurations to be assembled. The configurations change at critical values of the phase angle denoted ϕ_i *(i =1 to 6).* The critical phase angles are shown in Table 8.1 for *y = 1.25* and *1.5.*

Configuration A, $\phi_1 \le \phi \le 90°$

Consider the sector configuration given in Figure 8.10a.

In material I, starting from the upper crack face, this configuration consists of a CS-II sector, a CF-II sector, a general CS sector, and a CF-I sector;

In material II: starting from the lower crack face the configuration comprise, a CS-I sector, a CF-II sector, a general CS sector, a CF-I sector, and a general CS sector.

There are 7 sector boundaries and 13 constants for the stresses. The conditions for determining these 20 unknowns are: 16 traction continuity conditions at 7 sector boundaries and 1 material interface, 3 conditions from enforcing yielding in 3 general CS-sectors, and equation 8.4 relating the interface tractions. Thus, the 20 unknowns from these 20 conditions can be determined when a phase angle ϕ is specified (Sham, Li and Hancock, 1997). The details of the expressions for the sector angles and stresses for this configuration, and others to follow, are given in Appendix 2.

As the phase angle ϕ is decreased from 90^0 the sector boundary at θ_6 rotates anticlockwise towards the one at θ_8 and the angular extent of the CF-II sector in the range $\theta_6 \leq \theta \leq \theta_8$ gradually decreases. When ϕ reaches ϕ_1, this centred fan vanishes and the two neighbouring constant stress sectors collapse into one CS-II sector, resulting in the limiting configuration depicted in Figure 8.10b.

The remaining six configurations are assembled in a similar way and are shown in Appendix 1.

Based on numerical solutions, the phase angles for each level of mode mixity for *y=1.25* and *1.5* are shown in Table 8.2. The analytical angular variations of the stress components were calculated for each phase angle and compared with the corresponding numerical solutions, as shown in Figures 8.11 and 8.12 for *y=1.25* and *1.5* respectively. It is clear that there is full agreement between the analytical solutions given by lines and the numerical solutions given as data points.

8.4 Strain hardening

Attention is now focused on the effect of strain hardening on strength mismatched fields. A modified power-law relationship between uniaxial stress and strain is used.

$$\frac{\varepsilon}{\varepsilon_o} = \left(\frac{\sigma}{\sigma_o}\right)^n \qquad \sigma \geq \sigma_o \qquad (8\text{-}11)$$

Here σ_o and ε_o are the stress and strain at yield in uniaxial tension, n is the hardening exponent. The total strain is decomposed into elastic ε_e and plastic ε_p components in the usual way:

$$\varepsilon = \varepsilon_p + \varepsilon_o \qquad (8\text{-}12)$$

The uniaxial stress-strain relations are generalised into multi-axial states of stress using the Mises yield criterion and the associated flow role. Strength

mismatch may occur due to either a difference in initial yield stress or different strain hardening rates. In the present analyses, only the former is considered. The two strength mismatched materials have the same strain hardening rate, n, but different initial yield strengths, σ_0^1 and σ_0^2.

Numerical calculations were performed with stain hardening exponents, *n=13* and *6* under mixed mode loading. To determine the plane on which the maximum principal stress and minimum shear occurs, the angular variation of the stress components under each level of mixity for *y=1.25* and *n=6, 13* are shown in Figures 8.13~14. The stresses are non-dimensionalised with respect to the uniaxial yield stress of soft material 1, σ_0^s. It was found that the continuity in shear and hoop stress across the boundary was always satisfied, as required by the equilibrium equations. The maximum hoop stresses appeared in the hard material and decreased with increasing mode II component. Figures 8.15~16 show the radial variation of maximum principal stresses and deviatoric stresses on the planes of the maximum hoop stresses for n=6 and 13 respectively. The radial distance from the crack tip, r, is non-dimensionlised by J/σ_0^s. It is significant to note that the stress profiles are parallel to each other. For weak and moderate strain hardening, the stress fields are qualitatively similar to the non-hardening case, and are devatorically similar but differ hydrostatically.

To investigate the effect of strength mismatch factor on the stress fields, the yield stress in the material 2 was increased to $1.5\sigma_0^s$. Figure 8.17 shows radial variation of maximum principal stress and deviatoric stress under mode mixities for *n=13*. The stresses profiles are similar to those for *y=1.25 (n=13)*.

Since the fields differ mainly hydrostatically, the constraint of all these fields may be correlated with the homogeneous mode I field in small scale yielding conditions. Take small scale yielding solutions of material 2 as reference field, the constraint parameter, Q, can be defined as the difference in mean stresses between the strength mismatched crack tip stress field and the reference field on the plane of maximum principal stress:

$$Q = \frac{\sigma_m - \sigma_m^{SSY}}{\sigma_0^2} \qquad (8\text{-}13)$$

Figure 8.18 illustrates the constraint parameter Q as function of elastic mode mixity at $r\sigma_0^s/J=2$ for hardening rate of $n=6$ and 13. By using this relationship, the corresponding J-Q locus from mode I experimental data shown in Figure 8.19 given by Betegón and Hancock (1991) can thus be mapped into the *J-mixity* locus for stress controlled fracture as shown in Figure 8.20.

8.5 Conclusions

Numerical and analytic solutions have been developed for the asymptotic small scale yielding crack fields of a crack located on the interface between two elastic perfectly-plastic solids, with matching elastic properties, but mismatched yield strengths. The results are expressed as plane strain slip line fields which comprise combinations of elastic sectors, centred fans and constant stress sectors. Solutions are developed under mixed mode loading as a function of the plastic mismatch between the two solids. Numerical solutions developed using finite element methods in which the small scale yielding field is modelled by boundary layer formulations agree well with analytic solutions.

By assuming the strength mismatch arises only from the difference in initial yield stress, the strength mismatched interfacial crack tip were also investigated in hardening materials. The maximum principal stresses decreases with the contribution from mode II but increases with strength mismatch. The planes of the maximum principal stresses are located in the hard material and rotate as the mode II component increases. On these planes, the stress profiles are parallel and differ mainly by a hydrostatic term for weak and moderate levels of strain hardening. For stress controlled failure, this allows these fields to be correlated with the homogeneous unconstrained mode I fields allowing the homogeneous mode I failure criterion to be used for strength mismatched materials.

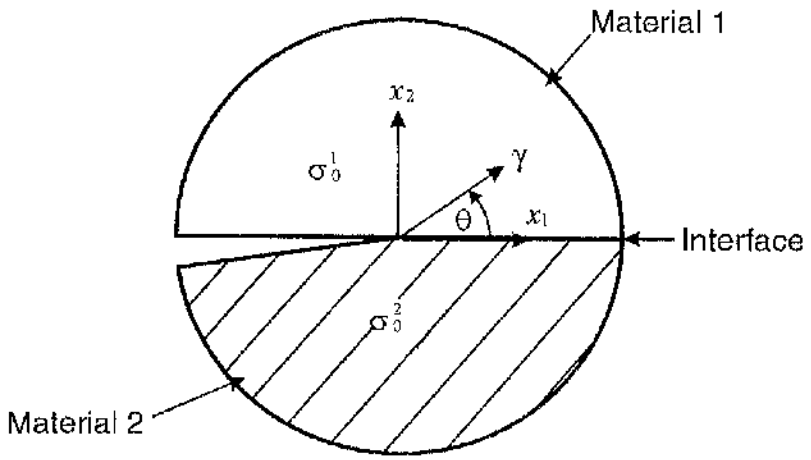

Figure 8.1 Schematic of a strength mismatched interfacial crack.

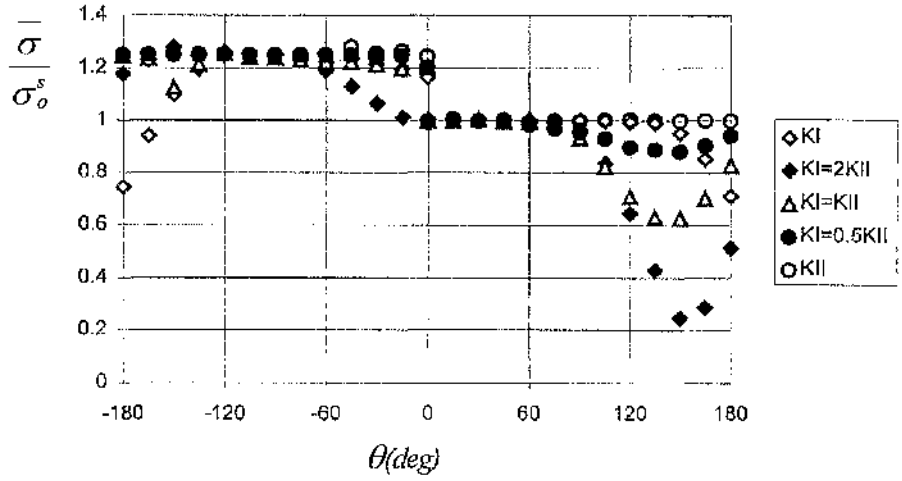

Figure 8.2 Angular distribution of the Mises stress at a strength mismatched interfacial crack tip y = 1.25.

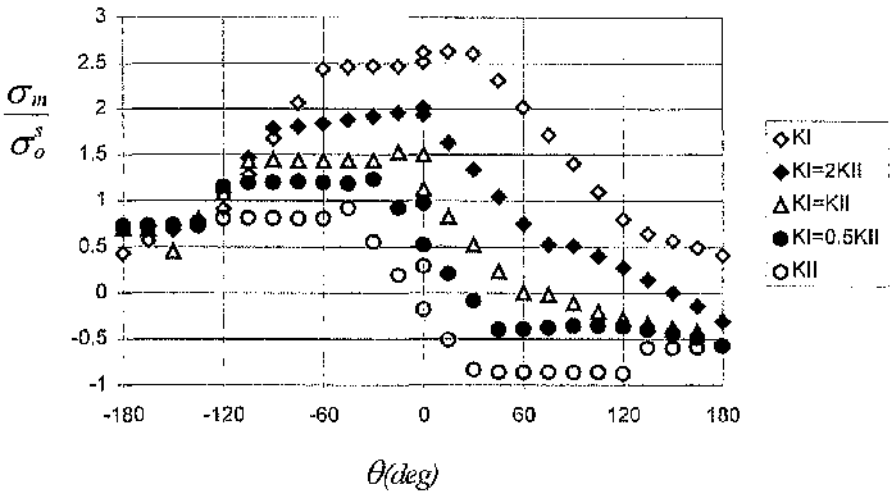

Figure 8.3 Angular distribution of mean stress at a strength mismatched interfacial crack tip y = 1.25.

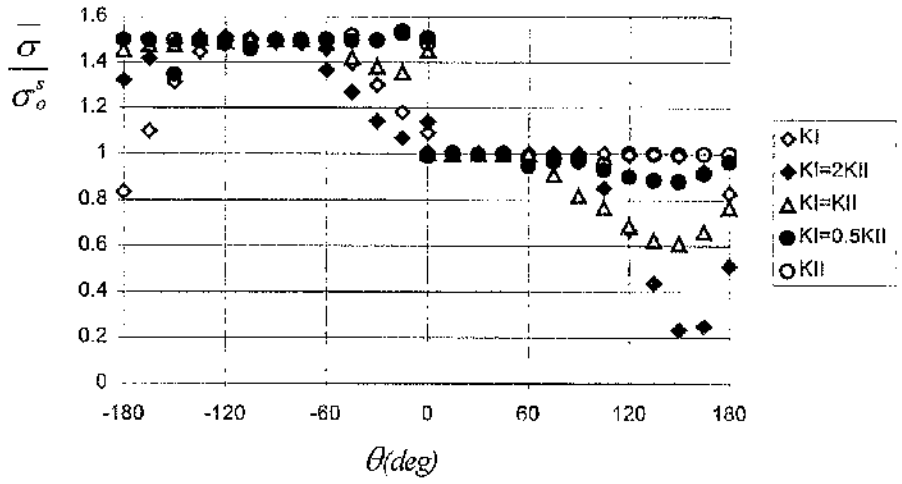

Figure 8.4. Angular distribution of the Mises stress at a strength mismatched interfacial crack tip y = 1.5.

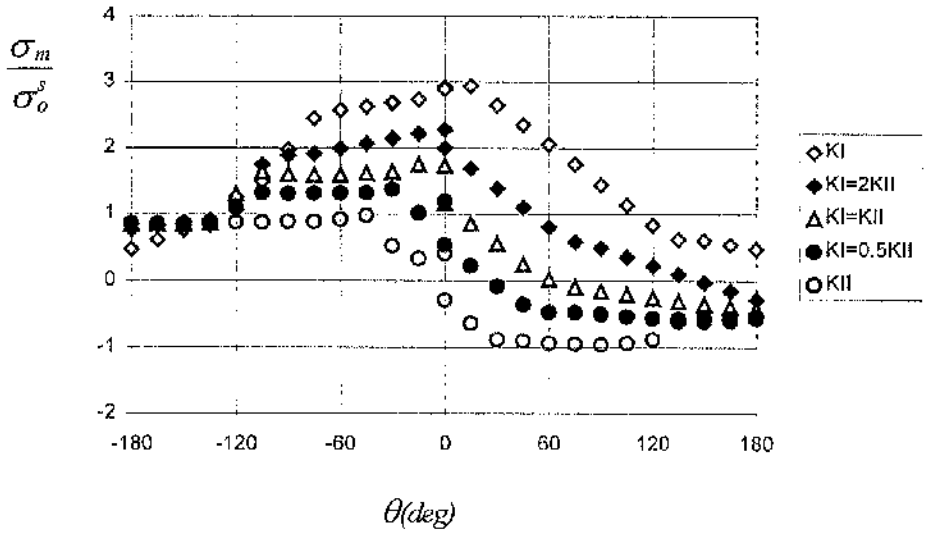

Figure 8.5. Angular distribution of mean stress at a strength mismatched interfacial crack tip y = 1.5.

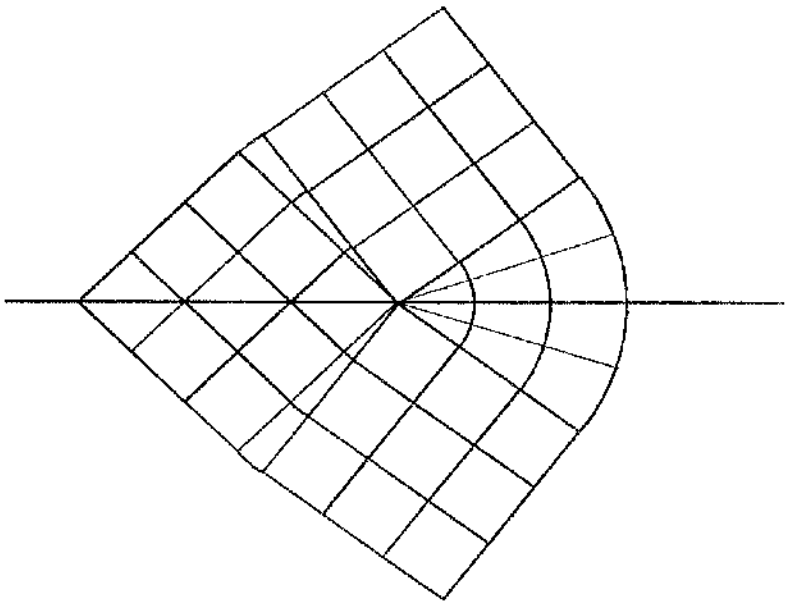

Figure 8.6 Mode II field after Hutchinson 1968.

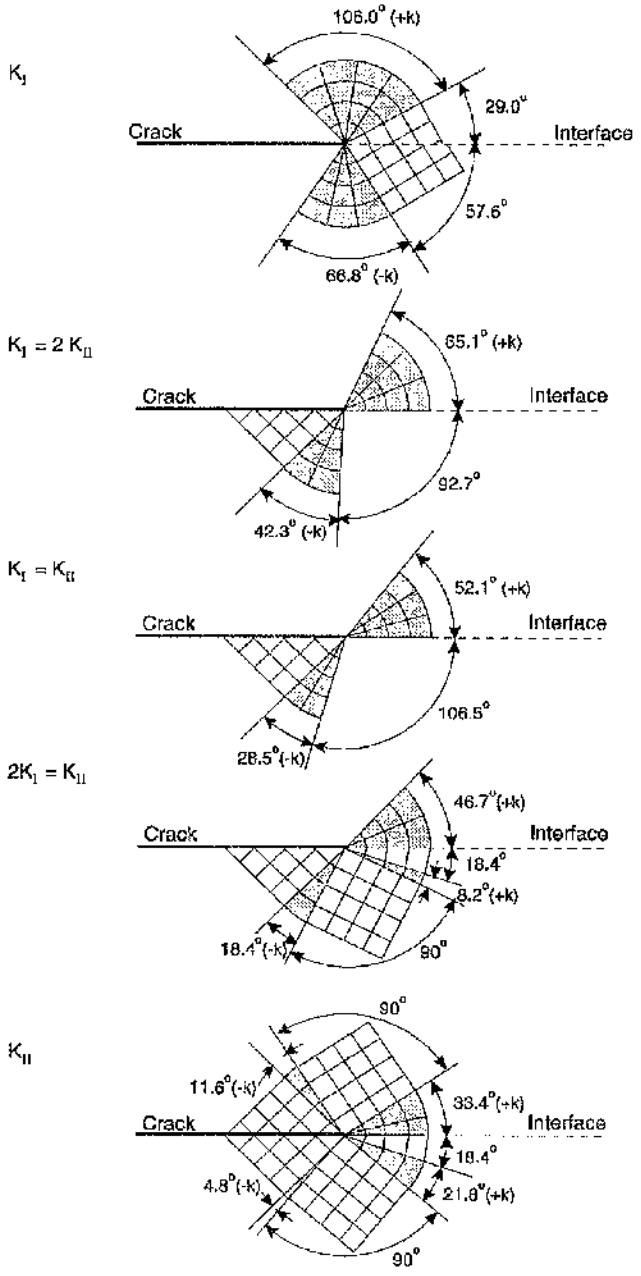

Figure 8.7 Slip line fields for a mismatch factor, y = 1.25.

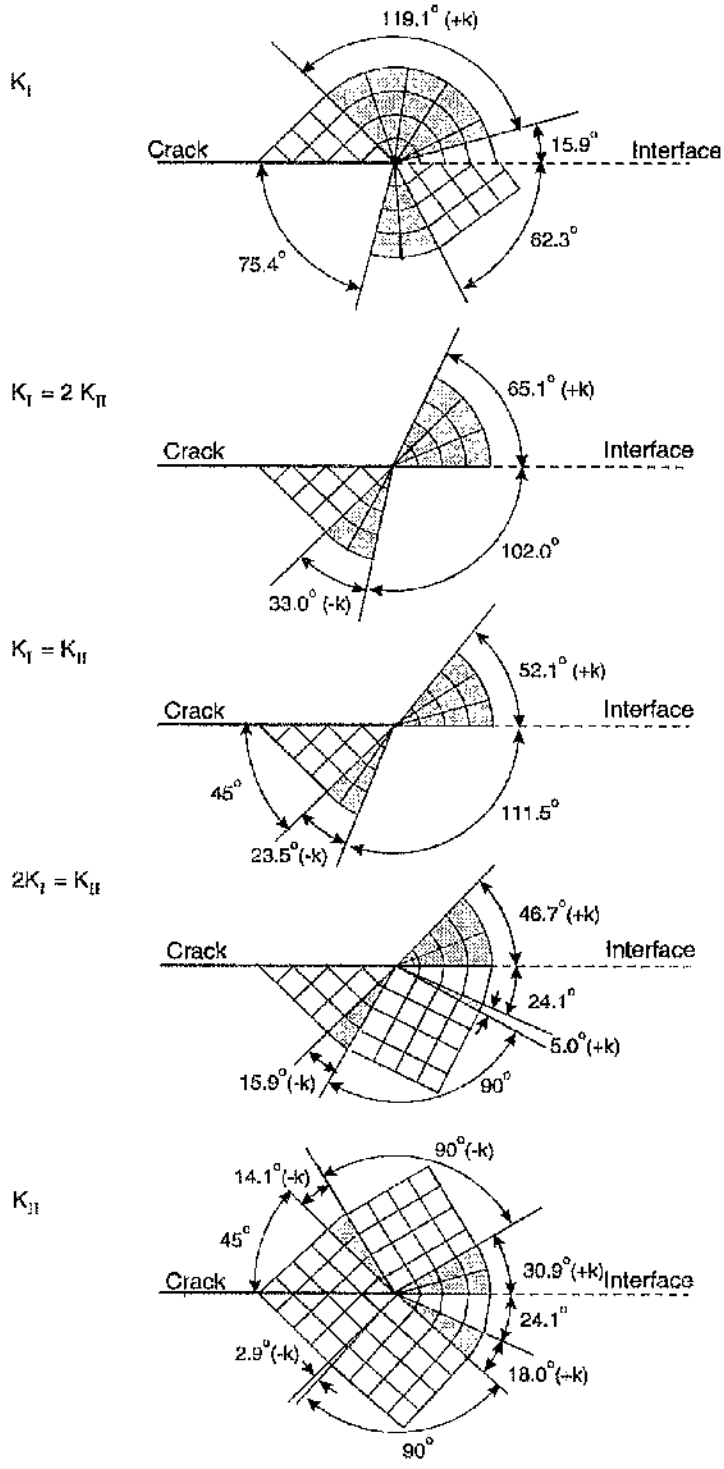

Figure 8.8. Slip line fields for a mismatch factor, y = 1.5.

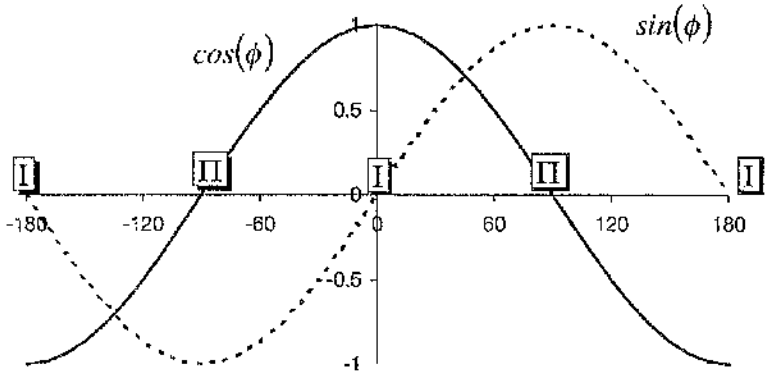

Figure 8.9 Illustration of phase plane. $cos(\phi)$ corresponds to hoop stress and $sin(\phi)$ to shear stress. I refers to local mode I and II to local mode II.

Table 8.1 Limiting phase angles

y	ϕ_1	$\phi_2(y)$	$\phi_3(y)$	$\phi_4(y)$	ϕ_5	$\phi_6(y)$
1.25	60.28°	31.08°	11.85°	6.40°	- 21.26°	- 56.61°
1.5	60.28°	34.11°	9.93°	9.93°	- 21.26°	- 54.20°

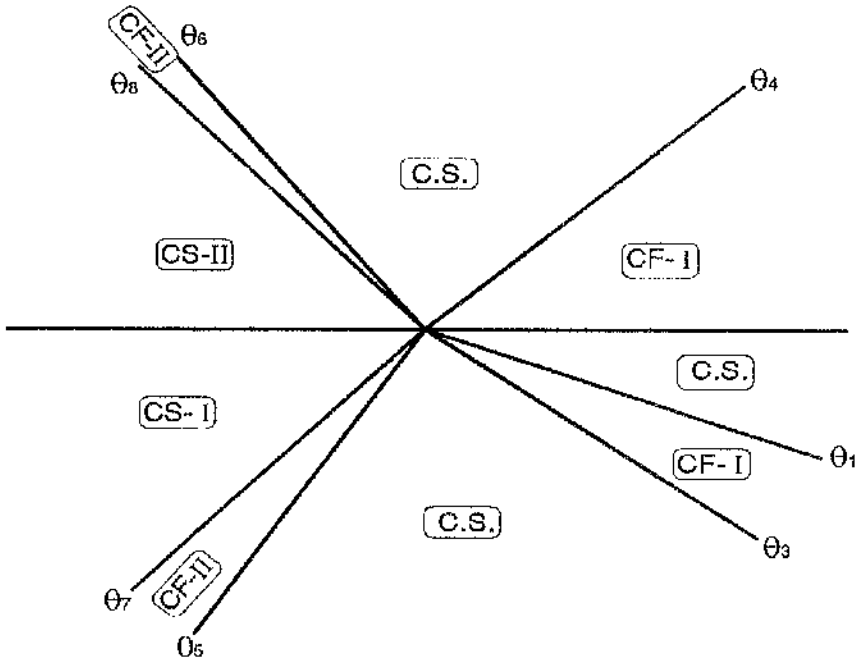

(a)

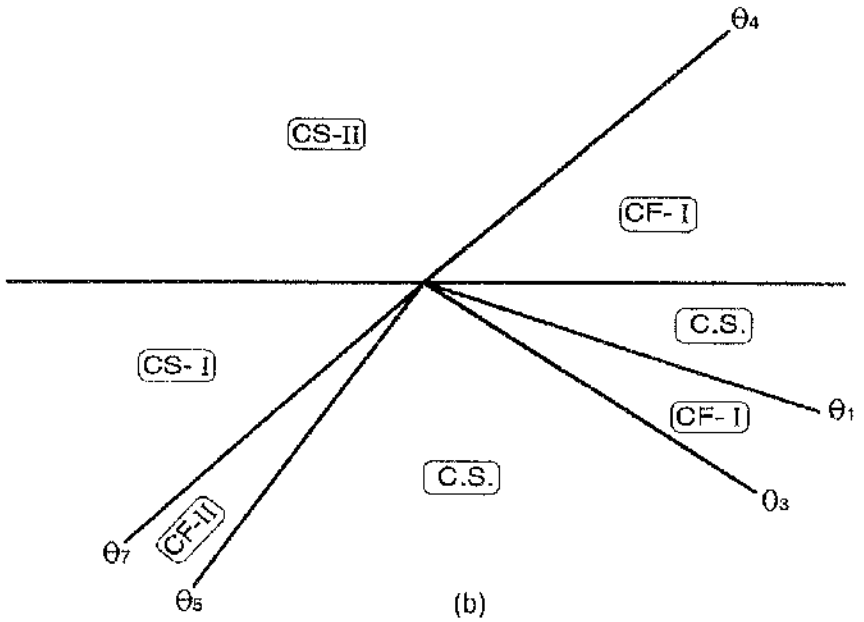

(b)

Figure 8.10 Sector configuration A (a) and Limiting configuration $\phi 1$, (b).

Table 8.2 Phase angle of strength mismatched interfacial crack

Strength mismatched factor	Elastic mode mixity	$\sigma_{\theta\theta}^{\theta=0} / \sigma_0^I$	$\sigma_{r\theta}^{\theta=0} / \sigma_0^I$	Phase angle $\phi(deg)$
y=1.25	KI	3.1167	0.2979	5.46
	KI=2KII	1.9554	0.5779	16.46
	KI=KII	1.1129	0.5777	27.43
	KI=0.5KII	0.5433	0.5758	46.66
	KII	-0.1388	0.5734	103.6
y=1.5	KI	3.2301	0.4831	8.51
	KI=2KII	1.9554	0.5779	16.46
	KI=KII	1.1358	0.5796	27.04
	KI=0.5KII	0.5462	0.5762	46.53
	KII	-0.2362	0.5722	112.43

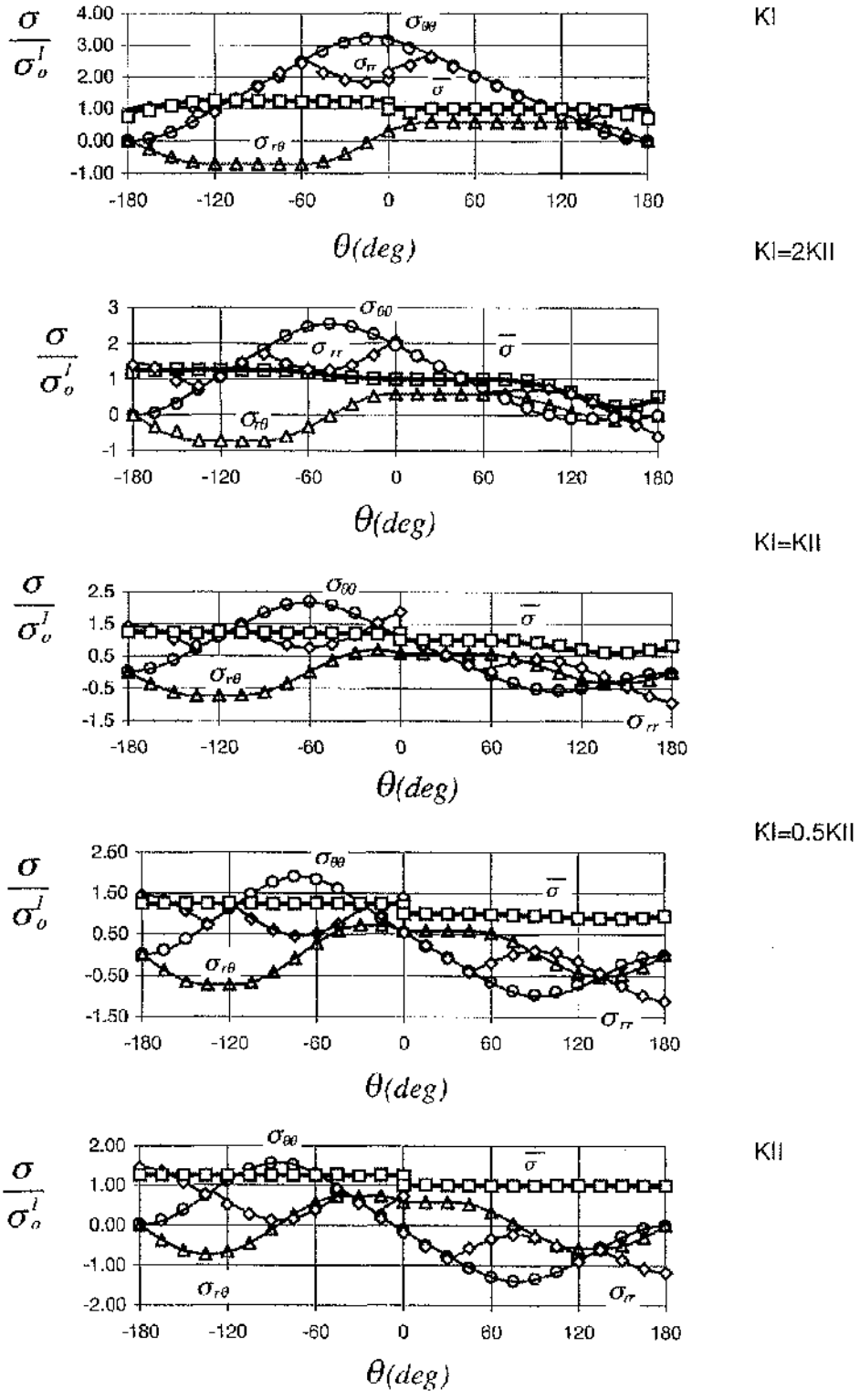

Figure 8.11. Comparison of the analytic and numerical solutions for the hoop, radial shear and Mises stresses at the phase angles given in Table 8.2 and a mismatch factor y = 1.25.

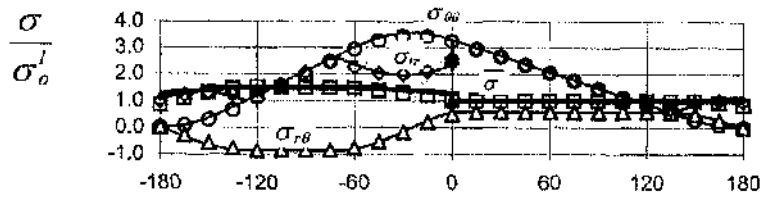

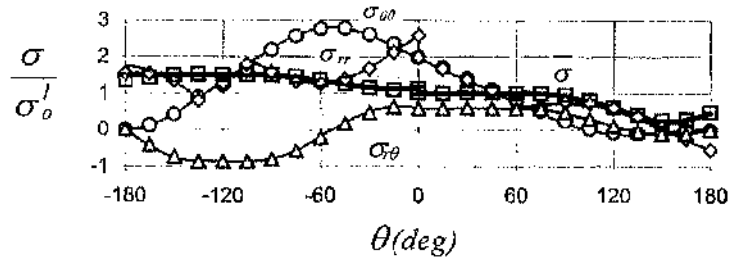

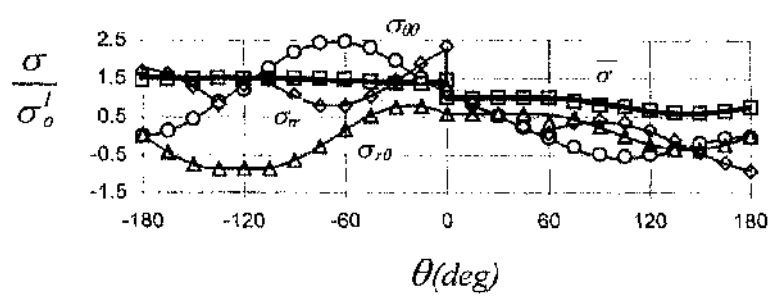

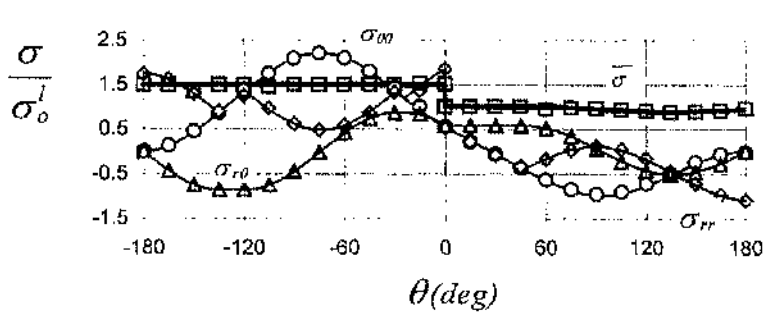

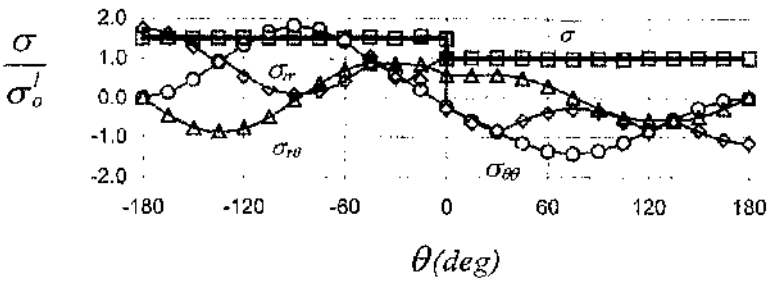

Figure 8.12. A comparison of the analytic and numerical solutions for the hoop, radial, shear and Mises stresses at the phase angles given in Table 8.2 and a mismatch factor y = 1.5.

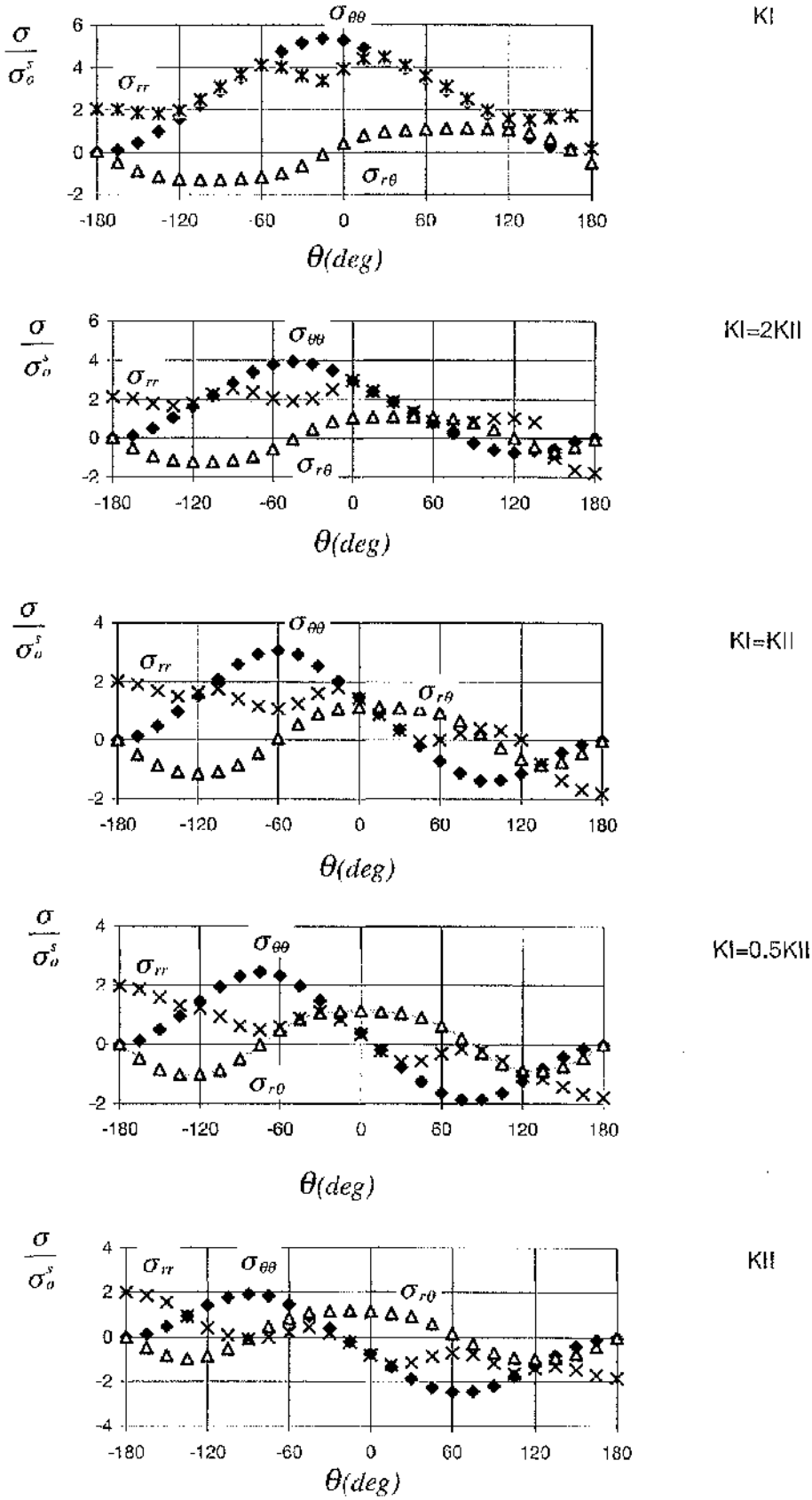

Figure 8.13 Stresses around a strength mismatched interfacial crack tip for n=13, y=1.25.

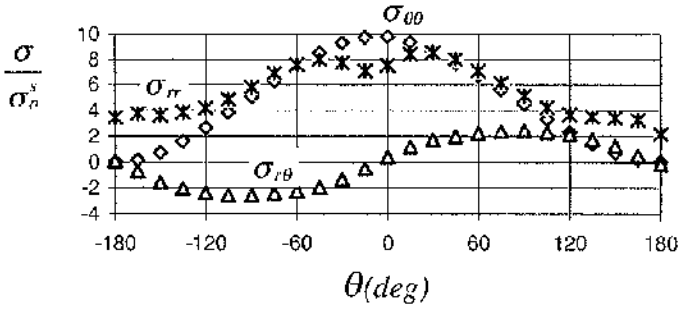

KI

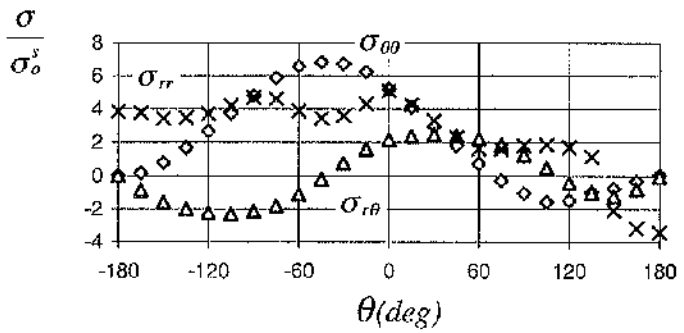

KI=2KII

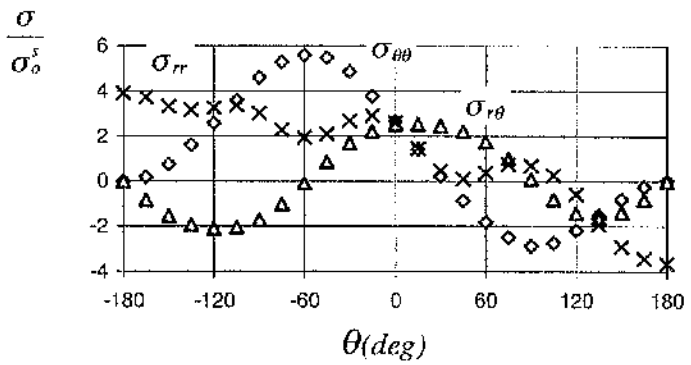

KI=KII

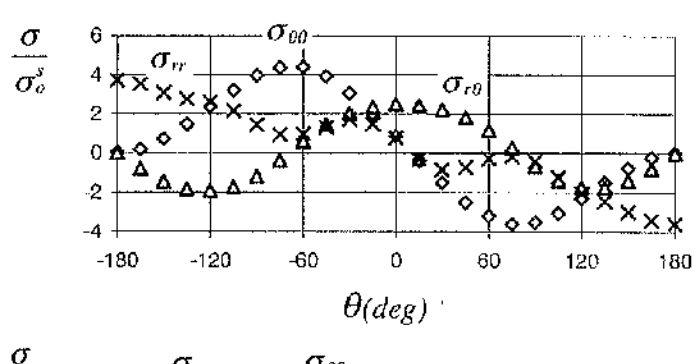

KI=0.5KII

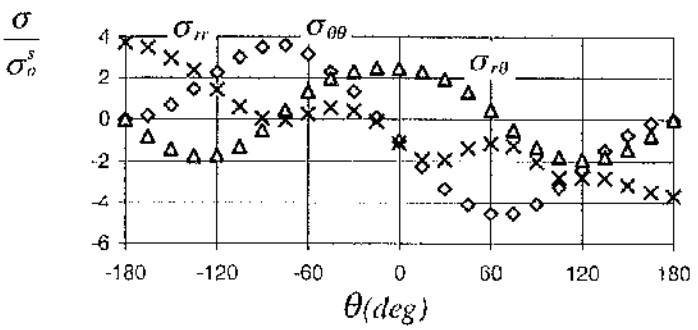

KII

Figure 8.14 Stresses around a strength mismatched interfacial crack tip for n=6, y=1.25.

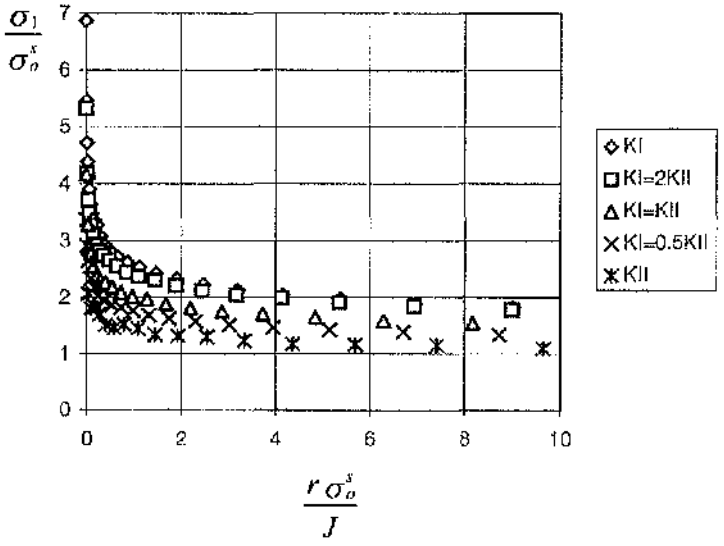

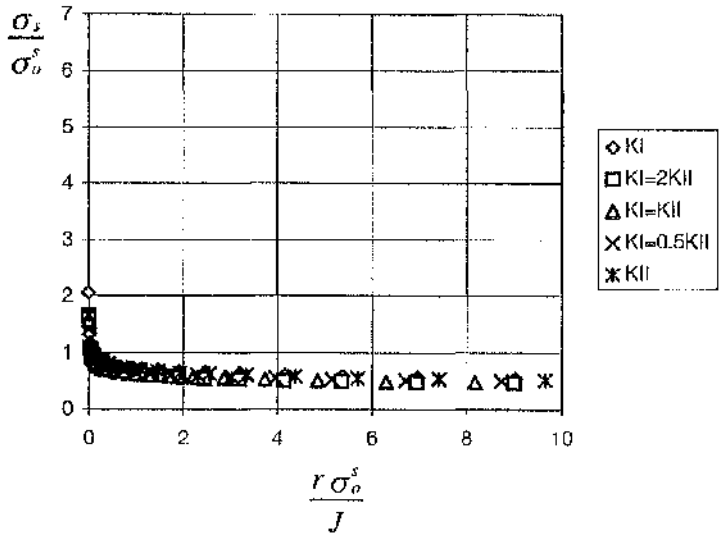

Figure 8.15 Radial variation of the maximum principal and deviatorical stresses from a strength mismatched interfacial crack tip for n=6, y=1.25

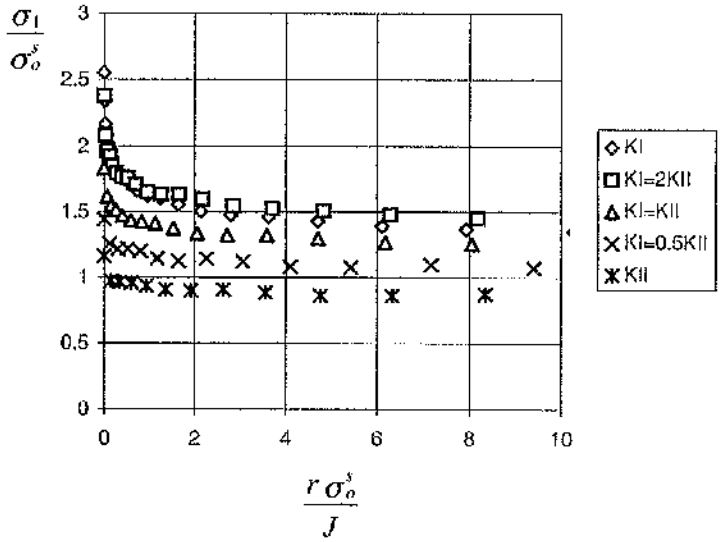

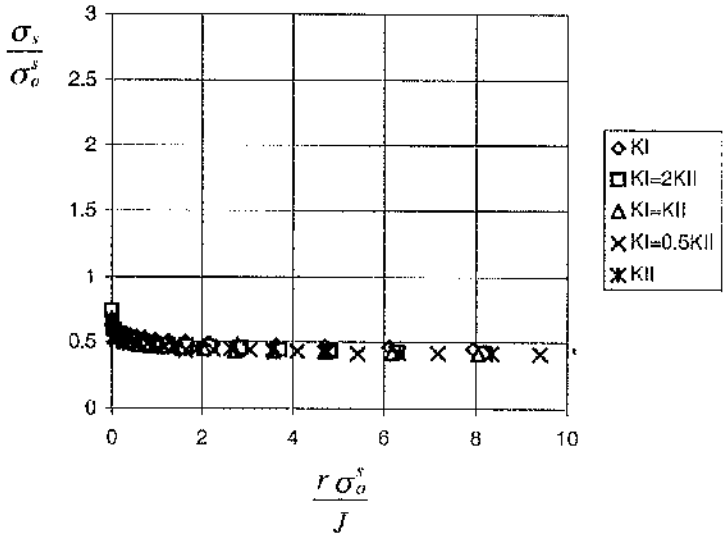

Figure 8.16 Radial variation of the maximum principal and deviatorical stresses for n=13, y=1.25.

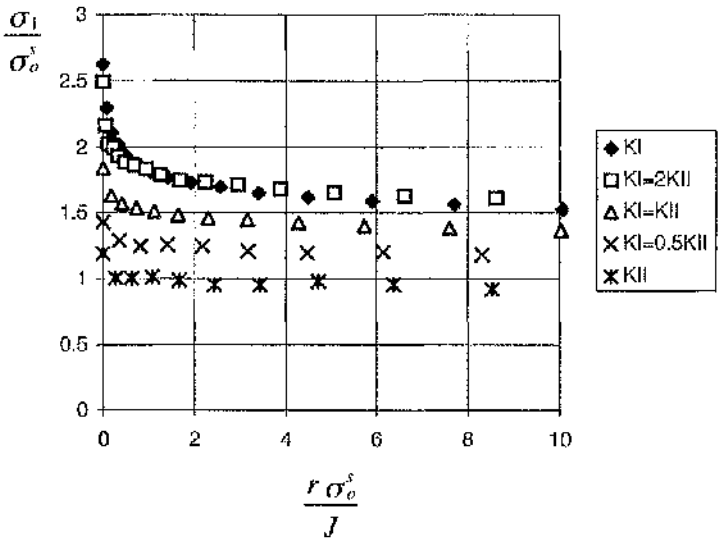

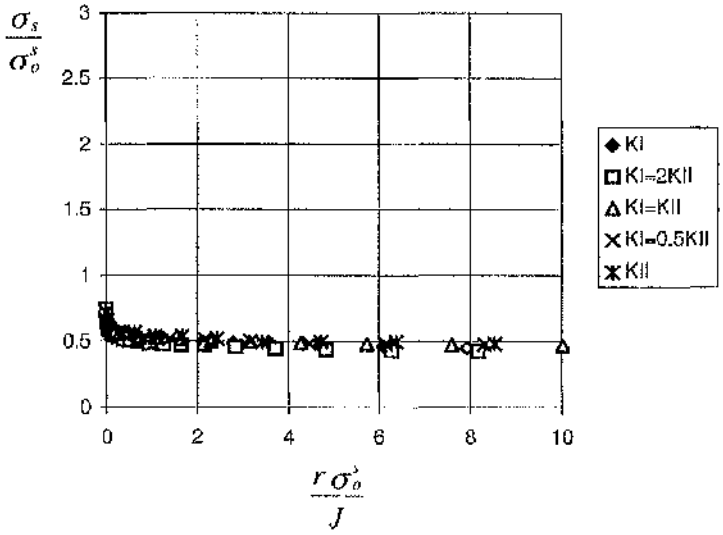

Figure 8.17 Radial variation of the maximum principal and deviatoric stresses from a strength mismatched interfacial crack tip for n=13, y=1.5.

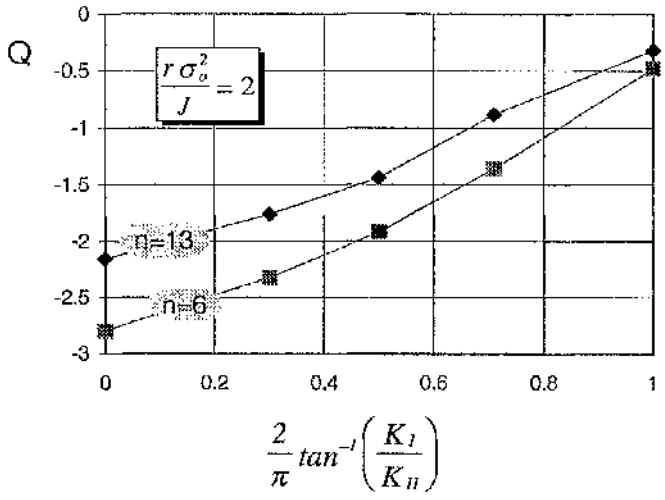

Figure 8.18 Constraint parameter as function of elastic mode mixity, y=1.25.

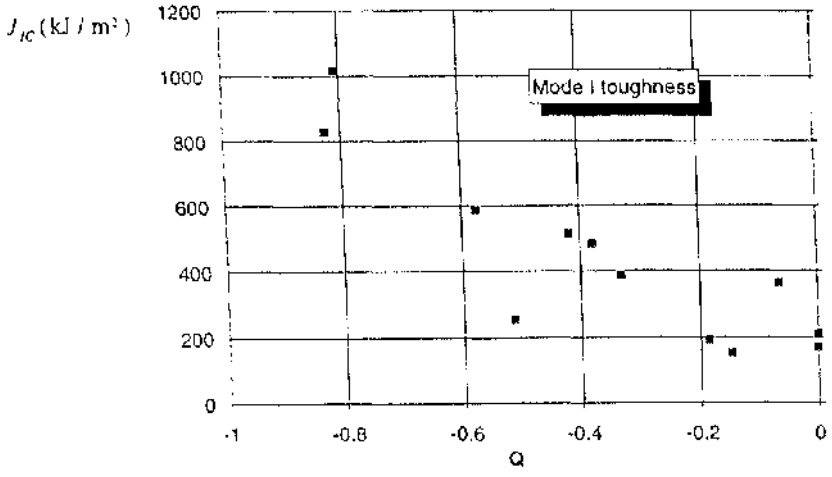

Figure 8.19 Experimental data in a *J-Q* locus for 3PB test from Betegón (1991).

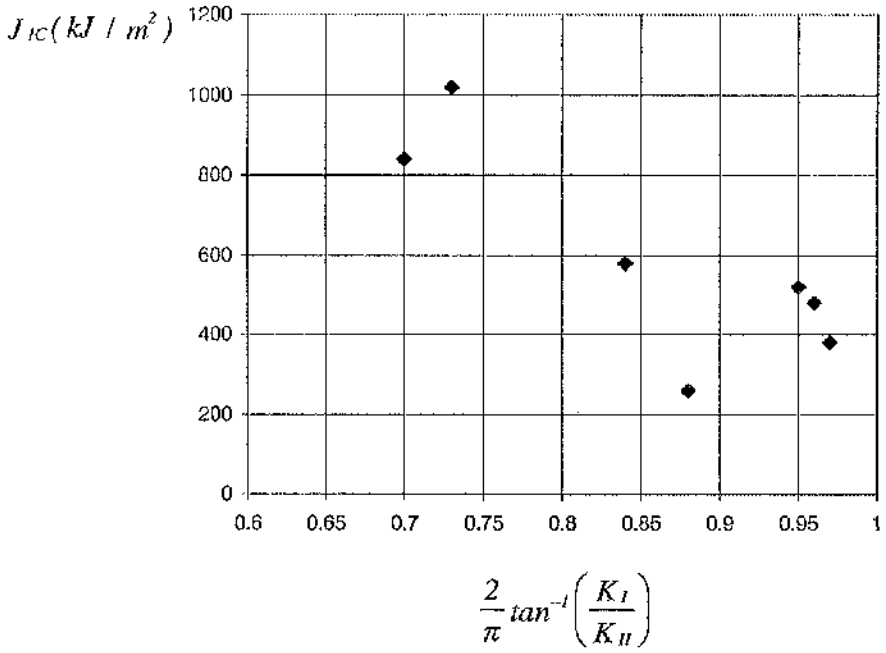

Figure 8.20 J-Mel Locus for strength mismatched interfacial crack. y=1.25, n=13.

Chapter 9 A crack normal to a strength mismatched interface

9.1 Introduction

In welded structures cracks often occur in a hard phase, such as a heat affected zone adjacent to a softer phase such as the parent plate. A similar configuration occurs in composite materials when high strength fibres embedded in a ductile matrix may crack. Such cracks may lie in the interface or be normal to it. This chapter investigates the features of cracks normal to a strength mismatched interface under mode I and mixed mode loading.

9.2 Model description

As usual in-plane Cartesian co-ordinates (x_1, x_2) and cylindrical co-ordinates (r, θ) centred at the crack tip are employed. The crack flanks lie on the $-x_1$ axis ($\theta=\pm\pi$) while the interface lies on $\pm x_2$, $x_1=0$, $\theta=\pm\pi/2$ as illustrated in Figure 9.1. The crack tip is located in the interface between two elastically identical but strength mismatched materials. Material 1 is located in the right half space, $x_1>0$ and material 2 is located in the left half space, $x_1<0$. Both materials are either compressible or almost incompressible ($\nu=0.49$). Material 1 has an elastic-plastic response with a yield strain ($\sigma_0/E=0.0005$). Material 2 is elastically identical, but has an infinite yield strength so that the strength mismatch factor is infinity ($y=\infty$). Plastic deformation of the matrix is limited to small scale yielding under plane strain conditions, using the highly focused mesh described in Chapter 5 (see Figure 3.13). The boundary conditions correspond to a boundary layer formulation for a homogenous crack tip field. Displacement loading characterised by stress intensity factors K_I and K_{II} for a homogenous material was applied to the outer circumference of the mesh. Calculations were then performed with both compressible and incompressible responses under the five levels of elastic mode mixity shown in Table 6.1, as well as mode I with different levels of T stress. The stresses at the crack tip were taken from the central integration points of each element and extrapolated linearly along radial lines to the tip such that the tip was approached asymptotically at different angles. Post

processing was carried out using Matlab (1992) which is a commercial software designed for matrix calculations.

9.3 Compressible deformation with a non hardening response

Figures 9.2 and 9.3 show the angular variation of the Mises and hydrostatic stresses under five levels of mode mixity with compressible elastic deformation. The deformation of the plastic sections is interpreted in terms of slip line fields which is justified by the almost incompressible plastic response. The corresponding slip line fields shown in Figure 9.4 are assembled in the following way: firstly, the angular span of the elastic sectors is determined from the angular range over which the yield criterion is not satisfied. Secondly the span of the centred fan is determined from the angular range over which the mean stress varies linearly with angle. Finally the constant stress sector is identified as the region in which the mean stress does not change with angle. For both pure mode I and pure mode II loading, the fields are symmetric with respect to the crack but this symmetry is lost under mixed mode loading. The mode I slip line field comprises a diamond directly ahead of crack and a centred fan between the diamond and the strength mismatched interface on each side of the crack. The plane of the maximum principal stress is oriented radially out through the constant stress sector. The maximum principal stress under mode I loading is thus located directly ahead of the crack. Under mainly mode I loading, the same fields are also admissible fields if material 1 is rigid because the slip lines are orthogonal to the interface. As the contribution from mode II increases, the constant stress diamond and the maximum principal stress direction rotate clockwise. Under pure mode II loading, the maximum principal stress occurs on the interface. For stress controlled brittle fracture, failure can be expected occur at these orientations in which the propagating crack extends locally in mode I.

9.4 Incompressible deformation with a non hardening response

Poisson's ratio has a significant effect on the development of crack tip plasticity. Figures 9.5~6 show the angular variation of both the Mises stress and the hydrostatic stress under five levels of mode mixity with incompressible deformation. The corresponding slip line fields shown in Figure 9.7 are

determined in the way described previously. It may be noted that the mode I slip line field in Figure 9.7a differs from that in Figure 9.4a in which the Poisson ratio is 0.3. In Figure 9.7a, plasticity does not completely surround the material 1 and an elastic sector appears directly ahead of the crack. Within this sector the mean stress has similar features to the constant stress sector in Figure 9.4a, in that a homogenous stress field is developed. When mode II loading starts to contribute, the span of the centred fan above the crack plane in material 1 has a span of 90^0. The span of the fan decreases with the contribution from mode II. Below the crack plane in material 1, a constant stress diamond appears under largely mode I loading. As the contribution from mode II increases, the constant stress sector rotates clockwise and becomes incomplete as it intersects the interface, while the span of the elastic sector increases. Under pure mode II loading, the slip line field is identical to Figure 9.4e with ν=0.3. The effect of mode mixity for an incompressible material is therefore similar to that for a compressible material.

9.5 Analytic solutions

To verify the numerical solutions, analytic solutions can be derived by using slip line theory for plastic sectors and elastic wedge solutions for the elastic sectors. For a given constraint or mean stress directly ahead of the crack, the whole field can be determined by ensuring the continuity of hoop and shear stress on the boundaries of the sectors but allowing a jump in radial stress across the strength mismatched interface. A comparison of the mean stresses obtained from both numerical and analytical methods is shown in Figure 9.8 for the pure mode I case and in Figure 9.9 for mixed mode cases. It is clear that they agree well.

9.6 Effect of T stress

The loss of constraint caused by a compressive T stress at a crack tip in homogeneous material has been investigated by Du and Hancock (1991). In order to examine the effect on a crack normal to a strength mismatched interface, the angular variation of the Mises stress and the mean stresses under mode I with different levels of T stress are plotted in Figures 9.10~11. With zero and positive T stresses, plasticity does not fully surround the crack tip in the

material 1 and the magnitude of the mean stresses are very similar. In comparison with the mean stress directly ahead of a crack in a homogenous material, the non-dimensionlised mean stress, *2.7*, was higher than that for a homogenous material (*2.3* under pure mode I). This indicates that the constraint of a crack normal to a strength mismatched interface is higher than that in a homogeneous material and hence lower toughness is expected.

Although plasticity develops at all angles in the soft material when the *T* stress was $-1.0\sigma_0$, the mean stress in the elastic sector ahead of the crack under positive or zero *T* stress has the same features as a plastic constant stress sector. The mean stress within this elastic sector also decreases as the *T* stress becomes more negative. This implies that compressive *T* stress causes a loss of constraint at the crack tip. A crack tip constraint parameter, Q, for a crack normal to the strength mismatched interface can be defined as the reduction in hydrostatic stress with respect to the homogenous SSY mode I field, $\sigma^{SSY}_{m(\theta=0)}$.

$$Q=\frac{\sigma_{m(\theta=0)}-\sigma^{SSY}_{m(\theta=0)}}{\sigma_0} \qquad (9\text{-}1)$$

Based on the numerical calculation, the relationship between Q and *T* for $n=\infty$ can be expressed approximately as

$$Q=2.34T/\sigma_0+0.42 \qquad T/\sigma_0 \le 0 \qquad (9\text{-}2)$$

Figure 9.12 shows the slip line fields under different levels of *T* stress.

9.7 Strain hardening

With a plastically non-hardening material, the fields can only differ by a hydrostatic term. Attention is now focused on investigating whether this feature is retained with a strain hardening response of the soft material 1.

In uniaxial tension the soft material is assumed to have elastic response for the stresses less than the uniaxial yield stress σ_0. Yield is determined by the von

Mises criterion. At stress greater than the yield stress, material 1 follows the uniaxial stress-strain relation shown in section 8.4. Figure 9.13 shows the stress-strain relation for both hardening and non-hardening materials. Material 2 is assumed to have the same elastic properties but an infinite yield stress.

9.7.1 Mode I field

The maximum principal stress under mode I loading occurs directly ahead of the crack due to the symmetry of applied loading and geometry. Figures 9.14~15 show the radial variation of the maximum principal and deviatoric stresses directly ahead of the crack tip for both strain hardening materials (*n=13, 6*). It is clear that they are deviatorically similar but differ hydrostatically. The relationship between *Q* and *T* for *n=13* can be expressed approximately as

$$Q=1.46T/\sigma_o+0.09 \qquad T/\sigma_o \leq 0 \qquad (9\text{-}3)$$

Using this relation, the data of *J-T* locus for mode I homogenous field given by (Sumpter, 1993) shown in Figure 3.17 can be mapped into *J*-Q plot for the crack normal to a strength mismatched interface as shown in Figure 9.16.

9.7.2 Mixed mode fields

In order to determine the plane of maximum principal stresses under mixed mode loading, the angular variation of hoop stresses for *n=13* and *6*, shown Figures 9.17~18, were obtained by extrapolating the data from the central integration station of each element to the tip. The plane of the maximum hoop stress is the plane of maximum principal stress. It may be noted that the maximum hoop stress decreases with mode mixity.

For both strain hardening rates, the radial variation of the maximum principal stress and the corresponding deviatoric stress under five levels of mode mixity on the plane of the maximum principal stress direction are shown in Figures 9.19~20. The stresses are non-dimensionlised with respect to the uniaxial yield stress of material 1, σ_o, while the radial distance from the crack tip, *r*, is non-

dimensionlised by J/σ_0. The important point is that the fields with weak and moderate strain hardening differ mainly hydrostatically but remain deviatorically similar.

The relationship of the constraint parameter, Q, and the elastic mode mixity, M_{el}, is thus illustrated in Figure 9.21 for hardening exponents $n=13$. For stress controlled fracture, the J-Q locus from mode I data given by Betegòn (1991) shown in Figure 8.26 can now be mapped into mixed mode data, *J-mixity* locus shown in Figure 9.22 for $n=13$, by using the Q-M_{el} relationship given in Figure 9.21.

9.8 Conclusions

The asymptotic stress field for a crack normal to a strength mismatched interface has been investigated by using boundary layer formulations under mode I with different levels of T stress and mixed mode loading. With incompressible and non-hardening deformation, the mean stress directly ahead of the crack tip under mode I with zero and positive T stress is higher than that in the corresponding homogeneous SSY field. Higher constraint and lower toughness than mode I homogenous field are thus expected for a crack normal to a strength mismatched interface. With weak and moderate strain hardening, the loss of constraint due to a compressive T stress gives rise a family of fields which differ in a largely hydrostatic manner. This allows the toughness in homogenous material under mode I loading to be correlated with a crack normal to a strength mismatched interface.

A feature of mixed mode fields which is similar to that of homogeneous materials, is that, mode II component causes a loss of constraint at the crack tip. On the plane of the maximum principal stress for a weak and moderate strain hardening material, there is a family of fields which are deviatorically similar but hydrostatically different. For stress controlled fracture, this allows the constraint based homogeneous mode I failure J-Q locus to be mapped into the strength mismatched mixed mode data, *J-mixity* locus.

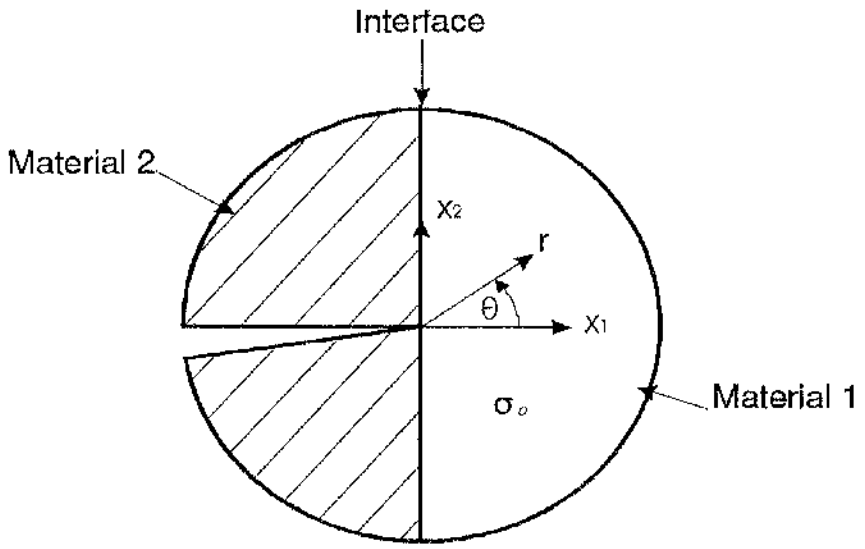

Figure 9.1 Illustration of a crack normal to a strength mismatched interface.

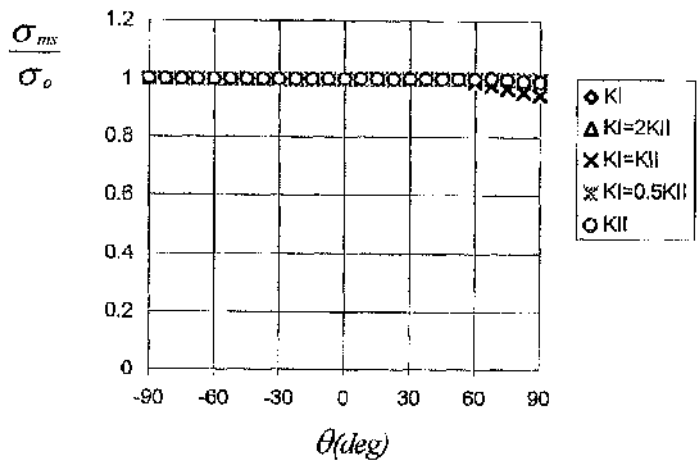

Figure 9.2 Mises stress around the tip of a crack normal to a strength mismatched interface. y=oo, $\nu = 0.3$

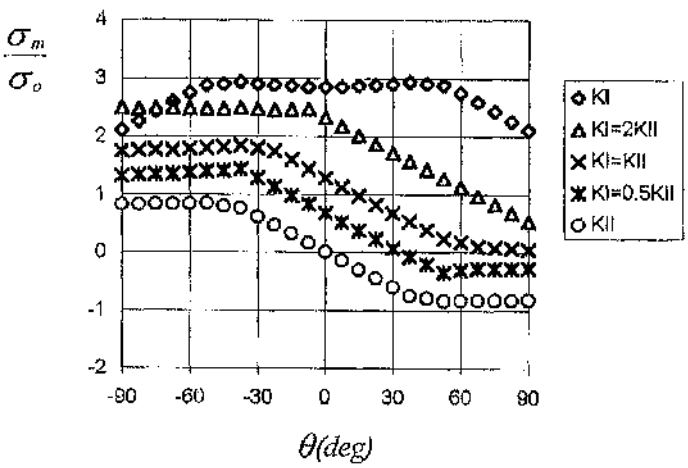

Figure 9.3 Mean stress around the tip of a crack normal to a strength mismatched interface. y=oo, $\nu = 0.3$

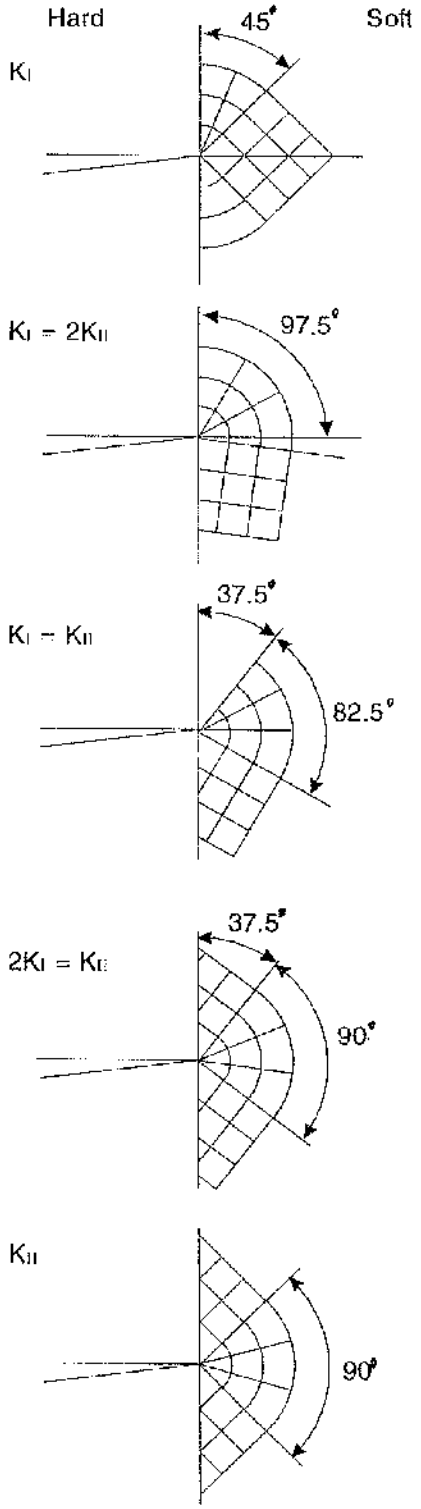

Figure 9.4 Slip line fields for a crack normal to a strength mismatched interface, ν=0.3.

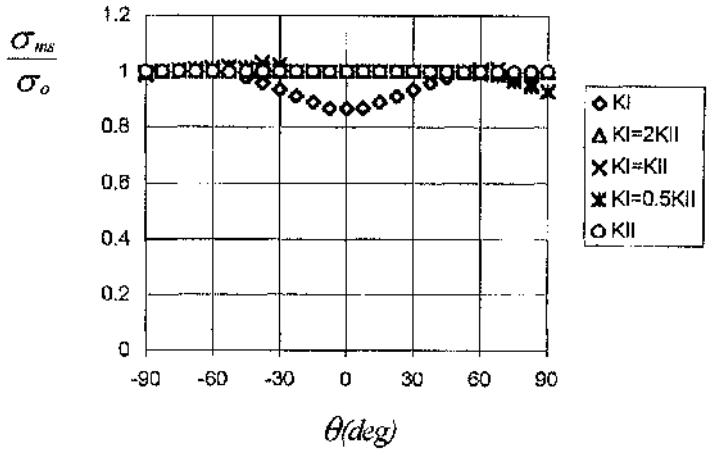

Figure 9.5 Mises stress around the tip of a crack normal to a strength mismatched interface. y=oo, $\nu = 0.49$

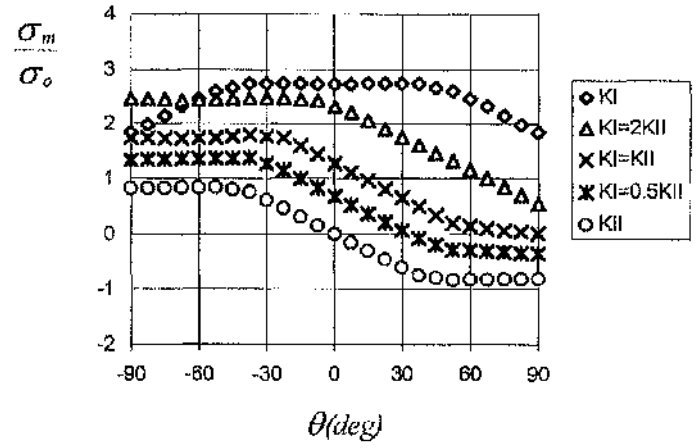

Figure 9.6 Mean stress around the tip of a crack normal to a strength mismatched interface. y=oo, $\nu = 0.49$

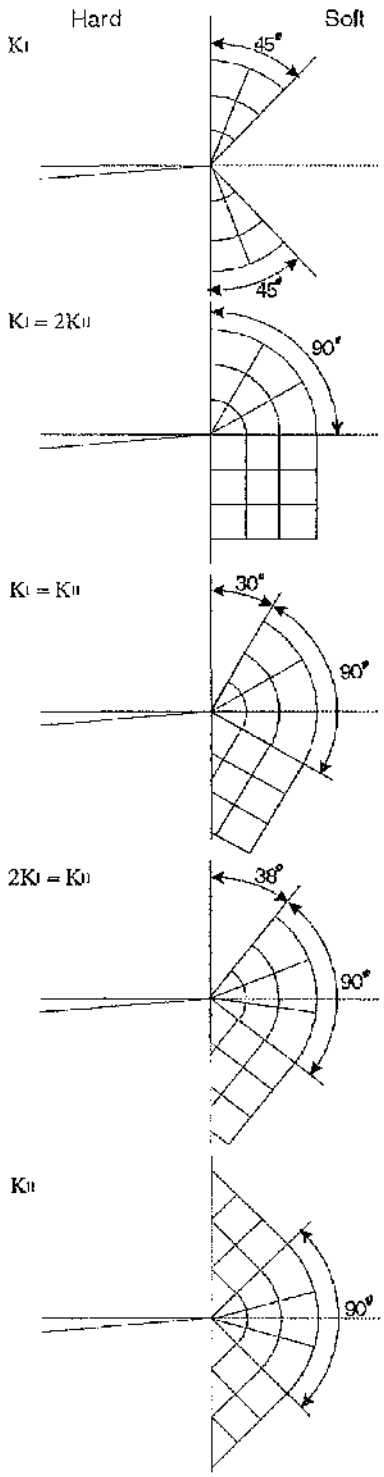

Figure 9.7 Slip line fields for a crack normal to a strength mismatched interface, ν=0.49.

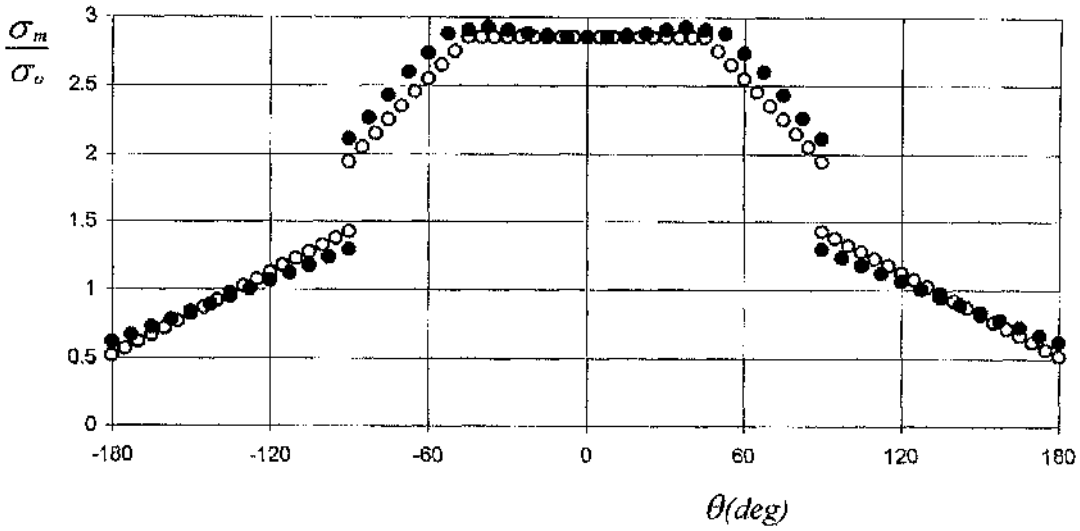

Figure 9.8 A comparison of mean stresses obtained from analytic solution (open circles) and numerical solution (solid data points) for a crack normal to a strength mismatched interface under mode I loading, $\nu = 0.3$

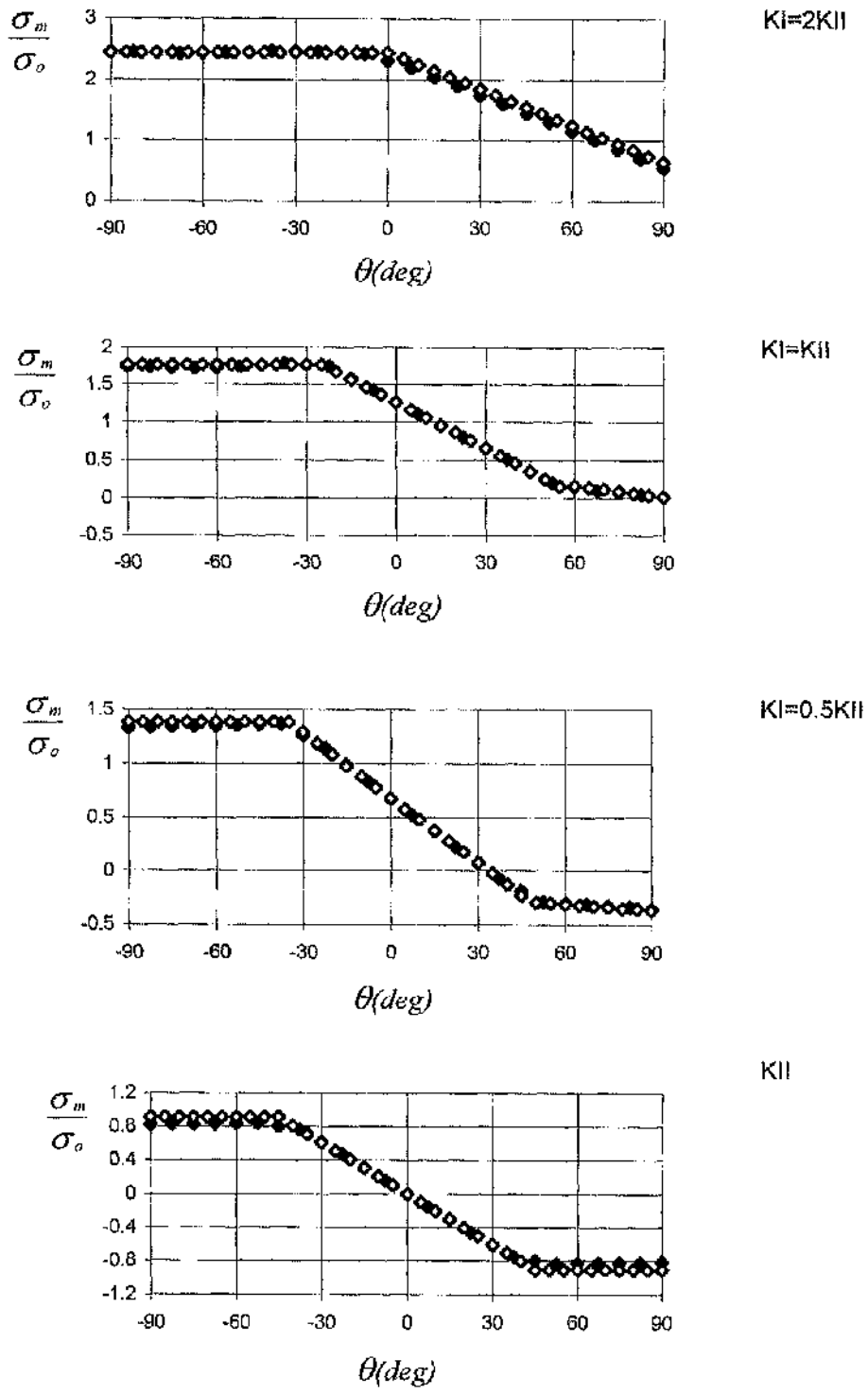

Figure 9.9 A comparison of mean stresses obtained from analytic solution (open data points) and numerical solution (solid data points) for a crack normal to a strength mismatched interface under mixed mode loading, $\nu = 0.49$

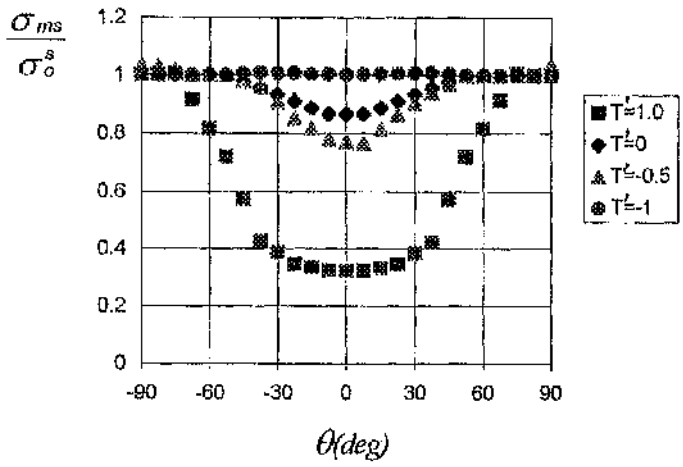

Figure 9.10 Mises stress around the tip of a crack normal to a strength mismatched interface. y=oo, $\nu = 0.49$, $T' = T / \sigma_o$

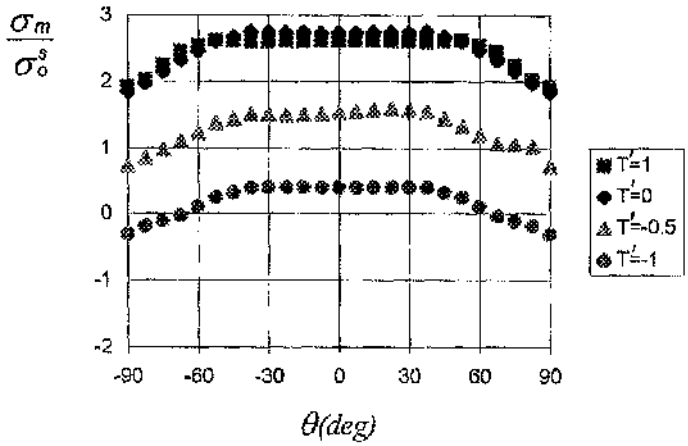

Figure 9.11 Mean stress around the tip of a crack normal to a strength mismatched interface. y=oo, $\nu = 0.49$, $T' = T / \sigma_o$

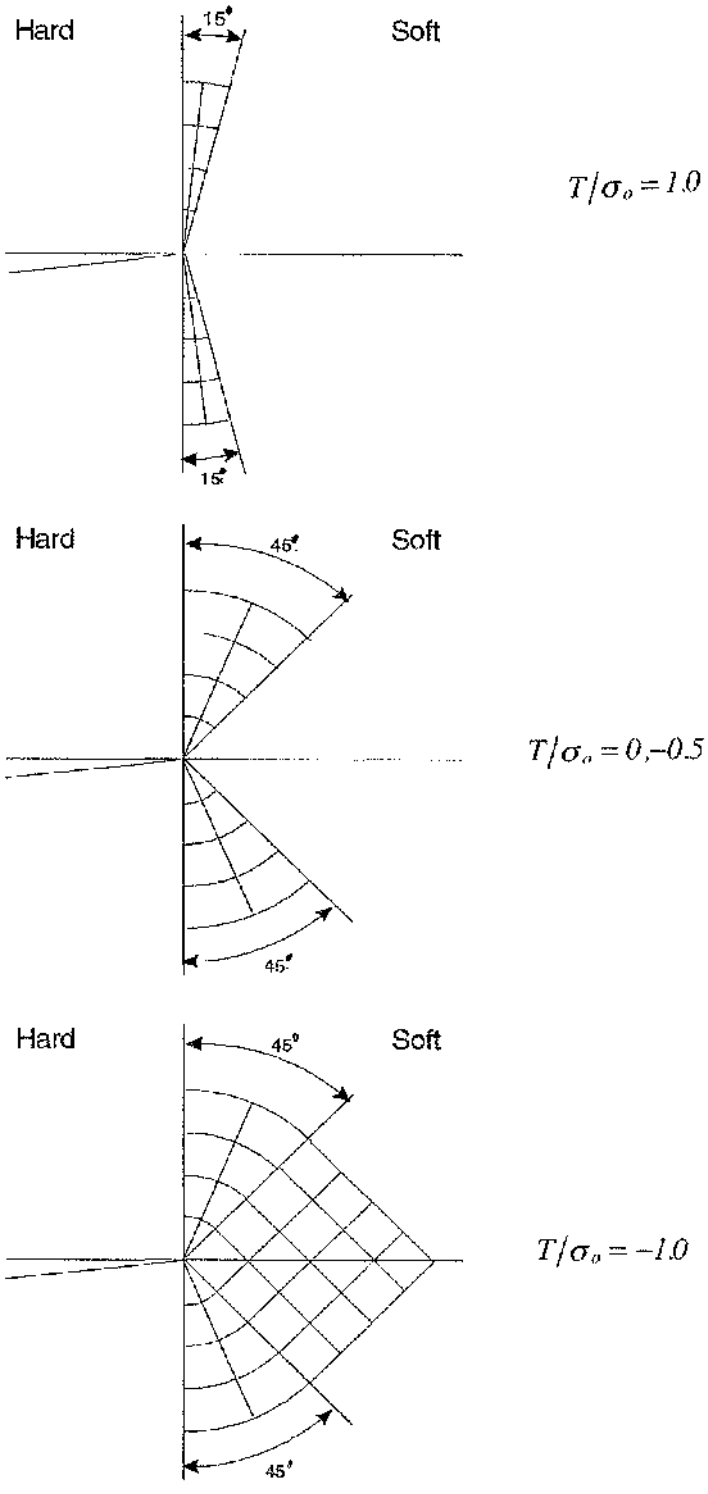

Figure 9.12 Slip line fields for a crack normal to a strength mismatched interface under different levels of T stress.

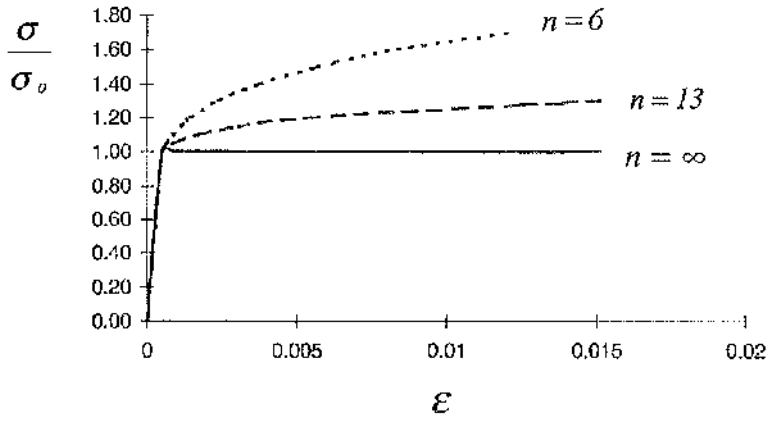

Figure 9.13 Stress strain relations for soft material.

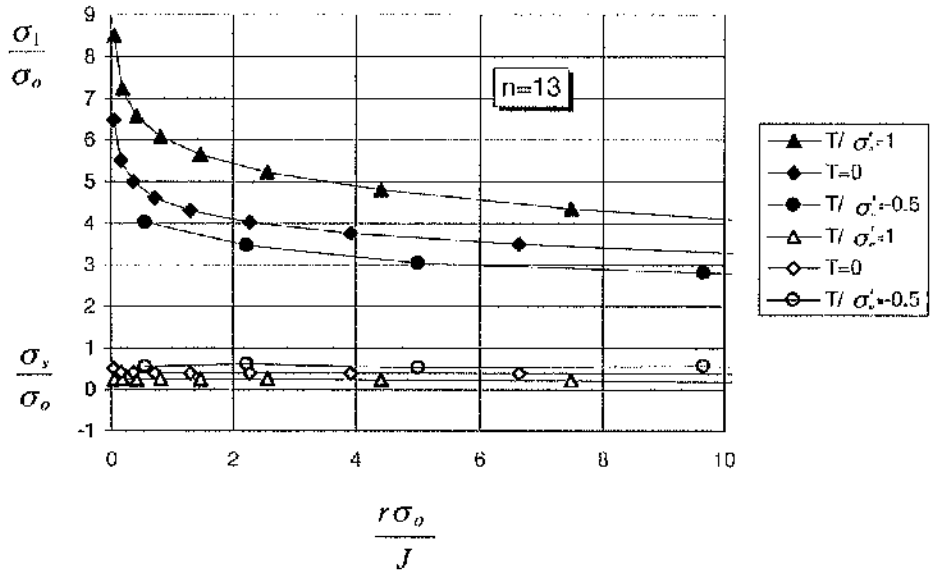

Figure 9.14 Radial variation of the maximum principal stress (solid data points) and deviatoric stress (open marks).

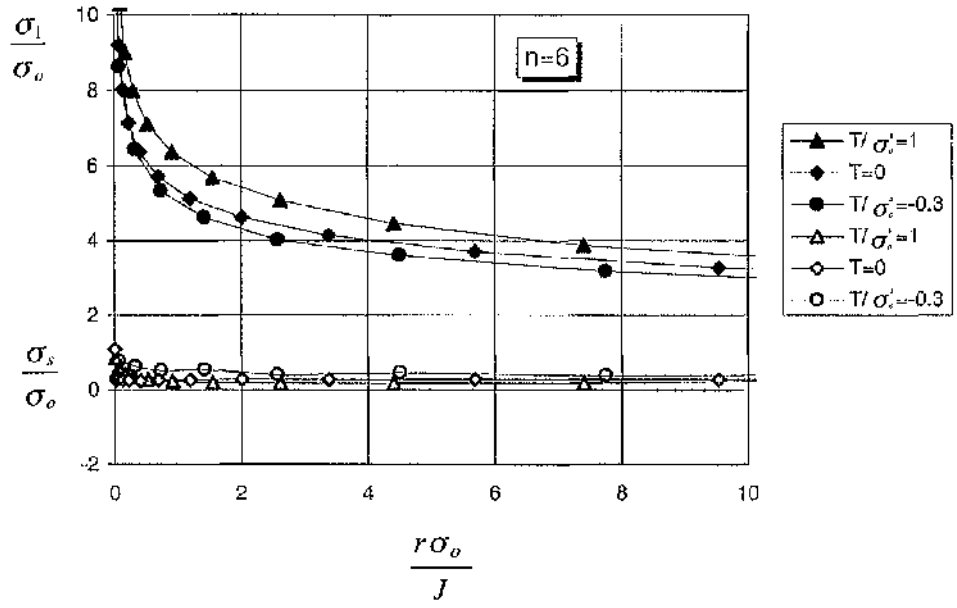

Figure 9.15 Radial variation of the maximum principal stress (solid data points) and deviatoric stress (open data points).

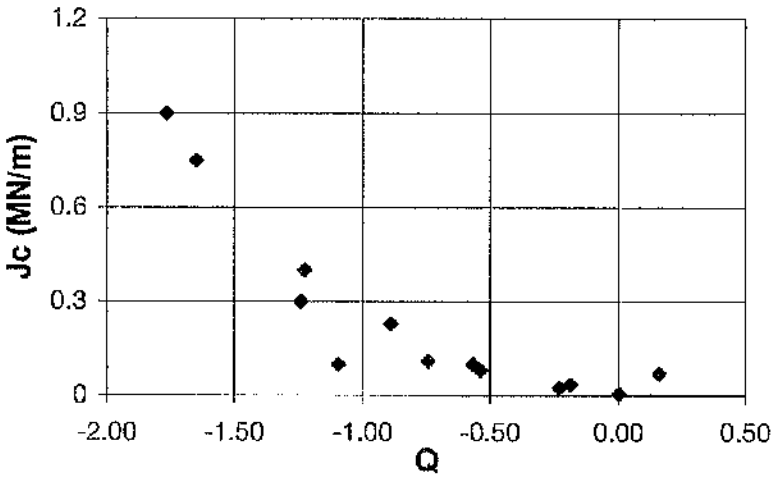

Figure 9.16 Mapping of a J-T locus (Sumpter, 1993) into a J-Q locus for a crack normal to a strength mismatched interface, n=13.

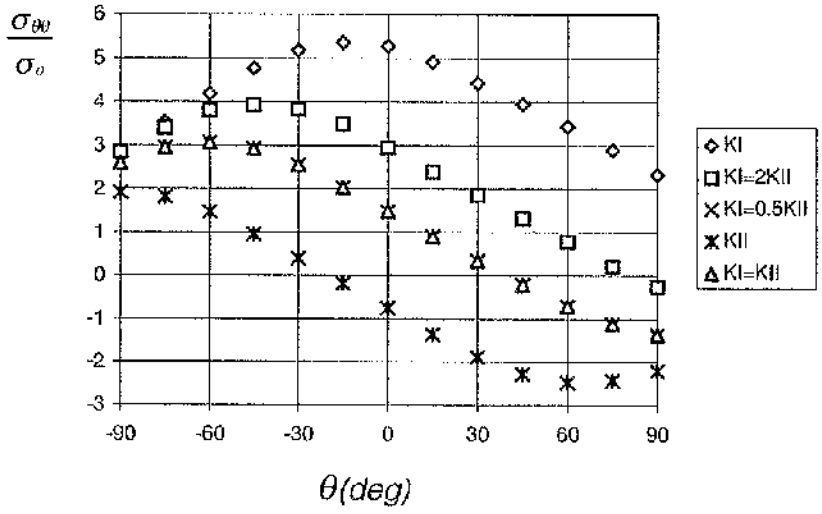

Figure 9.17 Angular variation of hoop stresses under mixed mode loading for a crack normal to a strength mismatched interface, n=13.

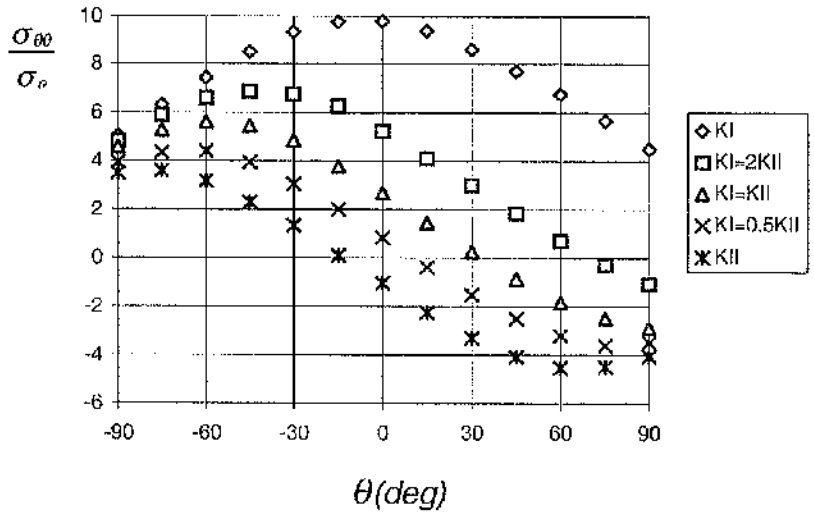

Figure 9.18 Angular variation of hoop stresses under mixed mode loading for a crack normal to a strength mismatched interface, n=6.

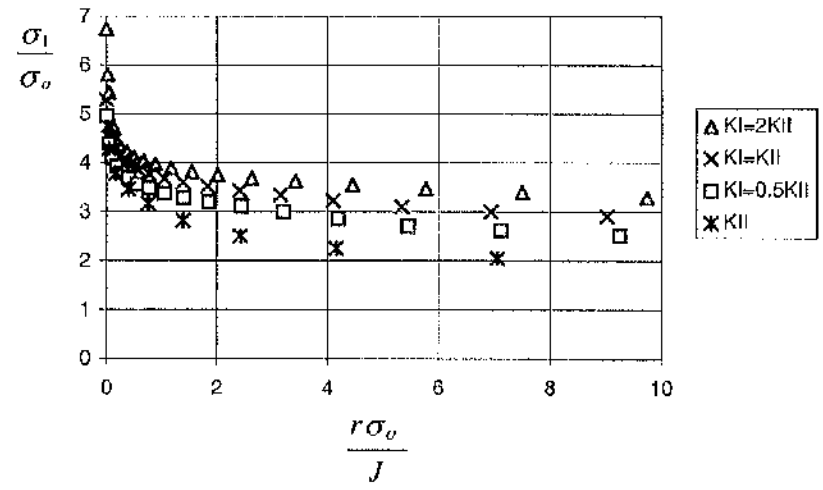

(a)

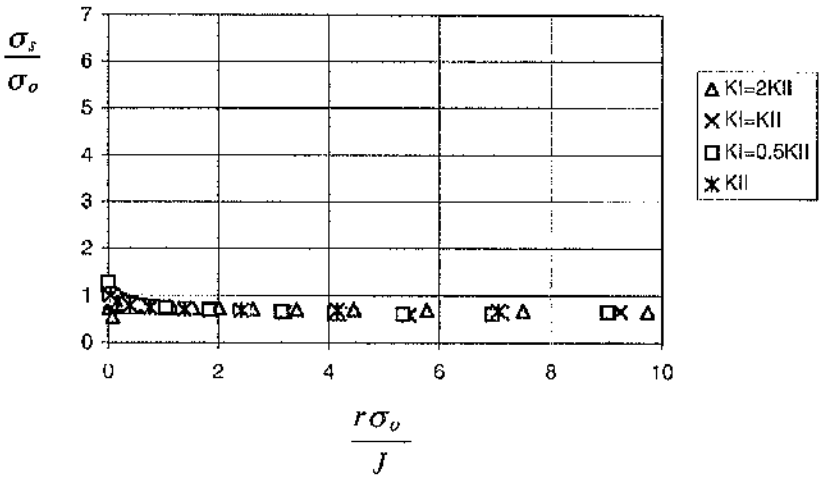

(b)

Figure 9.19 Radial variation of Maximum principal (a) and deviatoric (b) stresses under mixed mode loading for a crack normal to the interface, n=13.

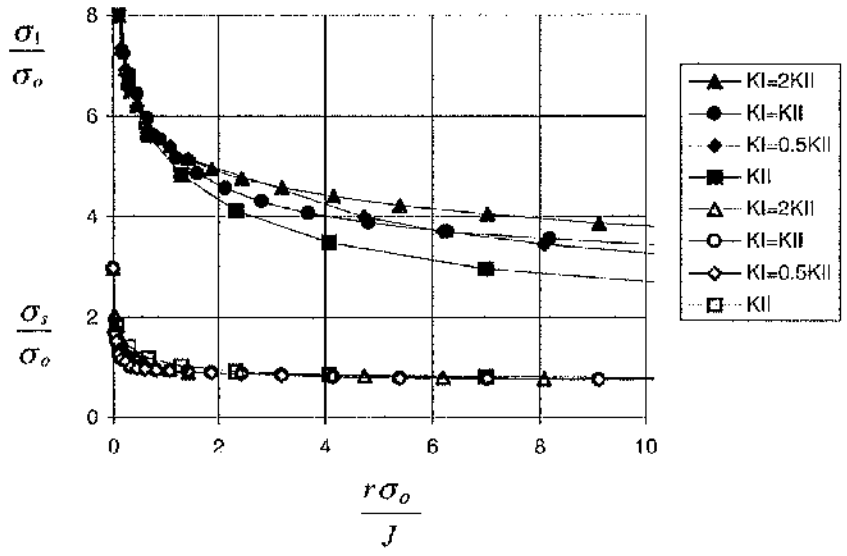

Figure 9.20 Radial variation of the maximum principal (solid data points) and deviatoric (open data points) stresses under mixed mode loading for a crack normal to a strength mismatched interface, n=6.

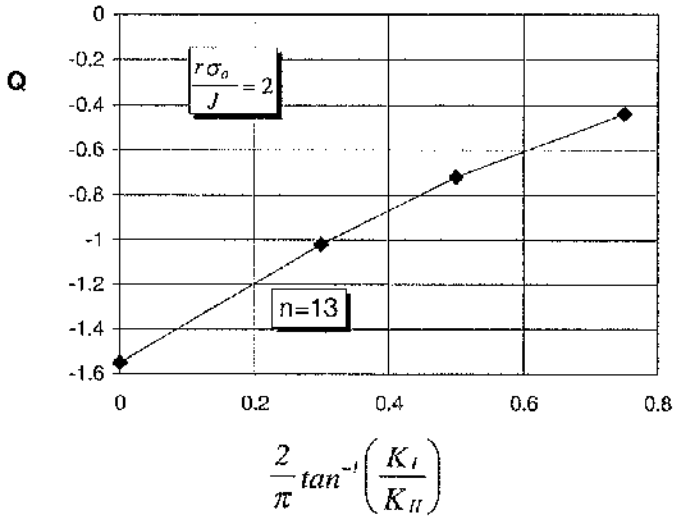

Figure 9.21 Constraint parameter as a function of elastic mode mixity for a crack normal to a strength mismatched interface.

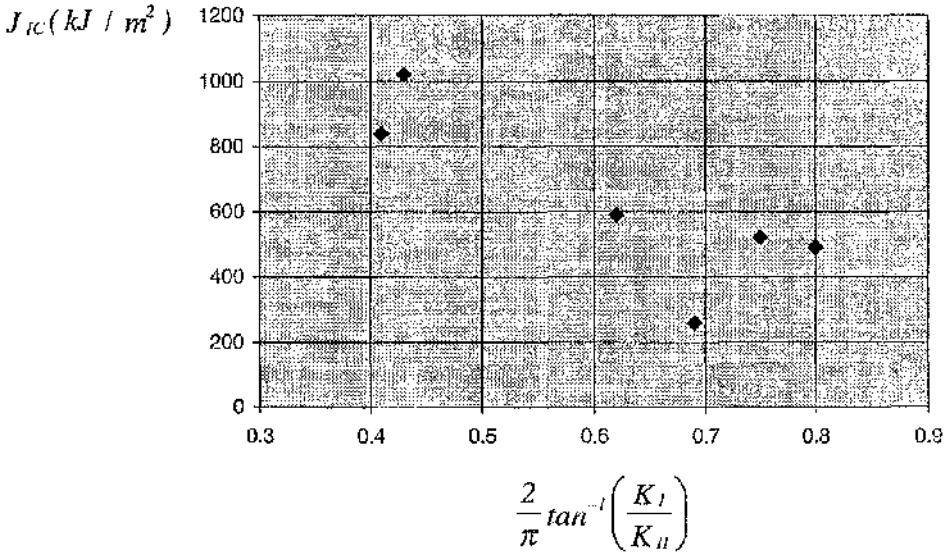

Figure 9.22 J-Mel Locus for a crack normal to a strength mismatched interfacial crack.

Chapter 10 Conclusions and future work

10.1 Conclusions

Asymptotic plane strain solutions for Mode I fields have been constructed using slip line solutions for plastic sectors and semi-infinite wedge solutions for elastic sectors. The fields, which exhibit full continuity of tractions, have been verified by numerical calculations using modified boundary layer formulations. The loss in crack tip constraint depends on the T stress. This feature is retained by weak and moderately strain hardening materials. The loss in constraint can be quantified by Q, which can be determined analytically for non-hardening deformation. The relevant fracture toughness depends on constraint through a J-Q/T failure locus.

For homogeneous materials mixed mode loading also results in a loss in crack tip constraint. On the plane of the maximum hoop stress, the mixed mode fields are hydrostatically different but deviatorically similar for both non hardening and moderately strain hardening materials. This has allowed relations to be established between constraint and remote elastic mode mixity.

For cracks lying an interface between a rigid substrate and an elastic-plastic material subject to a mixed mode loading with negative shear stresses, the maximum principal stress is located in matrix rather than interface. This may lead to matrix failure provided the interface is strongly bonded. On the plane of maximum hoop stress the fields can be interpreted as belonging to a single family which differ hydrostatically but are deviatorically similar, for both non hardening and moderate hardening rates.

A combination of numerical and analytic methods have been developed for the asymptotic small scale yielding crack fields of a crack located on the interface between two elastic-plastic solids, with matching elastic properties, but mismatched yield strengths. The results have been expressed as plane strain slip line fields which comprise combinations of elastic sectors, centred fans and

constant stress sectors. Solutions are developed under mixed mode loading as a function of the plastic mismatch between the two solids. Numerical solutions developed using finite element methods in which the small scale yielding field was modelled by boundary layer formulations agree well with analytic solutions. With strain hardening material, the maximum principal stress decreases with the contribution from mode II but increases with the strength mismatched factor. The planes of maximum principal stresses are located in the hard material and rotate clockwise as the mode II component increases. On these planes, the non-dimensionalised stress profiles are parallel and differ mainly by a hydrostatic term for weak and moderate levels of strain hardening. This allows stress controlled fracture to be correlated with the toughness measured in the unconstrained mode I fields of homogenous materials.

The crack tip stress field for a crack normal to a strength mismatched interface under mode I with different level of T stresses has been shown to exhibit a loss of constraint due to a compressive T stress. This gives rise a family of fields which differ in a largely hydrostatic manner for both non hardening and strain hardening materials. Under mixed mode loading, the Mode II component causes a loss of constraint at the crack tip. On the plane of maximum principal stress in the hardening material, there is a family of fields which are deviatorically similar but which differ hydrostatically.

For all these fields, the strength of the dominant singularity in the leading sectors around the plane of maximum hoop stress is similar to the unconstrained mode I fields. Constraint loss can be expressed by the introduction of a distance independent second order term which is largely hydrostatic in nature. The fracture resistance of these configurations can thus be unified by a single constraint based homogeneous fracture toughness locus for stress controlled failure.

10.2 Future work

Strength mismatch may occur due to either a difference in initial stress or different strain hardening rate. The ratio of the strain hardening rates may have a strong effect on the strength mismatched interfacial crack tip stress field under mixed mode loading. This should be investigated in the future.

Since the T-stress and mode II loading both cause a loss of constraint at the crack tip, the correlation of the effects of T-stress and mode II loading may need to be explored experimentally to determine the theoretically proposed criterion between crack extension in homogenous materials and bi-material interface.

Relations between local and remote fields have yet to be established analytically. For example the relation between the remote elastic mixity and the local plastic mixity (phase angle) can only be established computationally. Similarly the connection between T-stress and constraint has yet to be established analytically.

• Chapter 11 References

- ABAQUS, V.5.4 (1994). ABAQUS Manual. Hibbitt, Karlsson and Sorenson Inc. Providence Rhode Island.
- Al-Ani, A. M. and Hancock, J. W. (1991). "J-dominance of short cracks in tension and bending". *Journal of Mechanics and Physics of Solid* ***39(1)*** *pp.23-43.*
- ASTM (E339-83 1983). *Standard method for plane strain fracture toughness testing of metallic materials.* Vol. 03 01. American Society for testing and Materials. Philadelphia. pp. 487-511. Metal test methods and analytical procedures.
- Betegón, C (1990), Two parameter elastic-plastic fracture mechanics, PhD thesis. *Universedad de Oviedo, Spain.*
- Betegón, C and Hancock. J. W., (1991). Two parameter characterisation of elastic-plastic crack tip fields. *Journal of Applied Mechanics* **58,** *pp.104-110.*
- Bilby,B. A, Cardew, G. E., Goldthorpe, M. R. and Howard, I. C., (1986). "A finite element investigation of the effect of specimen size and geometry on the field of stress and strain at the tip of stationary cracks," *on Size effects in fracture, (I. Mech. E., Lond), pp.37-46.*
- British Standard (BS-7448 1991b). *Method for determination of* K_{IC}*, critical CTOD and critical J values of metallic materials.* London.
- Broek, D. (1991). Elementary Engineering Fracture Mechanics. *4 edn. Kluwer Academic Publisher. Dordrecht.*
- Budden, P. J. (1987). "The stress field near a blunting crack tip under mixed modes I and II", *Journal of Mechanics and Physics of Solid* ***35(4),*** *pp.457-478.*
- Champion, C. R., and Atkinson, C., (1991), "A crack at the interface between two power-low materials under plane strain loading", *Proceeding of Royal Society in London.* ***A432****, pp.547-553.*
- Chawla, K. K., (1987), Composite materials - Science and Engineering, *Springer-Verlag New York, Inc.*

- Comninou, M., (1977), "The interface crack", *Journal of Applied Mechanics. **44**, pp.631-636.*
- Comninou, M., (1990), "An overview of interface cracks". *Engineering Fracture Mechanics. **37**, pp.197-208.*
- Du, Z. Z and Hancock, J. W. (1991) The effect of non-singular stresses on crack tip constraint. *Journal of Mechanics and Physics of Solids, **39**, pp.555-567.*
- Du, Z. Z. and Betegón, C. and Hancock, J. W., (1991), "J dominance in mixed mode loading", *International Journal of Fracture, **52**, pp.191-206.*
- England, A. H., (1965), "A crack between dissimilar media", *Journal of Applied Mechanics, **32**, pp400-402.*
- Erdogan, F and Sih, G. C. (1963), *Journal of Basic Engineering, **85**, pp.519.*
- Ewing, J. W. (1968), "The plastic yielding of V notched tension bars with circular roots". *Journal of Mechanics and Physics of Solids, **16**, pp.305.*
- Fang, N. J.-J and Bassani. J. L., (1995), "Non-linear Analysis of Interfacial Cracks", *IUTAM Symposium on Non-linear Analysis of Fracture, University of Cambridge, pp.343-352.*
- Fang, N. J.-J and Bassani. J. L., (1996). "Non-linear fields of interfacial cracks - Part I. Asymptotic Solutions", Submitted to *Journal of Mechanics and Physics of Solids.*
- Ganti. S and Parks D. M, (1997). "Elastic-plastic fracture mechanics of strength-mismatched interface cracks", *Recent Advanced in Fracture, Edited by Mahidhara. R. K, et al, The Minerals, Metals & Materials Society. pp.13-25.*
- Geiringer, H., (1930). Beitrag zum Vollständigen ebenen Plastizitäts-problem, *Proceeding of 3rd International Conference of Applied Mechanics, **2** pp.185.*
- Green, A. P. (1953). "The plastic yielding of notched bars due to bending". *Quart. Journal of Mechanics and Applied Mathematics **6**, pp.223-239.*
- Griffith, A,A., (1920), "The phenomena of Rupture and flow in solids", *Philosophical Transactions, series A, Vol. **221**, pp.163-198.*
- Hancock J.W and Li. J, (1997), " Elastic plastic crack tip fields parameterised by constraint", *Published in Recent Advances in Fracture, edited by*

R.K.Mahidhara et,al, The Minerals, Metals and Materials Society, USA, pp.27-38.

- Hancock, J. W., Nekkal, A. and Karstensen, A. D. (1997) "Constraint effects in mixed mode loading". *Proceedings of the Ninth International Conference on Fracture, **4**, pp.2015-2023.*
- Hancock, J. W., Reuter W. A. and Parks. D. M., (1993). "Toughness and Constraint parameterised by T". *Constraint effects in Fracture ASTM STP **1171**, pp.121-40. Philadelphia, PA: American Society for Testing and Materials.*
- Hencky, H. Z. (1923), über einige statisch bestimmte Fälle des Gleichgewichts in plastischen Körpern, *Z. angew. Math. Mech., **3**, pp.241.*
- Hill, R. (1950) The Mathematical Theory of Plasticity, *Oxford University Press, Oxford.*
- Hutchinson, J. W. (1968a). Singular behaviour at the end of a tensile crack in a hardening material. *Journal of Mechanics and Physics of Solids **16**, pp.13-31.*
- Hutchinson, J. W. (1968b). Plastic stress and strain fields at a crack tip. *Journal of Mechanics and Physics of Solids **16**, pp.337-347.*
- Hutchinson, J. W., (1990), "Mixed mode fracture mechanics of interfaces". *Metal Ceramic Interfaces. pp. 295-306. Eds. M. Ruhle, A.G. Evans, M. F. Ashby, and J. P. Hirth, Pergamon Press.*
- Hutchinson, J. W., (1987), "Crack Paralleling an Interface Between Dissimilar Materials", *Journal of Applied Mechanics. Vol. **54**, pp.828-832.*
- Irwin, G. R., (1957), *Encyclopedia of Physics, S. Flugge (ed), Vol. Springer pp.551-590.*
- Karstensen, A. D, Nekkal, A. and. Hancock, J. W.,(1997). "Constraint of elastic-plastic crack tip fields". *Proceedings of the Ninth International Conference on Fracture. **4**, pp.2007-2015.*
- Karstensen, A. D. (1996). Constraint estimation schemes in fracture mechanics. *Department of Mechanical Engineering, University of Glasgow. PhD, Thesis.*
- Kelly, A and Groves, G. W., (1970). Crystallography and crystal defects, *Longman Group Limited, London.*

- Kfouri A.D. (1986). "Some evaluations of the elastic T term using Eshelby's method". *International Journal of Fracture Mechanics, **30**, pp.301-313.*
- Kim Yun-Jae, Lin. G, Cornec. A (1996), "Non-singular stress in elastically dissimilar bimaterials and its effect on crack-tip constraint in SSY", *To appear in International Journal of Solid and Structures.*
- Kirk, M. T., Koppenhoefer, K. C. and Shih, C. F. (1993). "Effect of constraint on dimensions needed to obtain structurally relevant toughness measures, Constraint effects in fracture." *American Society for Testing and Materials ASTM STP **1171**, pp.121-40. Philadelphia, PA: American Society for Testing and Materials.*
- Kocak, el al., (1988). "CTOD testing of HAZ and analysis of pop-in behaviour", *Proceeding of the 7th Conference on Offshore Mechanics And Arctic Engineering. ASME, pp.297-304.*
- Larsson and Carlsson, (1973). "Influence of non-singular terms on the specimen geometry on small scale yielding at crack tip in elastic-plastic materials". *Journal of Mechanics and Physics of Solids, **21**, pp.263-277.*
- Leevers, S. G. and Radon, J. C. (1983). " Influence of non-singular stress terms and specimen geometry on small-scale yielding at crack tips in elastic plastic material". *International Journal of Fracture **19**, pp.942-955.*
- Li, J and Hancock, W. J, (1996), " Mode I and mixed fields with incomplete crack tip plasticity" *International Journal of Solids and Structures. In press.*
- Li, Y and Wang, Z., (1986). "High-order asymptotic field of tensile plane-strain non-linear crack problem". Scientia Sinica ***A29**, pp.941-955.*
- Li. J and Hancock. J.W., (1997), " Plane strain elastic plastic crack tip fields unified by constraint", *Published in Anales De Mecanica De La Fractura, Numero **14**, p1-11, Ano 1997, Ribadesella, Spain.*
- Li. J and.Hancock. J. W, (1997). " A combined Numerical and analytical method for constructing plane strain slip line fields in cracked solids", *Presented in 5th ACME Conference in April, 1997. London.*
- Matlab (1992,) Matlab manual. *The Math Works Inc. Version 4.*
- McClintock F. A. and Argon A. S., (1966). Mechanical Behaviour of Materials. *Addison-Wesley Publishing Company, Inc, Reading, Massachusetts, USA.*

- McClintock, F .A., (1971), Plasticity aspects of fracture, *In Fracture: an advanced treatise (ed. H. Liebowitz).* ***3****, pp.47-225, London: Academic Press.*
- McMeeking, R. M. and Parks, D. (1979). "On criteria for J-dominance of crack tip fields in large scale yielding". *In Elastic Plastic Fracture, ASTM STP* ***668****, pp.175-194. Philadephia, PA: American Society for Testing and materials.*
- Minami, F, Toyoda.M, Thaulow. C and Hauge.M, (1994), "Effect of strength mismatch on fracture mechanical behaviour of HAZ-notched weld joint". *Proceeding Of the 2nd Workshop on Constraint Effects on the Structural Performance of Welded Joints, Osaka, Japan.*
- Nadai. A., (1963). Theory of Flow and Fracture of Solids. *Volume II, published by McGraw-Hill Book Company, Inc. pp.210-217.*
- Nekkal, A. (1991). A two parameter approach to elastic-plastic fracture mechanics. *Msc thesis. Department of mechanical engineering, University of Glasgow.*
- Nemat-Nasser. S and Obata. M, (1984). On stress field near a stationary crack tip. *Mechanics of Material,* ***3****, pp.235-243.*
- O'Dowd, N. P. and Shih, C. F., (1991a). "Family of crack tip fields characterised by a triaxiality parameter: Part I - Structure of fields." *Journal of Mechanics and Physics of Solid,* ***39,*** *pp.939-963.*
- O'Dowd, N. P. and Shih, C. F., (1991b). "Family of crack tip fields characterised by a Triaxiality parameter: Part II - Fracture applications." *Journal of Mechanics and Physics of Solid,* ***39,*** *pp.989-1015.*
- PATRAN V.2.5, (1994). User's Manual. *PDA Engineering, California*
- Prandtl, L., (1920), *Nachr. Ges. Wiss.,* Gottingen.
- Quanxin Guo and Keer, L. M. (1990), "A crack at the interface between an elastic-perfectly plastic solid and a rigid substrate", *Journal of Mechanics and Physics of Solids.* ***38****, pp.843-857.*
- Rice, J. R. (1974). "Limitations to the small scale yielding approximation for crack tip plasticity". *Journal of the Mechanics and Physics of Solids* ***22,*** *pp.17-26.*

- Rice, J. R. and Rosengren, G. F. (1968) "Plane strain deformation near a crack tip in a power low hardening material". *Journal of the Mechanics and Physics of Solids,* ***16,*** *pp.1-12.*
- Rice, J. R. and Tracey, D. M., (1973). In *Numerical and computational Methods in structural mechanics,* edited by S. J. Fenves *et al.*. Academic Press, New York.
- Rice, J. R., (1966), Fracture, *volume II, edited by Liebowitz, H, Academic press New York and London, pp.191-311.*
- Rice, J. R., (1968a), "A path independent integral and the approximate analysis of strain concentration by notches and cracks". *Journal of Applied Mechanics.* ***35,*** *pp.379-386.*
- Rice, J. R., (1968b), Fracture: an advanced treatise, *edited by H. Liebowitz,. Academic Press, New York,* ***2,*** *pp. 47.*
- Rice, J. R., (1982), "Elastic-plastic crack growth", in *Mechanics of Solid - The Rodney Hill 60th anniversary Volume* edited by H.G. Hopkins and M. J. Sewell, Pergamon Press Ltd, UK.
- Rice, J. R., (1988), "Elastic fracture mechanics concepts for interfacial cracks", *Journal of Applied Mechanics.* ***55,*** *pp.98-103.*
- Rice, J. R., and Sih,G. C., (1965), "Plane problems of cracks in dissimilar media," *ASME Journal of Applied Mechanics,* ***32,*** *pp. 418-423.*
- Sham, T. L, Li. J and Hancock. J. W (1998), "A family of crack tip fields for interface cracks in strength mismatched non-hardening solids". *Submitted to Journal of Mechanics and Physics of Solids.*
- Sham, T. L. (1991). "The determination of the elastic T-term using higher order weight functions". *International Journal of Fracture,* ***48,*** *pp.81-102.*
- Sharma, S and Aravas, N., (1993), "On the development of variable-separable asymptotic elastic solutions for interfacial cracks", *International Journal of Solids and Structures.* ***30,*** *pp.695-723.*
- Sharma, S. M and Aravas, N. J., (1991), "Determination of higher order terms in asymptotic elasto-plastic crack tip solutions". *Journal of Mechanics and Physics of Solids,* ***39,*** *pp.1043-1072.*
- Shih C. F (1974). "Small-scale yielding analysis of mixed mode plane strain crack problems." *Fracture Analysis, ASTM STP,* ***560,*** *pp.187-210.*

- Shih, C. F. and German, M. D., (1981). "Requirements for a one parameter characterisation of crack tip fields by the HRR singularities", *International Journal of Fracture,*. ***17, pp.27-43.***
- Shih, C. F., (1983). Tables of Huntchinson-Rice-Rosengren Singular field quantities, *Brown University report, MRL E-147.*
- Shih, C. F., (1991), "Cracks on bimaterial interfaces: Elasticity and plasticity aspects", *Material of Science and Engineering. **A143**. pp.77.*
- Shih, C. F., and Asaro, R. J. (1988), "Elastic-plastic analysis of cracks on bimaterial interfaces: Part I -- Small-scale yielding", *Journal of Applied Mechanics. **55**, pp.299-316.*
- Shih, C. F., andO'Dowd, N, P. (1992), " A fracture mechanics approach based on a toughness locus." *In Dawes, M. G. (Ed). Shallow crack fracture mechanics, toughness tests and applications. The Welding Institute publishing, Abington Cambridge, England.*
- Slater, R. A. C. (1977). Engineering plasticity. The Macmillan press Ltd, London and Basingstoke.
- Sumpter, J. and Hancock, J. W.,(1994), "Status review of the J plus T stress fracture analysis method", *In 10th fracture conference on fracture. pp.617-626.*
- Sumpter, J. D. G. (1993), "An experimental investigation of the stress approach". *In Hackett, E. M., Schwalbe, K. H. and Dodds, R. H (Eds.). 'Constraint Effect in Fracture, ASTM STP 1171'. American Society for Testing and Materials. Philadephia, PA. pp. 492-502.*
- Sumpter, J. D. G. and Forbes, A. T. (1992). "Shallow crack fracture mechanics, Toughness Tests and applications". *The Welding Institute. Publishing, Abington Cambridge, England, Edited by Dawes, M. G.*
- Thaulow. C, Paauw,A. J, Hauge. M, Toyoda. M, and Minami, F. (1994) "Fracture property of HAZ-notched weld joint with mechanical mis-matching – part II. *Mis-matching of welds. ESIS **17**. Mechanical Engineering Publications, London, pp.417-432.*
- Timoshenko, S. P. and Goodier, J. N. (1970). Theory of Elasticity *3rd edition, McGraw-Hill, New York.*

- Tracey, D., (1976), "Finite element solutions for crack tip behaviour in small scale yielding." ASME *Journal of Engineering Materials and Technology.* ***98,*** *pp.146-151.*
- Wang, T. C. (1990). "Elastic-plastic Asymptotic Fields for Cracks on Bimaterial Interfaces", *Engineering Fracture Mechanics,* ***37,*** *pp.527-538.*
- Williams, M, L., (1959), "The stresses around a fault or crack in dissimilar media," *Bulletin of the seismological Society of America.* ***49,*** *pp.199-204.*
- Williams, M. L. (1957) "On the stress distribution at the base of a stationary crack". *Journal of Applied Mechanics* ***24,*** *pp.111-114.*
- Williams, M. L. and Ewing, P. D. (1972). *International Journal of Fracture* ***8,*** *pp.441.*
- Xia, L., Wang, T. C. and Shih, C. F. (1993). "Higher-order analysis of crack tip fields in elastic power-law hardening materials". *Journal of Mechanics and Physics of Solids* ***41,*** *pp.665-687.*
- Yang, S., Chao, Y. J. and Sutton, M. A. (1993a). "Higher order asymptotic crack tip fields in a power-law hardening material". *Engineering Fracture Mechanics,* ***45(1),*** *pp.1-20.*
- Yang, S., Chao, Y. J. and Sutton, M. A. (1993b). "Complete theoretical analysis for higher order asymptotic terms and the HRR zone at a crack tip for mode I and mode II loading of a hardening material". *Acta mechanics* ***98,*** *pp.79-98.*
- Zhang, Z. L., Hauge, M and Thaulow, C., (1997). "The effect of T stress on the near tip stress field of an elastic-plastic interface crack', *Proceedings of the Ninth International Conference on Fracture,* ***4,*** *pp.2643-2650.*
- Zywicz, Z and Parks, D. M., (1989). "Elastic yield zone around an interfacial crack tip", *Journal of Applied Mechanics,* ***56,*** *pp.577-584*
- Zywicz, Z and Parks, D. M., (1992). "Small-scale Yielding interfacial crack-tip fields", *Journal of Mechanics and Physics of Solids,* ***40,*** *No3, pp.511-536.*

Appendix 1

Seven asymptotic crack tip configurations have been identified for an interface crack between elastically similar but strength mismatched materials. The configurations are described in terms of angle ϕ_i (i=1,6).

Configuration A, $\phi_1 \leq \phi \leq 90^0$

The angles ϕ_i (i=1 to 6) are shown in Table 8.1 for y=1.25 and 1.4. Consider the sector configuration given in Figure A1.1a. This configuration consists of:

Material I: starting from the upper crack face, CS-II sector, CF-II sector, general CS sector, and CF-I sector;

Material II: starting from the lower crack face, CS-I sector, CF-II sector, general CS sector, CF-I sector, and general CS sector.

There are 7 sector boundaries and 13 constants for the stresses. The conditions for determining these 20 unknowns are: 16 traction continuity conditions at 7 sector boundaries and 1 material interface, 3 conditions from enforcing yielding in 3 general CS-sectors, and equation 8.4 relating the interface tractions. Thus, the 20 unknowns from these 20 conditions can be determined when a phase angle ϕ is specified (Sam,1997). The details of the expressions for the sector angles and stresses for this configuration, and others to follow, are given in the Appendix 2.

As the phase angle ϕ is decreased from 90^0 the sector boundary at θ_6 rotates anticlockwise towards the one at θ_8 and the angular extent of the CF-II sector in the range $\theta_6 \leq \theta \leq \theta_8$ gradually decreases. When ϕ reaches ϕ_1, this centred fan vanishes and the two neighbouring constant stress sectors collapse into one CS-II sector. This $\phi = \phi_1$ limiting configuration is depicted in Figure A1.1b.

Configuration B, $\phi_2(y) \le \phi \le \phi_1$

As the phase angle ϕ is further decreased from ϕ_1, the stress level within CS-II sector in material I cannot sustain yield and a new sector configuration involving an elastic sector emerges as shown in Figure A1.2a. This configuration consists of:

Material I: starting from the upper crack face, elastic sector, and CF-I sector;

Material II: starting from the lower crack face, CS-I sector, CF-II sector, general CS sector, CF-I sector, and general CS sector.

There are 5 sector boundaries and 13 constants for the stresses. The conditions for determining these 18 unknowns are: 12 traction continuity conditions at 5 sector boundaries and 1 material interface, 2 traction free conditions for the upper crack face, 2 conditions from enforcing yielding in 2 general CS sectors ,1 condition from enforcing yielding of the elastic stress state at sector boundary θ_4, and equation 8.4 relating the interface tractions. Thus, we can determine these 18 unknowns from these 18 conditions when a phase angle ϕ is specified. The details are given in the Appendix 2. As the phase angle ϕ is decreased from ϕ_1, the angular extent of the CF-I sector in the range $\theta_3 \le \theta \le \theta_1$ gradually decreases. When ϕ reaches $\phi_2(y)$, this centred fan vanishes and the two neighbouring constant stress sectors emerge into one general CS sector. This $\phi=\phi_2(y)$ limiting configuration is depicted in Figure A1.2b.

Configuration C, $\phi_3(y) \le \phi \le \phi_2(y)$

As the phase angle ϕ is decreased from $\phi_2(y)$, the stress level within the general CS sector in material II cannot sustain yield and a new sector configuration involving an additional elastic sector emerges as shown in Figure A1.3a. This configuration consists of:

Material I: starting from the upper crack face, elastic sector, and CF-I sector;

Material II: starting from the lower crack face, CS-I sector, CF-II sector, and elastic sector.

There are 3 sector boundaries and 10 constants for the stresses. The conditions for determining these 13 unknowns are: 8 traction continuity conditions at 3 sector boundaries and 1 material interface, 2 traction free conditions for the upper crack face, 2 conditions from enforcing yielding of the elastic stress state at sector boundaries θ_4 and θ_1 and equation 8.4 relating the interface tractions. Thus, we can determine these 13 unknowns from these 13 conditions when a phase angle ϕ is specified. The details are given in the Appendix 2.

As the phase angle ϕ is decreased from $\phi_2(y)$ the sector boundary at θ_1 which separates the CF-II sector and the elastic sector in material II gradually rotates anticlockwise towards the interface and the stress level within the elastic sector increases. When the phase angle ϕ is decreased to $\phi_3(y)$, the elastic stress state in the angular range $\theta_1 \leq \theta \leq 0$ reaches yield in the entire sector. Thus, this elastic sector becomes a general CS sector in this limit. The $\phi=\phi_3(y)$ limiting configuration is depicted in Figure A1.3b.

Configuration D, $\phi_4(y) \leq \phi \leq \phi_3(y)$

As the phase angle ϕ is decreased from $\phi_3(y)$, an additional constant stress sector bordering the material interface is required in the new sector configuration as shown in Figure A1.4a. This configuration consists of:

Material I: starting from the upper crack face, elastic sector, CF-I sector, and general CS sector;

Material II: starting from the lower crack face, CS-I sector, CF-II sector, and general CS sector.

There are 4 sector boundaries and 12 constants for the stresses. The conditions for determining these 16 unknowns are: 10 traction continuity conditions at 4 sector boundaries and 1 material interface, 2 traction free conditions for the upper crack face, 2 conditions from enforcing yielding in 2 general CS-sectors, 1 condition from enforcing yielding of the elastic stress state at sector boundary θ_β in material I, and equation (8.4) relating the interface tractions. Thus, these 16 unknowns can be determined from these 16 conditions when a phase angle ϕ is specified. The details are given in the Appendix 2.

As the phase angle ϕ is decreased from $\phi_3(y)$, the sector boundary at θ_β in material I which separates the elastic sector and the CF-I sector rotates gradually towards the upper crack face and the stress state within the elastic sector elevates. When the phase angle ϕ is decreased to $\phi_4(y)$, the elastic stress state within the angular range $\theta_\beta \le \theta \le \pi$ reaches yield and this elastic sector is turned into a CS-I sector. This $\phi=\phi_4(y)$ limiting configuration is depicted in Figure A1.4b.

Configuration E $\phi_5(y) \le \phi \le \phi_4(y)$

As the phase angle ϕ is decreased from $\phi_4(y)$, the stress state within the CS-I sector in material II of Figure A1.4b cannot sustain the yield level. A new configuration involving an elastic sector emerges. This new sector configuration is shown in Figure A1.5a. This configuration consists of:

Material I: starting from the upper crack face, CS-I sector,CF-I sector, and general CS sector;

Material II: starting from the lower crack face, elastic sector, CF-II sector, and general CS sector.

There are 4 sector boundaries and 12 constants for the stresses. The conditions for determining these 16 unknowns are: 10 traction continuity conditions at 4 sector boundaries and 1 material interface, 2 traction free conditions for the lower crack face, 2 conditions from enforcing yielding in 2 general CS-sectors, 1 condition from enforcing yielding of the elastic stress state at sector boundary θ_7 in material II, and equation (8.4) relating the interface tractions. Thus, we can determine these 16 unknowns from these 16 conditions when a phase angle ϕ is specified. The details are given in the Appendix 2.

As the phase angle ϕ is decreased from $\phi_4(y)$, the sector boundaries at θ_4 in material I and at θ_7 in material II rotate anti-clockwisely. When ϕ is decreased to ϕ_5, a limiting configuration is realised where $\theta_4 = 90^0$ and the general CS sector in the angular range $0 \le \theta \le \theta_4$ becomes, in the slip-line terminology, a diamond sector. This $\phi=\phi_5$ limiting configuration is depicted in Figure A1.5b.

Configuration F, $\phi_6(y) \le \phi \le \phi_5$

As the phase angle ϕ is decreased from ϕ_5, an additional centred fan in material I bordering the interface is required. This new configuration is shown in Figure A1.6a. This configuration consists of:

Material I: starting from the upper crack face, CS-I sector, CF-I sector, general CS sector, and CF-II sector.

Material II: starting from the lower crack face, elastic sector, CF-II sector, and general CS sector.

There are 5 sector boundaries and 13 constants for the stresses. The conditions for determining these 18 unknowns are: 12 traction continuity conditions at 5 sector boundaries and 1 material interface, 2 traction free conditions for the lower crack face, 2 conditions from enforcing yielding in 2 general CS-sectors, 1 condition from enforcing yielding of the elastic stress state at sector boundary θ_3 in material II, and equation 8.4 relating the interface tractions. Thus, we can determine these 18 unknowns from these 18 conditions when a phase angle ϕ is specified. The details are given in the Appendix 2.

As the phase angle ϕ is decreased from ϕ_5, the sector boundary at θ_3 in material II rotates anti-clockwisely towards the interface and the stress state within the elastic sector in material II elevates. When ϕ is decreased to $\phi_6(y)$, the sector angle θ_3 becomes $-\pi/4$ and the stress state within the elastic sector reaches yield. This $\phi=\phi_6(y)$, limiting configuration is depicted in Figure A1.6b.

Configuration G, $-90^0 \le \phi \le \phi_6$

As the phase angle ϕ is decreased from ϕ_6, a new configuration emerges as shown in Figure A1.7. This configuration consists of:

Material I: starting from the upper crack face, CS-I sector, CF-I sector, general CS sector, and CF-II sector;

Material II: starting from the lower crack face, CS-II sector, CF-I sector, general CS sector, CF-II sector, and general CS sector.

There are 7 sector boundaries and 13 constants for the stresses. The conditions for determining these 20 unknowns are: 16 traction continuity conditions at 7 sector boundaries and 1material interface,3 conditions from enforcing yielding in 3 general CS-sectors, and equation 8.4 relating the interface tractions. Thus, we can determine the 20 unknowns from these 20

conditions when a phase angle ϕ is specified. The details are given in the Appendix 1. This configuration persists as the phase angle ϕ is decreased from $\phi_6(y)$ towards -90^0.

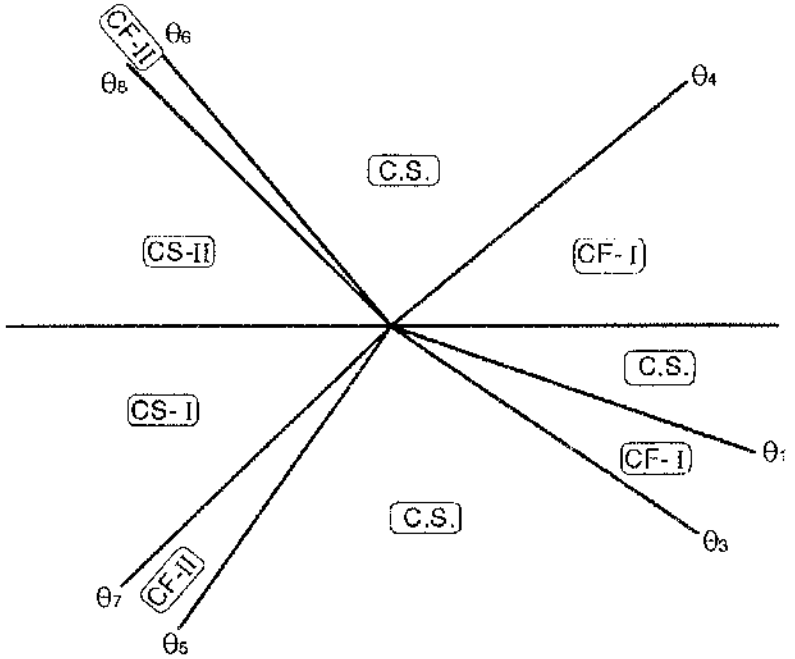

(a)

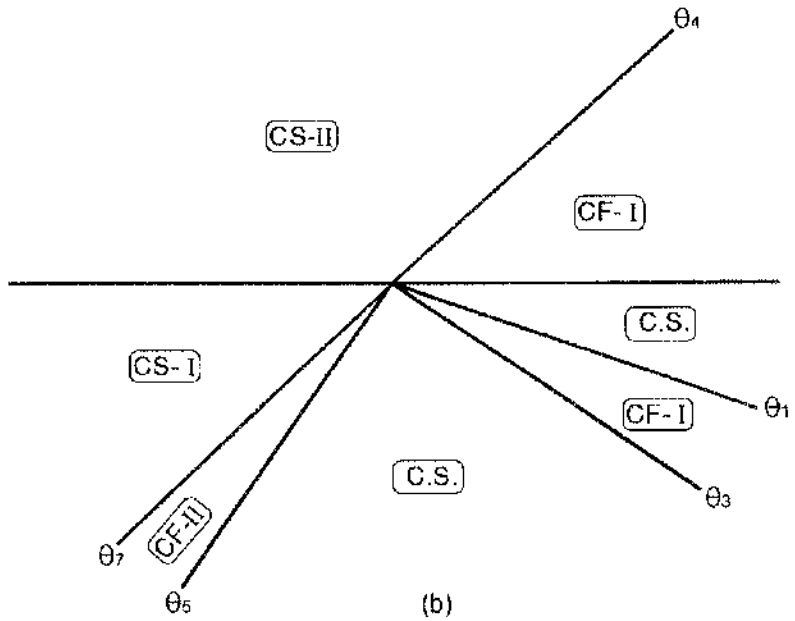

(b)

Figure A1-1 Sector configuration A (a) and Limiting configuration ϕ_1, (b).

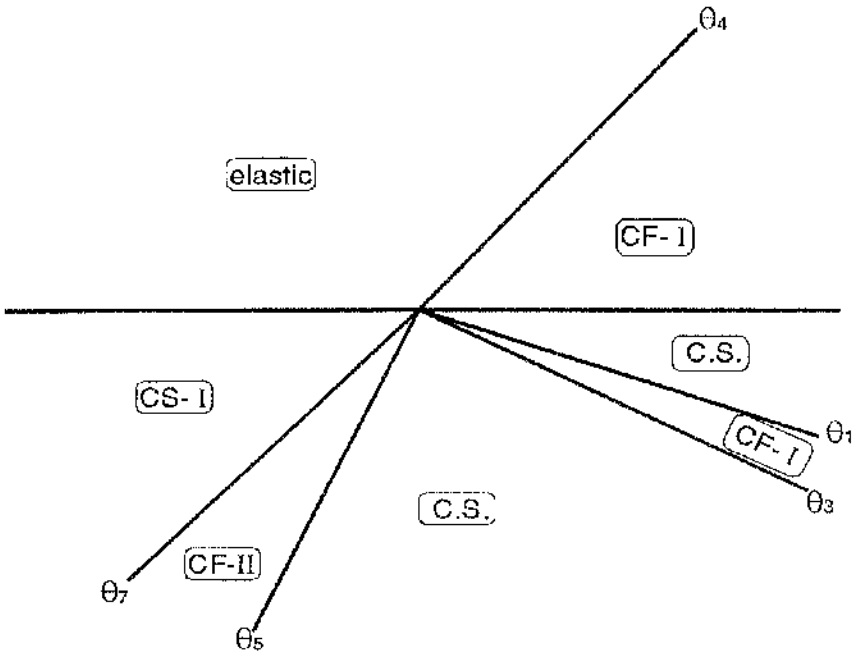

(a)

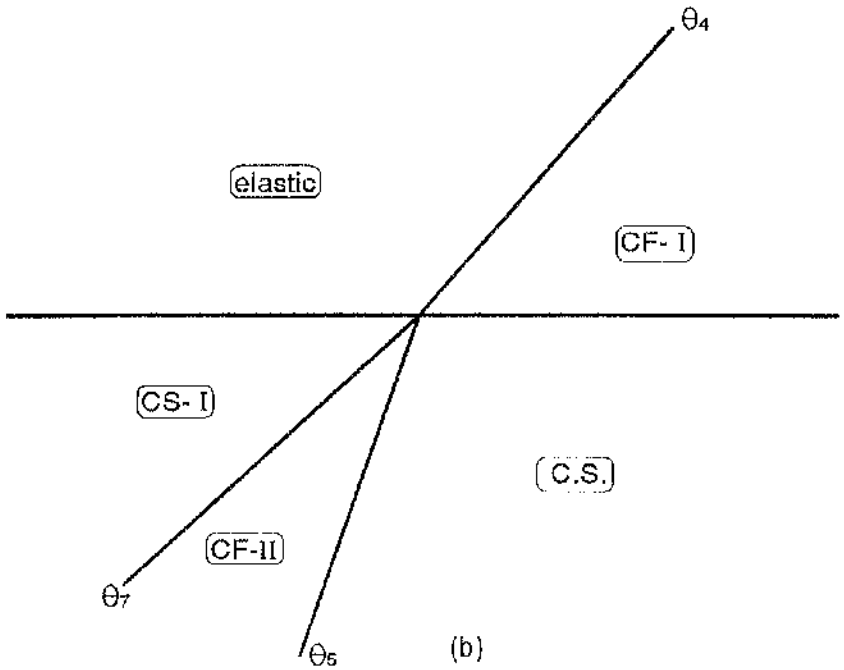

(b)

Figure A1-2 Sector configuration B (a) and Limiting configuration ϕ_2, (b).

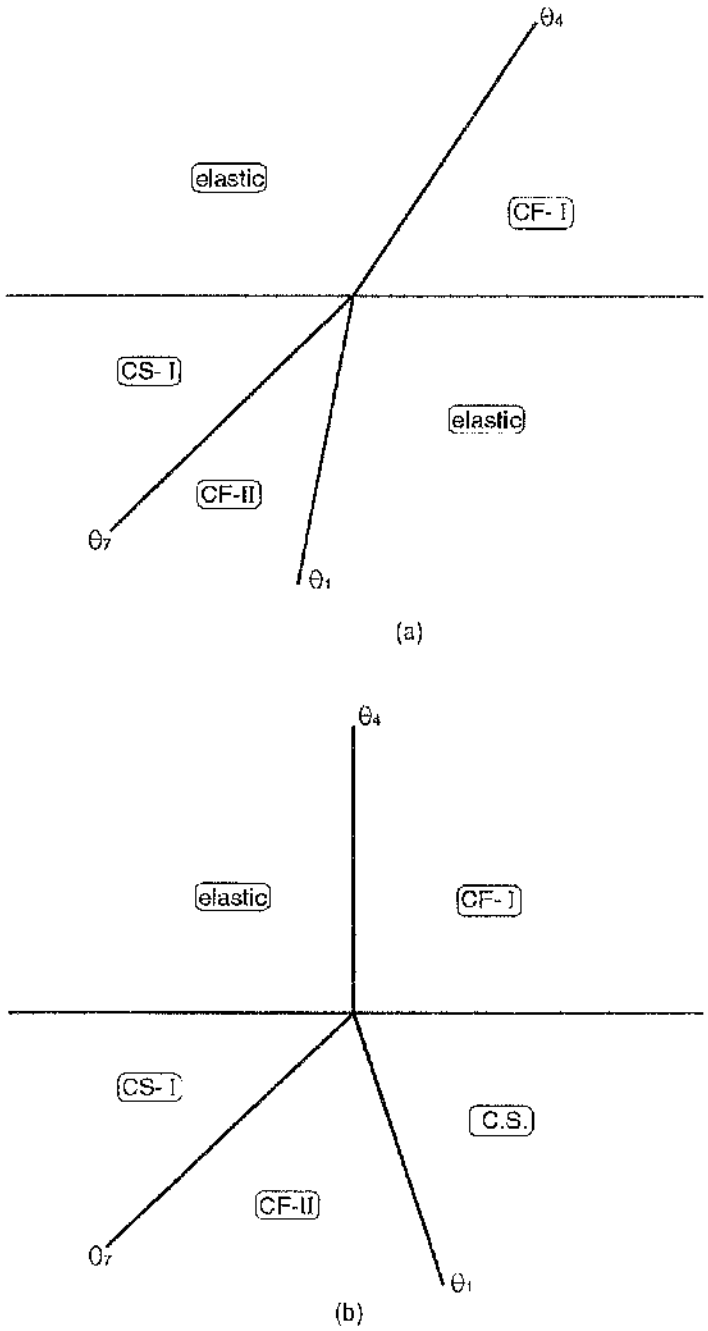

Figure A1-3 Sector configuration C (a) and Limiting configuration ϕ_3, (b).

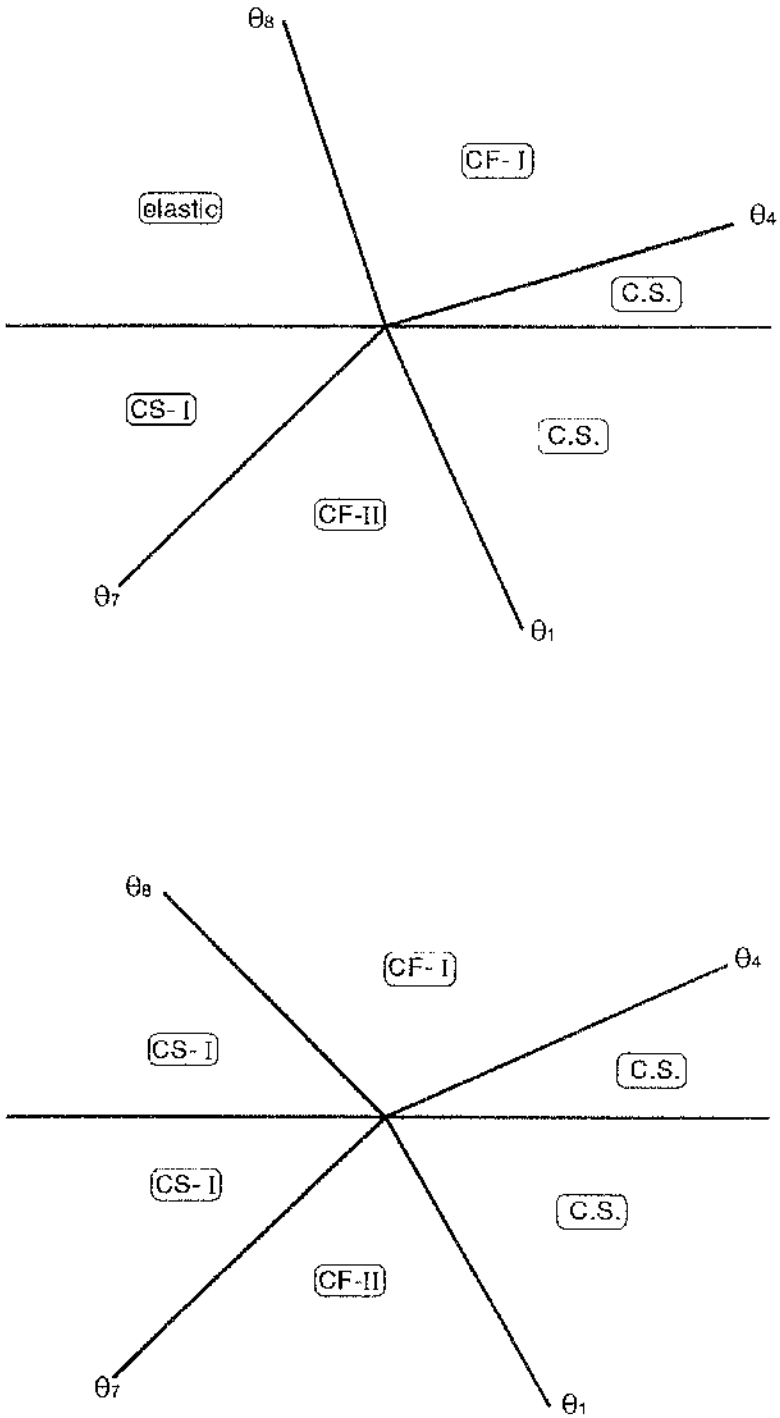

Figure A1-4 Sector configuration D (a) and Limiting configuration ϕ_4, (b).

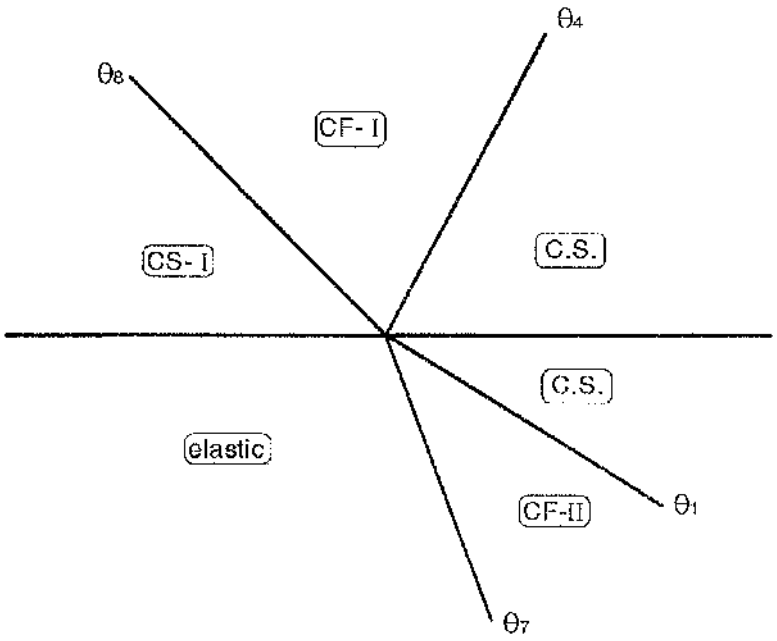

(a)

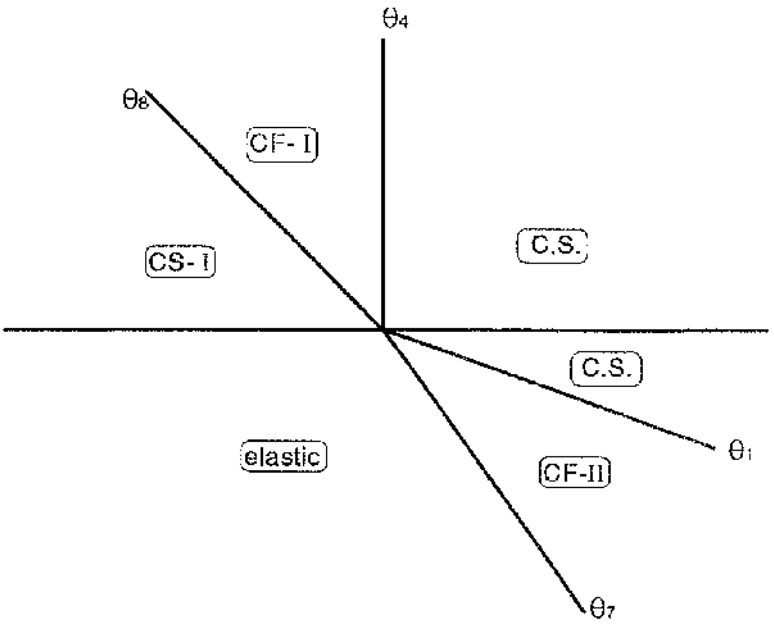

(b)

Figure A1-5 Sector configuration E (a) and Limiting configuration ϕ_5, (b).

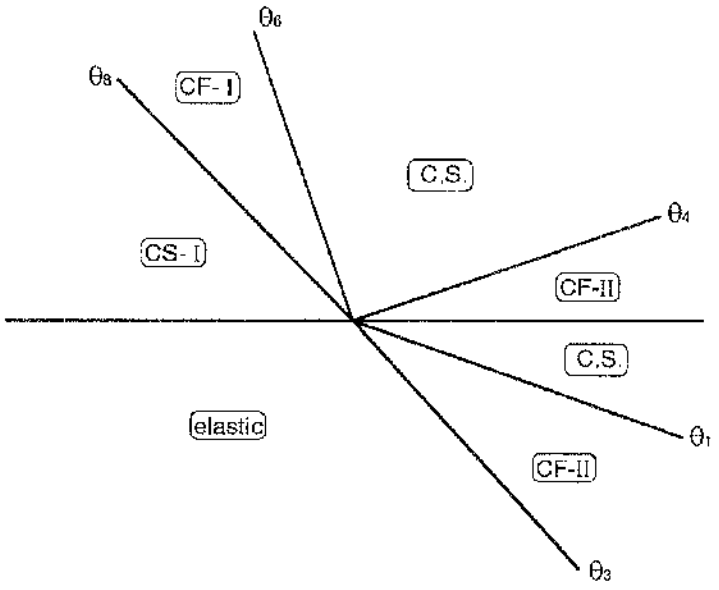

(a)

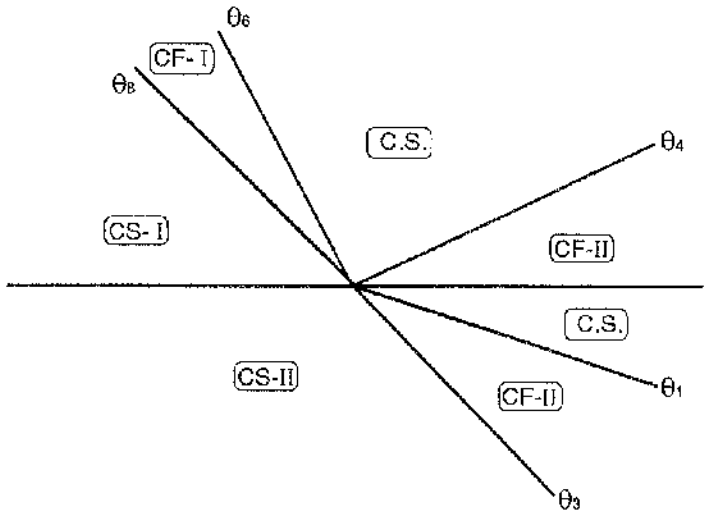

(b)

Figure A1-6 Sector configuration F (a) and Limiting configuration ϕ_6, (b).

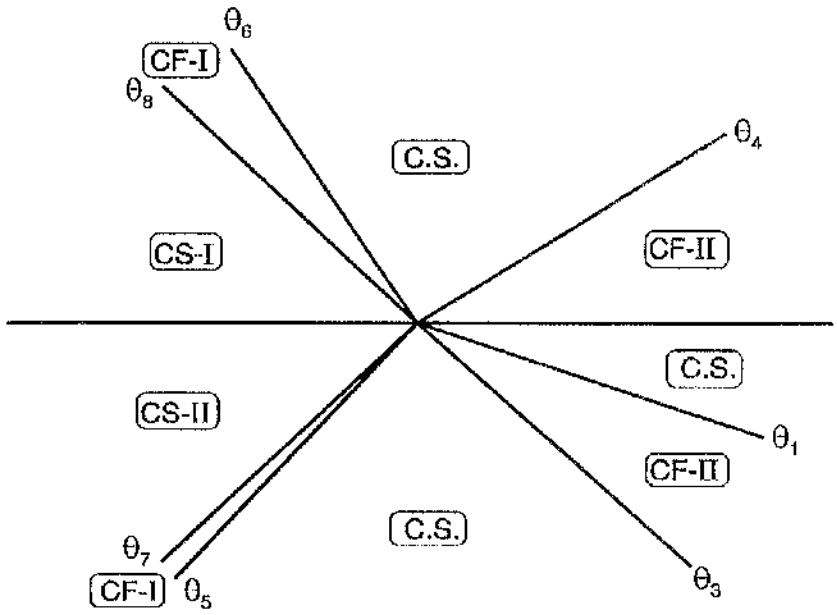

Figure A1-7 Sector configuration G.

Appendix 2

In this appendix, the details of the assembled crack tip sectors are presented for sector configurations covering the phase angles in the range $-90° \le \phi \le 90°$. The stress components are normalized with respect to k_1 which is the yield stress in shear in material I. These assemblies are for a mismatched yield strength factor, y, greater than 1.

1.1. Configuration A, $\phi_1 \le \phi \le 90°$

$$\theta_4 = (\cot\phi + 1)/4 + \pi/8 , \quad \theta_6 = \theta_4 + \pi/2 , \quad \theta_8 = 3\pi/4 , \quad \theta_5 = \theta_3 - \pi/2 , \quad \theta_7 = -3\pi/4$$

CS-II sector, $\theta_8 \le \theta \le \pi$

$$\bar{\sigma}_{11} = -2 , \quad \bar{\sigma}_{12} = \bar{\sigma}_{22} = 0 , \quad \bar{\sigma}_{33} = -1 .$$

CF-II sector, $\theta_6 \le \theta \le \theta_8$

$$\bar{\sigma}_{rr} = \bar{\sigma}_{\theta\theta} = \bar{\sigma}_{33} = -1 - 3\pi/2 + 2\theta , \quad \bar{\sigma}_{r\theta} = -1 .$$

General CS-sector, $\theta_4 \le \theta \le \theta_6$

$$\bar{\sigma}_{11} = \sin2\theta_6 + 2\theta_6 - 1 - 3\pi/2 , \quad \bar{\sigma}_{22} = -\sin2\theta_6 + 2\theta_6 - 1 - 3\pi/2 ,$$
$$\bar{\sigma}_{12} = -\cos2\theta_6 , \quad \bar{\sigma}_{33} = \tfrac{1}{2}(\bar{\sigma}_{11} + \bar{\sigma}_{22})$$

CF-I sector, $0 \le \theta \le \theta_4$

$$\bar{\sigma}_{rr} = \bar{\sigma}_{\theta\theta} = \bar{\sigma}_{33} = \cot\phi - 2\theta , \quad \bar{\sigma}_{r\theta} = 1 .$$

General CS-sector, $\theta_1 \le \theta \le 0$

$$\bar{\sigma}_{11} = -y\,(\sin2\theta_1 - 4\theta_3 + 2\theta_1 - 1 - \pi/2) , \quad \bar{\sigma}_{22} = -y\,(-\sin2\theta_1 - 4\theta_3 + 2\theta_1 - 1 - \pi/2) ,$$
$$\bar{\sigma}_{12} = y\cos2\theta_1 , \quad \bar{\sigma}_{33} = \tfrac{1}{2}(\bar{\sigma}_{11} + \bar{\sigma}_{22})$$

CF-I sector, $\theta_3 \le \theta \le \theta_1$

$$\bar{\sigma}_{rr} = \bar{\sigma}_{\theta\theta} = \bar{\sigma}_{33} = y\,(1 + \pi/2 + 4\theta_3) - 2y\theta , \quad \bar{\sigma}_{r\theta} = y .$$

General CS-sector, $\theta_5 \le \theta \le \theta_3$

$$\bar{\sigma}_{11} = y\,(-\sin2\theta_3 + 2\theta_3 + 1 + \pi/2) , \quad \bar{\sigma}_{22} = y\,(\sin2\theta_3 + 2\theta_3 + 1 + \pi/2) ,$$
$$\bar{\sigma}_{12} = y\cos2\theta_3 , \quad \bar{\sigma}_{33} = \tfrac{1}{2}(\bar{\sigma}_{11} + \bar{\sigma}_{22})$$

CF-II sector, $\theta_7 \le \theta \le \theta_5$

$$\bar{\sigma}_{rr} = \bar{\sigma}_{\theta\theta} = \bar{\sigma}_{33} = y\,(1 + 3\pi/2) + 2y\theta , \quad \bar{\sigma}_{r\theta} = -y .$$

CS-I sector, $-\pi \le \theta \le \theta_7$

$$\bar{\sigma}_{11} = 2y \ , \qquad \bar{\sigma}_{12} = \bar{\sigma}_{22} = 0 \ , \qquad \bar{\sigma}_{33} = y \ .$$

The sector angles θ_1 and θ_3 are given by the equations:

$$f_1(\theta_1) \equiv 1 - y \cos 2\theta_1 = 0 \ , \qquad \text{with } -\pi < \theta_1 < 0 \tag{A.1}$$

$$f_2(\theta_1, \theta_3) \equiv y \sin\phi \ (\sin 2\theta_1 + 1 + \pi/2 + 4\theta_3 - 2\theta_1) - \cos\phi = 0 \tag{A.2}$$

A limiting sector configuration is realized as the phase angle ϕ is decreased from 90° towards $\phi = \phi_1$ at which the CF-II sector in the angular range $\theta_6 \le \theta \le \theta_8$ vanishes. The limiting phase angle ϕ_1 can be obtained by setting $\theta_6 = 3\pi/4$ in the above equations for the sector angles. This gives

$$\theta_4 = \pi/4 \ , \qquad \phi_1 = \cot^{-1}(-1 + \pi/2) = 60.28° \ . \tag{A.3}$$

Using these angles for the sector boundaries, the expressions given above can be used to obtain the stresses in the remaining sectors in this limiting configuration.

1.2. Configuration B, $\phi_2(y) \le \phi \le \phi_1$

$$\theta_5 = \theta_3 - \pi/2 \ , \qquad \theta_7 = -3\pi/4 \ , \qquad \cos 2\theta_4 \neq 1$$

Elastic sector, $\theta_4 \le \theta \le \pi$

The stress components in this elastic sector are given by equations (1.22). The constants, as normalized by k_1, are given by

$$\bar{E}_3 = 4\bar{E}_1 \ , \qquad \bar{E}_4 = 2\bar{E}_2 - 4\pi\bar{E}_1 \ ,$$

$$\bar{E}_1 = \frac{\cos 2\theta_4}{1 - \cos 2\theta_4} \ , \qquad \bar{E}_2 = -\frac{\sin 2\theta_4}{1 - \cos 2\theta_4} \ ,$$

CF-I sector, $0 \le \theta \le \theta_4$

$$\bar{\sigma}_{rr} = \bar{\sigma}_{\theta\theta} = \bar{\sigma}_{33} = -(\sin 2\theta_4 + 2\pi \cos 2\theta_4 - 2\theta_4) / (1 - \cos 2\theta_4) - 2\theta \ , \qquad \bar{\sigma}_{r\theta} = 1 \ .$$

General CS-sector, $\theta_1 \le \theta \le 0$

$$\bar{\sigma}_{11} = y \ (-\sin 2\theta_1 + 4\theta_3 - 2\theta_1 + 1 + \pi/2) \ , \qquad \bar{\sigma}_{22} = y \ (\sin 2\theta_1 + 4\theta_3 - 2\theta_1 + 1 + \pi/2) \ ,$$

$$\bar{\sigma}_{12} = y \cos 2\theta_1 \ , \qquad \bar{\sigma}_{33} = \tfrac{1}{2} (\bar{\sigma}_{11} + \bar{\sigma}_{22})$$

CF-I sector, $\theta_3 \le \theta \le \theta_1$

$$\bar{\sigma}_{rr} = \bar{\sigma}_{\theta\theta} = \bar{\sigma}_{33} = \nu \ (1 + \pi/2 + 4\theta_3) - 2y\theta \ , \qquad \bar{\sigma}_{r\theta} = y \ .$$

General CS-sector, $\theta_5 \le \theta \le \theta_3$

$$\bar{\sigma}_{11} = y \ (-\sin 2\theta_3 - 2\theta_3 + 1 + \pi/2) \ , \qquad \bar{\sigma}_{22} = y \ (\sin 2\theta_3 + 2\theta_3 + 1 + \pi/2) \ ,$$

$$\bar{\sigma}_{12} = y \cos 2\theta_3 \ , \qquad \bar{\sigma}_{33} = \tfrac{1}{2} (\bar{\sigma}_{11} + \bar{\sigma}_{22})$$

CF-II sector, $\theta_7 \le \theta \le \theta_5$

$$\bar{\sigma}_{rr} = \bar{\sigma}_{\theta\theta} = \bar{\sigma}_{33} = y\ (\ 1 + 3\pi/2\ ) + 2y\theta\ , \qquad \bar{\sigma}_{r\theta} = -\ y\ .$$

CS-I sector, $-\pi \le \theta \le \theta_7$

$$\bar{\sigma}_{11} = 2y\ , \qquad \bar{\sigma}_{12} = \bar{\sigma}_{22} = 0\ , \qquad \bar{\sigma}_{33} = y\ .$$

The sector angles θ_1, θ_3 and θ_4 are given by the equations:

$$f_1(\theta_1) \equiv 1 - y\ \cos 2\theta_1 = 0\ , \qquad \text{with} \quad -\pi < \theta_1 < 0 \tag{A.4}$$

$$f_2(\theta_1, \theta_3, \theta_4) \equiv \Big[\ y\ (\ -2\theta_1 + 4\theta_3 + \pi/2 + \sin 2\theta_1 + 1\ ) - 2\pi\ \Big]\ \cos 2\theta_4$$

$$+\ y\ (\ -\sin 2\theta_1 + 2\theta_1 - 4\theta_3 - \pi/2 - 1\ ) + 2\theta_4 - \sin 2\theta_4 = 0\ . \tag{A.5}$$

$$f_3(\theta_4) \equiv (\ 2\theta_4 - \sin 2\theta_4 - 2\pi\ \cos 2\theta_4\ )\ \sin\phi - (1 - \cos 2\theta_4)\ \cos\phi = 0, \tag{A.6}$$

From eqn (A.6), it can been seen that the condition of $\cos 2\theta_4 \neq 1$ is satisfied as $\phi \neq 0$ for the range of phase angles that this sector configuration is valid.

A limiting sector configuration is approached as the phase angle ϕ is decreased from $\phi = \phi_1$ towards $\phi = \phi_2(y)$ at which the CF-I sector in the angular range $\theta_3 \le \theta \le \theta_1$ vanishes. This limiting phase angle $\phi_2(y)$ for a given mismatched factor y can be obtained by the following steps.

Given y, solve for θ_1 from eqn (A.4). Set $\theta_3 = \theta_1$ and use eqn (A.5) to solve for θ_4. Once θ_4 is found, we can solve for the limiting phase angle $\phi_2(y)$ from eqn. (A.6).

1.3. Configuration C, $\phi_3(y) \le \phi \le \phi_2(y)$

$$\theta_7 = -\ 3\pi/4\ , \qquad \cos 2\theta_4 \neq 1\ , \qquad \theta_1 \neq 0$$

Elastic sector I, $\theta_4 \le \theta \le \pi$

The stress components in this elastic sector are given by equations (1.22). The constants, as normalized by k_1, are given by

$$\bar{E}_3 = 4\bar{E}_1\ , \qquad \bar{E}_4 = 2\bar{E}_2 - 4\pi\bar{E}_1\ ,$$

$$\bar{E}_1 = \frac{\cos 2\theta_4}{1 - \cos 2\theta_4}\ , \qquad \bar{E}_2 = -\ \frac{\sin 2\theta_4}{1 - \cos 2\theta_4}\ ,$$

CF-I sector, $0 \le \theta \le \theta_4$

$$\bar{\sigma}_{rr} = \bar{\sigma}_{\theta\theta} = \bar{\sigma}_{33} = -\ (\sin 2\theta_4 + 2\pi\ \cos 2\theta_4 - 2\theta_4)\ /\ (1 - \cos 2\theta_4) - 2\theta\ , \qquad \bar{\sigma}_{r\theta} = 1\ .$$

Elastic sector II, $\theta_1 \le \theta \le 0$

The stress components in this elastic sector are given by equations (1.22). The constants E_1, E_2 and E_3, as normalized by k_1, are given by

$$\bar{E}_1 = (\ y\ (2 + 3\pi) - \bar{E}_4\ )\ \cos 2\theta_1\ /\ (4\theta_1)\ , \qquad \bar{E}_2 = -\ (\ y\ (2 + 3\pi) - \bar{E}_4\ )\ \sin 2\theta_1\ /\ (4\theta_1) \tag{A.7a}$$

$$\bar{E}_3 = (\ y\ (\ 4\theta_1 + 2 + 3\pi\ ) - \bar{E}_4\ )\ /\ \theta_1 \tag{A.7b}$$

CF-II sector, $\theta_7 \le \theta \le \theta_1$

$$\bar{\sigma}_{rr} = \bar{\sigma}_{\theta\theta} = \bar{\sigma}_{33} = y\ (\ 1 + 3\pi/2\ ) + 2y\theta\ , \qquad \bar{\sigma}_{r\theta} = -\,y\ .$$

CS-I sector, $-\pi \le \theta \le \theta_7$

$$\bar{\sigma}_{11} = 2y\ , \qquad \bar{\sigma}_{12} = \bar{\sigma}_{22} = 0\ , \qquad \bar{\sigma}_{33} = y\ .$$

The sector angles θ_1 and θ_4 and the constant $\bar{E}_4$ for elastic sector II are given by the following equations:

$$f_1(\theta_1) \equiv (\bar{E}_4 - (2 + 3\pi)\ y)\ \cos2\theta_1 + (2 + 3\pi + 4\theta_1)\ y + 4\theta_1 - \bar{E}_4 = 0\ , \qquad \text{with} \quad -\pi < \theta_1 < 0 \qquad \text{(A.8)}$$

$$f_2(\theta_1, \theta_4, \bar{E}_4) \equiv \Big[\ -\sin2\theta_1(2 + 3\pi)\ y + \bar{E}_4(-\,2\theta_1 + \sin2\theta_1) + 8\pi\theta_1\ \Big]\ \cos2\theta_4$$

$$+ \sin2\theta_1(2 + 3\pi)\ y + 4\theta_1\ (\sin2\theta_4 - 2\theta_4) - \bar{E}_4\ (\sin2\theta_1 - 2\theta_1) = 0\ , \qquad \text{(A.9)}$$

$$f_3(\theta_4) \equiv \Big[\ 2\theta_4 - \sin2\theta_4 - 2\pi\ \cos2\theta_4\ \Big]\ \sin\phi - (1 - \cos2\theta_4)\ \cos\phi = 0\ . \qquad \text{(A.10)}$$

Again, we find from eqn (A.10) that the condition of $\cos2\theta_4 \neq 1$ is satisfied as $\phi \neq 0$ in the range of phase angles that this sector configuration is valid.

A limiting sector configuration is realized as the phase angle ϕ is decreased from $\phi = \phi_2(y)$ towards $\phi = \phi_3(y)$ at which the stress state of elastic sector II reaches yield everywhere within the angular range $\theta_1 \le \theta \le 0$. To determine such a limiting configuration, we may use the general expressions for the elastic stresses given in eqns (1.22) to evaluate the yield function f. If the elastic stress state reaches yield within the entire sector, we must have

$$f\ (\theta) = 0\ , \qquad \text{and} \qquad df\ (\theta)/d\theta = 0\ . \qquad \text{(A.11)}$$

The second condition leads to

$$(\ E_1\ \sin2\theta + E_2\ \cos2\theta\ )\ E_3 = 0$$

which is satisfied everywhere in the sector if $E_3 = 0$. Using $\bar{E}_3 = 0$ in eqn (A.7b), we find

$$\bar{E}_4 = y\ (\ 4\theta_1 + 2 + 3\pi\ )\ ,$$

and the constants $\bar{E}_1$ and $\bar{E}_2$ in (A.7a) are reduced to

$$\bar{E}_1 = -\,y\ \cos2\theta_1\ , \qquad \bar{E}_2 = y\ \sin2\theta_1\ .$$

Using these constants in eqns (1.23), we find

$$\bar{\sigma}_{11} = y\ (\ \sin2\theta_1 + 2\theta_1 + 1 + 3\pi/2\ )\ , \qquad \bar{\sigma}_{22} = y\ (\ -\sin2\theta_1 + 2\theta_1 + 1 + 3\pi/2\ )\ ,$$

$$\bar{\sigma}_{12} = -\,y\ \cos2\theta_1\ , \qquad \bar{\sigma}_{33} = \tfrac{1}{2}\ (\bar{\sigma}_{11} + \bar{\sigma}_{22})\ .$$

It can be verified that these stresses satisfy the yield condition and hence they represent the stress state of a general CS sector.

In this limit, we find further that eqn (A.8) is simplified to

$$f_1(\theta_1) = 1 + y\ \cos2\theta_1 = 0\ , \qquad \text{with} \quad -\pi < \theta_1 < 0\ . \qquad \text{(A.12)}$$

For a given value of y, eqn (A.12) gives two roots in the said range of θ_1. The more negative root corresponds to the limiting configuration for $\phi = \phi_2(y)$. The less negative root gives the value of θ_1 for the limiting configuration $\phi = \phi_3(y)$. To determine the limiting phase angle $\phi_3(y)$ for a given y, substitute the appropriate value of θ_1 and the corresponding $\bar{E}_4$ from above into eqn (A.9). Determine θ_4 from the resulting equation.

The limiting phase angle $\phi_3(y)$ can then be determined from eqn (A.10).

1.4. Configuration D, $\phi_4(y) \le \phi \le \phi_3(y)$

$$\theta_7 = -3\pi/4 , \qquad \cos2\theta_8 \neq 1$$

Elastic sector, $\theta_8 \le \theta \le \pi$

The stress components in this elastic sector are given by equations (1.22). The constants, as normalized by k_1, are given by

$$\bar{E}_3 = 4\bar{E}_1 , \qquad \bar{E}_4 = 2\bar{E}_2 - 4\pi\bar{E}_1 , \tag{A.13a}$$

$$\bar{E}_1 = \frac{\cos2\theta_8}{1-\cos2\theta_8} , \qquad \bar{E}_2 = -\frac{\sin2\theta_8}{1-\cos2\theta_8} , \tag{A.13b}$$

CF-I sector, $\theta_4 \le \theta \le \theta_8$

$$\bar{\sigma}_{rr} = \bar{\sigma}_{\theta\theta} = \bar{\sigma}_{33} = -(\sin2\theta_8 + 2\pi\cos2\theta_8 - 2\theta_8)/(1-\cos2\theta_8) - 2\theta , \qquad \bar{\sigma}_{r\theta} = 1 .$$

General CS-sector, $0 \le \theta \le \theta_4$

$$\bar{\sigma}_{11} = (2\pi - 2\theta_4 - \sin2\theta_4) - (2\pi - 2\theta_8 + \sin2\theta_8)(1+\cos2\theta)/\sin^2 2\theta_8 ,$$

$$\bar{\sigma}_{22} = (2\pi - 2\theta_4 + \sin2\theta_4) - (2\pi - 2\theta_8 + \sin2\theta_8)(1+\cos2\theta_8)/\sin^2 2\theta_8 ,$$

$$\bar{\sigma}_{12} = \cos2\theta_4 , \qquad \bar{\sigma}_{33} = \tfrac{1}{2}(\bar{\sigma}_{11} + \bar{\sigma}_{22})$$

General CS-sector, $\theta_1 \le \theta \le 0$

$$\bar{\sigma}_{11} = y\,(2\theta_1 + 3\pi/2 + 1 + \sin2\theta_1) , \qquad \bar{\sigma}_{22} = y\,(2\theta_1 + 3\pi/2 + 1 - \sin2\theta_1)$$

$$\bar{\sigma}_{12} = -y\cos2\theta_1 , \qquad \bar{\sigma}_{33} = \tfrac{1}{2}(\bar{\sigma}_{11} + \bar{\sigma}_{22})$$

CF-II sector, $\theta_7 \le \theta \le \theta_1$

$$\bar{\sigma}_{rr} = \bar{\sigma}_{\theta\theta} = \bar{\sigma}_{33} = y\,(1 + 3\pi/2) + 2y\theta , \qquad \bar{\sigma}_{r\theta} = -y .$$

CS-I sector, $-\pi \le \theta \le \theta_7$

$$\bar{\sigma}_{11} = 2y , \qquad \bar{\sigma}_{12} = \bar{\sigma}_{22} = 0 , \qquad \bar{\sigma}_{33} = y .$$

The sector angles θ_1, θ_4 and θ_8 are given by the following equations:

$$f_1(\theta_1, \theta_4) \equiv y\cos2\theta_1 + \cos2\theta_4 = 0 , \qquad \text{with} \quad -\pi < \theta_1 < 0 , \qquad 0 < \theta_4 < \pi \tag{A.14}$$

$$f_2(\theta_1, \theta_4, \theta_8) \equiv \Big[(2\theta_1 + 3\pi/2 + 1 - \sin2\theta_1)y - \sin2\theta_4 - 2\pi + 2\theta_4\Big]\cos2\theta_8$$

$$+ (-2\theta_1 - 3\pi/2 - 1 + \sin2\theta_1)y - \sin2\theta_8 + \sin2\theta_4 - 2\theta_4 + 2\theta_8 = 0 , \tag{A.15}$$

$$f_3(\theta_1) \equiv (\sin2\theta_1 - 1 - 2\theta_1 - 3\pi/2)\sin\phi - \cos2\theta_1\cos\phi = 0 \tag{A.16}$$

Appendix 3

Other Phase Angles and Yield Strength Mismatches

The results presented in the previous sections for a mismatch factor y>1 can be extended to the case of *y<1* in the following manner. Let the results for $y=\bar{y}<1$ at phase angle $\phi=\bar{\phi}$ be desired. Then the sector configuration for this case will be the same as the one for $y=1\backslash\bar{y}$ and $\phi=\bar{\phi}$. The stresses are obtained by using the following transformations:

$$\sigma_{rr}(\theta;\bar{y},\bar{\phi})=\sigma_{rr}(-\theta;1/\bar{y},-\bar{\phi}) \qquad \text{(A3-1)}$$

$$\sigma_{\theta\theta}(\theta;\bar{y},\bar{\phi})=\sigma_{\theta\theta}(-\theta;1/\bar{y},-\bar{\phi}) \qquad \text{(A3-2)}$$

$$\sigma_{33}(\theta;\bar{y},\bar{\phi})=\sigma_{33}(-\theta;1/\bar{y},-\bar{\phi}) \qquad \text{(A3-3)}$$

$$\sigma_{r\theta}(\theta;\bar{y},\bar{\phi})=\sigma_{r\theta}(-\theta;1/\bar{y},-\bar{\phi}) \qquad \text{(A3-4)}$$

For the same strength mismatch the previous results may be extended to cases for which the phase angle is outside the range $-90° \le \phi \le 90°$ in the following manner. Let $\phi=\bar{\phi}$, where $90°<|\bar{\phi}|<180°$ be a phase angle for which the crack tip stress field is desired. The sector configuration for $\phi=\bar{\phi}$ is the same as the one with a phase angle $\phi=\tilde{\phi}$.

$$\tilde{\phi}=\bar{\phi}\pm 180° \qquad \text{(A3-5)}$$

The plus or minus sign is selected so that $-90° \le \tilde{\phi} \le 90°$. The stresses for the desired phase angle $\bar{\phi}$ can be obtained by using the following transformations:

$$\sigma_{rr}\left(\theta;\bar{\phi}\right)=-\sigma_{rr}\left(-\theta;\tilde{\phi}\right) \tag{A3-6}$$

$$\sigma_{\theta\theta}\left(\theta;\bar{\phi}\right)=-\sigma_{\theta\theta}\left(-\theta;\tilde{\phi}\right) \tag{A3-6}$$

$$\sigma_{r\theta}\left(\theta;\bar{\phi}\right)=-\sigma_{r\theta}\left(-\theta;\tilde{\phi}\right) \tag{A3-6}$$

$$\sigma_{33}\left(\theta;\bar{\phi}\right)=-\sigma_{33}\left(-\theta;\tilde{\phi}\right) \tag{A3-6}$$